

# Acquisition and Processing Report of the MULSEDRO EIT RM Project from the Otanmäki Fe–Ti–V Deposit, Finland

## UAS and Ground-Based Magnetic and Hyperspectral Investigations in 2018

Robert Jackisch, Markku Pirttijärvi, Heikki Salmirinne, Kimmo Kärenlampi, Björn Heincke, Jouko Jylänki, Robert Zimmermann, Erik Vest Sørensen, Maarit Middleton, Yuleika Madriz and Richard Gloaguen

**GTK Open File Research Report 87/2019**

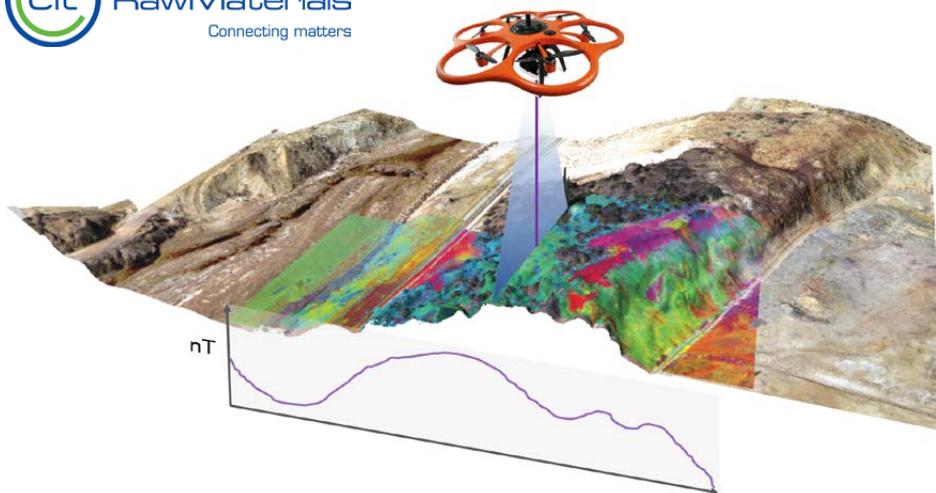


# GEOLOGICAL SURVEY OF FINLAND

Open File Research Report 87/2019

Robert Jackisch, Markku Pirttijärvi, Heikki Salmirinne, Kimmo Kärenlampi,  
Björn Heincke, Jouko Jylänki, Robert Zimmermann, Erik Vest Sørensen,  
Maarit Middleton, Yuleika Madriz and Richard Gloaguen

## Acquisition and Processing Report of the MULSEDRO EIT RM Project from the Otanmäki Fe–Ti–V Deposit, Finland – UAS and Ground-Based Magnetic and Hyperspectral Investigations in 2018



GEUS



radai



© S.Jakob@HIF

MULSEDRO –  
Multi-sensor Drones for Geology Mapping



Unless otherwise indicated, the figures have been prepared by the authors of the report.

Layout: Elvi Turtiainen Oy

Espoo 2019

**Jackisch, R., Pirttijärvi, M., Salmirinne, H., Kärenlampi, K., Heincke, B., Jylänki, J., Zimmermann, R., Sørensen, E. V., Middleton, M., Madriz, Y. & Gloaguen, R. 2019.** Acquisition and Processing Report of the MULSEDRO EIT RM Project from the Otanmäki Fe–Ti–V Deposit, Finland – UAS and Ground-Based Magnetic and Hyperspectral Investigations in 2018. *Geological Survey of Finland, Open File Research Report 87/2019*, 93 pages, 84 figures, 7 tables and 8 appendices.

MULSEDRO is an EIT RawMaterials project of a consortium of Finnish, German, Danish and Swedish institutions and companies that aims to develop multi-sensor drone systems for mineral exploration. In September 2018, a field campaign was performed to test the newly designed UAS systems at the Otanmäki Fe–Ti–V deposit in central Finland. In this report, the acquisition and processing of UAS-based magnetic, multi- and hyperspectral datasets in Otanmäki are described. In order to validate the drone-borne data, a ground magnetic survey was acquired and in situ measurements with hhXRF and VNIR-SWIR spectrometers, as well as magnetic susceptibility meter measurements, were performed. A strategy for integrating all the data is introduced, aiming to improve the mapping and evaluation of the near-surface oxide ore distributions.

The survey area was covered with four magnetic UAS surveys using both multi-copter and fixed-wing drones equipped with fluxgate magnetometers. The drones operated at different altitude levels (15, 40 and 65 m a.g.l.) and line spacings (7, 20, 35 and 40 m), resulting in magnetic information with very different scales of resolution. An equivalent layer modelling (ELM) procedure was jointly applied to all the magnetic datasets to present the magnetic surveys with very different acquisition parameters in one consistent total magnetic intensity plot and to evaluate the consistency of data from the different magnetic surveys. Multi- and hyperspectral data were acquired at a high resolution and geolocated with precisely spatially surveyed control points. Although the lichen and vegetation coverage reduced the total number of visible bare ground pixels by roughly 30%, the application of different band ratios and classification algorithms made it generally possible to adequately map iron-bearing alteration minerals such as hematite and goethite from the UAS-based datasets.

The combination of lightweight UAS technologies and ground truthing measurements was demonstrated to be advantageous in rapidly mapping ore-rich outcrops and created a multi-parameter and multi-scale dataset well suited to data integration. The magnetic maps correlated well with both susceptibility values from profiling and ore occurrences visible at the surface, and the iron-bearing phases could be successfully mapped by UAS-borne multi- and hyperspectral sensors in the VNIR. The acquired datasets partly complement each other, e.g. UAS-borne magnetic anomalies can be associated with ore lenses in areas where spectral features are hidden by lichen or vegetation.

**Keywords:** unmanned aerial vehicles, remote sensing, geophysics, magnetic methods, hyperspectral analysis, multispectral analysis, mineral exploration

*Robert Jackisch<sup>1</sup>, Markku Pirttijärvi<sup>2</sup>, Heikki Salmirinne<sup>3</sup>, Kimmo Kärenlampi<sup>4</sup>, Björn Heincke<sup>5</sup>, Jouko Jylänki<sup>6</sup>, Robert Zimmermann<sup>1</sup>, Erik Vest Sørensen<sup>5</sup>, Maarit Middleton<sup>3</sup>, Yuleika Madriz<sup>1</sup> and Richard Gloaguen<sup>1</sup>*

<sup>1</sup> Helmholtz-Zentrum Dresden-Rossendorf – Helmholtz Institute Freiberg for Resource Technology (HZDR-HIF), Freiberg, Germany

<sup>2</sup> Radai Oy, Oulu, Finland

<sup>3</sup> Geological Survey of Finland (GTK), Rovaniemi, Finland

<sup>4</sup> Oulu Mining School, University of Oulu, Finland

<sup>5</sup> Geological Survey of Denmark and Greenland (GEUS), Copenhagen, Denmark

<sup>6</sup> Otanmäki Mine Oy, Finland

E-mail: [jackis65@hzdr.de](mailto:jackis65@hzdr.de) (Robert Jackisch)

# CONTENTS

TECHNICAL ABBREVIATIONS .....	5
SUMMARY .....	6
1 INTRODUCTION .....	7
2 BACKGROUND INFORMATION .....	9
2.1 Geology .....	9
2.2 Mining History .....	10
2.3 Summary of previously collected geophysical data .....	10
2.4 Site description.....	11
3 FIELD ACTIVITIES AND MEASUREMENTS.....	17
3.1 Magnetic measurements by UASs .....	18
3.1.1 Fixed-wing magnetic survey .....	18
3.1.1.1 Magnetic fixed-wing system .....	18
3.1.1.2 Acquisition .....	20
3.1.1.3 Data processing .....	26
3.1.1.4 Equivalent layer modelling (ELM).....	28
3.1.1.5 Results .....	28
3.1.2 Multi-copter magnetic survey.....	39
3.1.2.1 Acquisition .....	42
3.1.2.2 Processing .....	44
3.1.2.3 Data evaluation and results.....	45
3.2 Optical remote sensing from UASs.....	53
3.2.1 Photogrammetry .....	53
3.2.2 UAS multi- and hyperspectral imaging.....	53
3.2.2.1 Multispectral imaging.....	53
3.2.2.2 Hyperspectral imaging.....	55
3.2.2.3 Multispectral Sequoia fixed-wing results.....	57
3.2.2.4 Rikola HSI copter-borne results .....	62
3.2.3 UAS LiDAR .....	68
3.3 Ground-based measurements .....	68
3.3.1 Ground magnetic survey .....	68
3.3.2 Other ground measurements .....	71
3.3.2.1 GNSS Surveying .....	72
3.3.2.2 VNIR-SWIR spectroscopy .....	72
3.3.2.3 Magnetic susceptibility.....	75
3.3.2.4 Handheld XRF .....	75
3.3.2.5 Sampling and geological mapping.....	75
4 DATA COMPARISON AND INTEGRATION.....	77
4.1 Relationships between ground-based hhXRF, magnetic susceptibility and spectroscopy data .....	77
4.2 Data integration .....	78
5 INTEGRATION OF ALL MAGNETIC DATASETS BY MEANS OF EQUIVALENT LAYER MODELLING....	83

6 CONCLUSION AND OUTLOOK .....	89
6.1 Closing remarks .....	89
6.2 Outlook .....	91
ACKNOWLEDGEMENTS .....	92
REFERENCES.....	92
APPENDICES .....	94
Appendix 1. Role of institutions in the MULSEDRO project	
Appendix 2. Participants in the Otanmäki field campaign	
Appendix 3. List of ground control points (Metsämalmi outcrop)	
Appendix 4. Agisoft Photoscan automatic processing report S.O.D.A	
Appendix 5. Agisoft Photoscan automatic processing report Sequioa	
Appendix 6. List of ground truth sampling point coordinates	
Appendix 7. List of handheld susceptibility measurements	
Appendix 8. List of hhXRF measurements	

## TECHNICAL ABBREVIATIONS

AGL – Above ground level  
CIR – Colour Infrared  
CMOS – Complementary metal oxide semiconductor  
DEM – Digital elevation model (digital surface model)  
ELM – Equivalent layer modelling  
FFT – Fast Fourier transform  
FWHM – Full width at half maximum  
GCP – Ground control point  
GNSS – Global Navigation Satellite System  
GSD – Ground sampling distance  
hhXRF – Handheld X-ray fluorescence  
HSI – Hyperspectral image  
IDW – Inverse distance weighting  
IPS – Integrated Positioning System  
LiDAR – Light detection and ranging  
MNF – Minimum noise fraction  
MVS – Multi-view stereo  
NDVI – Normalized Difference Vegetation Index  
NIR – Near infrared  
p-value – Probability value  
PCA – Principal component analysis  
r – Pearson correlation  
QA/QC – Quality assurance/quality control  
R<sup>2</sup> – Coefficient of determination  
REE – Rare earth element  
RGB – Red green blue  
RMS – Root mean square  
SfM – Structure from motion  
SNR – Signal-to-noise ratio  
SWIR – Short-wave infrared  
TMI – Total magnetic intensity  
VIS – Visible spectrum  
VNIR – Visible-near infrared  
UAS – Unmanned aerial system

## SUMMARY

MULSEDRO is an EIT RawMaterial project of a consortium of Finnish, German, Danish and Swedish institutions and companies that aims to develop multi-sensor drone systems for mineral exploration. In September 2018, a field campaign was performed to test the newly designed UAS systems at the Otanmäki Fe–Ti–V deposit in central Finland. The UAS systems are able to gather high-quality geophysical and remote sensing data relevant to the mining industry within short time and in a non-invasive manner. The main target was a cleaned bedrock exposure (Metsämalmi area) on the premises of the former Otanmäki mine, which produced iron, titanium and vanadium products until 1985. The company Otanmäki Mine Oy plans to re-open the mine in the near future, and in this context, the collected datasets could improve the precision of distribution mapping of ore lenses as a basis for a better ore grade estimation.

The UAS surveys comprised hyper-/multispectral, magnetic, photogrammetric and LiDAR surveys from fixed-wing and/or multi-copter drones. In addition, a ground magnetic survey was acquired, in situ measurements with hhXRF and VNIR-SWIR spectrometers, as well as magnetic susceptibility measurements, were performed along a number of scan lines, and rock samples were taken for laboratory measurements. These and legacy ground-based data collected from the mining companies enabled the linking of magnetic anomalies and features in the hyper-/multispectral image mosaics to the outcropping lithologies and variations in ore grade.

The fixed wing magnetic survey was conducted by Radai Oy, which covered an area of 1.14 km<sup>2</sup> (in-line/crossline spacing: 40 m/40 m; height above ground: 40 m) within a flight time of less than one hour. In doing so, the complete eastern part of the deposit could be mapped and strong magnetic anomalies could be associated with the magnetite-rich ore occurrences, which follow a synclinal structure.

In contrast, multi-copter magnetic surveys, acquired by HZDR–HIF, only focused on the smaller Metsämalmi outcrop area (size: ~100 x 300 m) and were repeated with different flight altitudes and line spacings. The lowest survey was performed at a nominal flight height of 15 m and with a dense survey line spacing of 7 m and 20 m for inlines and crosslines, respectively. The data provided com-

parable resolution to the ground magnetic survey. The UAS magnetic survey took less than one hour, while the ground survey took three field days. Although this was one of the first surveys with this setup, a proper acquisition strategy and a processing scheme were already defined. The noise level was kept acceptably low and artificial signals (e.g. from electric motors) were effectively reduced such that the resulting magnetic data were of generally good quality. High magnetic anomalies from the low-altitude UAS (and ground magnetic) surveys correlated well with the locations and shapes of high-grade ore lenses in the outcrop area. This demonstrates the potential of low-altitude operating UAS to map near-surface magnetite-rich ore bodies.

An equivalent layer modelling (ELM) procedure was jointly applied to all the available magnetic datasets to evaluate the consistency of data from the different magnetic surveys and to present magnetic surveys with very different acquisition parameters (different flight heights, line spacings and inline samplings) in one consistent total magnetic intensity plot. The results of this first integration test with ELM are very promising, but some further adjustments (i.e. finding proper weighting factors to balance individual datasets in the inversion) are required to use ELM as a standard procedure for merging magnetic datasets in the future.

The hyper- and multispectral surveys were acquired and processed by HZDR–HIF. The data were carefully pre-processed using in-house software routines to account for topographic and illumination distortions. Coverage with lichen and other vegetation in the outcrop area clearly reduced the surface portion (by up to 30%) for which reliable information on surface mineralogy could be obtained. Therefore, the most valuable results were achieved from a rather small areal of 30 x 10 m in the eastern part of the Metsämalmi outcrop, where the surface was cleaned with a high-pressure cleaner prior to data acquisition.

The multispectral survey was performed with a fixed-wing UAS and a full-frame camera with only 4 bands in the visible and near-infrared part of the electromagnetic spectrum. The hyperspectral survey was performed with a multi-copter UAS and a full-frame hyperspectral camera having a higher spectral resolution in the visible and near-infrared

part of the electromagnetic spectrum (50 discrete raw bands from 504–900 nm). The resulting grid sizes of the multi- and hyperspectral orthomosaics were in the range of ~10 cm and ~4 cm, respectively. In addition, a photogrammetric survey was flown with an RGB camera mounted on a fixed-wing UAS. The images collected during the survey were used to generate a digital surface model (DSM) and orthomosaic. The resulting grid cell sizes of the orthomosaics were in the range of ~15 cm and ~7 cm for the multi- and hyperspectral survey, respectively.

For both the multi- and hyperspectral orthomosaics, an MNF transformation was applied to enhance the spectral differences. Band ratios were calculated to visualize areas with increased surficial iron alterations. Due to the much higher spectral resolution of the hyperspectral data, their results can be considered as more precise for estimating iron alteration mineral abundances compared to the multispectral data. For the hyperspectral images, unsupervised and supervised classifications were applied to distinguish pixels that were predominantly associated with iron mineralization and the gabbroic host rock.

Comparison of the results from low-flying UAS magnetic and ground magnetic surveys with ground-based susceptibilities along the scan lines revealed that the distribution of surface susceptibilities and TMI values were correlated. Strong susceptibility variations within the ore and between the ore and host rocks led to high lateral magnetic contrasts visible in both the TMIs and the vertical derivative maps from all UAS and ground-based surveys. Careful survey planning with a properly selected line spacing and line direction that also considered information on local

geology and morphology was essential to map the anomalies present with a high resolution.

In the same way, areas where multi- and hyperspectral methods detected iron alteration coincided with locations where oxide ore lenses were identified from conventional surface mapping. The hyperspectral handheld spectra and the UAS HSI data at the same locations displayed a correlation. Finally, comparisons of handheld XRF and magnetic susceptibility measurements indicated that there was a distinct correlation between magnetic susceptibility and the iron oxide content. However, the relationship between induced magnetization, susceptibilities and the local magnetic field values from low-altitude UAS and ground-based surveys is non-trivial due to the strong variations in magnetic properties over short distances and the smoothed magnetic response that is associated with integration over a larger volume<sup>1</sup>. Nonetheless, the consistency of all these results indicates that it is possible to combine all the data in such a way that spatially uniform ore grade estimates along the Metsämalmi outcrop surface can be derived.

Note that the main objectives of this report are to describe the multi-sensor UAS systems and present the data acquisition and processing strategies, as well as to provide preliminary results. Because some of the systems have recently been developed (e.g. a multi-copter equipped with a magnetometer is still in the trial phase), a focus is on evaluating the reliability of the data acquisition and the quality of resulting data. The overall aims of the MULSEDRO project have been described by Heincke et al. (2019). More comprehensive and concise interpretations of UAS tests in Otanmäki have been published by Jackisch et al. (2019).

## 1 INTRODUCTION

The EIT Raw Material-funded MULSEDRO project (ID: 16-0193) is an international 3-year upscaling project with the objective to develop lightweight (<5 kg) multi-sensor drone systems for mineral exploration and geological mapping. More specifically, the scope is to integrate magnetic sensors and

(multi- and) hyperspectral sensors on both fixed-wing and multi-copter UASs. In addition, photogrammetry has been performed (from a fixed-wing drone) and a novel integrated positioning system (IPS) has been developed that operates without GPS. The partners in this project are the Geological

---

<sup>1</sup> To obtain better correlations between the magnetic responses and the susceptibilities, inversion or modelling strategies could be an option to determine susceptibility estimates along the surface (or model the magnetic responses on the basis of the susceptibility measurements). However, such approaches are also limited due to the low resolution of the magnetic method and the large ambiguities of magnetic modelling.

Survey of Denmark and Greenland (GEUS), the Geological Survey of Finland (GTK), the Finnish company RADAI Oy, the German Helmholtz-Zentrum Dresden-Rossendorf - Helmholtz Institute Freiberg for Resource Technology (HZDR-HIF), the German company DMT GmbH and LTU Business AB in Sweden (see Appendix 1 for the partners' roles in the project).

In the second year of the project (started in April 2017), a field campaign was scheduled to test the integration of all sensors on the different drone types in a mining environment. A location within the Otanmäki Fe–Ti–V deposit was selected as the test site, which is situated 150 km southeast of Oulu and about 5 km from the southern shore of Lake Oulujärvi in central Finland. Gabbroic intrusions in the area, Otanmäki and Vuorokas, were mined by Rautaruukki Oy for iron, titanium and vanadium from 1953 to 1985. The test was organized in close cooperation with the Finnish mining and exploration company Otanmäki Mine Oy, which is currently developing the Fe–Ti–V deposits in the area. The locations of the closed mines of Otanmäki and Vuorokas are indicated in Figure 1.

Drone-based magnetic and hyperspectral systems developed within the MULSEDRO project were tested at the beginning of September 2018 in the Metsämalmi area, which is located in the eastern part of the ore zone of the Otanmäki gabbroic intrusion. The Metsämalmi area ( $64^{\circ}07'13.0''\text{N}$ ;  $27^{\circ}07'26.5''\text{E}$ ;  $\sim 250 \times 200 \text{ m}$ ) was excavated in the early 1980s during preparations for open-pit mining. However, a decision to close the Otanmäki mine was made shortly afterwards and the Metsämalmi area was left unmined. For the ground validation of the UAS results, a ground magnetic survey and in situ magnetic susceptibility and spectroscopy measurements were conducted.

This report includes a summary of a) all the field activities and all UAS surveys, b) a short description of the processing of all collected datasets and c) a preliminary discussion of the results. The data and the report help to refine knowledge of the deposit and to gain more background information for re-establishing mining activities.

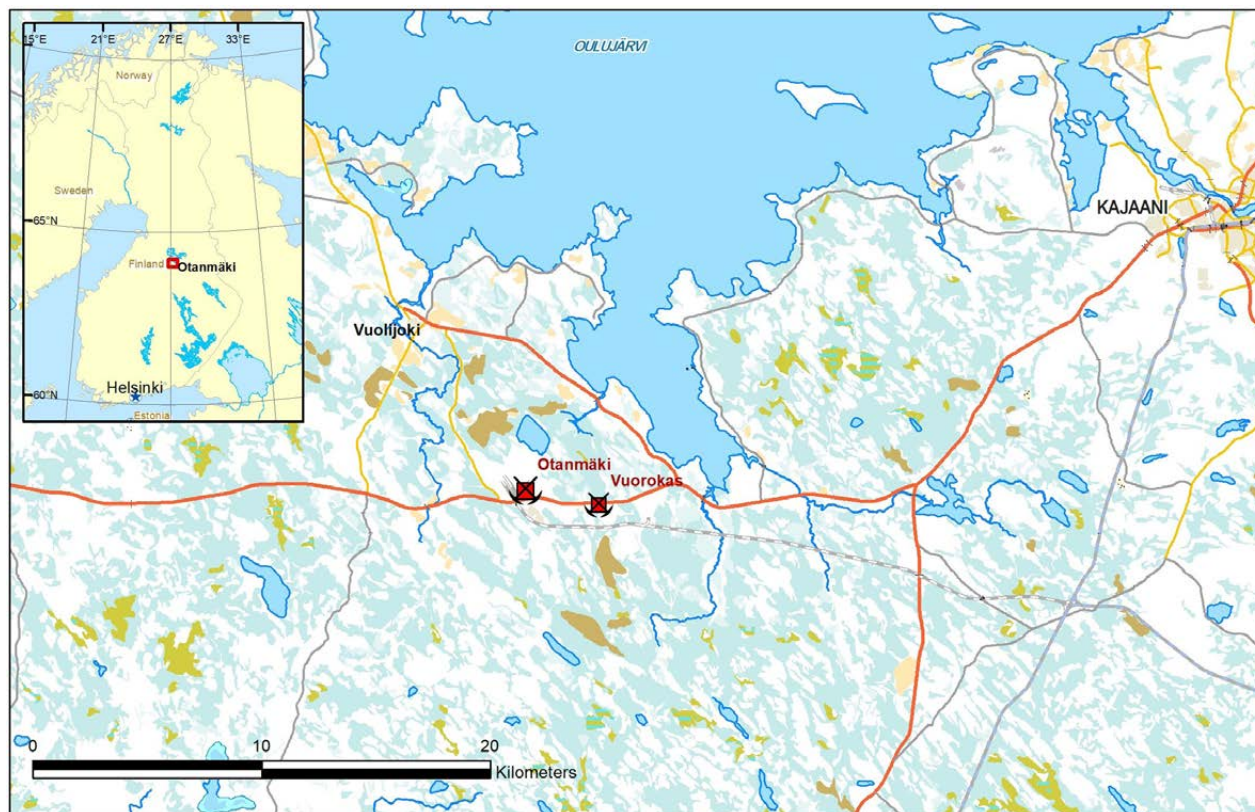


Fig. 1. Otanmäki area in central Finland near the southern shore of Lake Oulujärvi. Locations of the closed Fe–Ti–V mines Otanmäki and Vuorokas are indicated with symbols (Basemaps © National Land Survey of Finland).

## 2 BACKGROUND INFORMATION

### 2.1 Geology

The bedrock in the Otanmäki area is poorly exposed and rocks are typically covered by glacial overburden from 1 to 3 metres thick. For this reason, geophysical surveys have played an important role in regional studies, as the Fe–Ti–V ores were discovered by magnetic surveys (see section 2.2 Mining history).

The vanadiferous magnetite–ilmenite ore deposits in the Otanmäki area are located within 2.06 Ga gabbroic intrusions (Otanmäki intrusion complex), which host ore within zones composed of mixtures of metamorphosed gabbro, anorthosite and lensoidal bodies of massive to semi-massive magnetite–ilmenite ore (Lindholm & Anttonen 1980, Huhma et al. 2018, Mäkisalo 2019). The intrusions were emplaced into Archean TTG gneisses (Tonalite–Trondhjemite–Granodiorite), but they also have sharp, fault-defined contacts against ca. 2.05 Ga gneissic, anorogenic granites and intermediate rocks (Otanmäki A1-type suite), which host two Nb–Zr–REE mineralized zones (see geological map in Fig. 2; Lahti et al. 2018; Kärenlampi et al. 2019).

The magnetite–ilmenite ore bodies at the Otanmäki gabbro intrusion are scattered within a 50- to 200-m-wide and approximately 5-km-long zone having numerous unequally sized and irregularly shaped ore lenses. The ore lenses within this zone are typically sub-vertical, 2–200 m long and 3–50 m thick, generally E–W-trending and dipping N at 70–90°. In addition, the rocks in the ore zone were recrystallized and deformed during the Svecofenian orogeny (ca. 1.9–1.8 Ga), and the ore zone is folded into a syncline structure at its eastern end. Based on diamond drilling information, the ore zone is known to extend to a depth of at least 800 m, and gravity-based modelling suggests continuation of the gabbroic intrusion to a depth of 2 km (Lindholm & Anttonen 1980, Lahti et al. 2018).

The ore types at the Otanmäki mine are divided into three classes depending on their magnetite–ilmenite content: 1) (massive) high-grade ore (class I ore) 2), (semi-massive) medium-grade ore (class II ore) and 3) low grade (disseminated) ore (Hokka & Lepistö 2018). The average modal mineralogy of the Otanmäki high-grade ore is

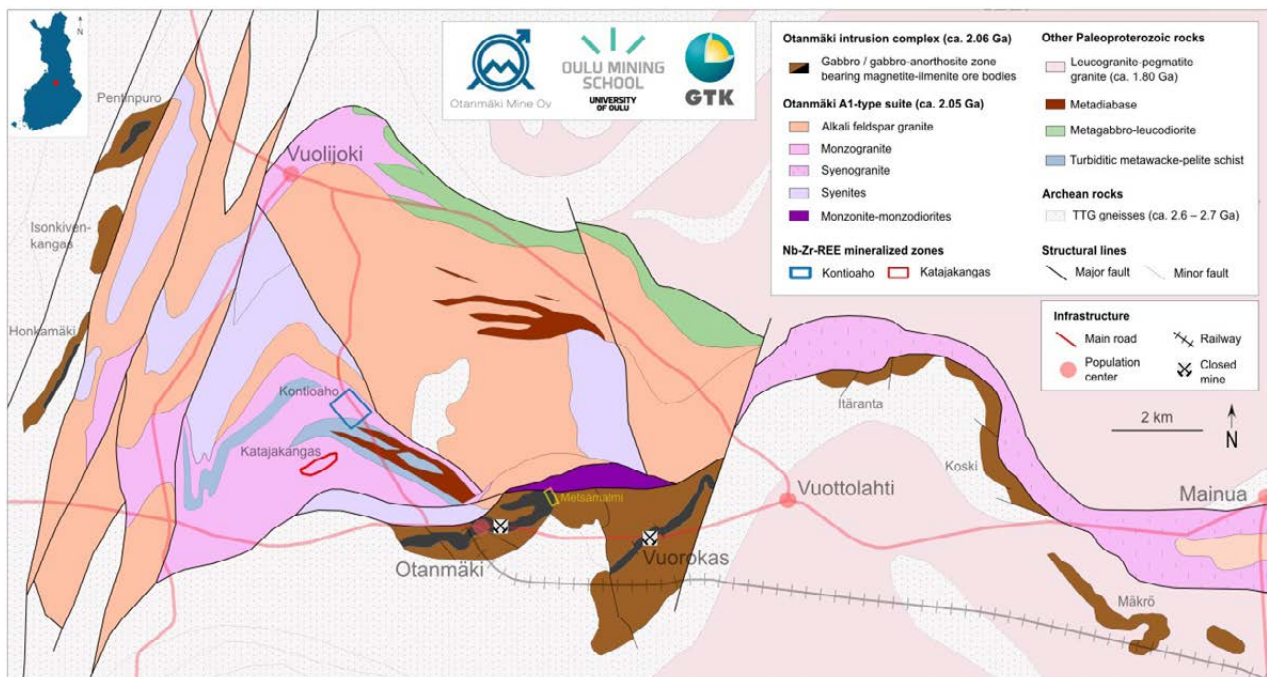


Fig. 2. Geological map of the Otanmäki area showing the location of the closed Otanmäki and Vuorokas Fe–Ti–V mines hosted by gabbroic intrusions, the Metsämalmi study area and A-type granite-related Nb–Zr–REE mineralized zones (Koutioaho, Katajakangas).

composed of magnetite (35–40%), ilmenite (25–30%) and sulphides (1–2%) (Hokka & Lepistö 2018). The main gangue are silicate minerals such as chlorite, hornblende and plagioclase. A good correlation is observed in the ore bodies between the magnetite content and the degree of magnetization, and magnetic susceptibility measurements

can be considered as a cost-effective technique to characterize the ore bodies. For example, during the mining operations, Rautaruukki Oy used susceptibility measurements from percussion drill holes in the underground mine to locate nearby ore lenses and estimate their size and grade.

## 2.2 Mining History

Exploration of the Otanmäki Fe–Ti–V ore deposit started in 1937, when magnetite–ilmenite ore boulders (glacial erratics) were found in the Sukeva municipality in central Finland. However, it was not until 1938 that the source of these boulders was localized at Otanmäki, about 30 km northwest of Sukeva, where strong magnetic anomalies had been observed. In 1939, the Vuorokas magnetite–ilmenite ore deposit was discovered 3 km to the east of the Otanmäki deposit, and a few smaller satellite deposits (e.g. Honkamäki, Pentinpuro; Fig. 2) were also found in the surrounding areas (Pääkkönen 1956).

After the Second World War, the state-owned company Otanmäki Oy was established in 1950 and the Otanmäki mine went into production in 1953. In 1968, Otanmäki Oy was merged with Rautaruukki Oy, which was responsible for mining for the rest of the mine's lifetime. The main products were vanadium pentoxide ( $V_2O_5$ ), Fe pellets and ilmenite

( $FeTiO_3$ ). When the mine was in production, Otanmäki was one of the major global vanadium producers. In the 1960s, vanadium pentoxide production at Otanmäki reached 10% of world production, and in the 1980s it still accounted for about 5%. The mine was operational until 1985, when the world market price of vanadium pentoxide made the mining economically unprofitable (Illi et al. 1985).

During the 32 years of mining operations, about 33.1 million tons of ores and waste rocks were mined from the Otanmäki and Vuorokas mines. About 31.2 million tons of this was mined from Otanmäki and 1.9 million tons from Vuorokas. Almost all mining was underground and only 250 000 tons were mined from an open pit (Otanmäki Mine Oy 2017, Illi et al. 1985). In 2012, Otanmäki Mine Oy was established with the goal of re-opening the mine and re-starting production between 2024 and 2025.

## 2.3 Summary of previously collected geophysical data

In the Otanmäki region, several airborne and ground geophysical surveys were conducted during the exploration and mining period by Otanmäki Oy and Rautaruukki Oy. Magnetic, gravity and electromagnetic Slingram (HLOOP) were the main ground-based methods used. Unfortunately, measurements from before the end of the 1970s are not available in a digital format, but at least some paper maps have been preserved and scanned for further use. At the beginning of the 1980s, Rautaruukki Oy carried out ground geophysical magnetic and Slingram surveys, which are available in GTK's databases. After the closure of the mine, magnetic surveys were carried out at the Pentinpuro, Honkamäki and Mäkrö satellite Fe–Ti–V deposits in 2013. The aerial coverage of these measurements is presented by Lahti et al. (2018).

At the Metsämalmi test site, no target-scale datasets from previous ground measurements are available in digital format. On a regional scale, the Otanmäki area has been covered by a high-resolution, low-altitude airborne geophysical survey that was conducted within GTK's national airborne geophysical programme. The survey in the Kajaani flight area was performed in 1979. On average, the flight altitude was 37 metres, line spacing was 200 metres and lines were oriented in a N–S direction. The survey included magnetic, electromagnetic and radiometric measurements. The sub-section of the airborne magnetic map around Otanmäki is presented in Figure 3.

In 1985, the Geological Survey of Finland carried out regional gravity surveys covering the Otanmäki and Vuorokas mines and surrounding areas. The

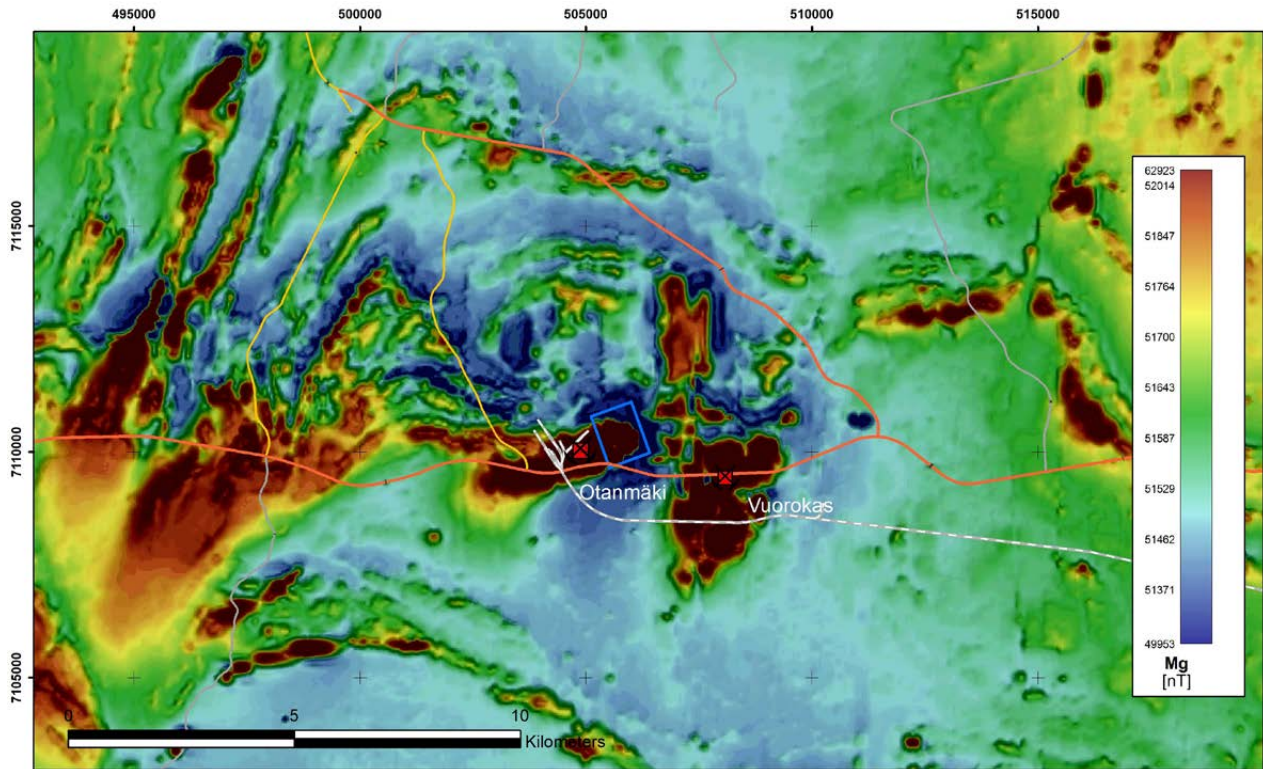


Fig. 3. Airborne magnetic map of the Otanmäki area based on GTK's airborne surveys in 1979. The location of the Metsämalmi UAS test area on the NE edge of the Otanmäki gabbroic intrusion is indicated by a blue polygon (Basemaps © National Land Survey of Finland).

data coverage was later further extended to the west in 1998 and 2006–2008. The average data density was 4 points/km<sup>2</sup>, which is appropriate for regional-scale investigations. The regional Bouguer anomaly has been used for 3D block

modelling of the Otanmäki and Vuorokas intrusions by Lahti et al. (2018). Based on the results, the depth extent of the intrusions is estimated to be at least 2 km.

## 2.4 Site description

The Metsämalmi test pit area has a size of 250 x 200 m and is located at the eastern end of the Otanmäki syncline structure (Hokka & Lepistö 2018) (Fig. 4). It was cleared in an early planning stage for expansion to an open pit in the early 1980s and is the only larger outcrop of the Otanmäki deposit.

The outcropping rock surface is slightly undulating with hummocks having a maximum height of 1–2 m, but otherwise the site has minor topographic variation and is well suited for systematic geophysical ground surveying and geological mapping from the ground (Fig. 5). However, some vegetation and particularly lichen cover on the rock surfaces significantly lowers the quality of mineral mapping with multi- and hyperspectral cameras. Therefore, Otanmäki Mine Oy cleaned up the rock

surface of an area of about 30 x 10 m in the central part of the outcrop with a high-pressure cleaner some days before the field campaign.

The heterogeneous nature of the ore zone is clearly visible in the Metsämalmi area, where variably sized and irregularly shaped ore lenses contain abundant gangue intrusions (Hokka & Lepistö 2018). The lenses are trending in a WNW–ESE direction in the northern part of the Metsämalmi area but turn more towards N–S further to the south (see Fig. 6) due to the folding of the syncline. Much of the outcropping bedrock area is mapped as high-grade ore classes I and II (Figs. 6. and 7), and the surrounding host rocks are mainly amphibolites, anorthosites and gabbros.

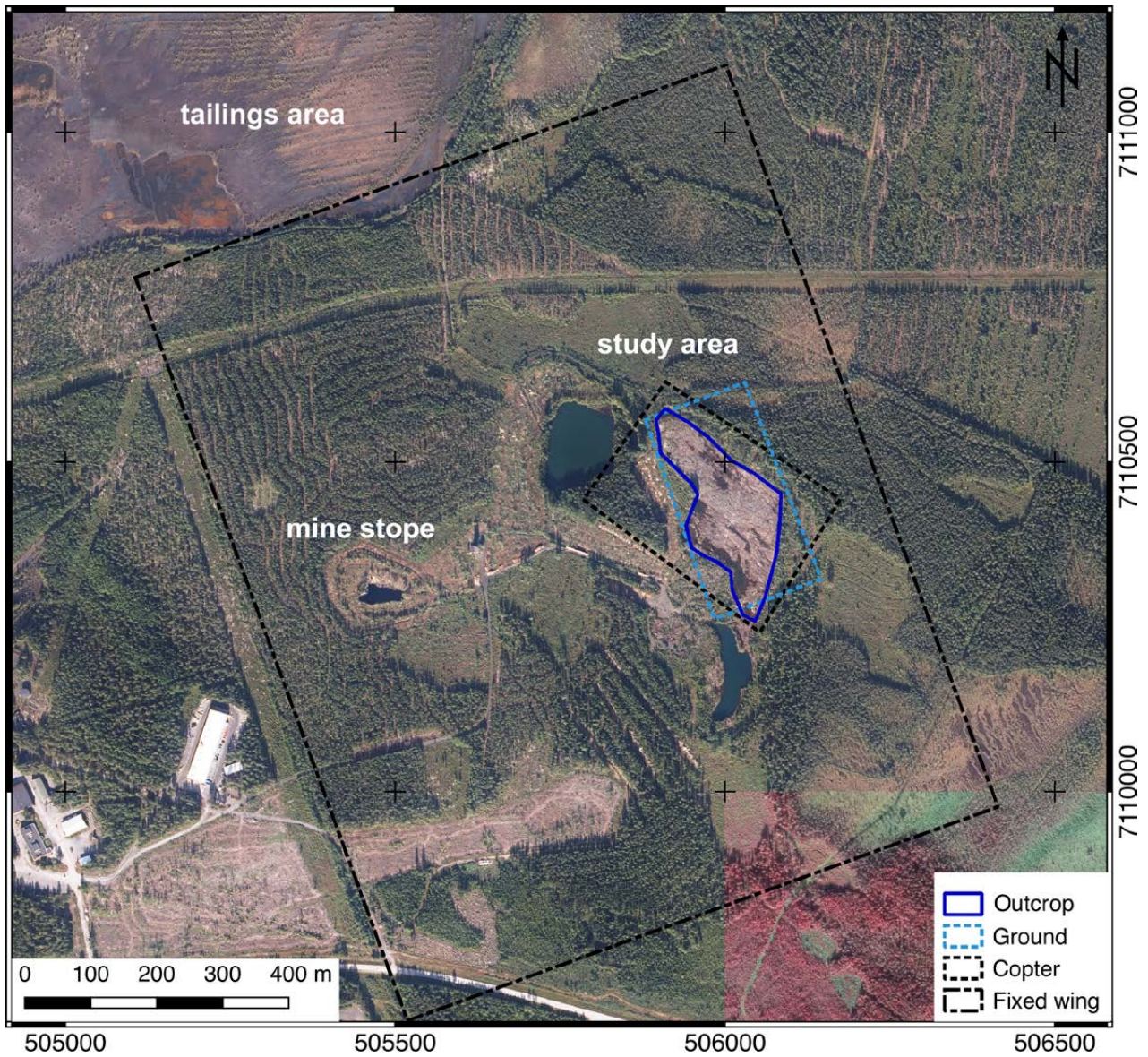


Fig. 4. Orthophoto of the Otanmäki study area. The dark blue continuous line encircles the Metsämalmi area, where an open-pit mine is planned. Radai's fixed wing magnetic surveys covered a larger area of >1 km<sup>2</sup>, also including larger parts of the earlier mining area, while magnetic and hyperspectral multi-copter surveys from HZDR-HIF focused on the outcrops of the Metsämalmi area (Basemaps © National Land Survey of Finland).



Fig. 5. Photo showing the Metsämalmi test pit site.

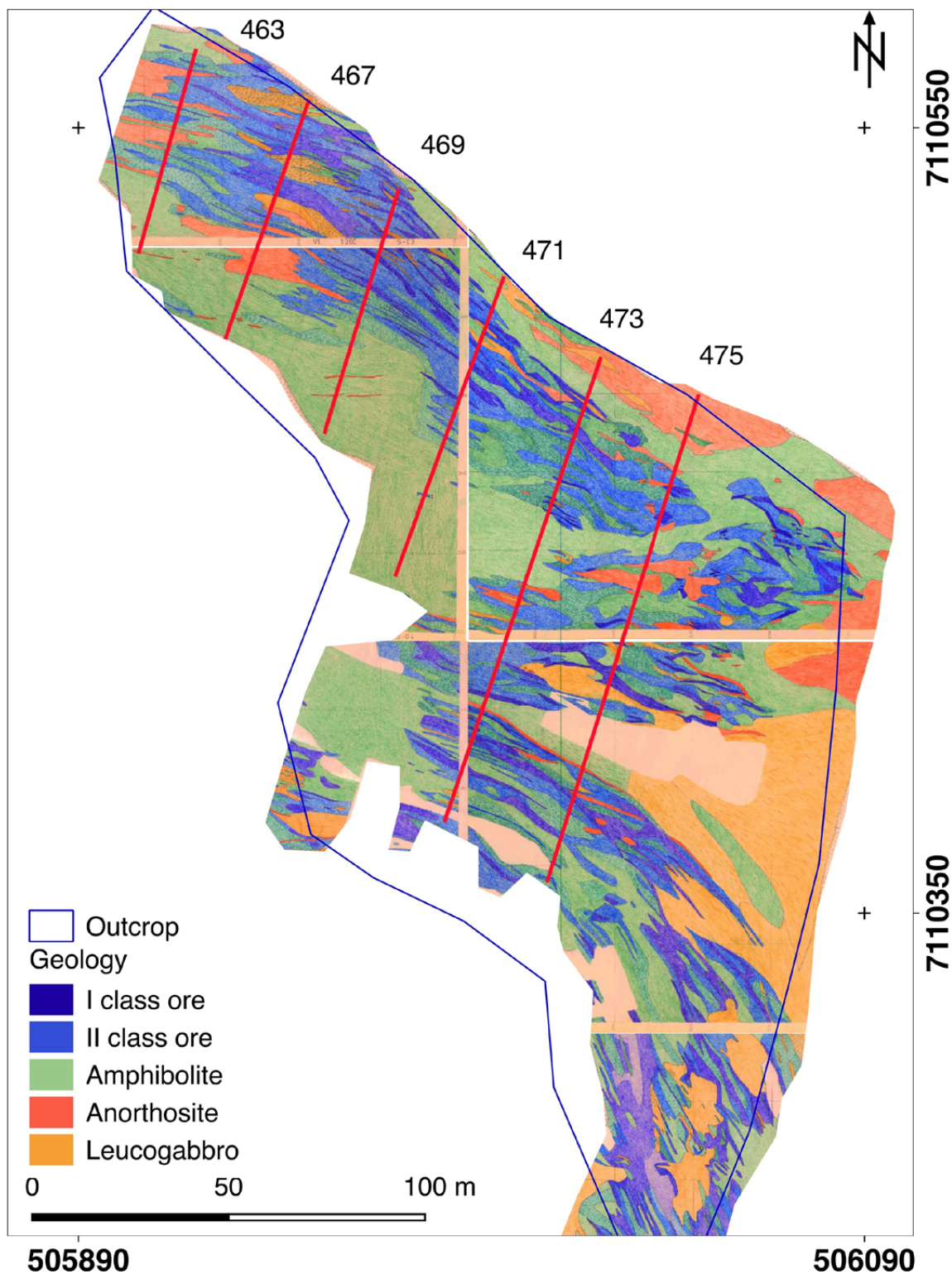


Fig. 6. Scanned geological map from the Metsämalmi site prepared by Rautaruukki Oy. The different distinguished ore classes and the main rock types are colour coded. The susceptibility scan lines collected by Otanmäki Mine Oy are highlighted by red lines and scan-line numbers are provided on the figure. Actual susceptibility values are shown in Fig. 8. The present outcrop is highlighted in blue. The original geological map was provided by Jouko Jylänki from Otanmäki Mine Oy.

Magnetic susceptibility measurements were conducted by Otanmäki Mine Oy along 9 parallel scan lines in a NNE–SSW direction perpendicular to the general orientation of the ore lenses (Fig. 6 shows the 7 profiles from which magnetic susceptibility data were accessible). The line spacing was about 30 m and the measurement interval along the profiles was 10 cm. The results indicate large variation in the magnetic susceptibility and a strong correlation with the mapped ore grade. The

highest measured susceptibility values are in the range of about 1 to 1.2 SI (Fig. 8).

In addition, Otanmäki Mine Oy conducted mini-drill sampling in the Metsämalmi area along three 50–100-m-long channel sampling profiles (one along profile 469; Fig. 6) to verify the thickness and grade of the ore lenses. The rock type, texture, quantity of magnetite, ilmenite and sulphides, ore class and rustiness were determined.



Fig. 7. Photographs in the upper panel show rock samples taken from the class II ore zone (left) and class I ore zone (right). Photographs in the middle and lower panels show different rock surfaces from the class I (and class II) ore zone in the Metsämalmi test pit area.

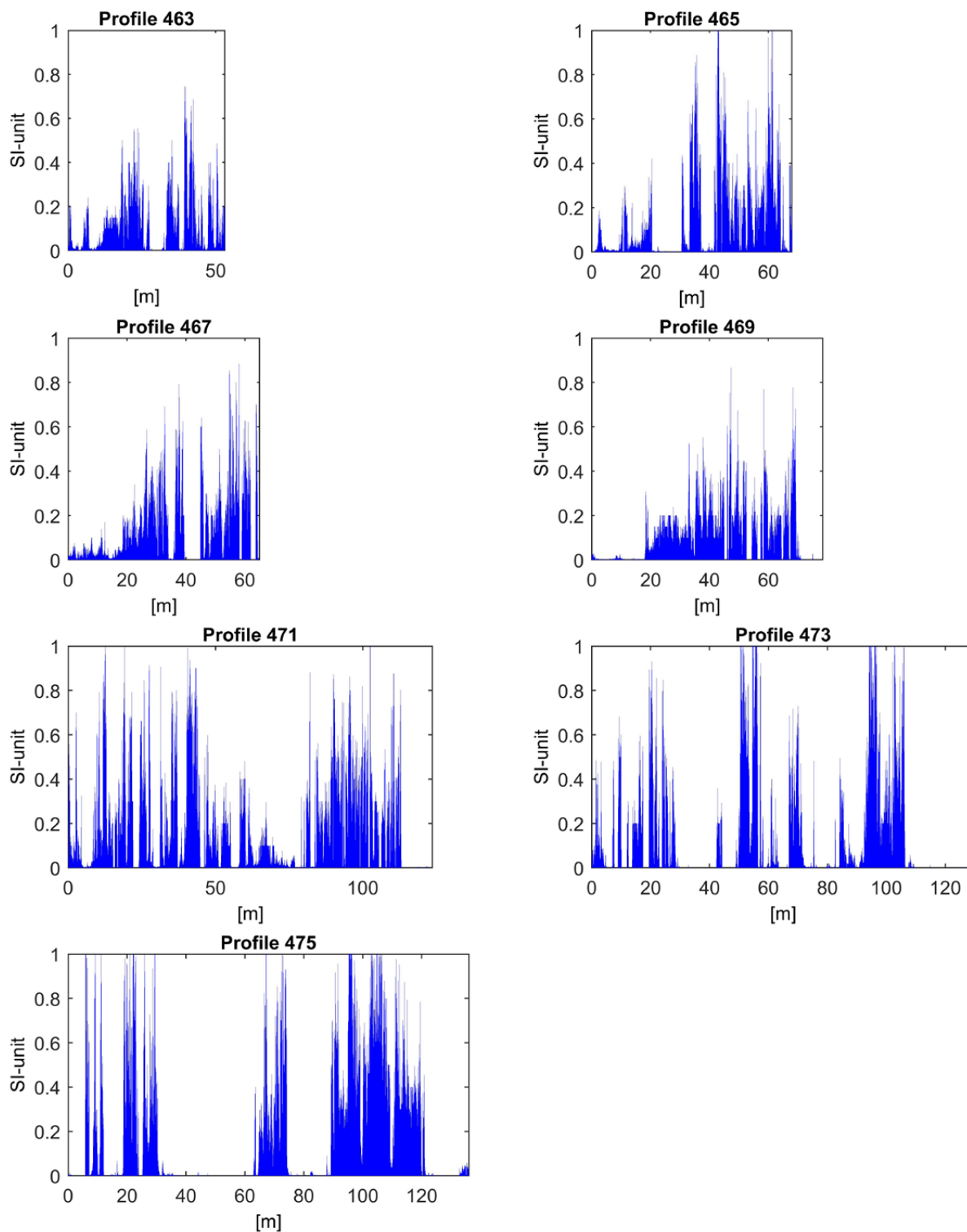


Fig. 8. Susceptibilities obtained along the profiles 463–475 (see Fig. 6). ( $x = 0$  is associated with the southern end of the scan lines.)

Several diamond drilling and a large number of percussion drilling boreholes were drilled by Rautaruukki Oy at the Metsämalmi test site and in the adjacent area to the south. Some of them reach depths of 50 m and in many of them magnetic susceptibility logging has been performed. Unfor-

tunately, the original in-hole susceptibility measurements are not available, and only the index codes are preserved, where magnetic susceptibility values were assigned to the different Otanmäki ore classes along the cores.

### 3 FIELD ACTIVITIES AND MEASUREMENTS

The Metsämalmi Otanmäki test pit area (64°07'13.0"N; 27°07'26.5"E) was surveyed between 4–7 September 2018. The weather was dry with some morning fog on 6 September. The sky was generally overcast and became sunny towards the late afternoons, and the wind was generally calm, with the wind speed reaching a maximum of 4 m/s.

In the field, data were acquired using various drone-borne sensors mounted on a fixed-wing drone and two multi-copters. The sensor types included magnetics, photogrammetry, multi- and hyperspectral imaging and LiDAR. Furthermore, an extensive ground survey over the area was conducted to cross-validate the drone-borne data and included ground spectroscopy, portable XRF and magnetic susceptibility measurements. In addition, representative rock samples were taken for the main lithologies of the Metsämalmi area and ground control points (GCP) were distributed within the survey area. The locations of all measurement points were determined with a differential GNSS system in PPK mode. The datasets were generally converted into ETRS89 / UTM zone 35N projection.

In detail, following work was conducted on the respective days:

Date	Activities
04.09.2018	– UAS magnetic (fixed-wing)
05.09.2018	– UAS hyperspectral (multi-copter) – UAS photogrammetry (fixed-wing) – UAS multispectral (fixed-wing) – Ground validation
06.09.2018	– UAS magnetics (multi-copter; @15 m altitude and @40 m) – Ground validation
07.09.2018	– UAS LiDAR (multi-copter) – UAS magnetics (multi-copter; @65 m altitude) – Ground validation and sampling

The drone types that were used for the different surveys at Otanmäki are listed in Table 1 and are further introduced in the sections on the implementation of the different sensors on the UASs.

Table 1. Table summarizing the main characteristics of the UASs used during the Otanmäki field campaign.

Model	Tholeg THO-R-PX8-12	AIBOTIX Aibot X6v.2	senseFly eBee Plus	Albatros VT
Operating institution	HZDR-HIF	HZDR-HIF	HZDR-HIF	Radai Oy
Type	Multi-copter	Multi-copter	Fixed Wing	Fixed wing
No. of Engines	8	6	1	1
Maximum take-off weight	10 000 g	7000 g	1100 g	7000 g
Size	70 x 70 x 35 cm	105 x 105 x 45 cm	110 cm wingspan	280 cm wingspan
Flight time	20–25 min	12–15 min	50 min	Up to 3 h
Velocity	0–40 km/h	0–30 km/h	40–110 km/h	55–110 km/h
Payload	4500 g	2000 g	~200 g	2000 g
Fail safe	Redundant propulsion	Redundant propulsion	Gliding	(Gliding)
Area covered per flight	10 000 m <sup>2</sup>	5000 m <sup>2</sup>	0.6–1.5 km <sup>2</sup>	5–7 km <sup>2</sup>
Sensor types	Div. cameras, magnetic	Div. cameras, magnetic	Two lightweight cameras	Magnetic

All UAS surveys could be performed without any major problems. Only the magnetic compass of the multi-copters suffered some disturbance due to the large magnetic anomaly within the survey area, leading to some heading deviations. Furthermore, some magnetic data (~1%) acquired from the multi-copter were clipped for low flight heights of 15 m, because the iron magnetite-rich ore zones were responsible for extreme magnetic anomalies (>75 000 nT). However, these difficulties had no major impact on the good overall quality of the data gathered from the UASs.

The key coordinator at the Otanmäki field site was Heikki Salmirinne from GTK and the different datasets were collected by HZDR-HIF, Radai Oy,

GTK and DMT<sup>2</sup>. Jouko Jylänki from Otanmäki Mine Oy and Kimmo Kärenlampi from Oulu University introduced the field crew to the field site and provided the team with all relevant background information on the regional geology and mining activities. Jouko Jylänki also cleaned a part of the Metsämalmi outcrop from vegetation before the field campaign to improve the results of hyperspectral measurements. (Participants in the field campaign are listed in Appendix 2).

In the following sections, the acquisition and processing of the different datasets is described and observations and preliminary results from the 2018 fieldwork are reported.

### 3.1 Magnetic measurements by UASs

Magnetic surveys were performed from both a fixed-wing drone and a multi-copter. Since their survey areas as well as the acquisition parameters (line spacing and flight heights) were largely different, their objectives also differed. The fixed-wing surveys covered a larger area with rather coarse line spacing and were intended to gain a general overview of the magnetic anomaly in the eastern part of the Otanmäki ore zone. In contrast, the multi-copter surveys only covered the small excavated Metsämalmi area with dense line spacing and the intention was to map the ore zone here in greater detail, close to that obtained with the ground-based survey.

Because it is a general challenge to combine and integrate magnetic datasets that are gathered with different height levels and measuring point densities, we tested an approach based on equivalent layer modelling (ELM) to obtain one consistent magnetic total field map from all available magnetic data across the Metsämalmi site. In addition to the UAS-borne magnetic data, these included measured ground-based magnetic data (see Section 3.3.1) and regional magnetic data from GTK (see Section 2.3). The results of the equivalent layer modelling are presented later in Section 6.

#### 3.1.1 Fixed-wing magnetic survey

Radai Oy carried out an airborne magnetic survey with their fixed-wing UAS. Two flights were

recorded on 4 September 2018. The main objectives of the survey were to a) test a new, more effective datalogger that had been developed within the MULSEDRO project, b) gather magnetic data at the kilometre scale covering most of the eastern part of the Otanmäki ore deposit with dense line spacing and, hence, a high resolution and c) provide supporting background data for the more locally measured magnetic and hyperspectral data that were collected across the outcropping target area with the multi-copters from HZDR-HIF.

The following subsections describe Radai's magnetic UAS system, the magnetic survey, data processing and the final results. Final results are presented as maps of magnetic total field intensity that were obtained by equivalent layer modelling (ELM) from datasets recorded in two flights across the same area. In the first and second flight, respectively, Radai's former data logger (RT) and the new MULSEDRO data logger (MS) were used.

##### 3.1.1.1 Magnetic fixed-wing system

Radai's magnetic measurement system was installed into their fixed-wing UAS (Albatros VT; see Fig. 9), which was built for the MULSEDRO project. The magnetic field was measured using a digital 3-component fluxgate magnetometer located in the tail boom of the UAS. The X, Y and Z components of the magnetic field were recorded with a datalogger in combination with a measurement device

---

<sup>2</sup> DMT made test measurements of their newly developed integrated positioning system (IPS) system. These measurements were not performed on the Metsämalmi test site, but about 30 km apart from Otanmäki and are not described in this report.

developed by Radai. The measurement device also recorded the GPS time (UT), position (latitude, longitude and height) and barometric pressure. The datalogger used in this survey was designed for total field measurements and did not record UAS orientation (pitch, roll, yaw). This means that the individual magnetic field components were not further considered in processing and interpretation, but were only used to compute the total intensity of the magnetic field. The accuracy of the GPS positioning was about  $\pm 1$  m during flight operation. Technical information on Radai's UAS system is provided in Tables 1 and 2.

After take-off, the flight was controlled by an autopilot and followed predefined waypoints. The flight path was created with the RadaiPath software and the plane followed the terrain topogra-

phy, which was defined by a digital elevation model (DEM). The flight performance was controlled by the computer software Mission Planner both via a telemetry (radio) link and, whenever possible, a wireless mobile 3G/4G link in real time. The same software was used to download the waypoints from the computer to the autopilot. An SMS-based tracker device enabled the UAS to be located in case of an unwanted crash landing.

A magnetic base station and a nearby mobile telemetry/control station measured the temporal variation in the magnetic field (3-component fluxgate magnetometer) and barometric pressure, respectively. The magnetic field and altitude measured at the moving UAS platform were corrected for time-dependent variations by the base station data during post-processing.

Table 2. Technical information on Radai's UAS magnetic system used for surveying.

UAS parameters	Value
UAV magnetometer	Flux-gate
Noise level	$\pm 0.5$ nT
Dynamic range	$\pm 100$ $\mu$ T
Sampling frequency (RT)	10 Hz
Sampling frequency (MS)	50 Hz
Base station magnetometer	Flux-gate
Resolution	0.01 nT
Dynamic range	$\pm 70$ $\mu$ T
Sampling frequency	0.167 Hz



Fig. 9. Timo Åman (left) and Ari Saartenoja (right) are getting ready for take-off with Radai's Albatros VT3 UAS. (Photo by M. Pirttijärvi)

### 3.1.1.2 Acquisition

The survey area covered the eastern part of the old mine as well as the Metsämalmi outcrop. Its area is shown in Figure 10 and coordinates of the vertex points of the two survey sites are presented in Table 3. The map coordinates in this section are in given in the Finnish ETRS-TM35FIN system, which is very close to UTM zone 35N on the WGS84 ellipsoid. The terrain topography (10 m x 10 m grid) and the digital background map were provided by the National Land Survey of Finland.

The Otanmäki survey covered a surface area of about 1.4 km<sup>2</sup> and comprised a uniform pattern of orthogonal inlines and crosslines having a regular 40 m line spacing (Figs. 11 and 12). The survey consisted of 31 lines in an E–W direction and 25 lines in a N–S direction, and the total length of the survey lines was about 30 km (E–W) + 34 km (N–S), i.e. 64 km. The nominal flight altitude was set at 40 m above the ground surface.

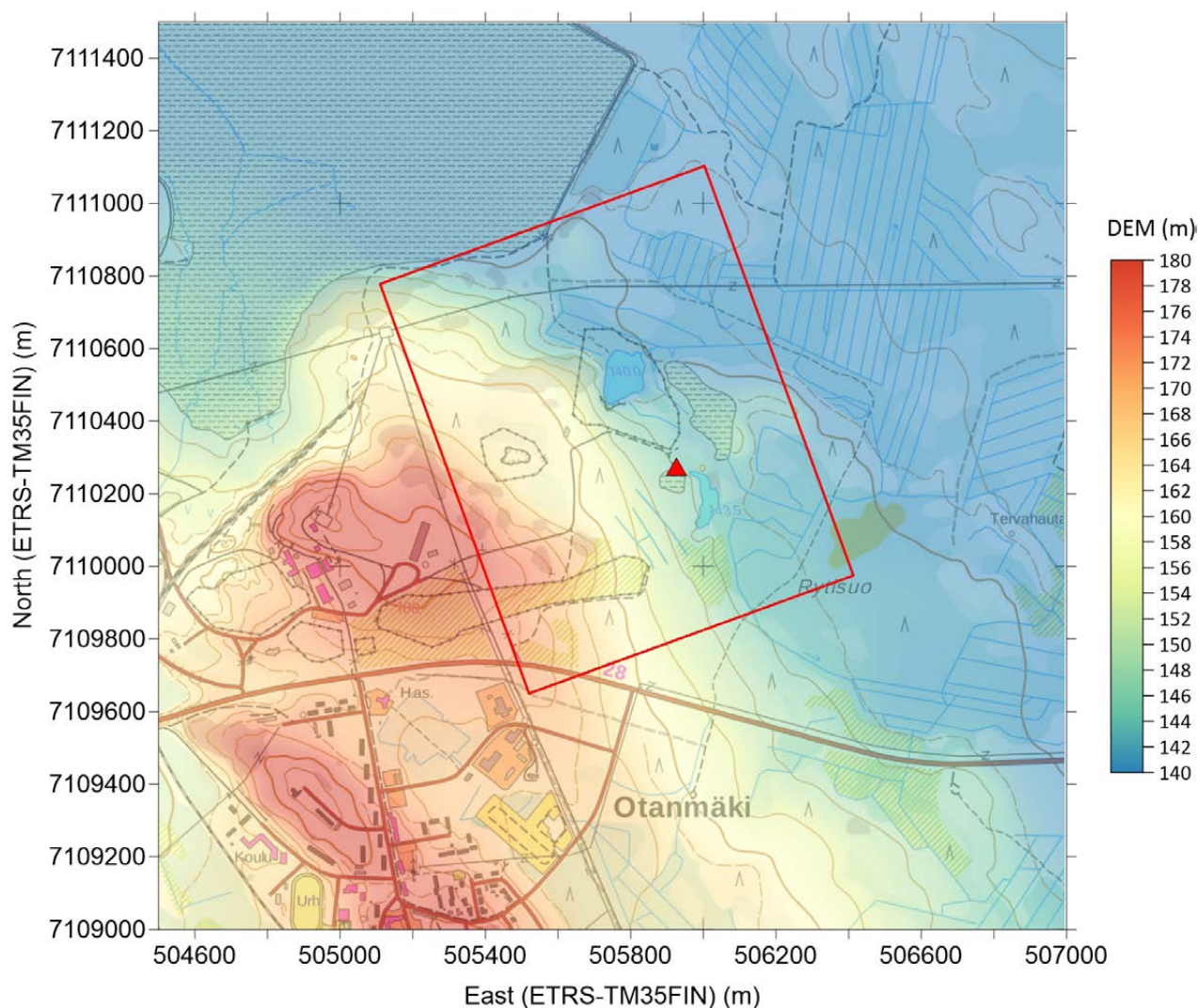


Fig. 10. Topographic map around the Otanmäki survey area, which is outlined by a red polygon. The red triangle depicts the location of the mobile control station (the magnetic base station is located outside the map). The digital elevation model (DEM) and background map are provided by the National Land Survey of Finland © 2018.

Table 3. Coordinates of the four corner points of the Otanmäki survey area.

EAST (WGS84)	NORTH (WGS84)	EAST (ETRS-TM35FIN)	NORTH (ETRS-TM35FIN)
<b>27.113315</b>	64.113349	505520	7109650
<b>27.104936</b>	64.123478	505110	7110778
<b>27.123287</b>	64.126380	506003	7111103
<b>27.131660</b>	64.116250	506413	7109975

Timo Åman was the principal pilot, and Ari Saartenoja and Markku Pirttijärvi were co-pilots. The survey consisted of two flights. In first flight (RT), Radai's old total field measuring data logger was used (without orientation). The second flight (MS) used the new MULSEDRO data logger, which has an approximately five times faster sampling rate of 50 Hz (see Table 2).

The flight paths are illustrated in Figures 11 and 12 for the RT and MS flights, respectively. In both flights, first only every third line was flown and the missing lines lying in between were filled in later in two repetitions of the flight plan. In other words, the UAV skipped the two next lines to allow smoother turns from one line to another.

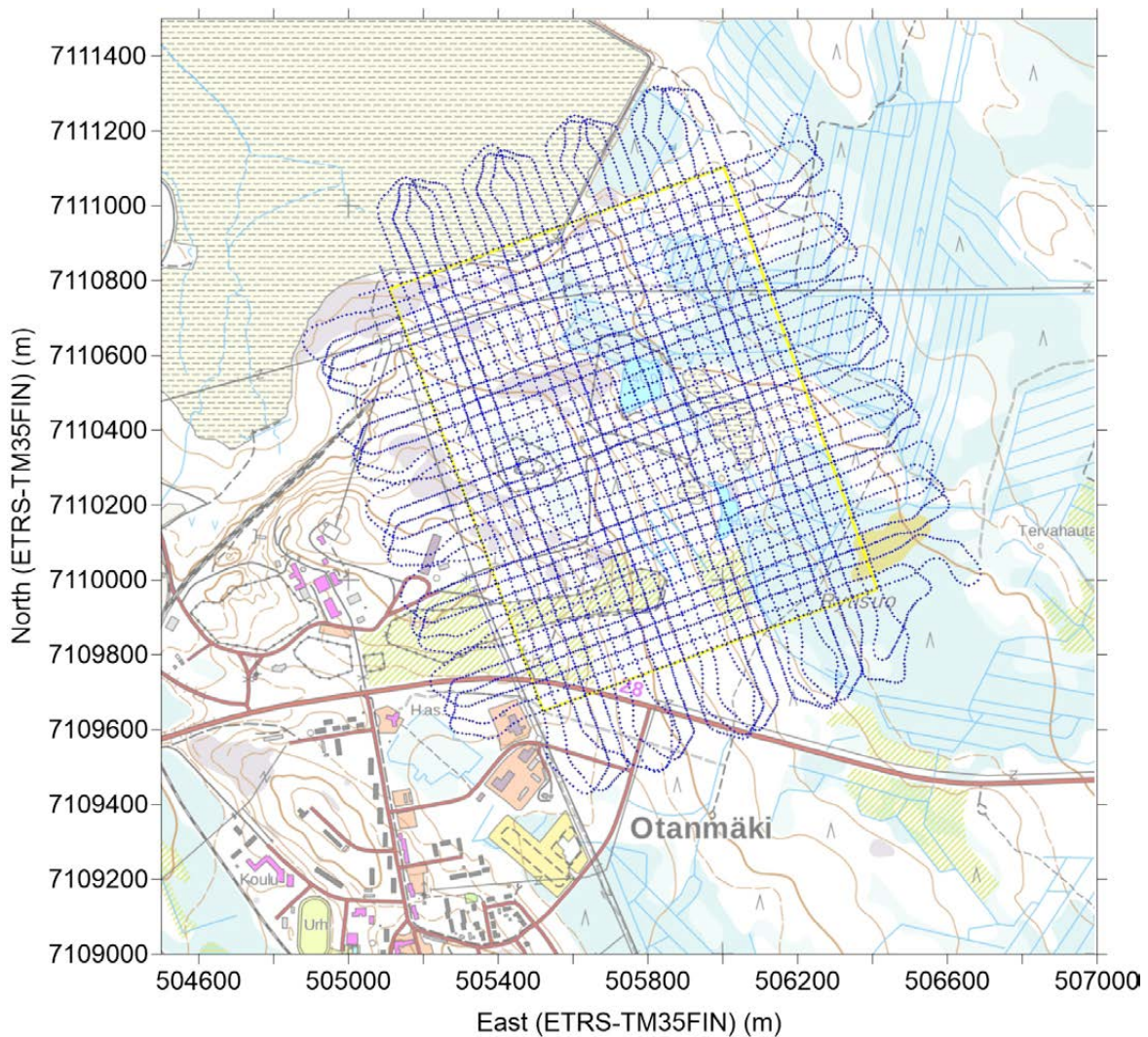


Fig. 11. The realized flight path of the first (RT) Otanmäki survey. The survey area is outlined by a yellow polygon. For clarity, only every fifth data point is plotted.

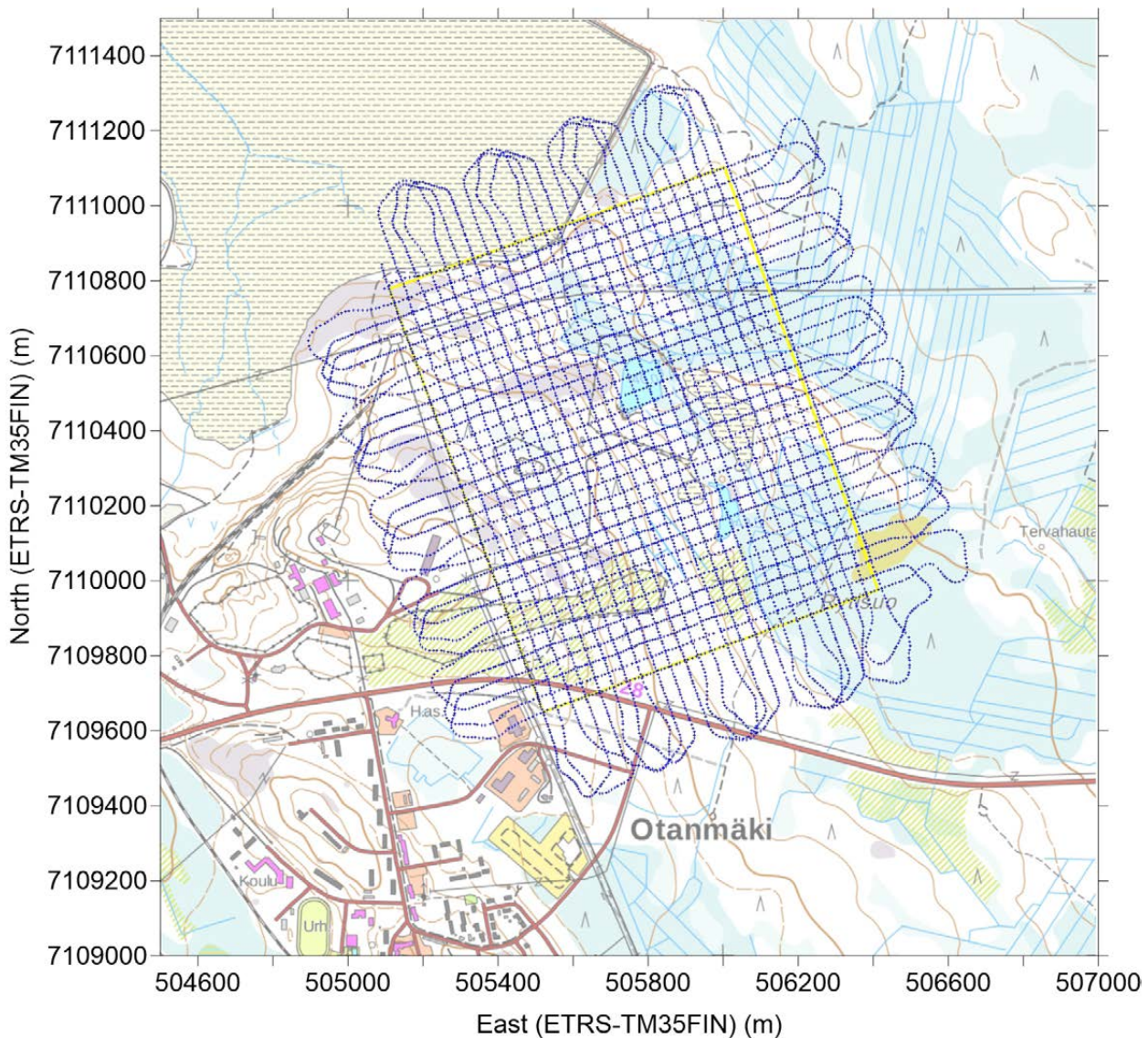


Fig. 12. The realized flight path of the second (MS) Otanmäki survey. The survey area is outlined by a yellow polygon. For clarity, only every thirtieth data point is plotted.

The height from the ground is shown in Figures 13 and 14 for the RT and MS flights, respectively. The flight altitude above sea level is presented in Figures 15 and 16 and the raw magnetic total field intensity in Figures 17 and 18. Despite differences of up to  $\pm 20$  m in the flight altitude (and height

from ground), the shape of the magnetic anomaly when measured with Radai's old logger (RT) and the new MULSEDRO logger (MS) was very similar. This is mainly because of the strong amplitude of the Otanmäki anomaly.

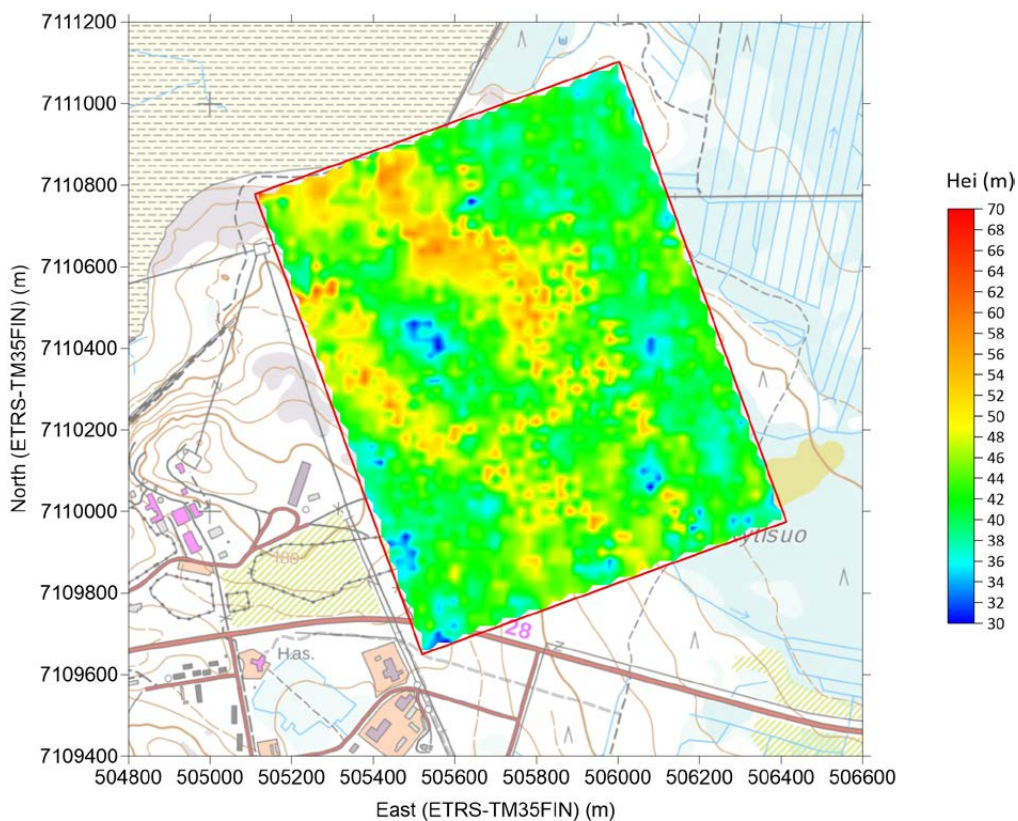


Fig. 13. Height from the ground of the first (RT) Otanmäki survey.

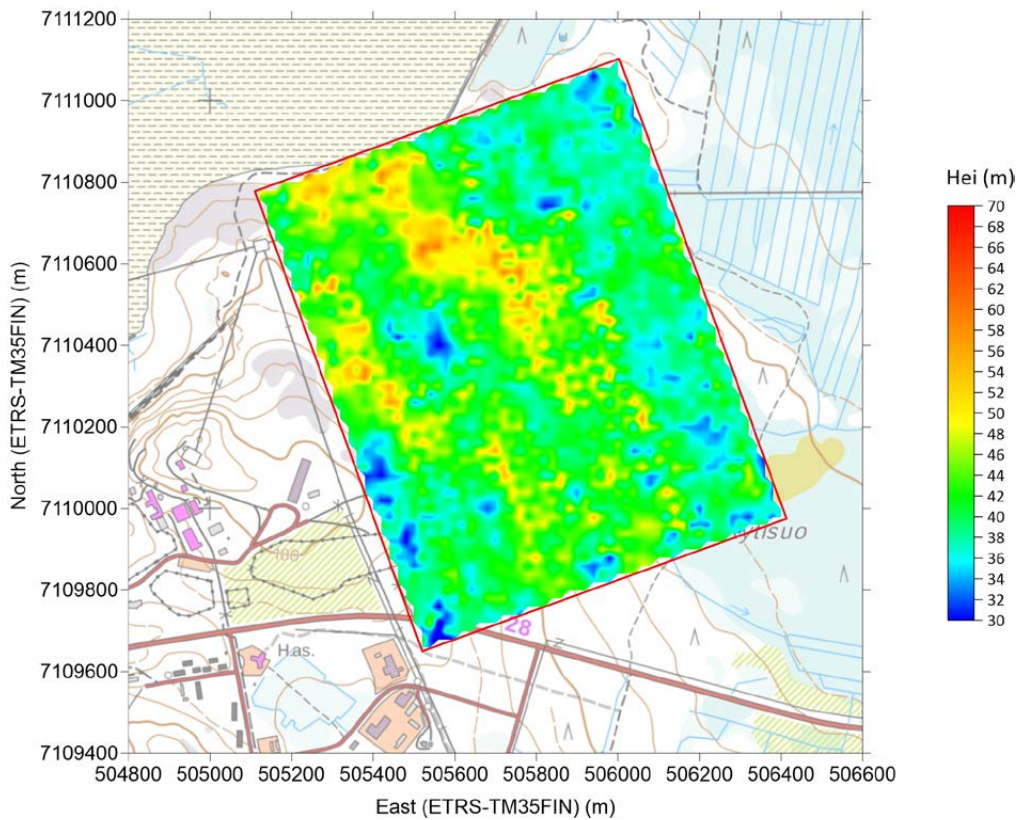


Fig. 14. Height from the ground of the second (MS) Otanmäki survey.

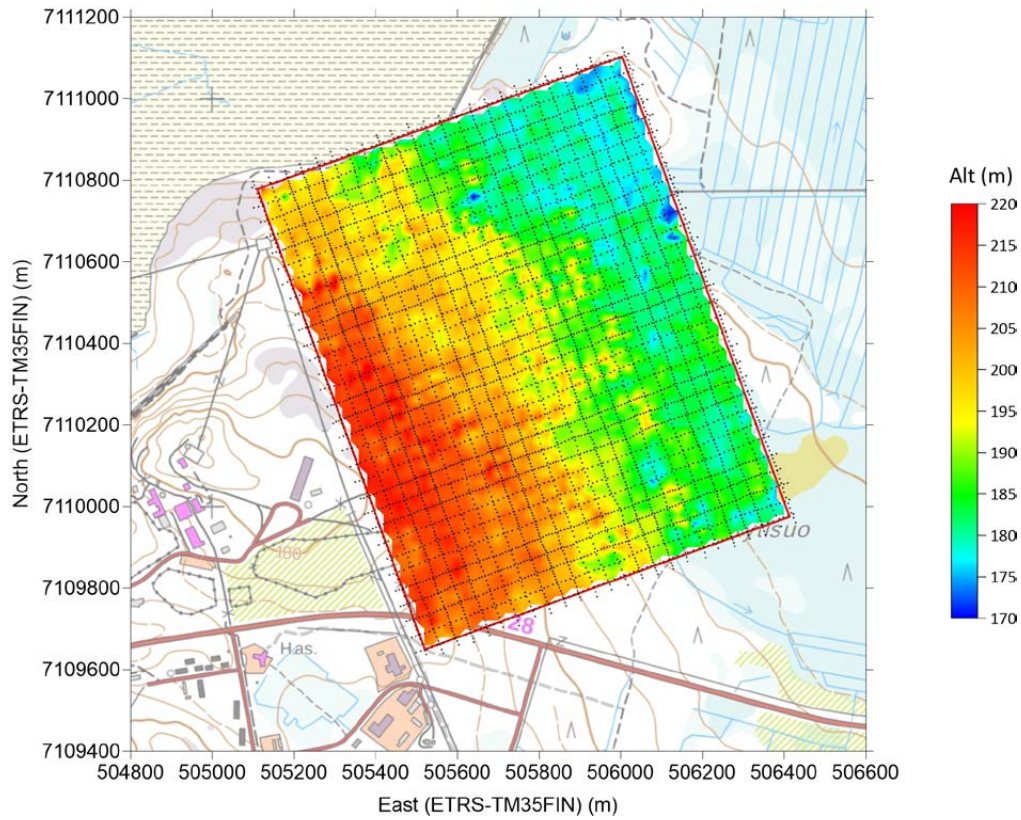


Fig. 15. Flight altitude and location of the clipped data of the first (RT) Otanmäki survey.

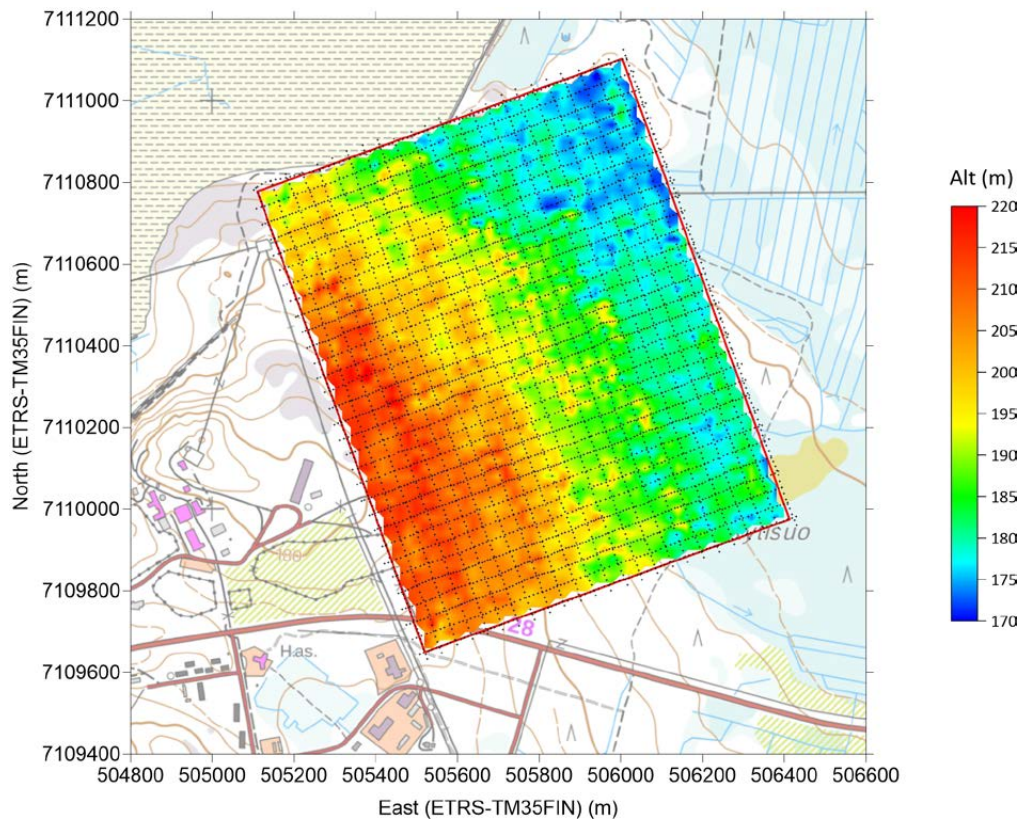


Fig. 16. Flight altitude and location of the clipped data of the second (MS) Otanmäki survey.

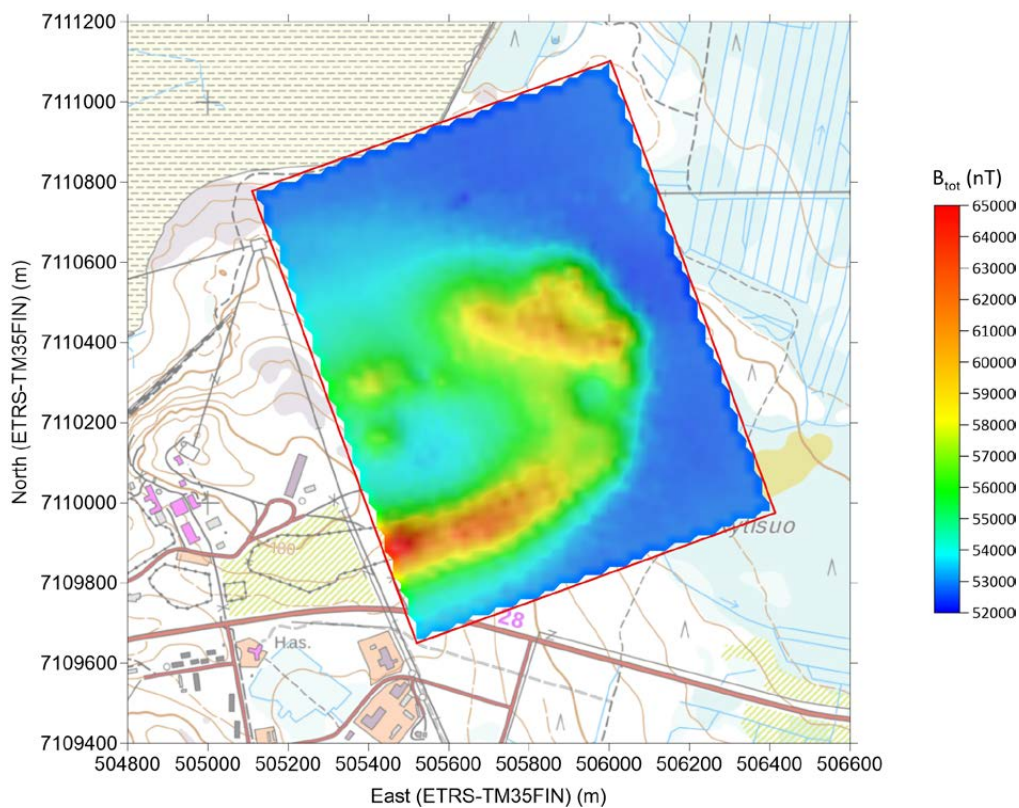


Fig. 17. Raw magnetic total field of the first (RT) Otanmäki survey.

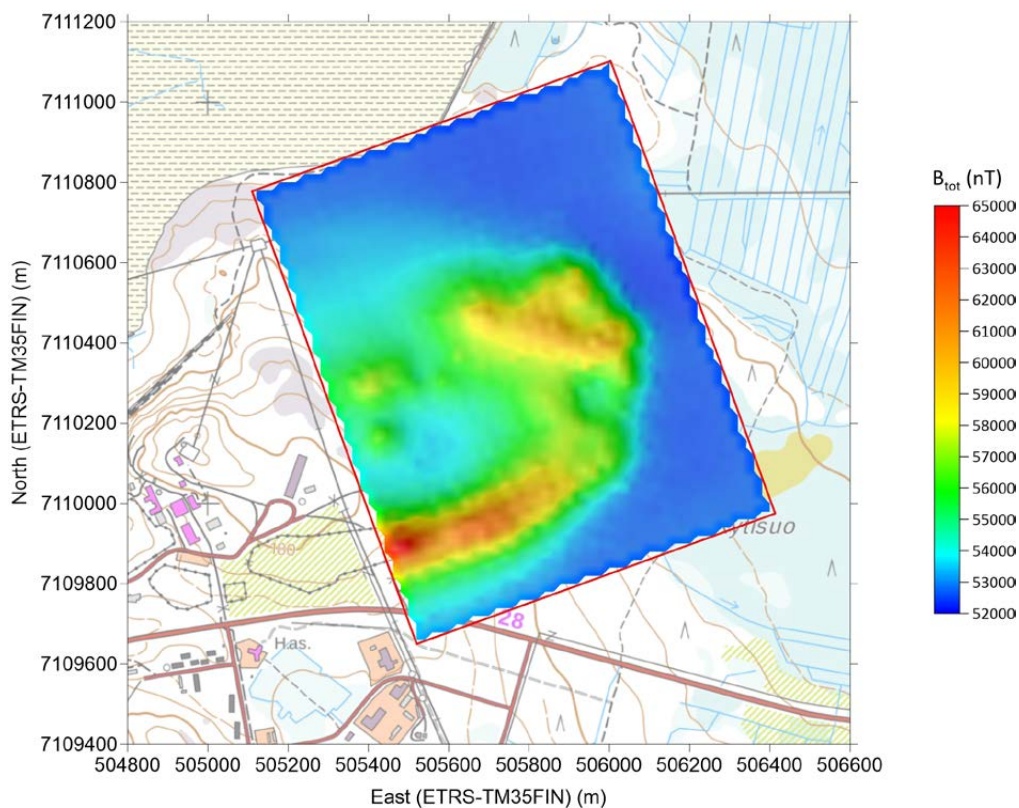


Fig. 18. Raw magnetic total field of the second (MS) Otanmäki survey.

### 3.1.1.3 Data processing

The data were processed using the interactive Radaipro (v. 1.9) software developed by Markku Pirttijärvi. The basic data processing steps executed on the raw data are listed below:

1. Removal of dummy/missing data values;
2. Removal/averaging of adjacent points with identical coordinates (optional);
3. Computation of the barometric height (relative altitude) from pressure data;
4. Computation of the rectangular X and Y coordinates (ETRS-TM35FIN);
5. Computation of the profile distance coordinate (i.e. cumulative distance along the flight path starting from the first measurement point) and azimuth/heading angle;
6. Application of flux-gate calibration parameters (derived from a separate calibration measurement);
7. Computation of the corrected total magnetic field from the X, Y and Z components;

### 8. Computation of IGRF reference field values ( $B_x$ , $B_y$ , $B_z$ , $B_{tot}$ , inclination and declination).

After the basic processing steps, 1) base station correction was applied to the magnetic total field and barometric altitude of both flights, 2) data points outside the survey area (with 15 m margins) were removed, and 3) a low-pass filter with a cut-off wavelength of about 25 metres was applied to the corrected magnetic total field.

The base station data are presented in Figures 19 and 20 for the RT and MS flight, respectively. The magnetic field changes exceeded only a few nanotesla during both surveys. The ca. 20 Pa change in barometric pressure accounts for an approximately 2-metre decrease in altitude during the first (RT) flight. The altitude estimate of the second (MS) flight changed by less than 1 m during the flight.

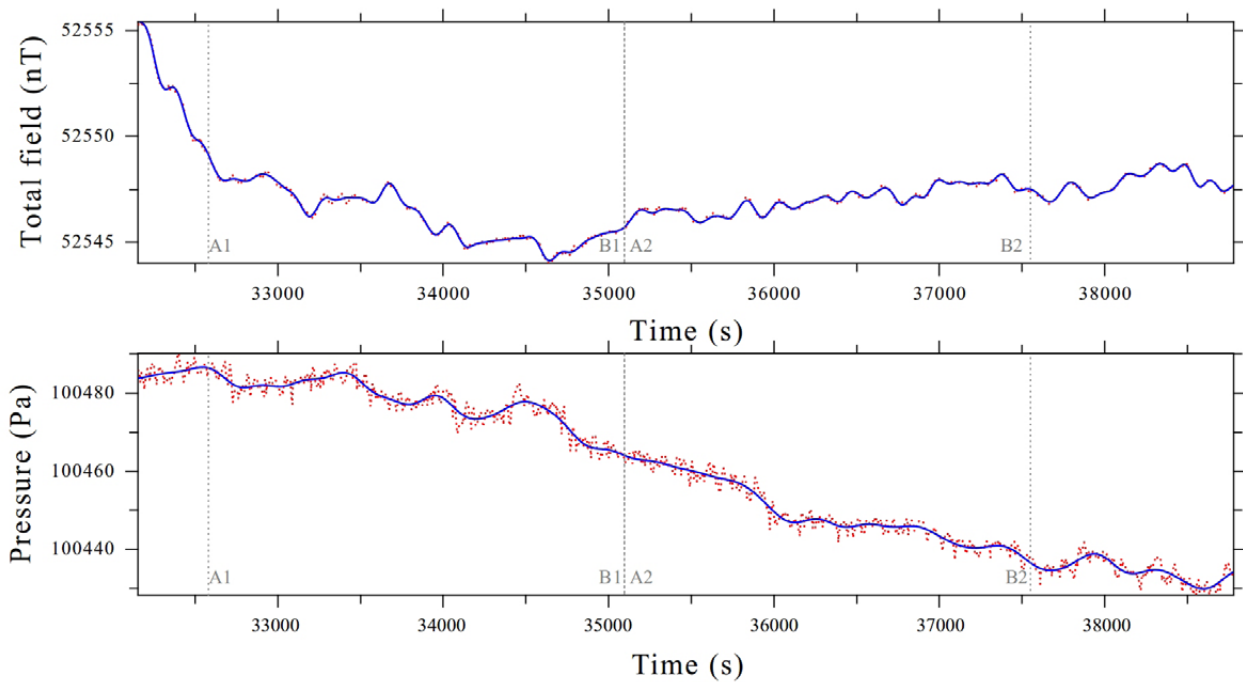


Fig. 19. Magnetic total field (top) and barometric pressure (bottom) during the first flight (RT) of the Otanmäki survey. During the time intervals A1–B1 and A2–B2, respectively, the E–W and N–S-directed flight lines were flown. The solid blue line indicates the low-pass filtered data used for base station correction.

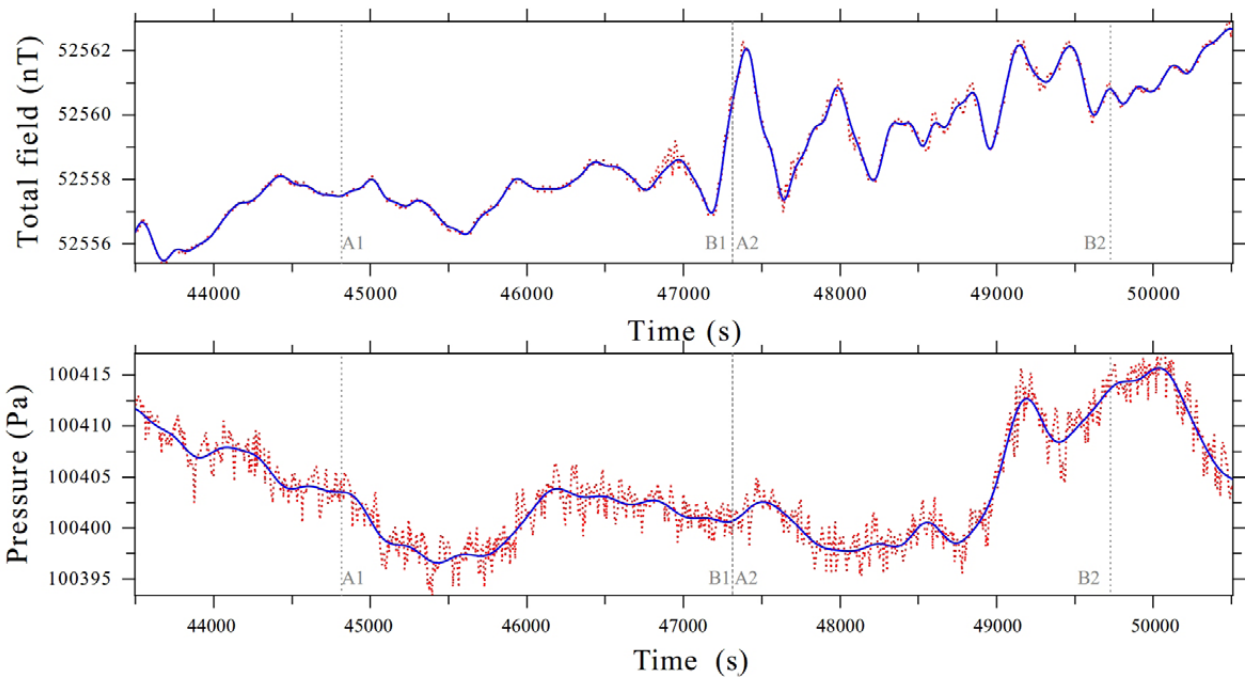


Fig. 20. Magnetic total field (top) and barometric pressure (bottom) during the second flight (MS) of the Otanmäki survey. During the time intervals A1–B1 and A2–B2, respectively, the E–W and N–S–directed flight lines were flown. The solid blue line indicates the low-pass filtered data used for base station correction.

Statistical information regarding the surveys is provided in Table 4. In the first survey (RT), the total number of data points (remaining after clipping) was about 30 000, the total survey length was about 63 km, the mean point distance was 2.1 m, the mean height was 43.5 m and the mean flight speed was 18.7 m/s. In the second survey (MS), the total number of data points (remaining after clipping) was about 166 000, the total survey length was about 70 km, the mean sample step was 0.4 m, the mean height was 41.6 m and the mean flight speed was 20.4 m/s.

The standard deviation of the 4-point difference ( $D_4$ ) is a measure of the noise level of the

data (Reeves 2005), which was about 150 nT in the raw magnetic data measured with Radai's RT logger and about 110 nT in raw data measured with the MULSEDRO logger. Thus, the MULSEDRO logger appears to be less sensitive to noise. On the other hand, the corresponding values were 0.3 nT and 4 nT for the low-pass filtered RT and MS data, respectively. The lower  $D_4$  values of the low-pass filtered RT data were due to the lower sampling rate (10 Hz) compared to data measured with the MS logger (50 Hz).

Table 4. Statistics from the two flights of the Otanmäki magnetic survey with Radai's old logger (RT) and the MULSEDRO logger (MS).

Parameter	Flight RT	RT EW	RT NS	Flight MS	MS EW	MS NS
Data points	30 670	15 019	15 651	165 813	95 009	70 804
Length (m)	62 993	31 615	31 378	69 609	35 294	34 315
Flight time (min)	56.0	27.3	28.7	57.0	28.9	28.1
Mean speed (m/s)	18.7	19.3	18.2	20.4	20.3	20.4
Mean sampling (m)	2.05	2.11	2.00	0.42	0.37	0.48
Mean height (m)	43.5	44.7	42.3	41.6	43.1	39.6
Min $B_{tot}$ (nT)	52 211	52 211	52 369	52 199	52 226	52 199
Max $B_{tot}$ (nT)	66 080	66 080	65 186	66 142	66 142	64 235
Mean $B_{tot}$ (nT)	54 421	54 407	54 434	54 270	54 267	54 273
Median $B_{tot}$ (nT)	53 540	53 609	53 476	53 378	53 437	53 337
Std $B_{tot}$ (nT)	2381.24	2263.95	2490.31	2373.38	2314.08	2438.20
Std D4 raw (nT)	150.22	150.18	150.27	110.82	118.70	99.27
Std D4 cor (nT)	0.28	0.30	0.27	3.72	4.00	3.30

#### 3.1.1.4 Equivalent layer modelling (ELM)

Equivalent layer modelling (ELM) is used to grid the total field data on a constant elevation level by applying a deterministic inversion to the measured magnetic data. The inversion is based on a linearized least squares method with adaptive damping (Pirttijärvi 2003) and lateral 2D constraining, as in the well-known Occam's method (Constable et al. 1987). ELM removes the effects of varying flight altitude and uneven sampling of the data points. ELM also removes high frequency noise and artefacts (e.g. from electric power lines and noise caused by the UAS engine), provided that their wavelength is short compared to the size of the elements used in the layer model. ELM is additionally used for levelling of datasets (including tie-line correction), making the heading correction and computing the total field at the original data locations with reduced errors and noise content.

In the ELM modelling of the Otanmäki magnetic survey, the horizontal size of the elements was  $40 \text{ m} \times 40 \text{ m}$ , their vertical extent was 50 m and the tops of the elements were located 5 m below the surface, which was considered to be flat. In

the final inversion, the total number of elements was  $34 \times 40 = 1360$ . In the case of the first survey (RT), the total number of (harvested) data points was 16 916, which was about 55% of all the data (30 670). The final root-mean-square (RMS) error was 0.453%. In the second survey (MS), the total number of (harvested) data points was 14 477, which was about 8.7% of all the data (165 813). The final RMS was about 0.377%. The intensity and the direction of the magnetic field were derived from IGRF ( $B_0 = 52942 \text{ nT}$ ,  $I = 75.3^\circ$ ,  $D = 11.2^\circ$ ) and the impact of remanence was ignored.

The magnetic susceptibility models obtained from the ELM were used to compute the magnetic field (and the first vertical derivative) on a regular ( $20 \text{ m} \times 20 \text{ m}$ ) grid at constant altitudes of 5 and 35 m.

#### 3.1.1.5 Results

Figures 21 and 22 present the final results as maps of magnetic total field intensity computed by ELM on an even grid at a constant height of 35 m above the ground surface. At first glance, the two sets of results appear almost identical. Figures 23 and 24

display the ELM-computed results at the height of 5 m above the surface. Comparison of these figures indicates that final results from the new MULSEDRO data logger are less affected by noise from the electric powerline in the northern part of the survey area. This is mainly due to its higher sample rate and its possibilities to better filter out high-frequency noise.

Figures 25 and 26 present the (final) corrected magnetic total field. “Corrected” means that the data contain the levellings, time trends and heading corrections obtained from ELM. The corrected data are interpolated from the actual positions of the flight lines, and they therefore contain the effect of varying flight altitude.

Figures 27 and 28 illustrate the differences between the raw and corrected total fields. Most of the differences are due to the heading corrections. Figures 29 and 30 display the differences between the measured and ELM-computed data at the original data locations. The misfit is smaller in the second (MS) flight.

To investigate the effect of flight altitude variations, Figures 31 and 32 display the differences between the ELM-modelled data at the constant altitude of 40 m and the total field computed at the original data locations. The maximum difference is over 1000 nT.

To investigate the differences between the two flights, Figures 33–35 show the misfit in a) ELM-

computed data at the altitude of 35 m, b) corrected data and c) computed data at the original data locations between the two flights. As expected, the misfit is smallest for the ELM-computed data at a constant altitude. The misfit in the ELM data at a constant altitude of 35 m is about as large as the difference between the measured and computed data in general (Figs. 29 and 30). This suggests that the model obtained from the ELM inversion of one dataset fits the other dataset almost equally well. This was confirmed through testing, but the results are not presented here.

Finally, Figures 36–39 present the first vertical derivative of the total magnetic field computed using ELM on an even grid at the heights of 5 and 35 m for the first (RT) and the second (MS) flight.

All in all, the results obtained with the new MS logger are very close to those obtained with Radai’s old data logger. The greatest benefit of the MS logger seems to be its higher sampling rate, which results in magnetic maps that are less affected by electrical disturbances such as powerlines. Another benefit of the MS logger is the improved quality of magnetic data from the individual X, Y and Z components, as the orientation is also sampled more densely. However, determination of the individual magnetic components is beyond the scope of this report.

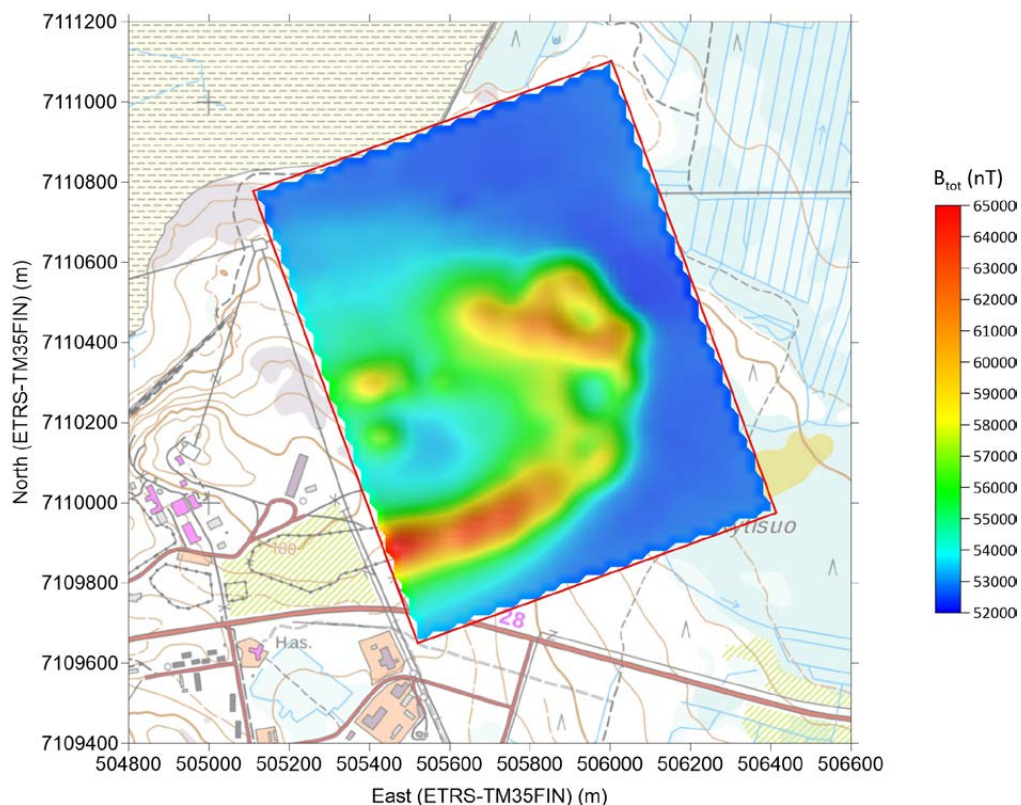


Fig. 21. Magnetic total field (with sun shading) of the first (RT) flight of the Otanmäki survey computed by ELM at the constant height of 35 m on an even grid.

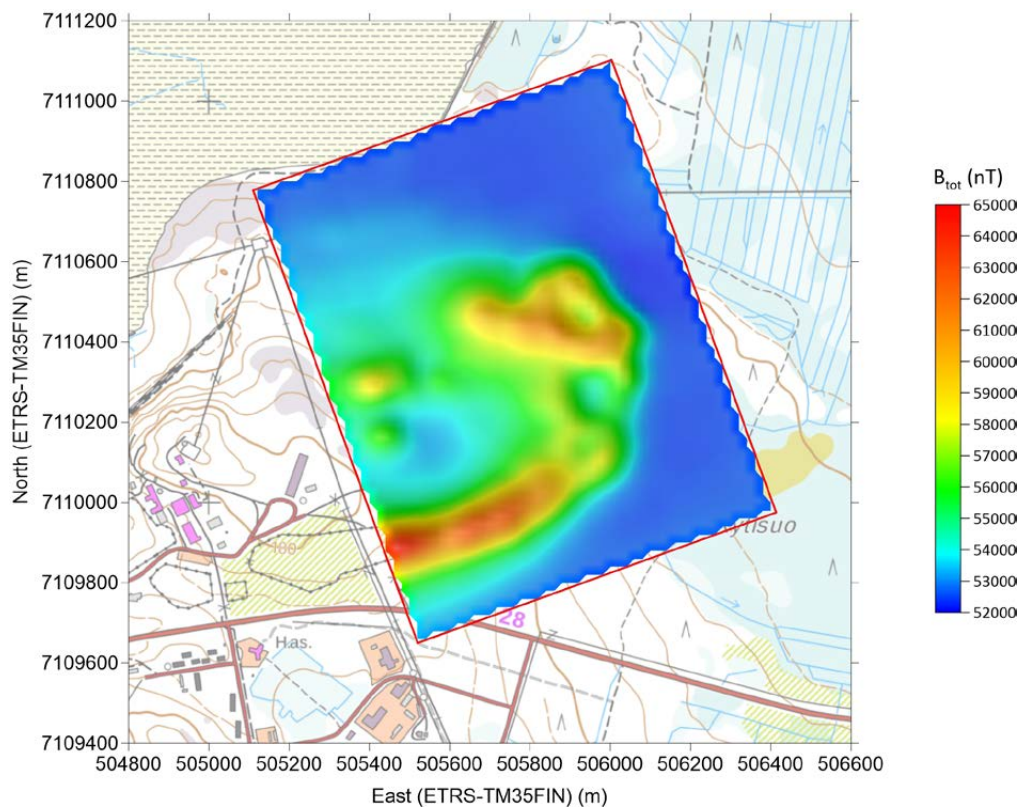


Fig. 22. Magnetic total field (with sun shading) of the second (MS) flight of the Otanmäki survey computed by ELM at the constant height of 35 m on an even grid.

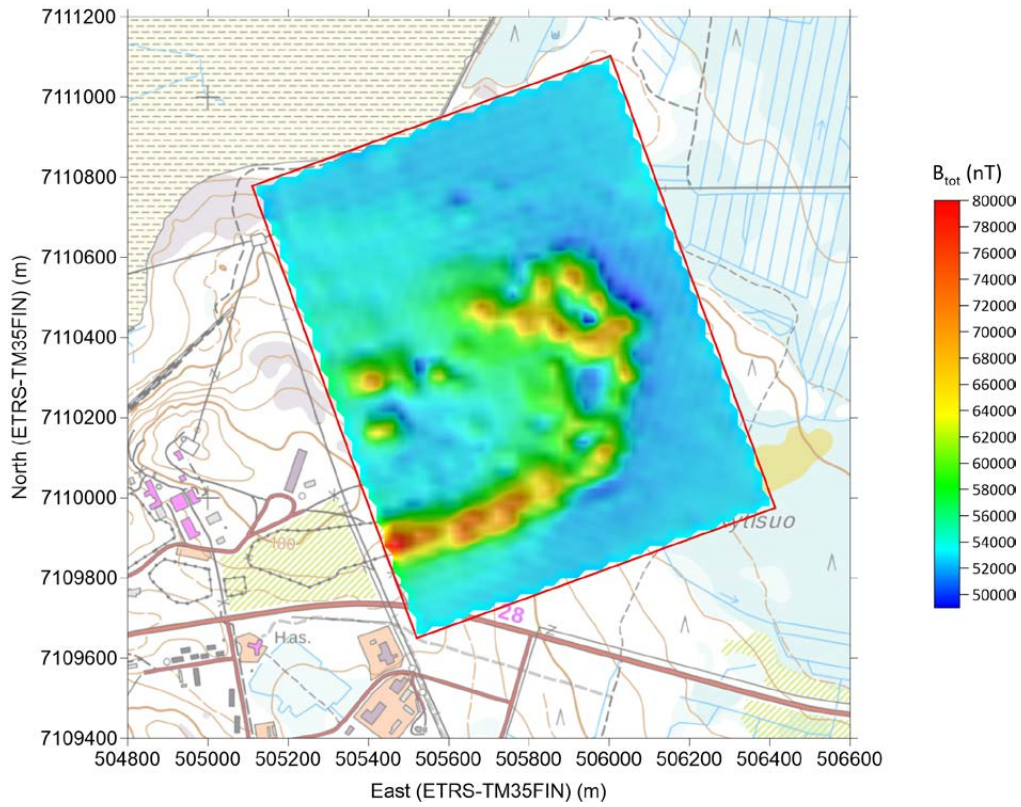


Fig. 23. Magnetic total field (with sun shading) of the first (RT) flight of the Otanmäki survey computed by ELM at the constant height of 5 m on an even grid.

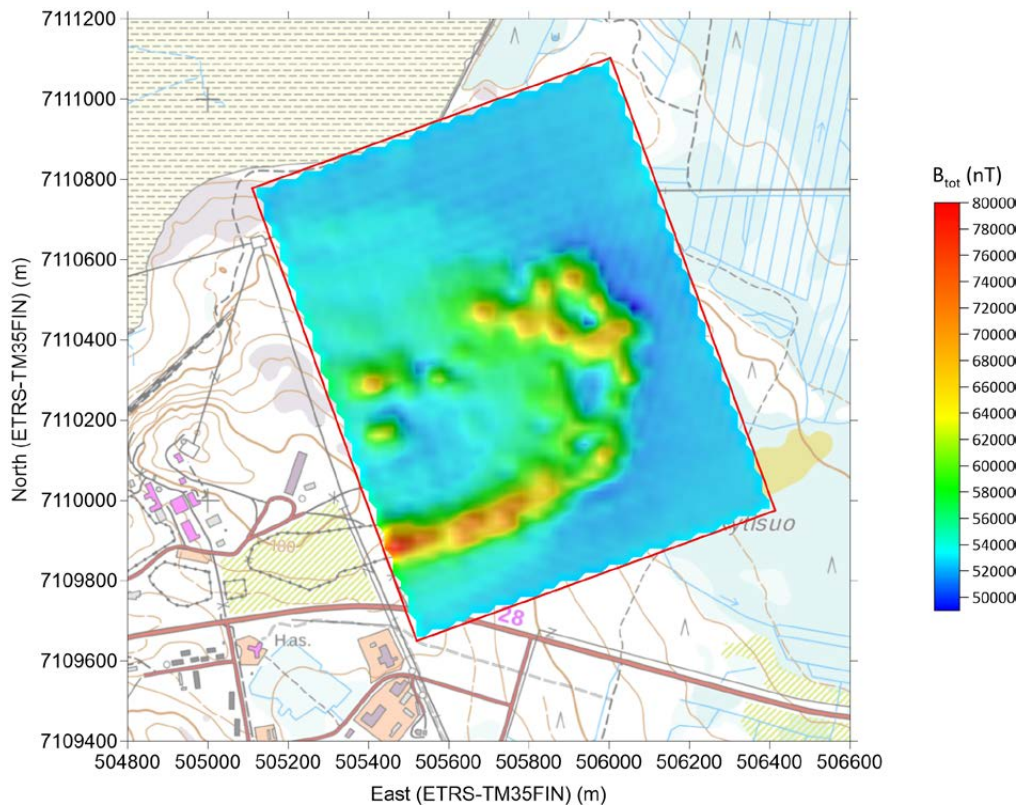


Fig. 24. Magnetic total field (with sun shading) of the second (MS) flight of the Otanmäki survey computed by ELM at the constant height of 5 m on an even grid.

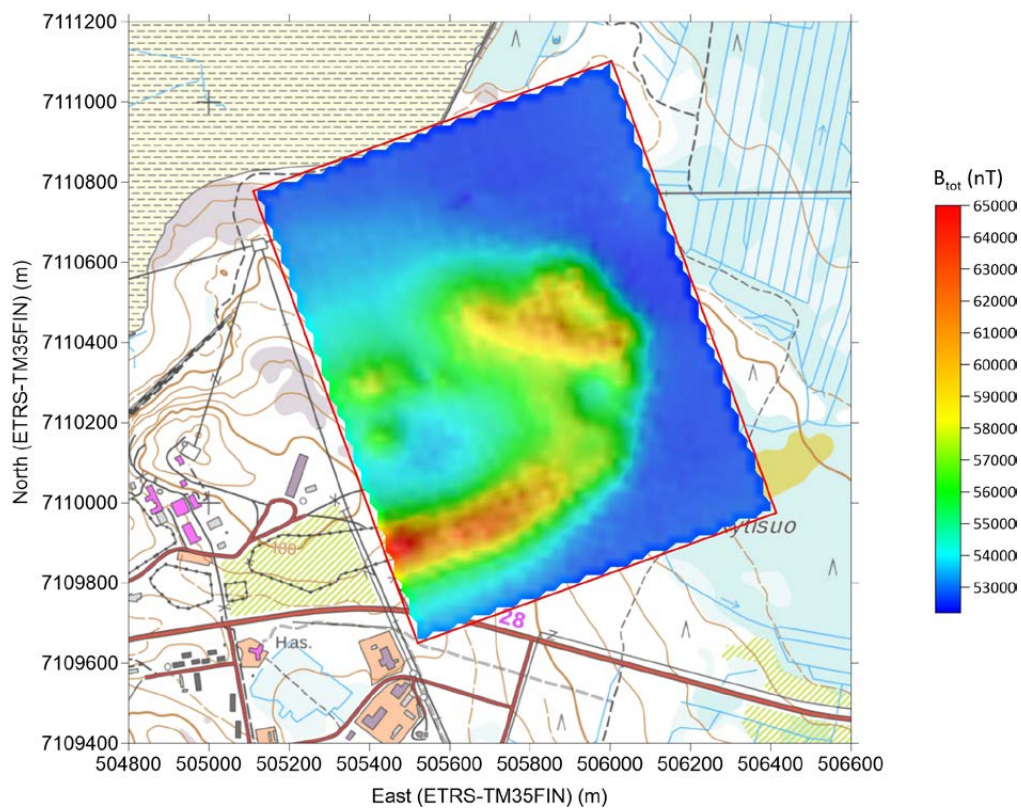


Fig. 25. Corrected magnetic total field (with sun shading) of the first (RT) flight of the Otanmäki survey.

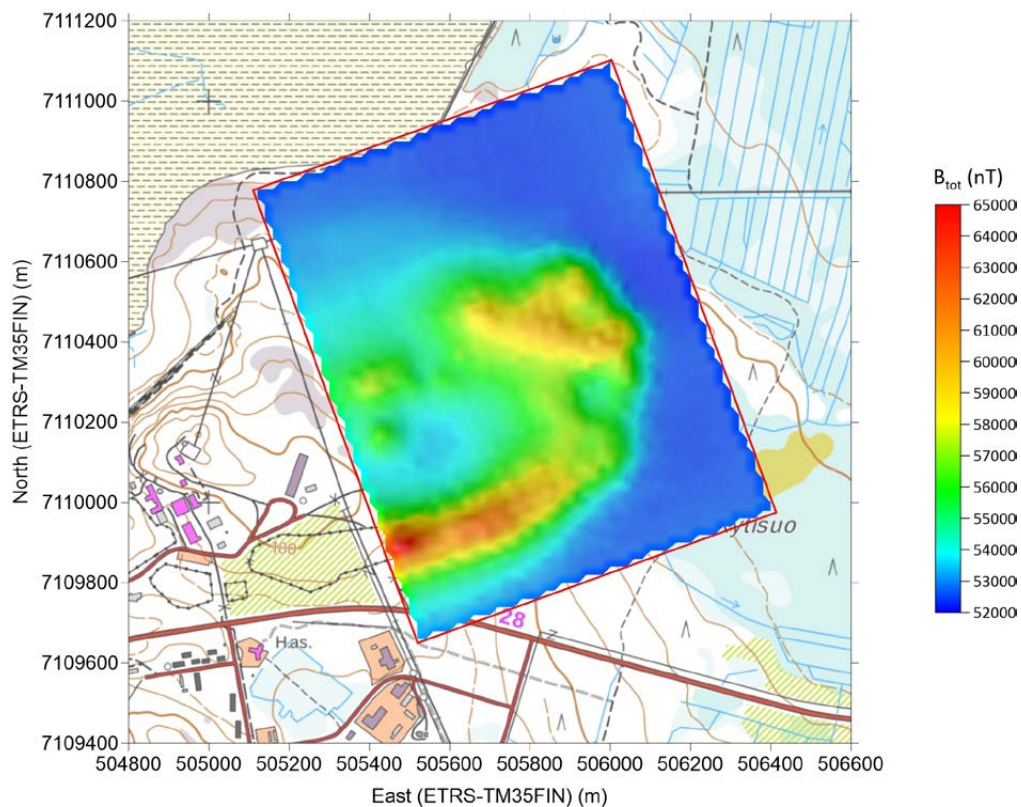


Fig. 26. Corrected magnetic total field (with sun shading) of the second (MS) flight of the Otanmäki survey.

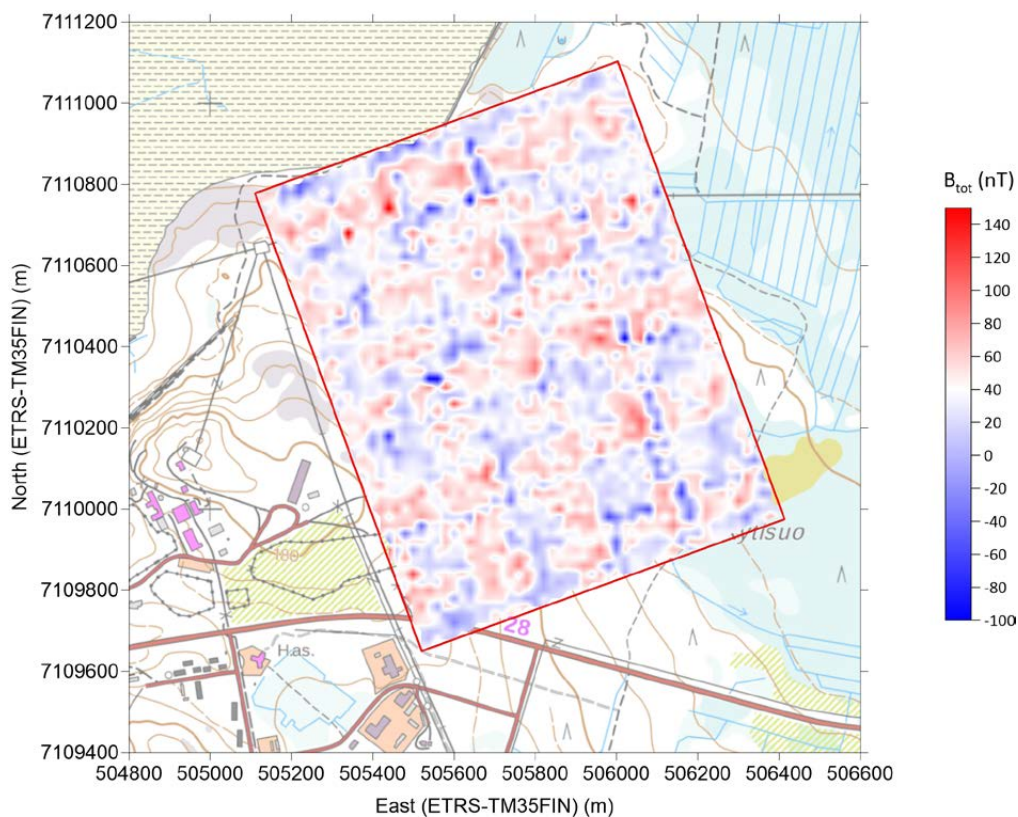


Fig. 27. Difference between the raw and the corrected total field at the original data locations for the first (RT) flight of the Otanmäki survey.

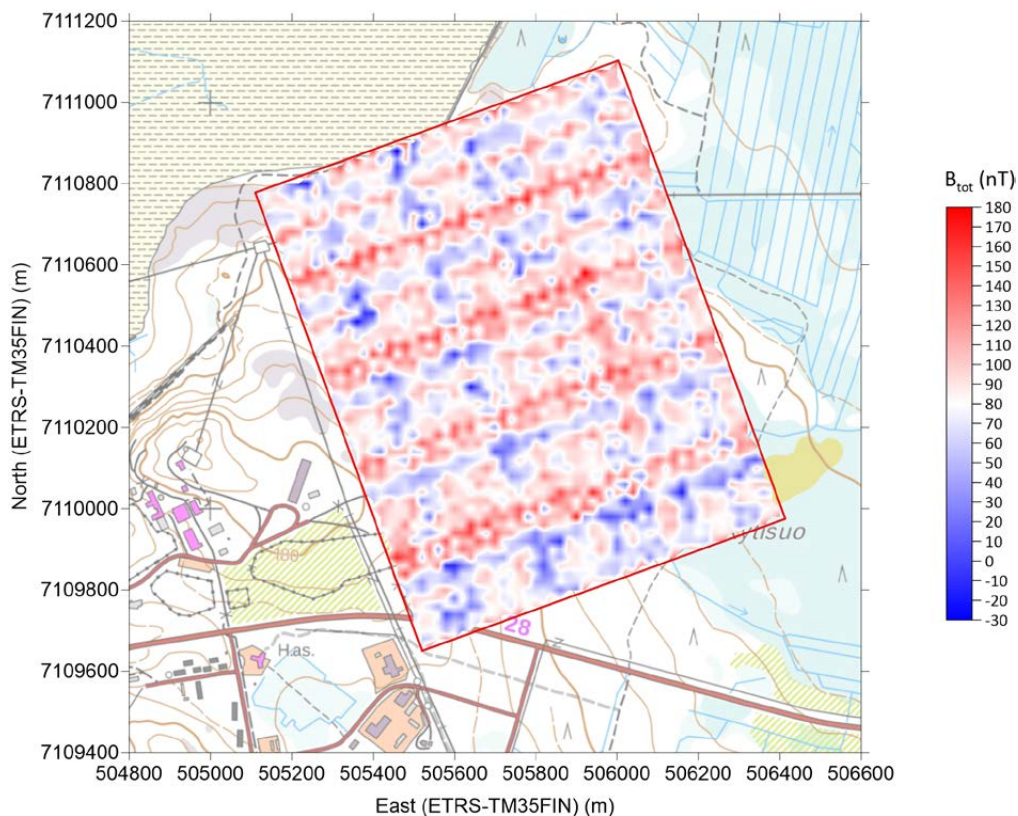


Fig. 28. Difference between the raw and the corrected total field at the original data locations for the second (MS) flight of the Otanmäki survey.

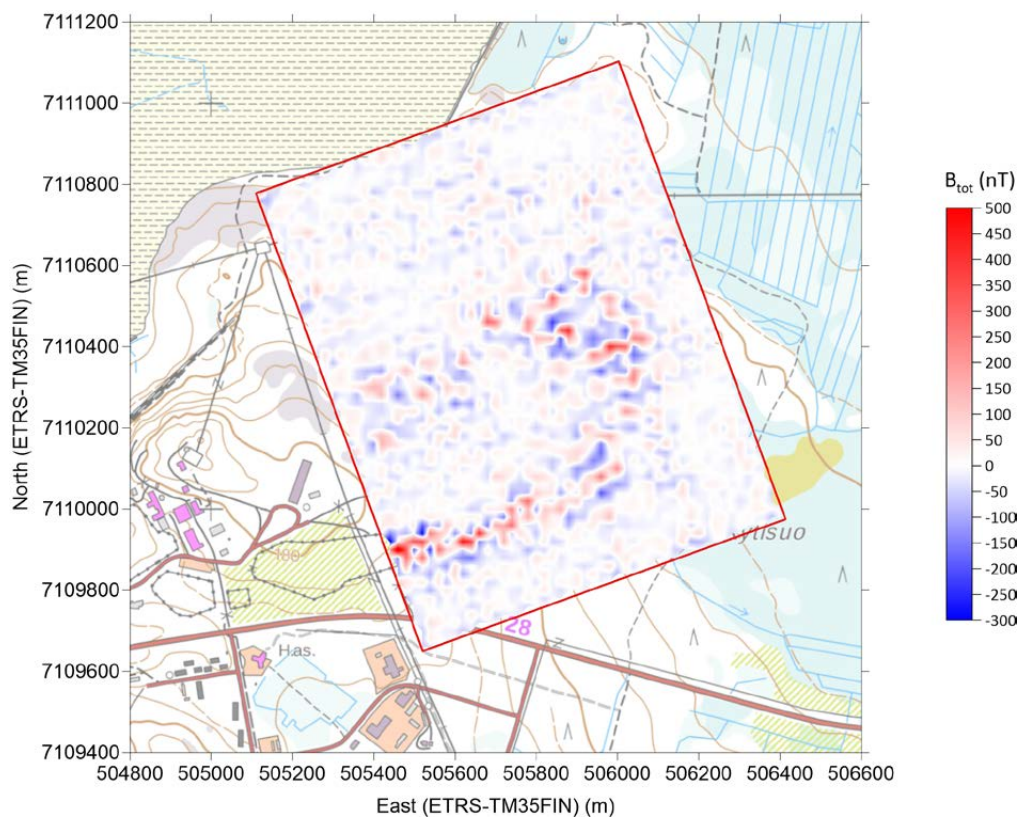


Fig. 29. Difference between the corrected and the ELM-computed total field at the original data locations for the first (RT) flight of the Otanmäki survey.

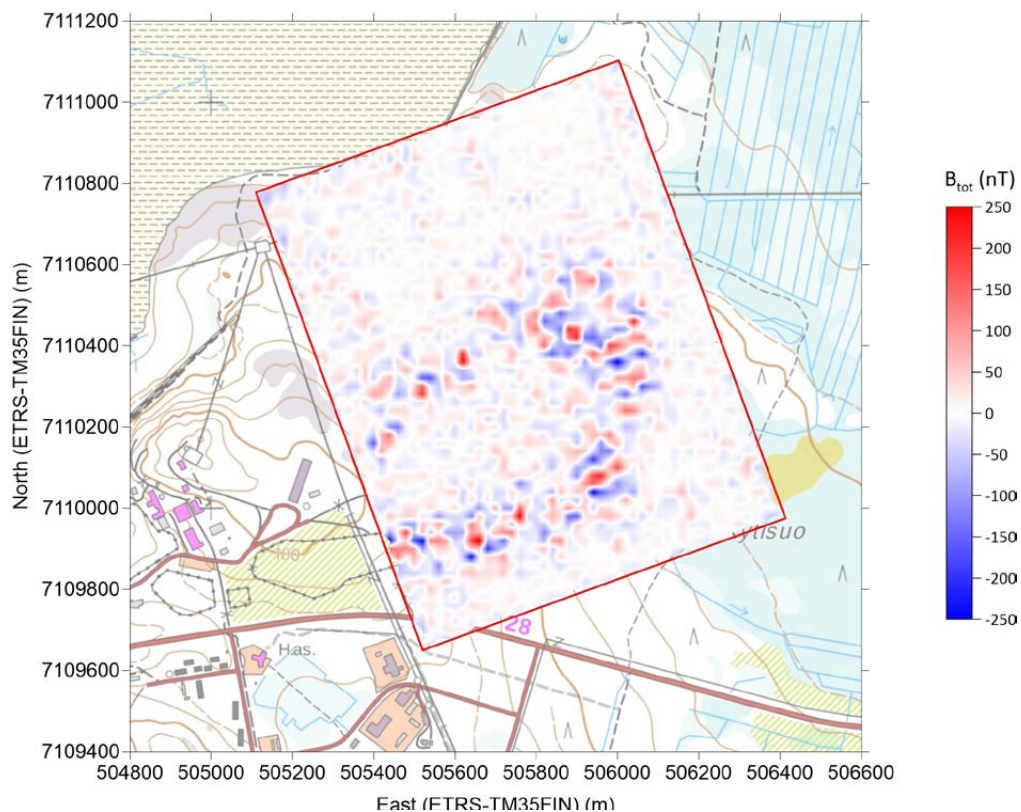


Fig. 30. Difference between the corrected and the ELM-computed total field at original data locations for the second (MS) flight of the Otanmäki survey.

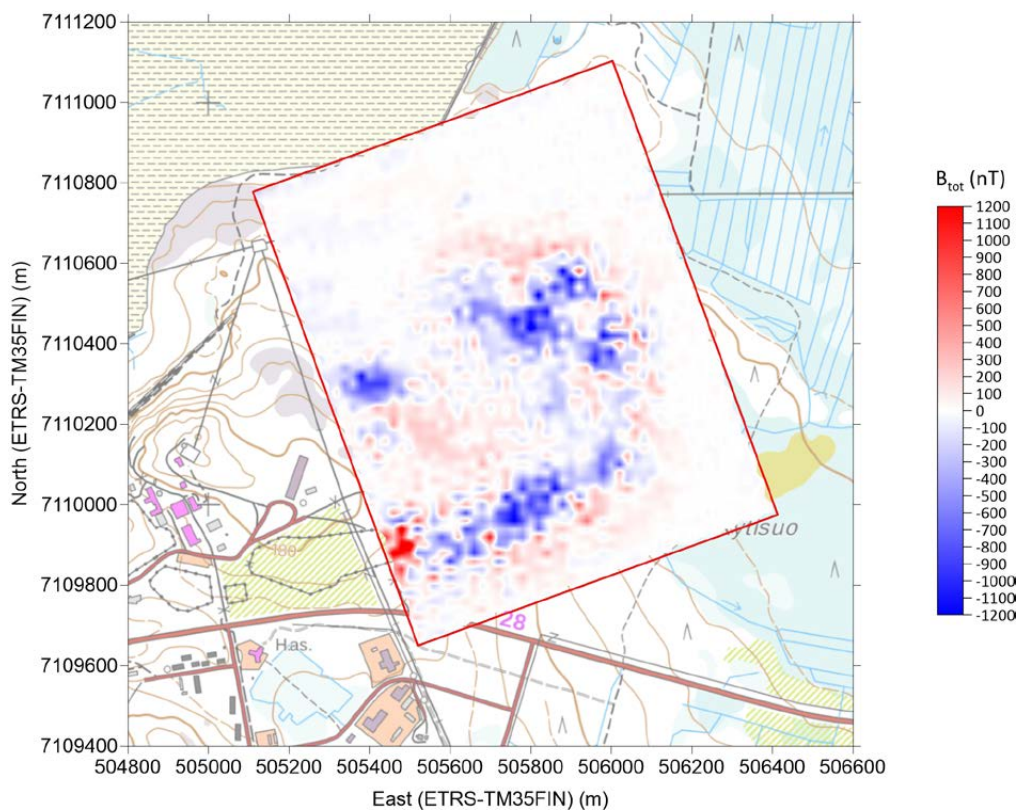


Fig. 31. Difference between the ELM-computed total field at the altitude of 40 m and the ELM-computed field at the original data locations for the first (RT) flight of the Otanmäki survey.

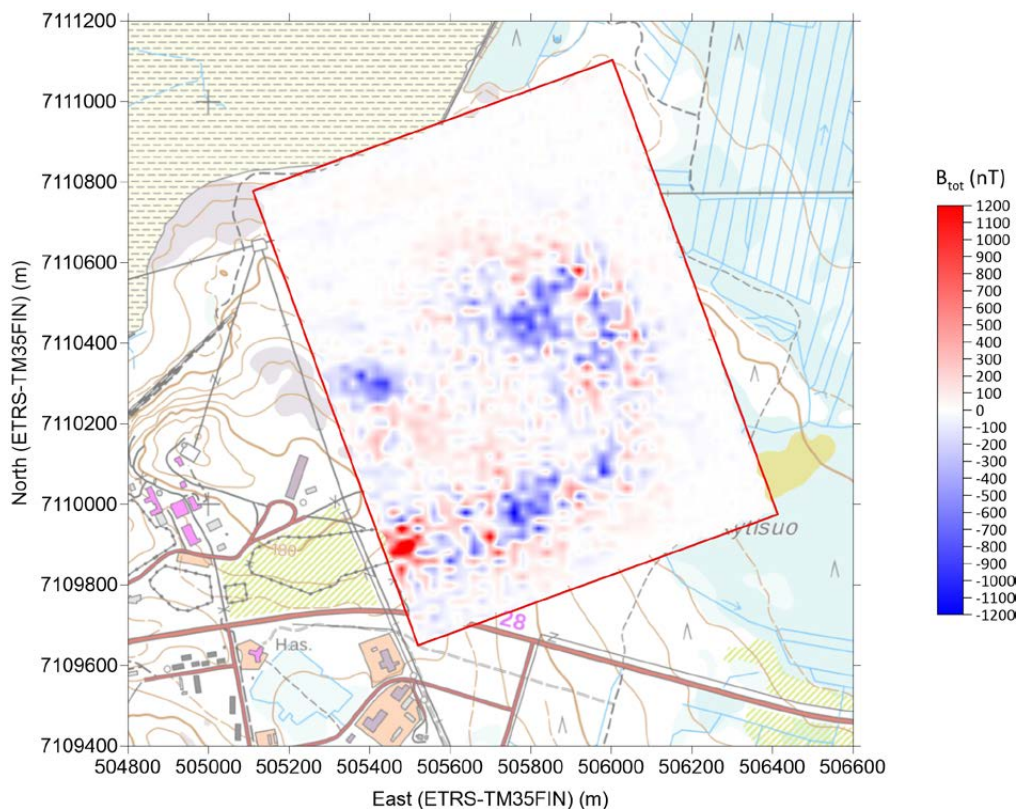


Fig. 32. Difference between the ELM-computed total field at the altitude of 40 m and the ELM-computed field at the original data locations for the second (MS) flight of the Otanmäki survey.

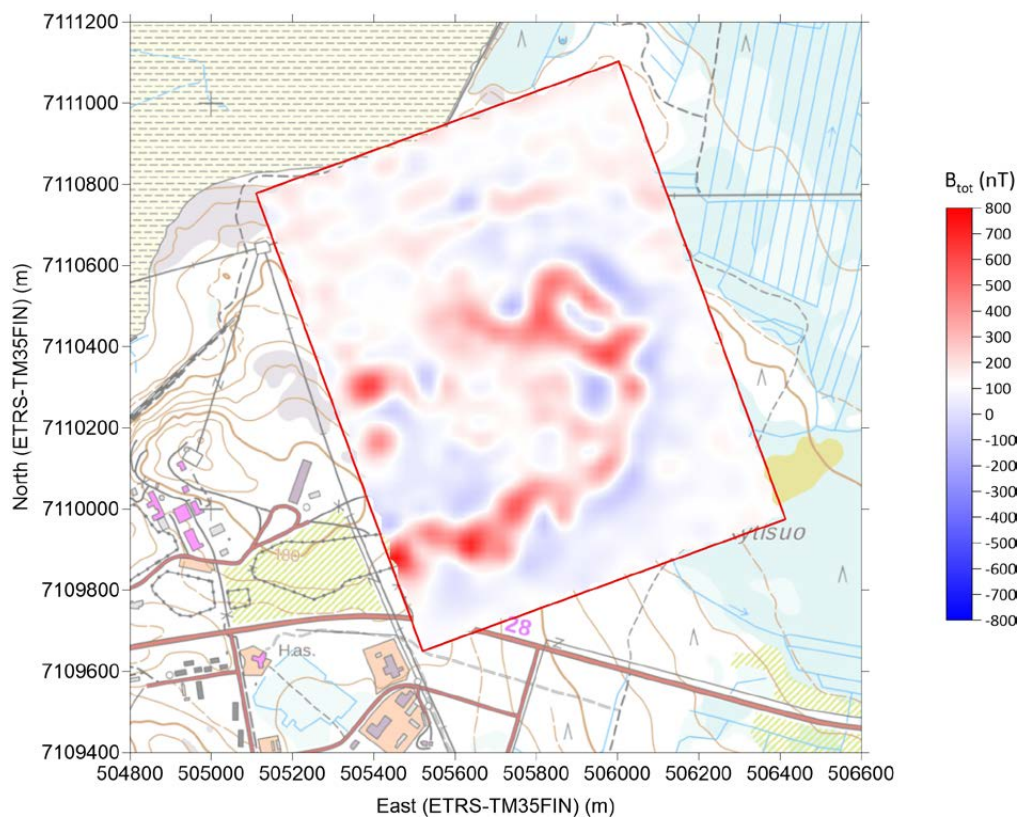


Fig. 33. Difference in the ELM-computed data at the height of 35 m between the first (RT) and the second (MS) flight.

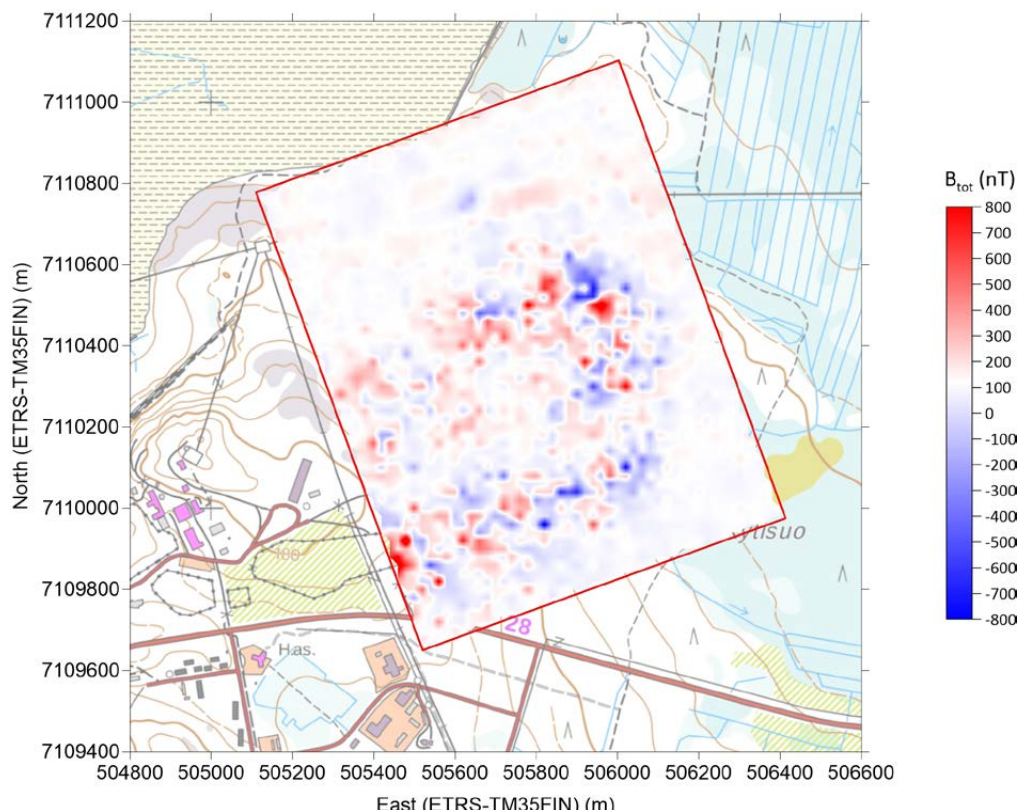


Fig. 34. Difference in the ELM-computed data at the original data locations between the first (RT) and the second (MS) flight.

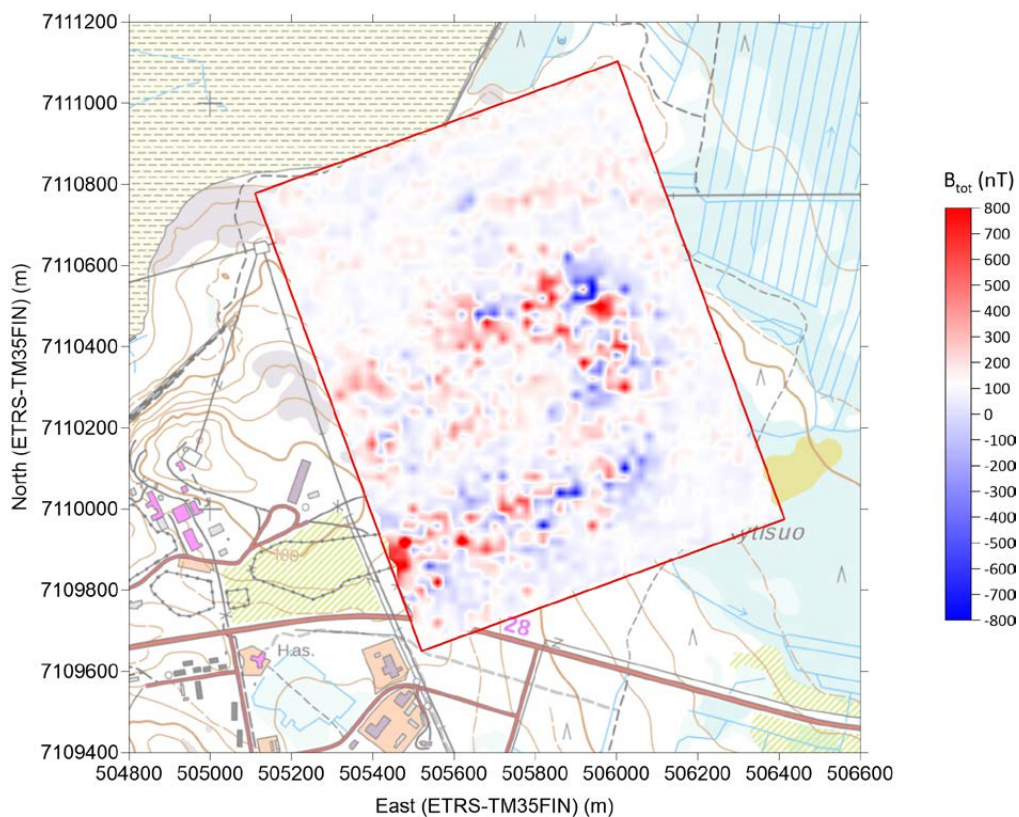


Fig. 35. Difference in the corrected total field data between the first (RT) and the second (MS) flight.

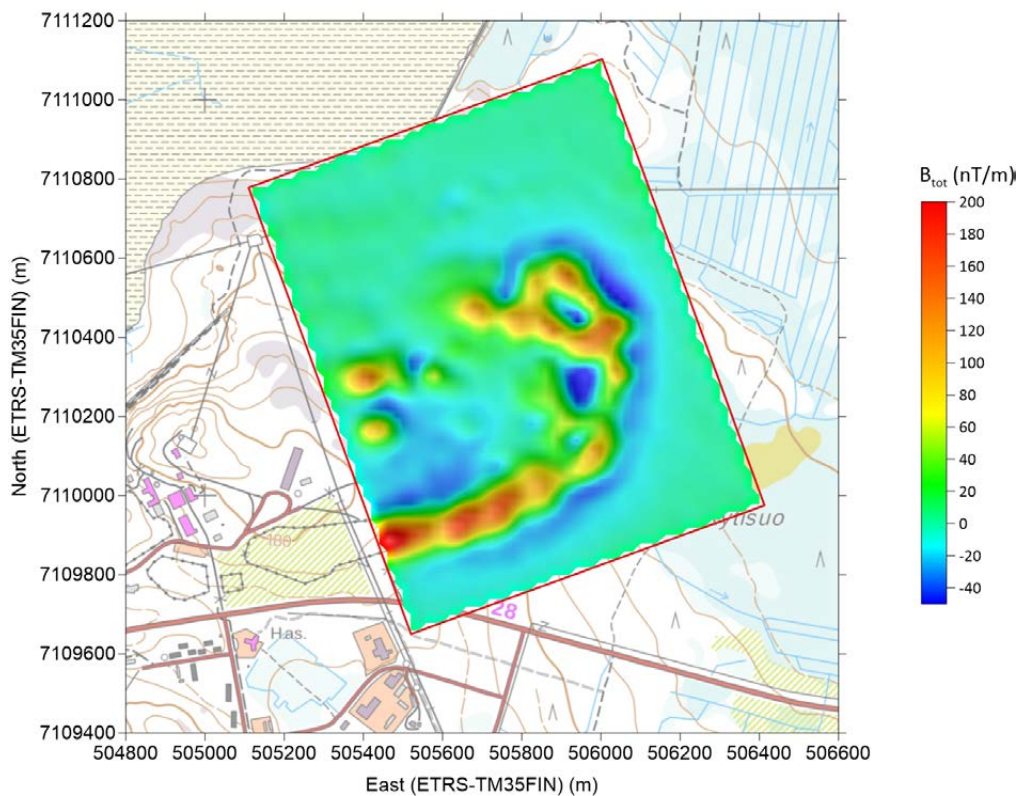


Fig. 36. First vertical derivative of the magnetic total field (with sun shading) for the first (RT) flight of the Otanmäki survey computed by ELM at the constant height of 35 m on an even grid.

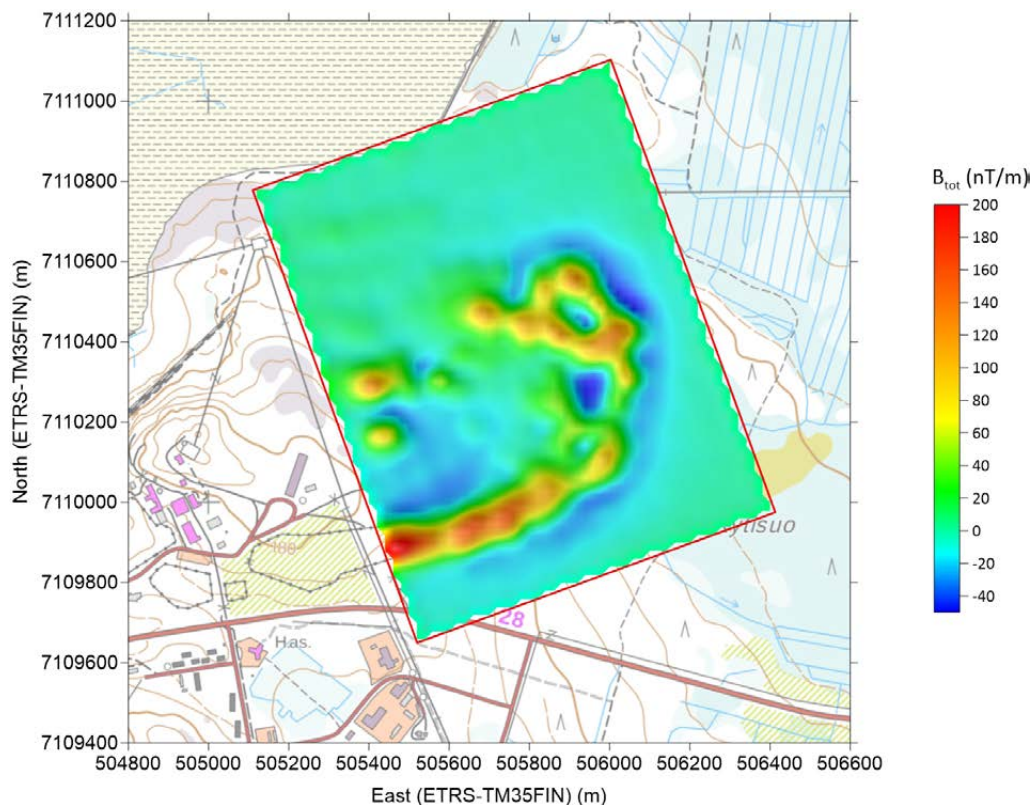


Fig. 37. First vertical derivative of the magnetic total field (with sun shading) for the second (MS) flight of the Otanmäki survey computed by ELM at the constant height of 35 m on an even grid.

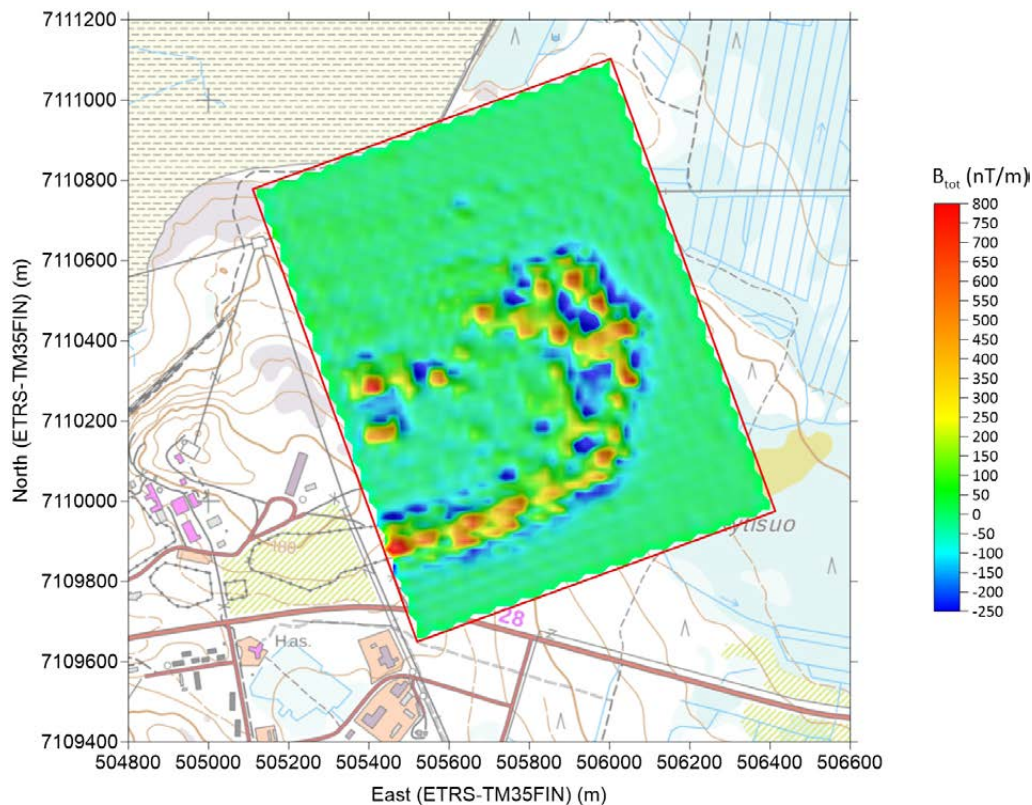


Fig. 38. First vertical derivative of the magnetic total field (with sun shading) for the first (RT) flight of the Otanmäki survey computed by ELM at the constant height of 5 m on an even grid.

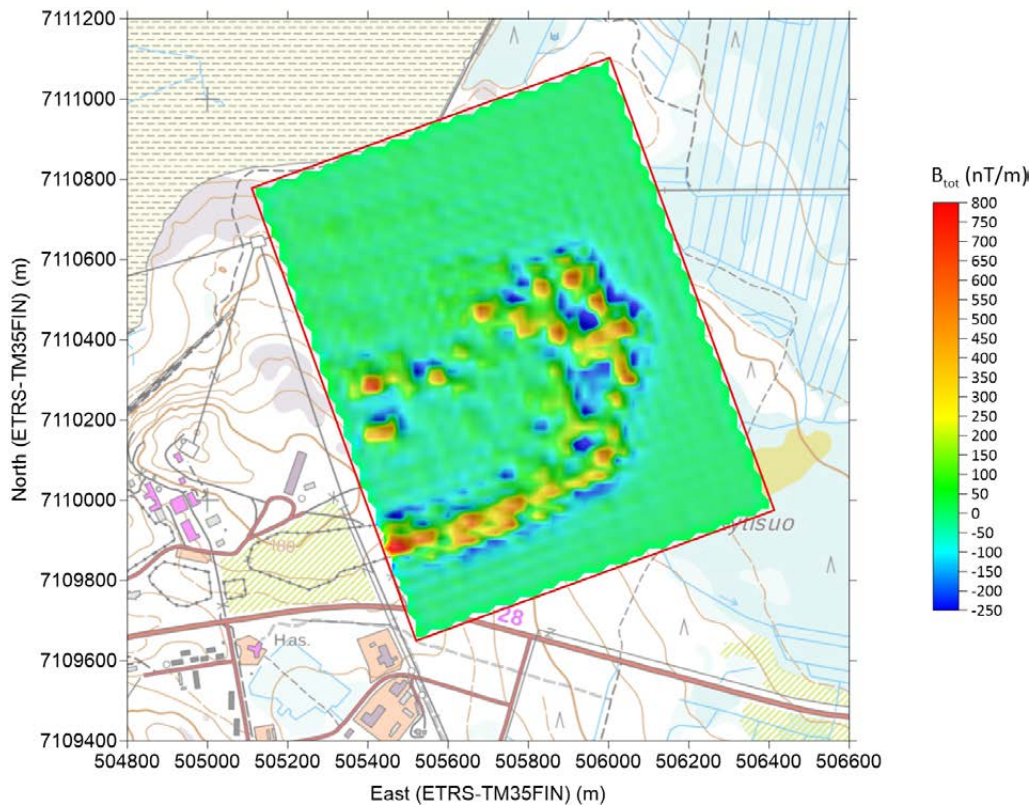


Fig. 39. First vertical derivative of the magnetic total field (with sun shading) for the second (MS) flight of the Otanmäki survey computed by ELM at the constant height of 5 m on an even grid.

### 3.1.2 Multi-copter magnetic survey

The Helmholtz-Zentrum Dresden-Rossendorf - Helmholtz Institute Freiberg for Resource Technology (HZDR-HIF) conducted for the first time a magnetic field survey with their integrated HSI-Mag-multi-copter system on 6 September 2018.

UAS-borne magnetic measurements were performed by using a three-component fluxgate magnetometer (SenSys MagDrone R1)<sup>3</sup>. An octo-copter (Tho-R-PX8-12) from Tholeg had been chosen as the UAS platform and the system was equipped with a FGM3D/75 fluxgate sensor that measures the magnetic flux density within a range of  $\pm 75\,000$  nT and at a sampling frequency of 200 Hz. The fully autonomous system has a battery charge that lasts for about 20–25 minutes and re-

records its GPS position (latitude, longitude, height, GPS time in UTC [hh:mm:ss.ms]) at 20 Hz intervals. The system is easy to operate and utilizes a simple switch on – switch off mechanism to record data. The data are saved on an internal solid-state memory module and are downloaded with the MagDrone v1.0 software package in column-wise spreadsheet format.

To account for the diurnal variations, a magnetic base station was set up and measured in parallel. A technically similar fluxgate magnetometer from SenSys (MagBase) to the one placed on the drone was used for the base station. Both the MagBase and MagDrone have a sampling rate of 200 Hz, but the sensitivity of the base station magnetometer is slightly higher, with  $0.1$  V/ $\mu$ T, and its measurement range is larger, with  $\pm 100\,000$  nT. The base station was placed at a distance of 1.7 km outside

<sup>3</sup> This fluxgate system is not intended to be part of the final MULSEDRO system, but instead, a Gem Systems GSMP-35U optical pumped potassium total field sensor will presumably be implemented in the future. It was not used in this field test due to integration difficulties (communication problems between the GPS and the PixHawk data logger). Therefore, only the total magnetic intensity value is presented in this report and used within the MULSEDRO project, although all three magnetic components were measured.

the survey area (and outside the high magnetic anomaly) and continuously recorded the three components of the Earth's magnetic field. The total field  $B_t$  was calculated and used to correct the drone-borne magnetic total field data.

Technical parameters of the magnetometer as provided by the manufacturer SenSys (SenSys 2018) are as follows:

- Max. declination between component directions and the optimal cartesian axes:  $\leq \pm 0.5^\circ$  (A fluxgate offset matrix is applied on MagDrone and MagBase data to account for deviations from orthogonality between the individual components)
- Resolution:  $< 0.15 \text{ nT}$
- Temperature drift:  $\leq \pm 0.3 \text{ nT/K}$
- Zero error:  $\leq \pm 0.5 \text{ nT}$
- Sensitivity:  $0.133 \text{ V}/\mu\text{T}$

The MagDrone system was rigidly attached to the UAS on a frame that was centred immediately below the drone (see Fig. 40(a)). The components of the magnetometer were aligned parallel and perpendicular to the main construction axis of the UAS fuselage. The spatial distance of the MagDrone to the Tholeg engines was roughly 50 cm. In the future, it is planned to correct small sensor misalignments in the orientations by analysing the magnetic field component behaviour during post-processing. An advantage of a rigidly attached magnetometer as opposed to free-hanging total field magnetometers is the known fixed position. Wire-attached magnetometers record less noise caused by UAS engines and electronics because of their greater distance from the drone. However, side and frontal winds can then cause

sudden movements of the UAS during the flight operation that again impose a sway on a hanging magnetometer, which can induce unwanted noise during the measurements. The noise from electric motors is, moreover, only critical if it cannot be distinguished in the frequency domain from signals associated with geological anomalies, which seems to have been possible in this case (see the following discussion and Fig. 41). Another advantage of a rigidly mounted magnetometer is that a quick-release connector could be developed for such a setup that allows the magnetometer to be attached and detached in a few minutes for quick field operations.

To demonstrate that the signal content and noise from electric motors can be separated to a large extent, a spectrogram of the total magnetic field raw data for the 15 m MagDrone flight is displayed in Figure 41. The spectrogram presents the time-frequency distribution by using consecutive short-time Fourier transforms (Oppenheim et al. 1999). The input signal is split into short segments of equal lengths to determine the time-frequency distribution for a specific period. The segments are tapered before discrete Fourier transform with a Tukey window (Harris 1978). Colour coding is associated with the power spectral density and computation is achieved with the Python module SciPy (Jones et al. 2014).

Most of the noise becomes visible in form of several erratic high-frequency signals of  $>50 \text{ Hz}$  in the upper half of the spectrogram. They mainly represent the engine noise of the UAS, but also other noise sources such as vibrations of the frame. The lower part from 0 to 10 Hz mainly displays signals containing geological information.



Fig. 40. (a) The Tholeg octocopter equipped with a MagDrone R1 magnetometer. (b) The UAS crew conducting a survey on the Metsämalmi outcrop.

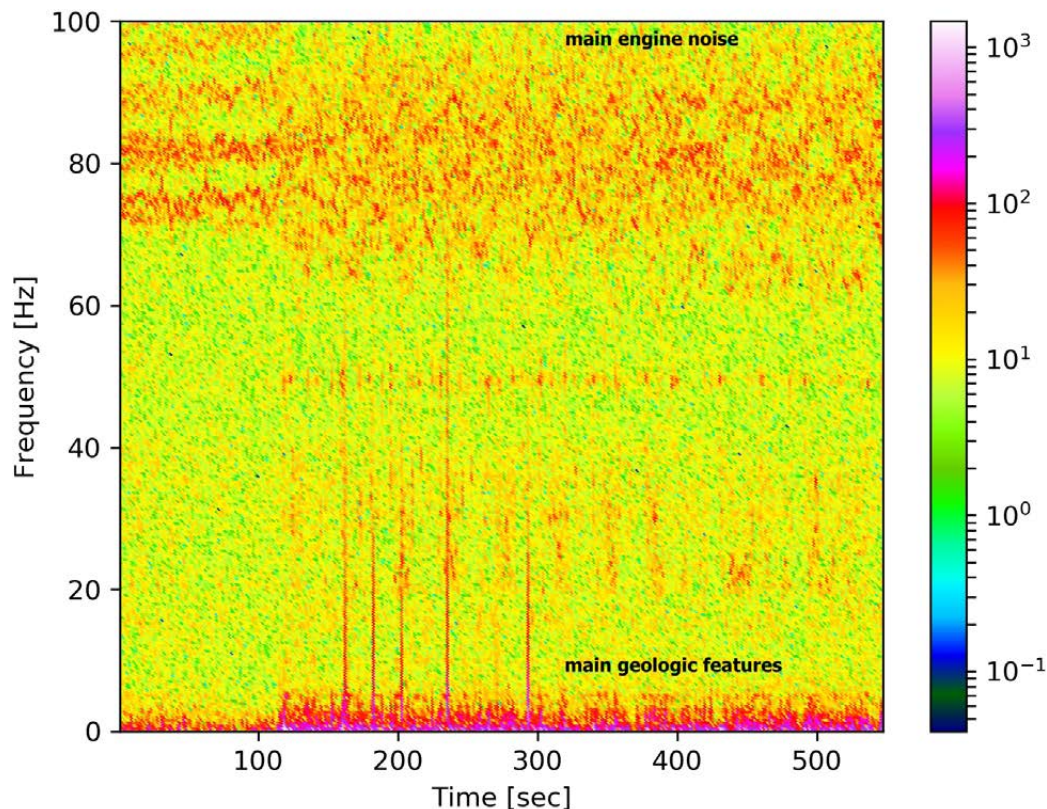


Fig. 41. Spectrogram from parts of a single copter flight at 15 m a.g.l. Engine noise and noise from vibrations are present at higher frequencies, but geological signatures are at low frequencies. The power spectral density in nT<sup>2</sup>/Hz is colour coded on a logarithmic scale.

### 3.1.2.1 Acquisition

The UAS MagDrone flight surveys were conducted on 6 and 7 September 2018. In total, surveys were performed with three different flight heights of 15 m, 40 m and 65 m that covered either the whole or parts of the Metsämäalmi outcrop area. Their inline spacing differed by 7 m, 20 m and 35 m for height levels of 15 m, 40 m and 65 m, respectively, and a number of tie lines (tie-line spacing: 20 m, 80 m and 60 m) were flown for all three height levels. The different survey areas had sizes of 0.019 km<sup>2</sup>, 0.037 km<sup>2</sup> and 0.065 km<sup>2</sup> (see flight line patterns in Fig. 42 and Table 5 for further flight information).

The intention of performing surveys at different height levels was to generate results at varying scales of resolution for the following applications:

- Survey at 15 m height level: UAS data were collected as close to the surface as possible and with a dense spatial coverage to obtain a magnetic dataset that is similar to that of a ground survey in terms of resolution. The chosen flight height was still high enough to ensure that it would be within acceptable safety margins.
- Survey at 40 m height level: Copter and fixed-

wing data were compared at the same operating height.

- Survey at 65 m height level: A high-altitude UAS survey was performed to examine the more regional influence of the anomaly and to have a dataset that could serve as a reference for upward continuations of the resulting total magnetic fields from the other surveys.

The survey at a flight height of 65 m was conducted on 7 September 2018 and took place from 10:18 p.m. (local time) until landing at 10:38 p.m. The surveys with flight heights of 15 m and 40 m were acquired on 6 September 2018 and took place between 12:50 and 14:10 local time. The time span of these flights covered the take-off of the MagDrone and flight operations and ended shortly before switching off the device after landing.

The average point distances in the inline direction were ~0.025 m, having a 200 Hz fluxgate sampling rate and a cruising speed of 5 m/s. However, the sampling interval of the GPS positions (20 Hz) was ten times lower such that the real coordinate positions of these measurements had to

be acquired from interpolation of the GPS markers during processing and resulted in point distances that were clearly coarser by ~0.5 m (after resampling). The observed daily field variations in the total magnetic field did not exceed more than 15 nT during a single flight event (Fig. 43).

However, during the 15 m survey, the Z component of the MagDrone was saturated for about 1% of the collected magnetic data due to the combination of an extreme magnetic anomaly, low flight heights and a magnetometer with a limited measurement range. Because the anomaly was so

extreme, it is unlikely that such oversaturation will occur again with this setup across other targets. However, this can be easily avoided by using a similarly constructed fluxgate magnetometer having a larger range (e.g.  $\pm 120\,000$  nT; see [www.sensys.com](http://www.sensys.com)).

Figure 40 presents the MagDrone configuration and the principle operation procedure during the Metsämalmi field surveys. While the pilot started and landed the UAS manually and watched the drone during the automatic flight operation, the assistant pilot monitored the flight plan as well as

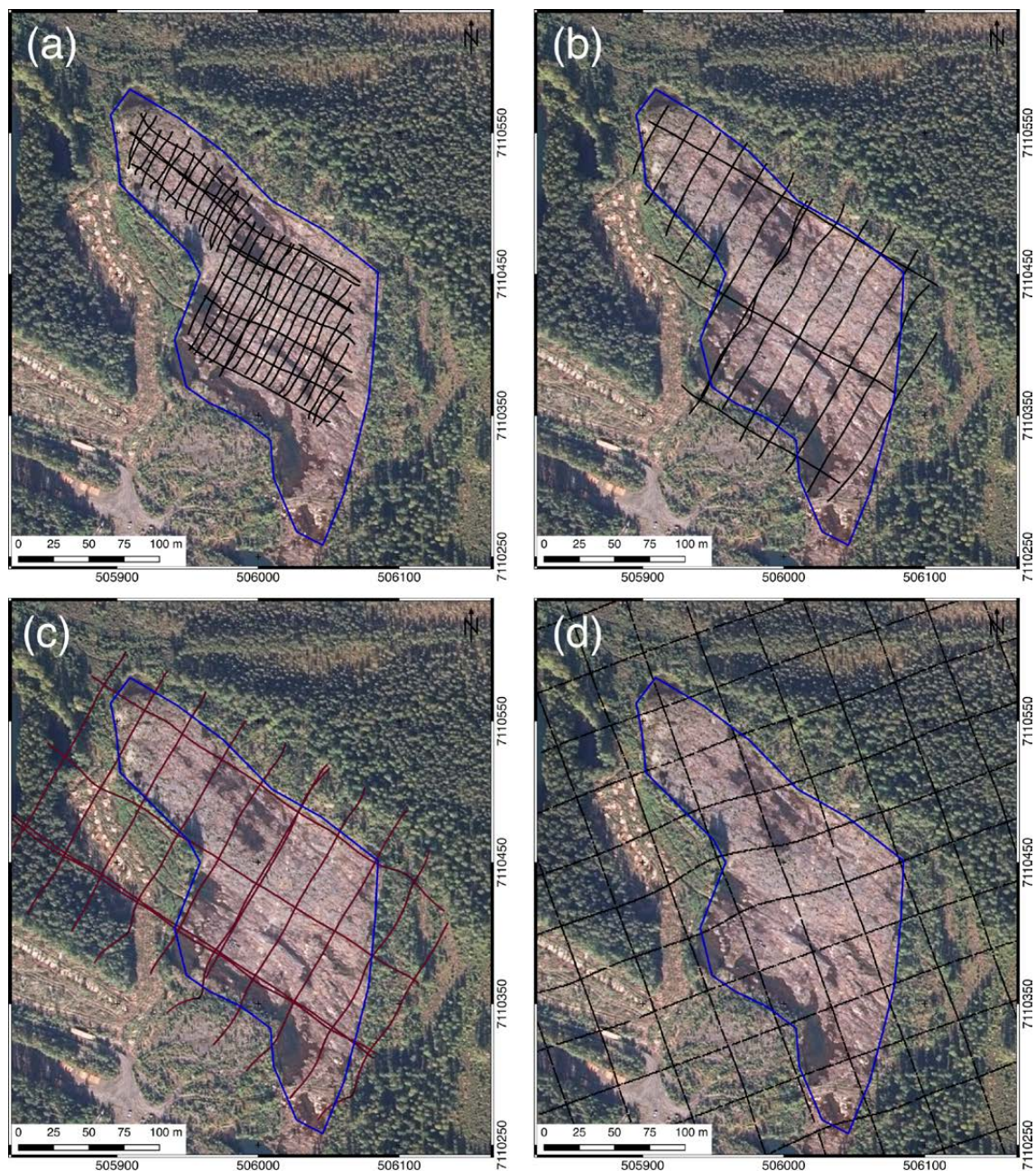


Fig. 42. (a) – (c). Flight paths for the three different altitudes of the HZDR–HIF copter survey. Pictures (a), (b) and (c) show the flight operation at 15, 40 and 65 m height above ground level (a.g.l.), respectively. The flight paths from Radai's survey are presented in (d) for comparison.

### Base station observation 07.09.2018

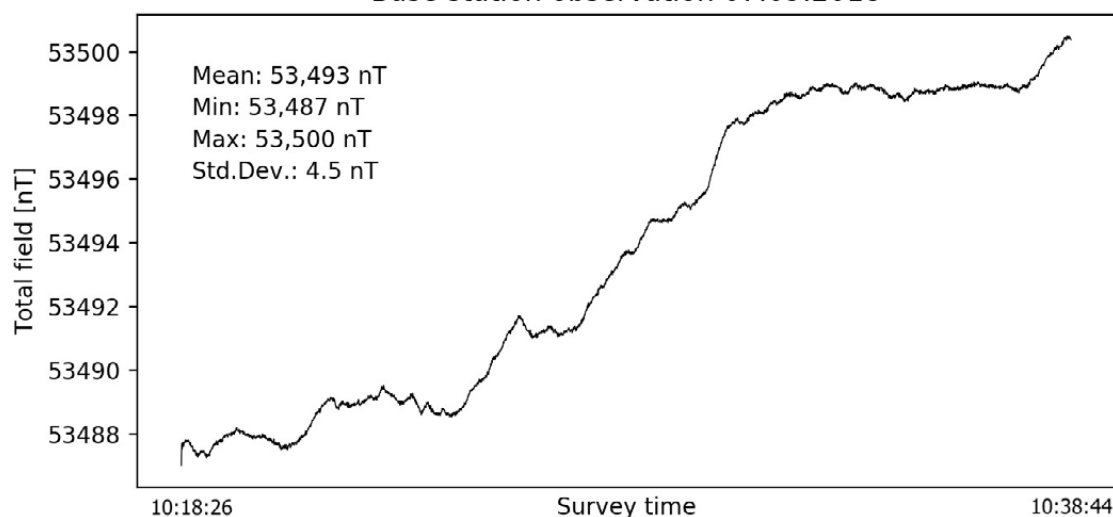


Fig. 43. The base station recording (07.09.2018, total field data in nT) shows a maximum difference of 13.2 nT during the flight operation of the survey 65 m above the ground level.

the live link to the UAS base station. In the unlikely circumstance of a signal loss, the pilot would be able to interfere immediately.

In summary, the magnetic data acquisition with the multi-copter across the Metsämäalmi area was performed rapidly and without any major complications, and flight planning for the MagDrone was optimized to cover as much of the outcrop as possible while remaining under the maximum battery endurance of the UAS. Because the strong magnetic anomaly disturbed the orientation of the compass used for navigation, the flight lines (Fig. 42) show some deviations from the original flight plan. However, these inaccuracies had no major impact on the data quality.

#### 3.1.2.2 Processing

The preprocessing procedure of the MagDrone data was developed in parallel with the field campaign in Otanmäki, and the current workflow for the data processing includes the following:

1. Importing of a) data files from the MagDrone magnetometer (in .csv format) and b) base station information (GPS positioning data, timestamps, data from magnetic components) with Sensys software;
2. Loading of the data in a self-written Matlab-based processing workflow (Madriz 2019);
3. Manual removal of computed total field values, where at least one fluxgate component was oversaturated;
4. Transformation of coordinates from Lat-Long to ETRS 89 UTM 35N;
5. Correction of MagBase and MagDrone component data with a fluxgate offset matrix (provided by the manufacturer) to reduce inaccuracies from sensor axis alignments;
6. Removal of data errors and spikes from the base station data either manually or by using a 5th order polynomial filter;
7. Calculation of the median or mean values for a moving window as a low-pass filter to reduce noise from the copter engines and to down-sample data to 1–10 Hz along the flight path;
8. Merging of the base station and UAS data via GPS time stamps;
9. Performing of base station correction on MagDrone data by subtracting base station variations from the magnetic field;
10. Computation of heading correction for MagDrone data;
11. Preparation of the flight lines (e.g. removal of data at UAS flight turns and corners);
12. Tie-line levelling (performed manually);
13. Export to Geosoft Montaj;
14. Gridding of the data with minimum curvature interpolation using varying cell sizes;
15. (Optional) Application of a Gaussian low-pass filter (Geosoft 2013) to attenuate the remaining higher frequency noise, e.g. from engines;
16. Importing of final mapping product to Quantum GIS for interpretation.

The “fluxgate” correction (step 5 in the workflow) is the matrix multiplication of the magnetic field vector of each data point with the offset matrix and the subtraction of an offset vector (both the offset matrix and vector are provided by the manufacturer, SenSys). This correction is required because the axes of the three fluxgate components are not perfectly orthogonally aligned in their designated building form. Details of the calculation procedure are not provided by the manufacturer SenSys, but the basic calculation resembles those applied in magnetic compass corrections, e.g. hard and soft iron corrections of the distorted magnetic readings of a fluxgate compass. In order to clarify this point, a practical example is given. To build a correction matrix, the fluxgate compass is rotated around all three axes with a minimum of a full cycle. The acquired values are fitted on a geometric plane, usually an ellipsoid, by different algorithms. The eigenvalues of the three-dimensional fitted surface give the correction values.

In step 7 of the current magnetic processing workflow, a running median filter was used for resampling of the input signal. Using 10 Hz or 1 Hz resampling provides proper results in terms of reducing the amount of data without losing potential geological signals. To obtain proper data estimates for the heading correction (step 10), a calibration figure was flown with the UAS at the beginning of each flight at a high altitude. The clipped data from the flight at 15 m height were manually removed before step 3 in the workflow. These gaps were then “re-filled” by means of minimum curvature gridding (step 14). This, however, means

that these values may be underestimated and may be partly higher in reality. The Gaussian low-pass filter (step 15) was applied with a standard deviation of  $\sigma = 50$  m as a spatial cut-off frequency using the MAGMAP filter package in Oasis Montaj. Any further steps of data integration were conducted later on in a combined QGIS project.

Note that none of the applied processing steps for the MagDrone datasets implicitly consider variations in the flight altitude, as is the case for processing of the fixed-wing magnetic data with the ELM from Radai (see Section 3.1.1.4.). However, the processing will be adapted in the future to directly consider flight altitude information in the processing.

### 3.1.2.3 Data evaluation and results

In this section, we discuss the quality of the resulting TMI images and the efficacy of the applied workflow to reduce the different noise types. In this context, a major advantage in the evaluation of the multi-copter magnetic data is the existence of several other magnetic data sets from airborne and ground-borne surveys, as well as from fixed-wing magnetic flights. By using upward and downward continuations of the magnetic field, direct comparisons with good quality data from the ground and the fixed-wing magnetic is possible.

Table 5 below summarizes the main acquisition parameters and properties of the processed datasets for the four detailed magnetic surveys (the three multi-copter surveys and the ground-based survey) that focused on the Metsämalmi outcrop.

Table 5. Survey parameters and statistics of copter and ground magnetic data

Parameter	Flight 1 (Eastern part)	Flight 2	Flight 3	Ground mag.
Data points (after resampling)	5587	5286	7091	18783
Re-sampling frequency	10 Hz	10 Hz	10 Hz	10 Hz
Flight velocity	~ 5 m/s	~ 5 m/s	~ 5 m/s	–
Flight time	13.8 min; 18.2 min	18.6 min	24.6 min	–
Distance flown (incl. turns)	1825 m; 3634 m	3950 m	5752 m	–
Barometric altitude a.g.l.	15 m	40 m	65 m	1.7 m
Std. dev. survey height	1.0 m	1.0 m	1.9 m	–
Line spacing	7 m	20 m	35 m	10 m
Tie-line spacing	20 m	80 m	60 m	–
Area covered	2.0 ha	3.7 ha	6.5 ha	5.0 ha
$B_t$ Mean	68 583 nT	62 957 nT	62 869 nT	57 634 nT
$B_t$ Median	68 677 nT	63 241 nT	62 995 nT	52 585 nT
$B_t$ Min.	57 176 nT	55 377 nT	54 499 nT	34 488 nT
$B_t$ Max.	79 352 nT*	67 913 nT	70 477 nT	136 662 nT
$B_t$ std.	3776 nT	2147 nT	2116 nT	10 502 nT
D4 std. (mean)	114 nT	111 nT	327 nT	–

\*Values above 75 000 nT were obtained by data interpolation, because the measurement range of the fluxgate was exceeded

#### Estimation of the stochastic noise content:

An appropriate tool to determine the stochastic noise of aeromagnetic data is the 4-point difference calculation (D4) by using data points along the flight paths (Reeves 2005). The standard deviations of D4 sum up to 114.5 nT (raw data from flight operation at 15 m a.g.l.) and 111.1 nT (raw data from the flight operation at 40 m a.g.l.) and are, hence, comparable with the values from the unprocessed total field magnetic data of Radai's fixed wing survey (compare Tables 4 and 5). Occasional spikes in the MagDrone data were not removed for these calculations, in order to stay as close as possible to the acquired raw data.

In the processing workflow, the stochastic noise is already efficiently reduced, for example by polynomial fitting and spike removal (see step 6 in

workflow). In order to further reduce this noise level during processing in the future, we intend to employ the ELM used by Radai Oy in the processing workflow.

#### Calibration for heading correction and the impact of flight parameters on error variations:

Figure 44 shows the flight altitudes of the MagDrone for the four magnetic surveys. Measurements were taken from the barometric flight height recorder from the Pixhawk flight controller. Blue arrows mark the period when the calibration figure was flown that was used for the heading correction. For the two flights at a height level of 15 m, a high altitude was chosen to mitigate the influence of the strong local magnetic anomaly at Metsämalmi.

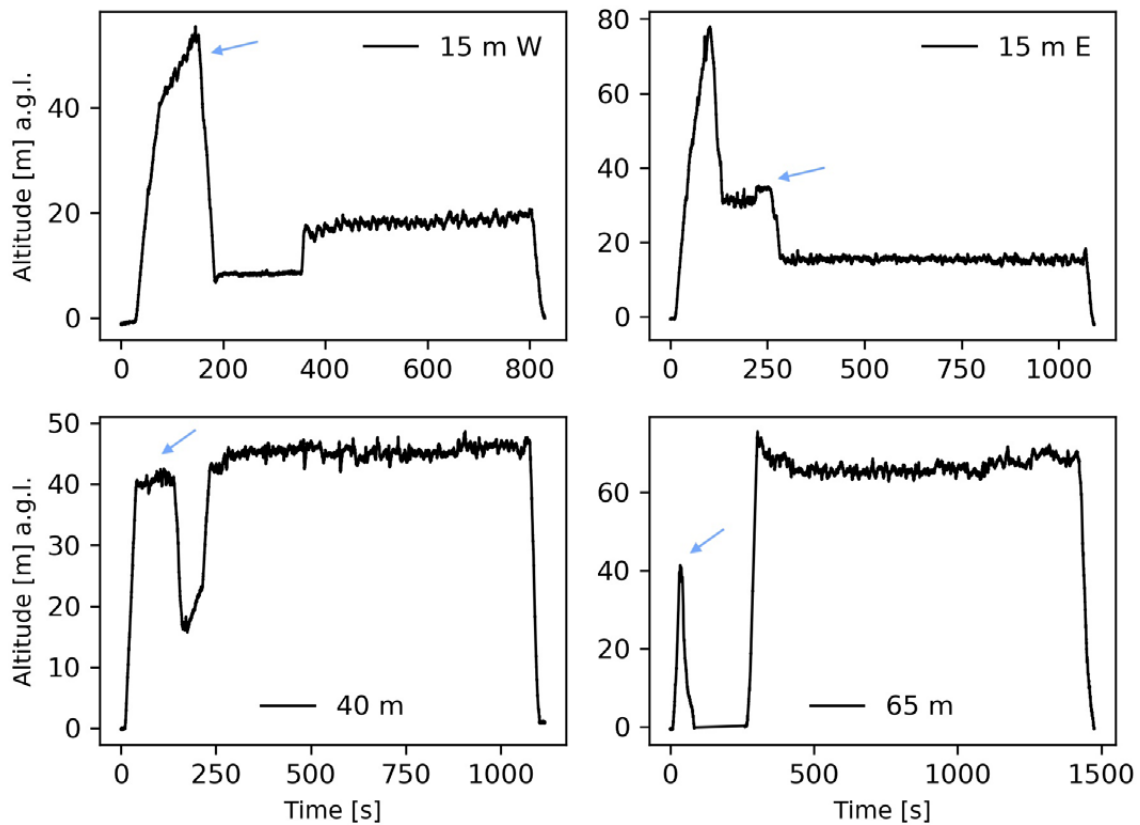


Fig. 44. Height profiles of the MagDrone copter flights. The blue arrows indicate time spans during which calibration patterns were flown that were used for heading corrections.

Data spikes in the recorded magnetic data are mainly present at the turning points of the flights, and probably originated from drone movements (micro-movements, vibrations).

The standard deviations of the flight height variations increase with increasing altitude and are probably caused by stronger winds at larger height levels. The flights (e.g. 15 m) were labelled according to the programmed target height, although the actual flight height typically varies by about  $\pm 1.0$  m during a copter survey.

**Resulting magnetic maps from the multi-copter flights at different height levels:**

The minimum curvature interpolation method from Oasis Montaj was used to create all the presented TMI maps. The gridding method is known to create smooth surfaces for such non-uniform data distributions, where data sampling is much denser in flight-line directions, and the method generates meaningful interpolation of the responses even for locations where the data coverage is rather sparse.

Figure 45 presents the TMI for the survey with a flight height of 65 m. For data interpolation, a

coarse grid with cell sizes of 10 m was chosen in order to avoid oversampling, and hence the creation of undulating artefacts. A major anomaly running in a WNW–ESE direction across the Metsämalmi test pit area can be observed for this higher altitude level. In general, the amplitude decreases towards the NE of the surveyed area, where the zone bearing iron ore ends at approximately the northern border of the outcrop area. Similar magnetic patterns are observable in the TMIs from the fixed-wing data (Fig. 22) and from the regional airborne data (Fig. 3).

More local and shallow magnetic anomalies become increasingly pronounced in Figure 46, where the survey was conducted at a lower altitude of 40 m and with denser line spacing. In particular, a strong anomaly is visible in the central part of the survey area, where large lenses of high-grade magnetite ore are present in the excavated area (see Fig. 6). Note that in this area, iron alteration minerals along the surface are observed in the images from the hyperspectral survey, which are an indicator of magnetite ore (see Figs. 62 and 62).

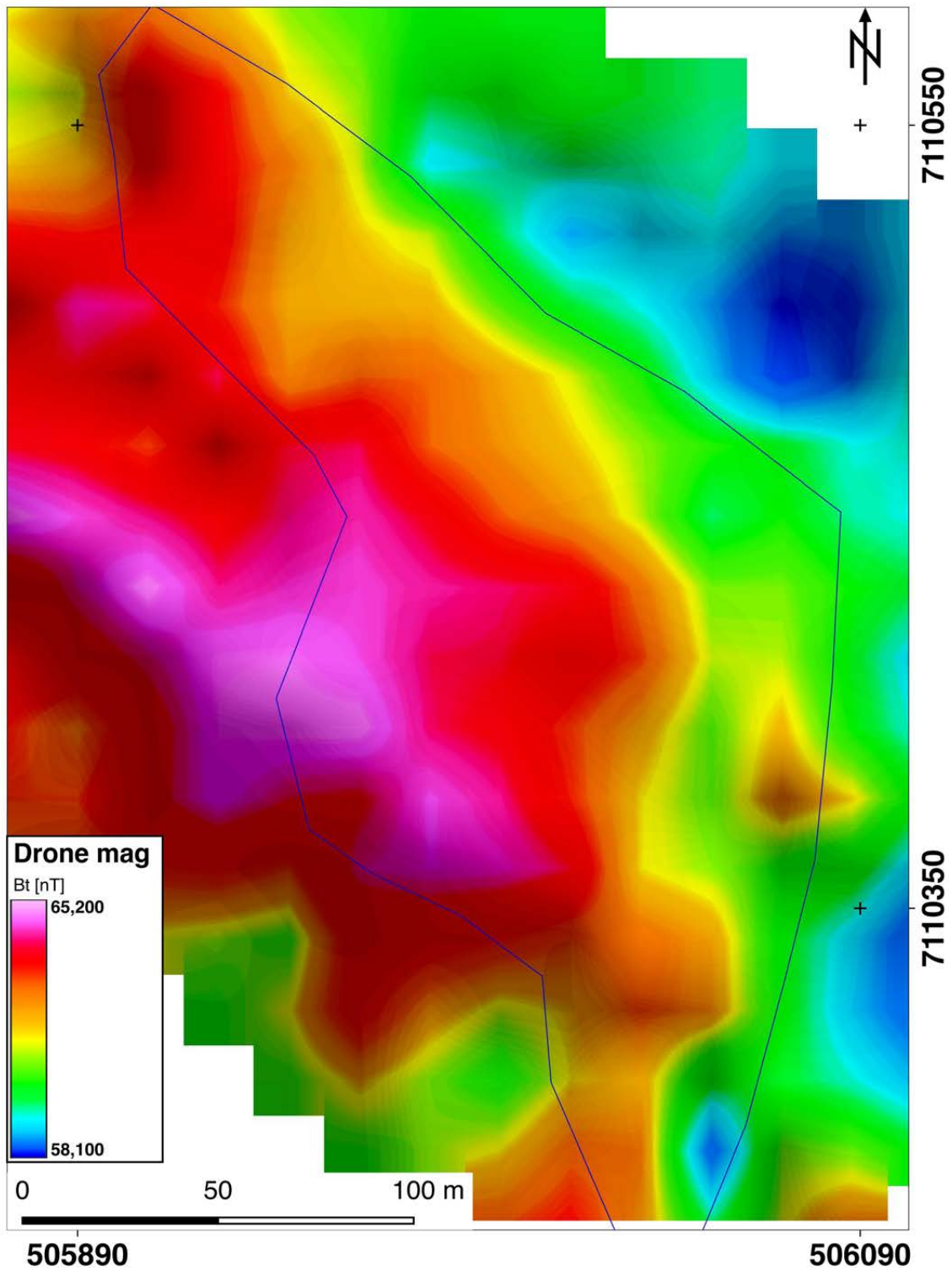


Fig. 45. Multi-copter-borne total field magnetic data collected on 07.09.2018 (flight height: 65 m a.g.l.); hill shading is used for increased visibility.

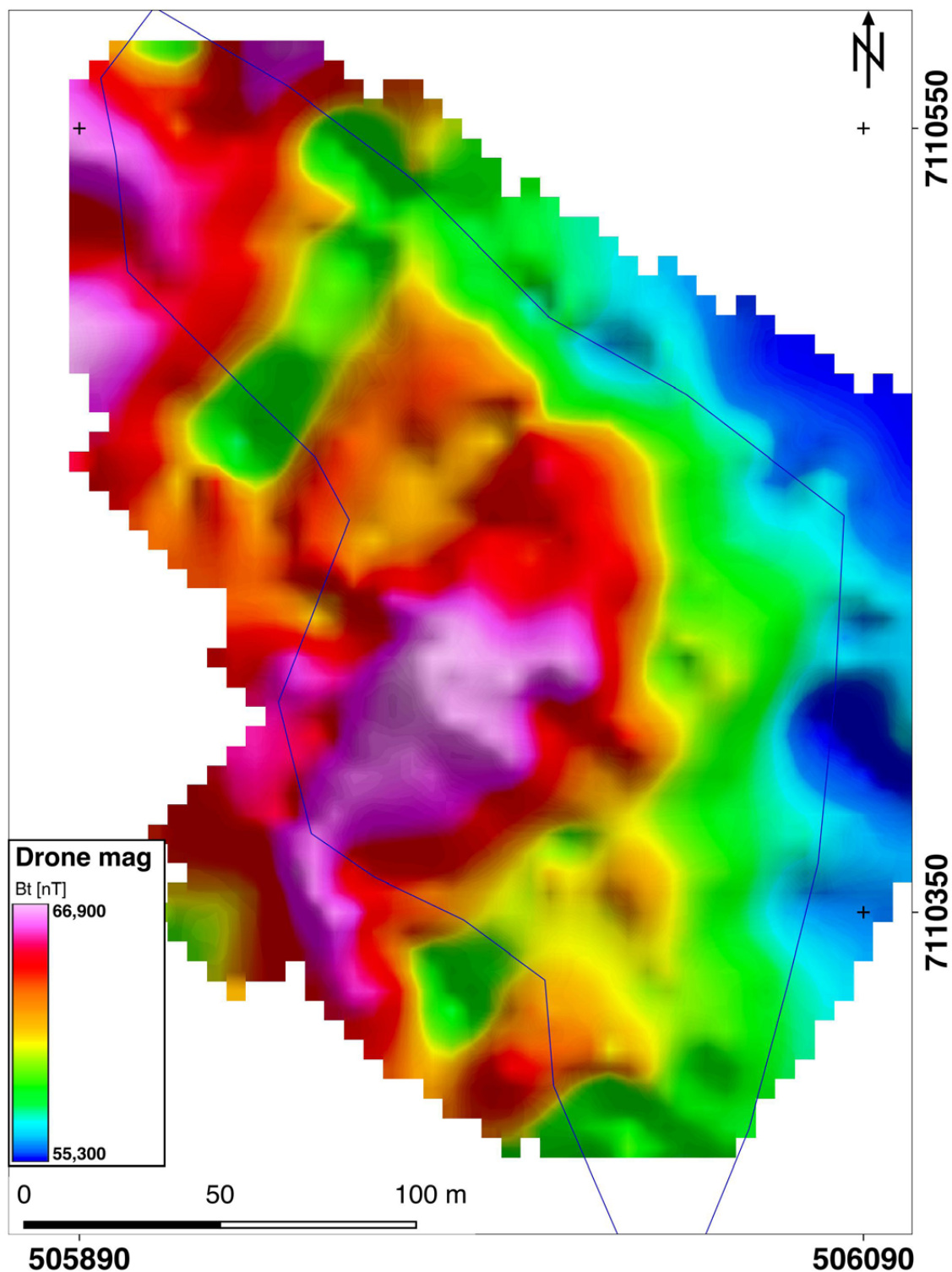


Fig. 46. Multi-copter-borne total field magnetic data collected on 06.09.2018 (flight height: 40 m a.g.l.); hill shaded for increased visibility.

The highest similarity with the results from the ground magnetics (see Figs. 64 & 65 in subsection 3.3.1) was achieved with the lowest altitude UAS flight at 15 m a.g.l. (Fig. 47; no Gaussian filter was applied to the TMI grid), and anomalies become visible in some detail in the TMI. In this context, it seems that the clipping of about 1% of its data

(occurring due to the oversaturation of single sensor components of the fluxgate magnetometer) could be properly refilled by means of gridding with minimum curvature interpolation without introducing significant interpolation artefacts. On the other hand, there are some stripping patterns following the flight line paths, which perhaps

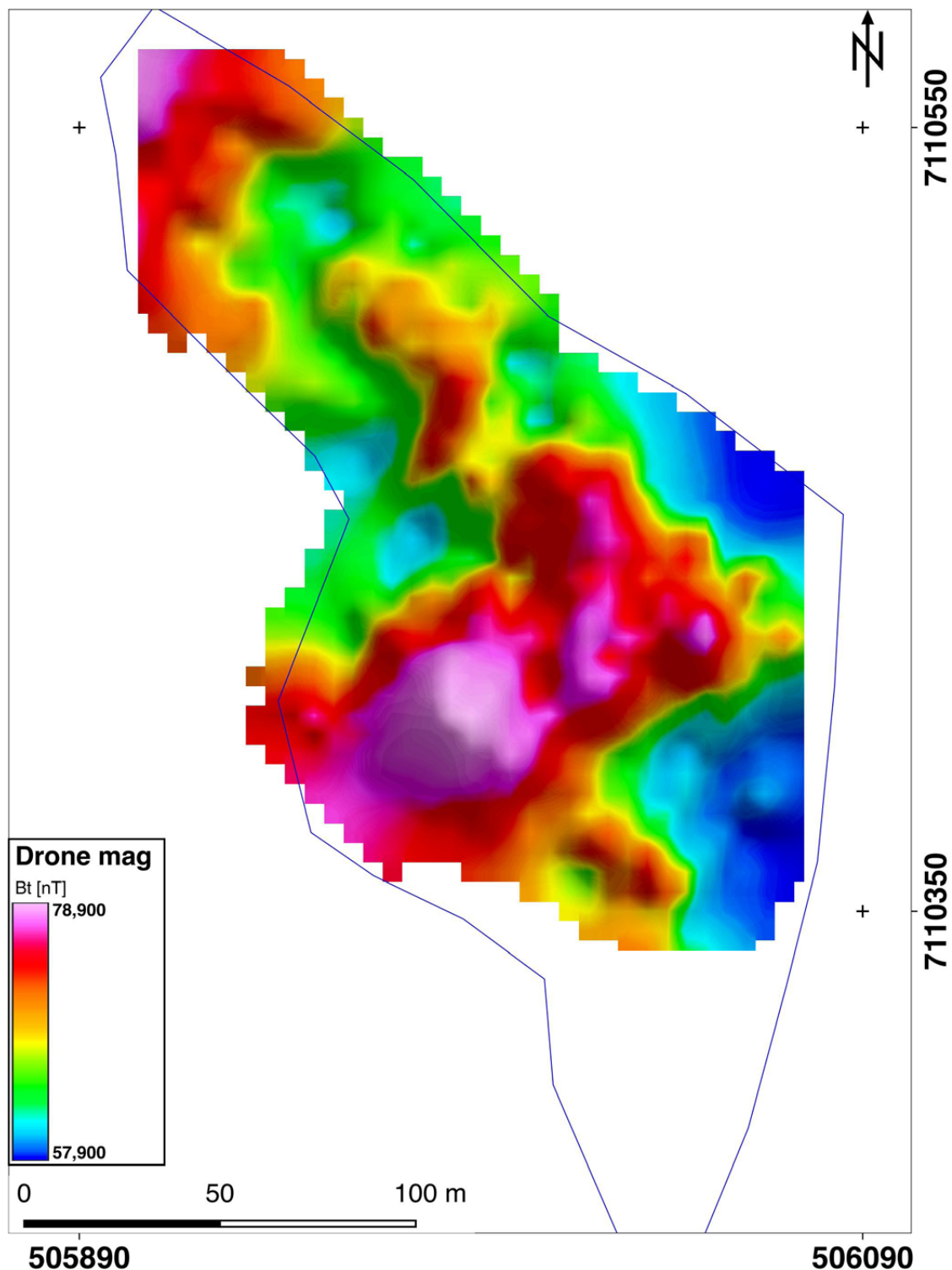


Fig. 47. Multi-copter-borne total field magnetic data collected on 06.09.2018 (flight height: 15 m a.g.l.); hill shaded for increased visibility.

indicate some remaining systematic noise from the multi-copter engines or levelling artefacts related to variable flight heights. To reduce these artefacts, a Gaussian low-pass filter (std. dev. = 50 m) was applied (see TMI after filtering in Fig. 48).

Stripping noise is indeed clearly reduced by the low-pass filter (compare Figs. 47 and 48). How-

ever, the application of the FFT filter may also reduce some real high-frequency magnetic signals associated with shallow anomalies. In the future, a better way to remove such noise while keeping more of the high-frequency signal content could be to apply the ELM from Radai Oy (see sections 3.1.1.4 and 5). Another option could be to add a

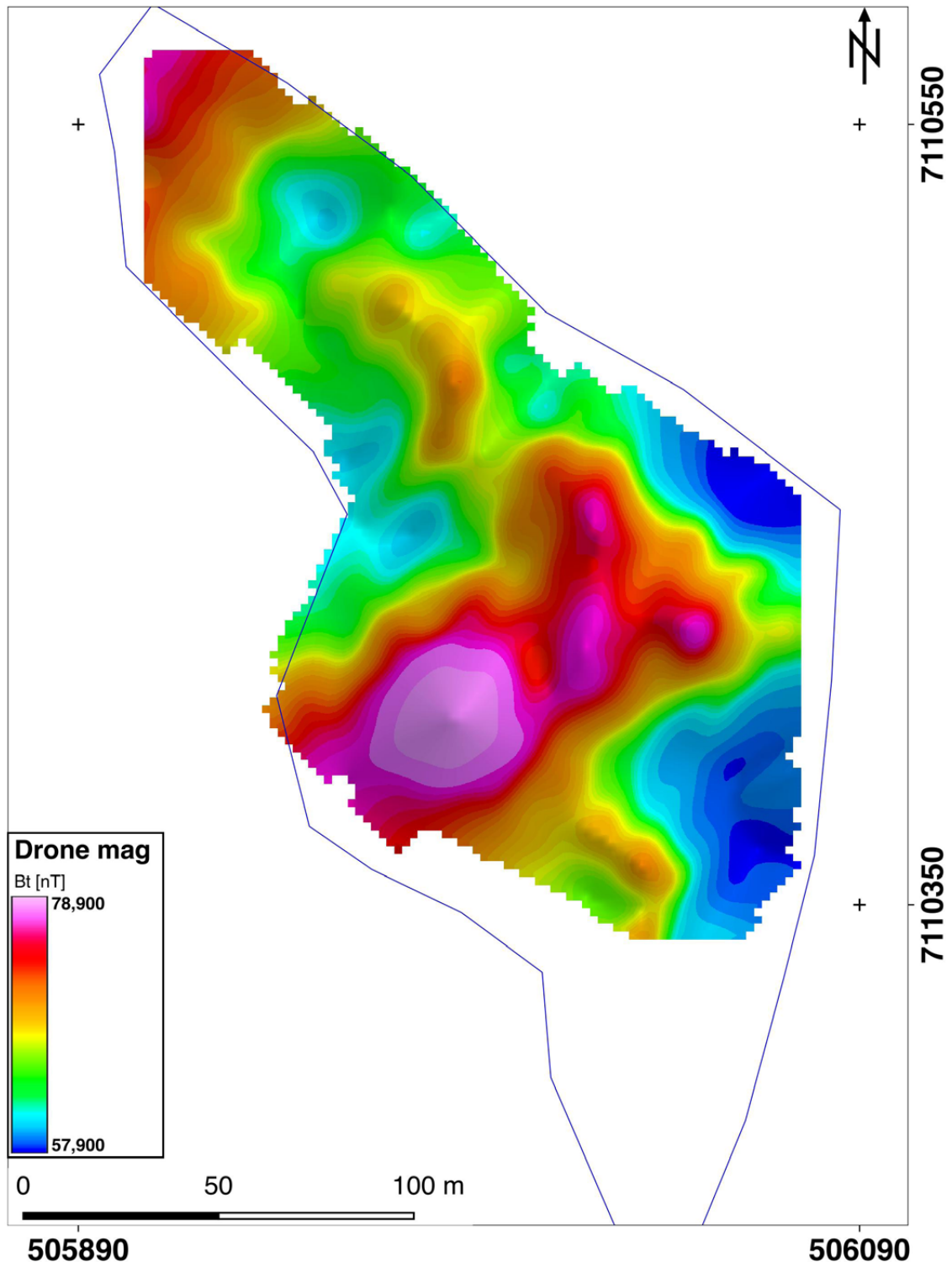


Fig. 48. TMI map for the copter flight with a height level of 15 m a.g.l. In contrast to Fig. 3.39, a Gaussian filter with std. dev. = 50 m was applied in addition to the common processing to mitigate the remaining artefacts.

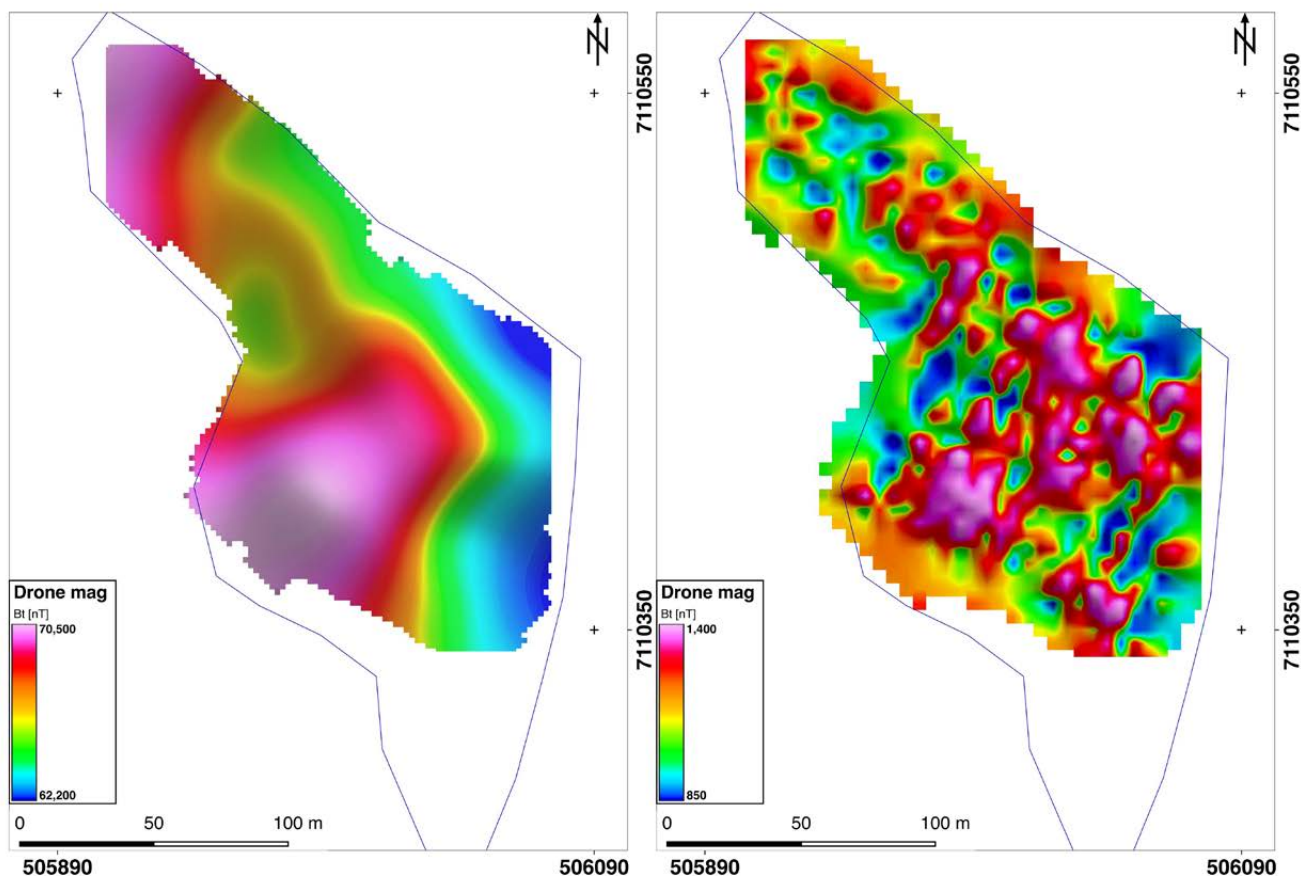


Fig. 49. Left: The TMI from the multi-copter dataset collected at 15 m height is upward continued to 40 m. Right: The first vertical derivative of the TMI from the same dataset.

micro-levelling approach in the processing workflow such that the stripping patterns are better mitigated and the application of a more careful low-pass filter is sufficient.

The aforementioned clipping due to oversaturation only occurred for rather few data points and was caused by the exceptionally high magnetic amplitude at Metsämalmi. A slight increase of 5 m in the flight altitude from 15 to 20 m could already fully solve this issue, but at the expense of resolution.

Figure 49 (left) shows the loss of resolution for the TMI from the survey at 15 m height, when an upward continuation to a flight height of 40 m a.g.l. is applied. Then, the deeper and more regional character with the strongly decreasing anomaly

from S towards NE is more clearly seen. However, comparison with the survey operated at a height of 40 m a.g.l. (Fig. 46) shows that the upward-continued TMI from the 15 m flight lacks more details and that low-pass filtering should be applied more carefully. Figure 49 (right) illustrates the first vertical derivative of the TMI of the 15 m dataset. Although a Gaussian regional filter was applied to the datasets before derivative calculation, some patterns of parallel stripes in the flight-line direction (inline direction) are still visible in this first derivative map. This indicates that the acquisition and processing strategy still has some potential for improvement, although the overall quality can already be considered as rather good.

### 3.2 Optical remote sensing from UASs

The following sections present the workflow and results for UAS-based optical remote-sensing surveys. Surveys with different spectral and spatial resolutions are used for the classification and interpretation of surface geology. Parts of the results are furthermore used for data integration of magnetics and remote sensing. Basically, two UAS types (multi-copter and fixed wing) are used for operation with different sensor set-ups. The technical characteristics of the UASs used by HZDR-HIF are summarized in Table 1.

#### 3.2.1 Photogrammetry

Orthophotos and digital surface models (DSM) of the Metsämalmi outcrop were created by SfM-MVS photogrammetry performed from a fixed-wing drone. The orthophoto and DSM spatially cover the complete Metsämalmi test pit area, also including the smaller focus area surveyed with the multi-copter equipped with a hyperspectral camera, and serve as reference datasets for further mapping and 2D imaging applications (see Figs. 4 and 50). The elevation model can be used to correct for altitude variations in magnetic data, while the high-resolution orthophoto can be used to interpret geological structures and serves as a reference image for ground sampling points.

A sensefly ebeePlus UAS featuring a 20 MP S.O.D.A. RGB camera was used to acquire overlapping nadir images. In total, 244 images with 80% forward and 70% sideward overlap (Fig. 50(a)) were taken at an average cruising altitude of 103 m above the ground, resulting in a ground sampling distance (GSD) of around 2.2 cm. In total, 12 ground control points (Fig. 50(c)) were randomly distributed within the area to precisely georeference the final photogrammetric model in absolute coordinates (Fig. 50(b)). The list of ground control points (GCP) is attached in Appendix 3.

A typical SfM workflow was performed using Agisoft PhotoScan Professional 1.2.5 and the following protocols recommended by, for example, Carrivick et al. (2016) and James et al. (2017b). Processing parameters for the image alignment were set to 'high quality' and reference preselection. Outlier tie points were subsequently removed using the gradual selection tool prior to the dense image matching (removing tie points detected in less than three images). The threshold for image

re-projection errors was set to 0.5 (41.69 pixels). Images with high residual tie-point errors were excluded from further dense cloud matching. Interior and exterior orientation parameters of the camera were estimated in Agisoft Photoscan based on bundle-block adjustment. The dense image matching or point cloud construction was run at 'high quality' with the depth filtering set to 'aggressive'. The accuracy of the SfM point cloud was validated based on the measured GCP positions and estimated GCP positions in Agisoft PhotoScan. The average error of the GCP is 8.04 cm (or 0.672 pix), where the z error is highest with 7.85 cm and below 1.5 cm in x–y directions. For a detailed overview of the RMS errors, see Appendix 4.

A digital surface model (DSM) was computed based on the dense cloud using IDW within Agisoft Photoscan with an average grid spacing of 4.3 cm/pixel. Finally, an orthophoto with a resolution of 2.2 cm/pixel was computed by seamlessly merging overlapping images. The DSM and orthophoto were both georeferenced in the ETRS89/UTM zone 35N coordinate system (EPSG:25835).

The final DSM is presented in Figure 50(d). For further details concerning the applied UAS photogrammetry workflow, we refer to Kirsch et al. (2018).

#### 3.2.2 UAS multi- and hyperspectral imaging

The multi- and hyperspectral surveys were conducted by Helmholtz-Zentrum Dresden-Rossendorf – Helmholtz Institute Freiberg for Resource Technology (HZDR-HIF). Multispectral imaging creates a rough spectral characterization of the area and its results give indications of the main geological structures and lithology. The results can be compared with the traditional geological mapping of the Metsämalmi outcrop. Hyperspectral results having a significantly higher spectral resolution are acquired to identify specific absorption features serving as proxies for mineral classes.

##### 3.2.2.1 Multispectral imaging

Multispectral imaging was conducted with a Sensefly ebee Plus and Parrot Sequoia 4-channel multispectral camera. Its multispectral bands are centred at 550 nm (green), 660 nm (red), 735 nm (red edge) and 790 nm (NIR) (see band locations and band widths together with the spectra for plants

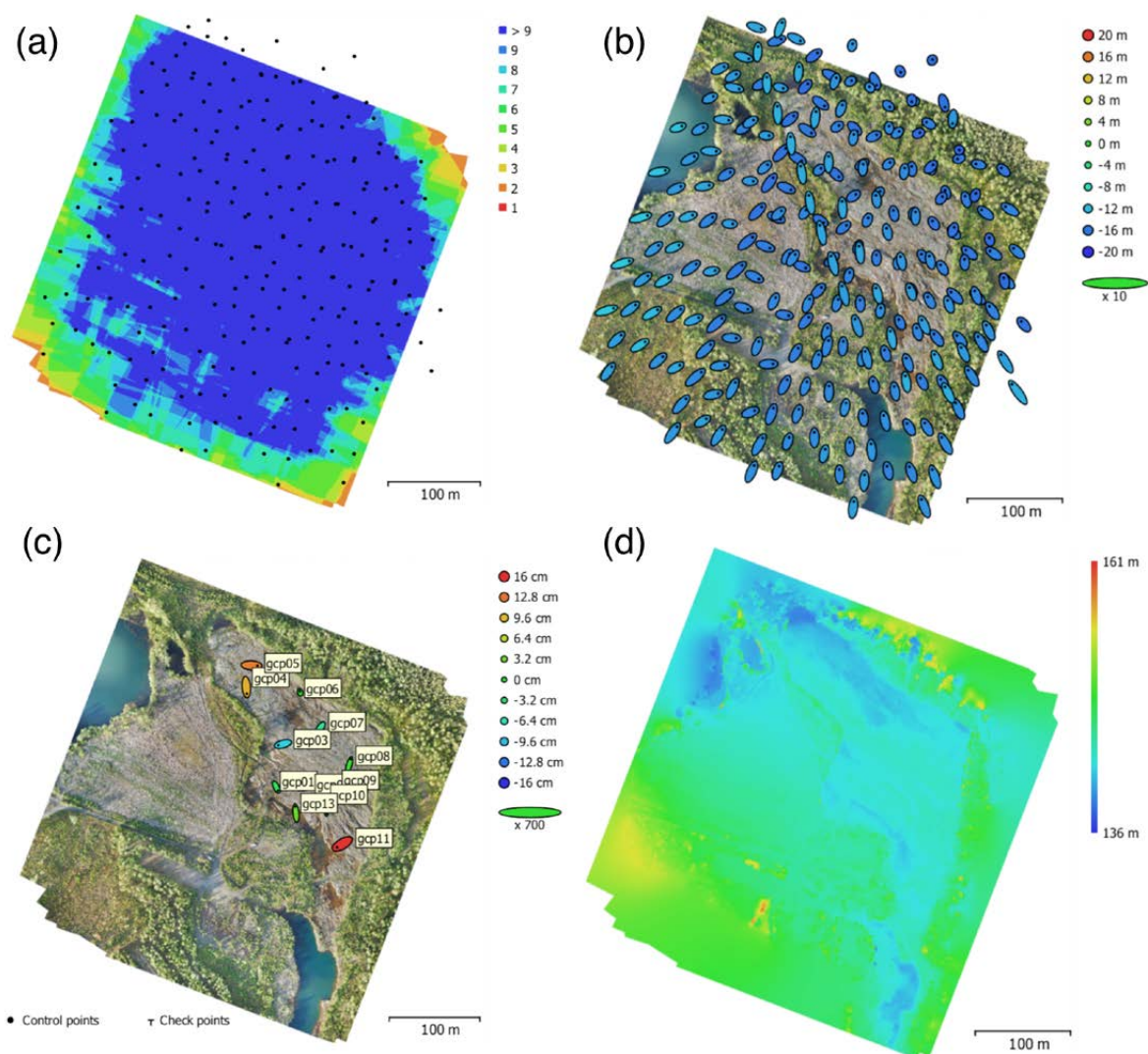


Fig. 50. (a) Camera locations (black dots) and image overlap for the 244 images used in photogrammetry. A blue colour signifies high overlap. (b) Error estimates for individual camera locations in X and Y directions are given by ellipse shapes, and in the Z direction by ellipse colours. (c) GCP positions and their error estimates for X and Y directions (ellipsoidal shapes) and the Z direction (ellipse colours). (d) Reconstructed digital surface model.

and soil in Fig. 51). Radiometric calibration was performed before the flight using a synthetic reference panel provided by the manufacturer. Images were normalized and scaled for reflectance prior to stitching. The multispectral orthomosaic was processed in Agisoft Photoscan software using a similar workflow and settings as for photogrammetric processing. Processing parameters for the image alignment were set to ‘high quality’, while the key point and tie point limit was set to 40 000 and 4000, respectively (see Appendix 5) and used with the reference preselection selected. Outlier tie points were manually removed using the gradual selection tool prior to dense image matching (maximum projection error of 0.2; 3.16 pixels) followed by optimization of the bundle adjustment.

The dense image matching or point cloud generation was run using the ‘high quality’ setting and depth filtering set to ‘aggressive’. Based on the resulting dense point cloud, an orthomosaic was generated using IDW within Agisoft Photoscan with a gridding of 14.8 cm/pixel. The orthomosaic was corrected for illumination differences and scaled to reflectance. Due to the low sun elevation of the northern hemisphere (Altitude 25 ° and Azimuth 228 ° at 16:00 local time) and late time of the day during data acquisition, a topographic correction was required and a c-factor correction was applied by using the Mephysto toolbox (Jakob et al. 2017).

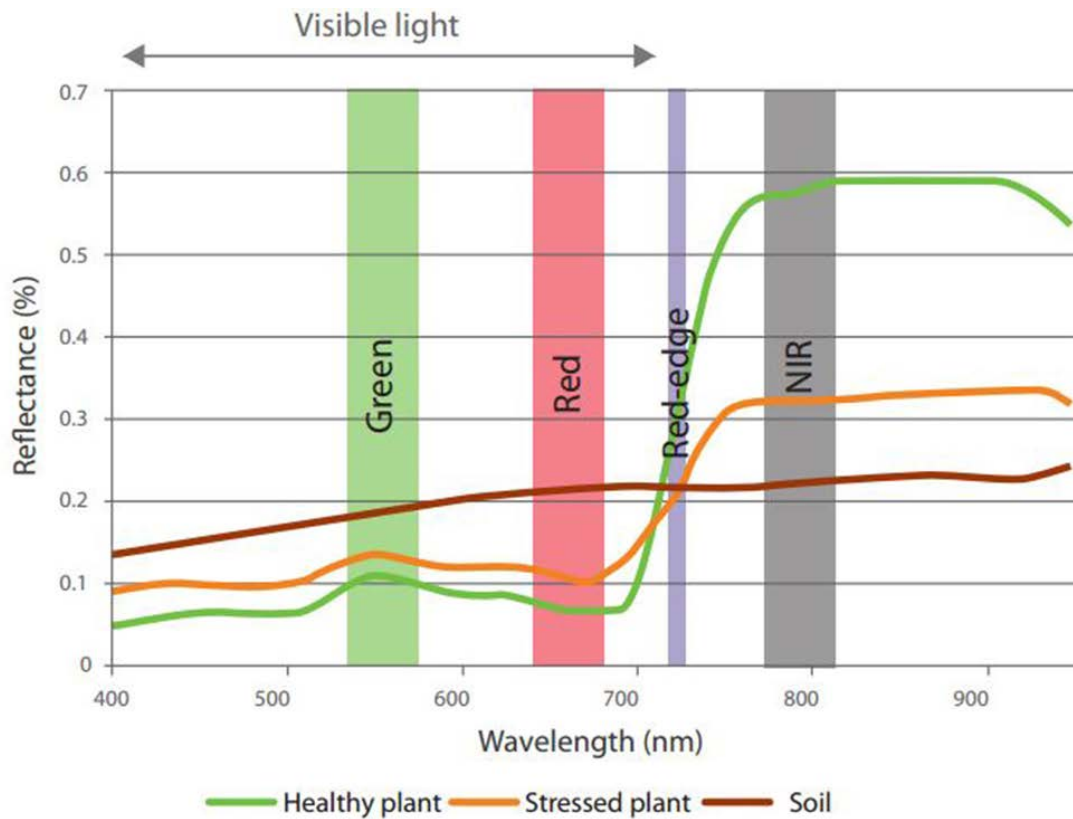


Fig. 51. Band distribution for the Sequoia multispectral camera are shown together with examples of spectra for vegetation (green and orange) and soil (brown). The image is taken from [www.sensefly.com](http://www.sensefly.com).

### 3.2.2.2 Hyperspectral imaging

The hyperspectral survey was flown with a back-up copter (type: Aibotix Aibot X6v2; see Fig. 52) due to hardware malfunction (telemetry and trigger) on the multi-copter (type: Tholeg THO-R-PX8-10) otherwise used in MULSEDRO. The telemetry was repaired later on 5 September 2018 such that magnetic and LiDAR could again be flown on 6 and 7 September 2018 with the Tholeg multi-copter. With both UAS systems, the Rikola hyperspectral camera was mounted on a gimbal to account for movements of the copter and to ensure a stable nadir viewing geometry.

The Rikola camera (Senop Oy, Kangasala, Finland) is a frame-based snapshot hyperspectral sensor. Compared to line scanners, the Rikola sensor has the advantage of acquiring full image frames starting at the lowest acquired wavelength. Single frames have high coherence towards each other, and images thus require less computational correction. The underlying Fabry-Perot interferometer technology of the Rikola camera provides the advantage of pre-defining spectral intervals with a minimum spectral step size of 1 nm. This enables the collection of data in up to 380 bands

(in USB mode) with a high signal-to-noise ratio (Mäkeläinen et al. 2013). In standalone mode, however, only 50 bands can be selected. It is important to note that the Rikola camera features two internal CMOS sensors, which detect the incoming signal for two wavelength ranges, creating an increment sensor shift of around 639 nm, which could create artificial spectral absorption features (from 624–671 nm). We mitigated this effect by removing five bands around that range. A camera setting of 50 image bands in the wavelength range from 500 to 900 nm and 8 nm spectral resolution was chosen (see Table 6). Empirical results demonstrate that this spectral resolution is optimal in terms of spectral sampling density versus quality of the spectra. As experience has shown, increasing the band number does not yield better resolved results, since the noise level is increased. Vegetation features, alteration minerals and artificial materials are distinguishable in the spectral range with high reliability, but a range of rocks and rock-forming minerals cannot be detected based on chemical composition alone, such as phyllosilicates, siliciclastic rocks and feldspars.

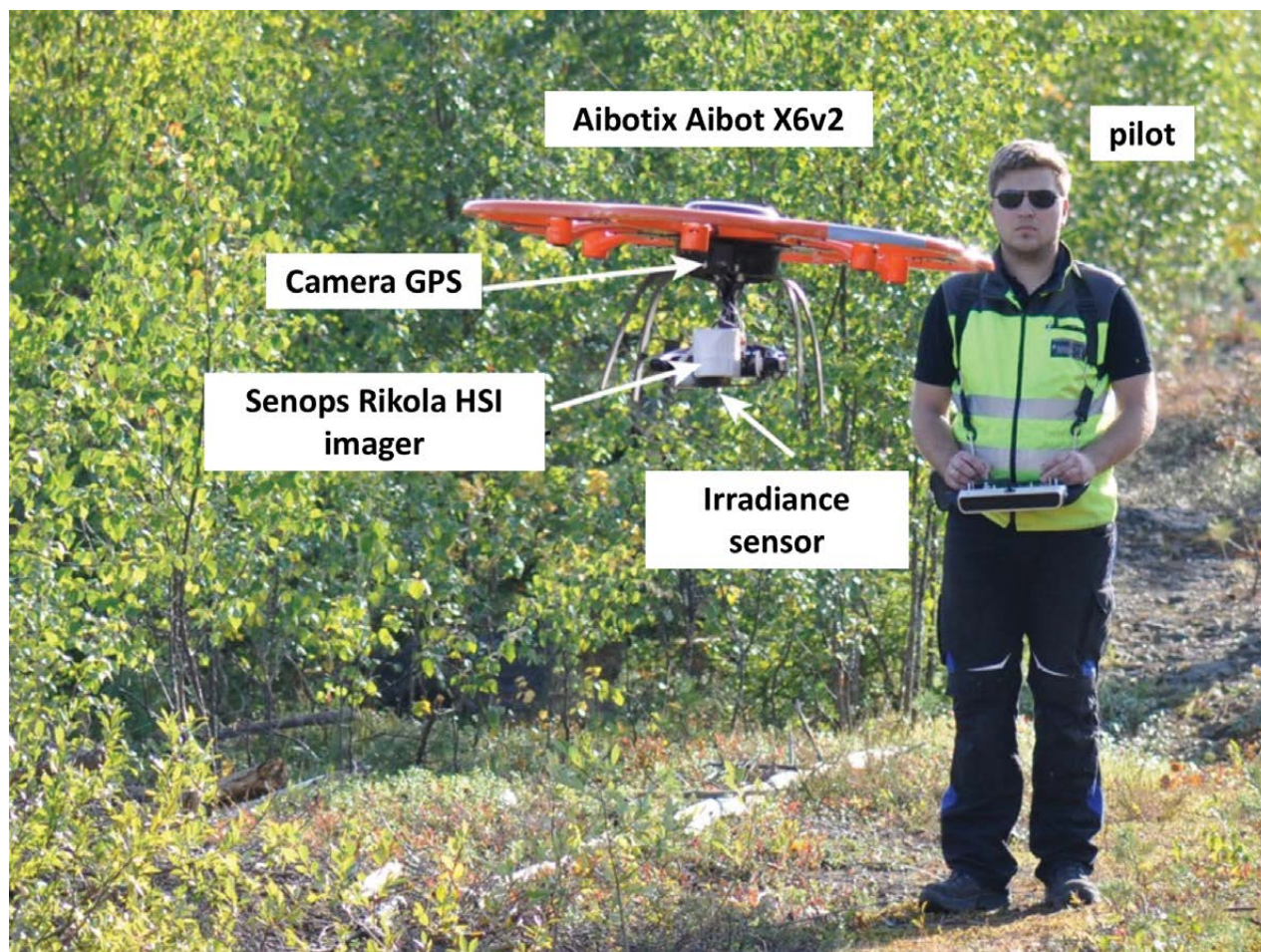


Fig. 52. Setup of the multi-copter system used for the hyperspectral survey at Otanmäki.

Table 6. Technical details of the Rikola hyperspectral imager

Parameter	Value
Field of View	36.5 °
Spectral range	504–900 nm
Focal length	~ 9 mm (fixed optics)
F-number	~ 2.8
Image bands	50 during flight; 80 on the ground; 380 max.
Spectral resolution	8 nm in flight; 5 nm on ground
Image resolution	1010 x 648 during flight operation
Band integration time	10–50 ms
Ground pixel resolution	6.5 cm at 100 m flight altitude

Pre-processing of the HSI data followed the workflow outlined by Jakob et al. (2017) using the in-house-developed, Python-based Mephysto toolbox. Images were co-registered, corrected for various geometric effects (lens correction, topographic correction, orthorectification) and geo-referenced on the RGB orthophoto. Radiometric conversion to reflectance was carried out via empirical line correction using three PVC panels (black, grey, white) with a known spectral signature within the scene. The hyperspectral scenes for the survey in Otanmäki were not continuously overlapping due to deviations of the UAS internal magnetic compass and the resulting problem of keeping the heading direction accurate during surveying. The compass interference was caused by the strong magnetic anomalies at the Metsämalmi test pit. Topographic correction with the Mephysto toolbox was applied to single Rikola scenes. Similarly to the multi-spectral survey (see Section 3.2.2.1.), the main factors to be corrected were the relatively low sun azimuth and illumination angles. Afterwards, a mosaic of the eastern part of the outcrop (see Fig. 59) was created, which is less covered by vegetation. The general workflow is presented below:

- Downloading of image data on each acquisition day and conducting of a first QA/QC to check whether the images cover the target area and at least one scene contains the calibration panels;
- Application of specific pre-processing steps (camera calibrations, distortion correction, co-registration) as described by Jakob et al. (2017);
- Geo-referencing (projecting UAS scans to the orthomosaic);
- Topographic correction (correcting shadow effects caused by local topography);
- Empirical line correction (conversion to reflectance using regression for each band based on known reference targets in the scene);
- Mosaicking;
- Masking of vegetation cover.

Complete mosaics were used for the image analysis. However, for more detailed spectral analysis of the Rikola data, single scenes were preferred. Since the focus of the study was the investigation of soil and rock surfaces, the in-scene vegetation was removed. For this purpose, the Normalized Difference Vegetation Index (NDVI; Tucker 1979) was calculated for both the multi- and hyperspectral mosaics (see Fig. 53) and a binary mask was

created by using an NDVI threshold of  $>0.3$ . This binary mask was applied to clip pixels with a high vegetation content from the eastern part of the HSI mosaic. Note that the vegetation indices can also be a proxy for specific mineral abundances or soil factors (e.g. Grebby et al. 2014). Furthermore, studies have indicated correlations between the lichen coverage and the underlying rock type (e.g. Salehi et al. 2017).

### 3.2.2.3 *Multispectral Sequoia fixed-wing results*

The eBee Plus Sequoia multispectral images have the potential to provide meaningful maps for lithological interpretation and classification of the Metsämalmi area and to give supplemental information for the results from the multi-copter hyperspectral data. While having limited spectral information, the increased spatial coverage is the main advantage of this multi-spectral fixed-wing survey. In the scope of MULSEDRO, a multi-spectral camera system with 16 bands for the fixed wing from Radai has been recently developed and the first test survey in autumn 2019 in Siilinjärvi, central Finland, yielded promising results. In this respect, the eBee Sequoia multispectral data gives an overview of the possibilities and limitations of such a multispectral system.

As Metsämalmi, the outcrop has already been excavated for some decades, and significant portions of the rock surface are covered by lichens and other vegetation. Thus, important surface features might be obliterated for the UAS cameras. The potential decrease in the representation capability of the image classification results should not be underestimated.

For the interpretation of the images, an NDVI image was firstly formed to create a vegetation mask and remove areas in the images that are strongly affected by vegetation. Figure 53 depicts the NDVI from the multispectral mosaic to illustrate the abundance of chlorophyll active vegetation that partially covers relevant ore bodies at the surface, such as a larger ore lens that correlates with a strong magnetic anomaly (anomaly of  $>60\ 000$  nT in the TMI from the multi-copter survey in Fig. 46).

Only a small amount of vegetation coverage can be observed in the eastern and southeastern parts of the outcrop, identified by pale green colours and NDVI values of  $<0.2$ . In these areas of the Metsämalmi test site, the rock surface was manually brushed and cleaned by Otanmäki mine personnel.

From user experience, an NDVI cut-off value of 0.3 yields reasonable masking while not removing too many pixels in a scene.

The RGB image of bands 3,2,1 of the survey across the Metsämalmi outcrop is presented in Figure 54 with the NDVI vegetation mask applied. The main features observed in the image are as-

sociated with the gabbroitic and anorthosite rocks and ilmenite–magnetite minerals in the southern part of the outcrop. Bright cyan spots in the central southern part of the map are related to gabbroitic zones and secondary iron minerals or products of iron weathering, which were identified in this area along the surface (dashed ellipse in Fig. 54).

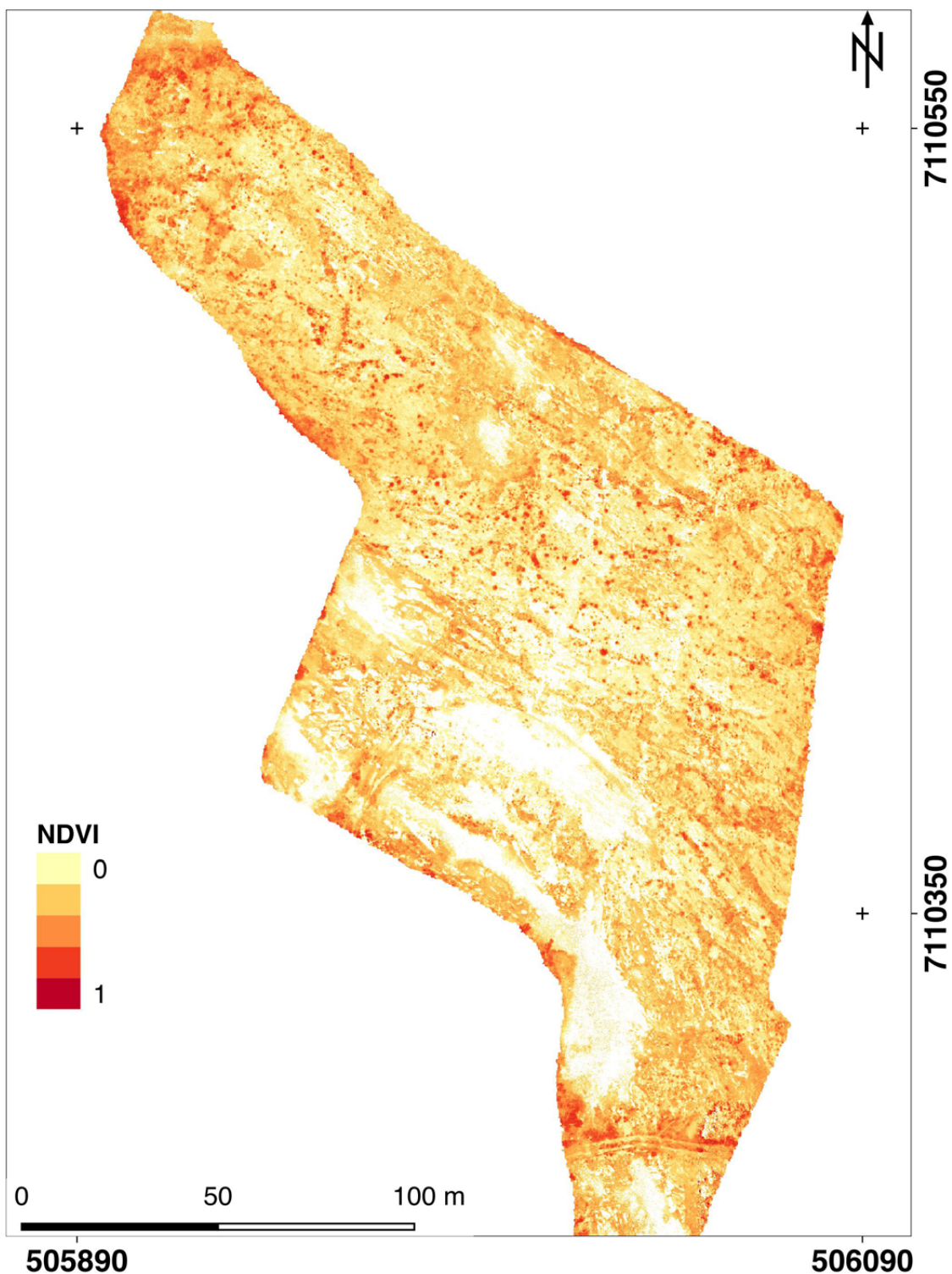


Fig. 53. NDVI scene obtained using the eBee Plus Sequoia sensor. High values indicate abundant vegetation.



Fig. 54. RGB image (bands 3,2,1) from the multispectral mosaic that covers the Metsämalmi outcrop. The dashed ellipse outlines the area where several cyan spots indicate gabbroitic zones.

Figure 55 depicts the MNF (minimum noise fraction; bands: 4,3,1) false colour image. In the MNF transformation, the four Sequoia input bands are re-arranged from their highest to lowest variance content and with increasing noise from the first to the last bands (Green et al. 1988). This means that the MNF separates image components with different noise fractions and therefore enhances spectral

features in the multi-spectral mosaic by applying the advanced principal components rotations to the data. Accordingly, geological characteristics become more pronounced and structures can be more easily traced, such as the shape of outcropping ore bodies. Two parallel channels, created by surface sampling with a rock saw, are emphasized in the image centre after MNF transformation.

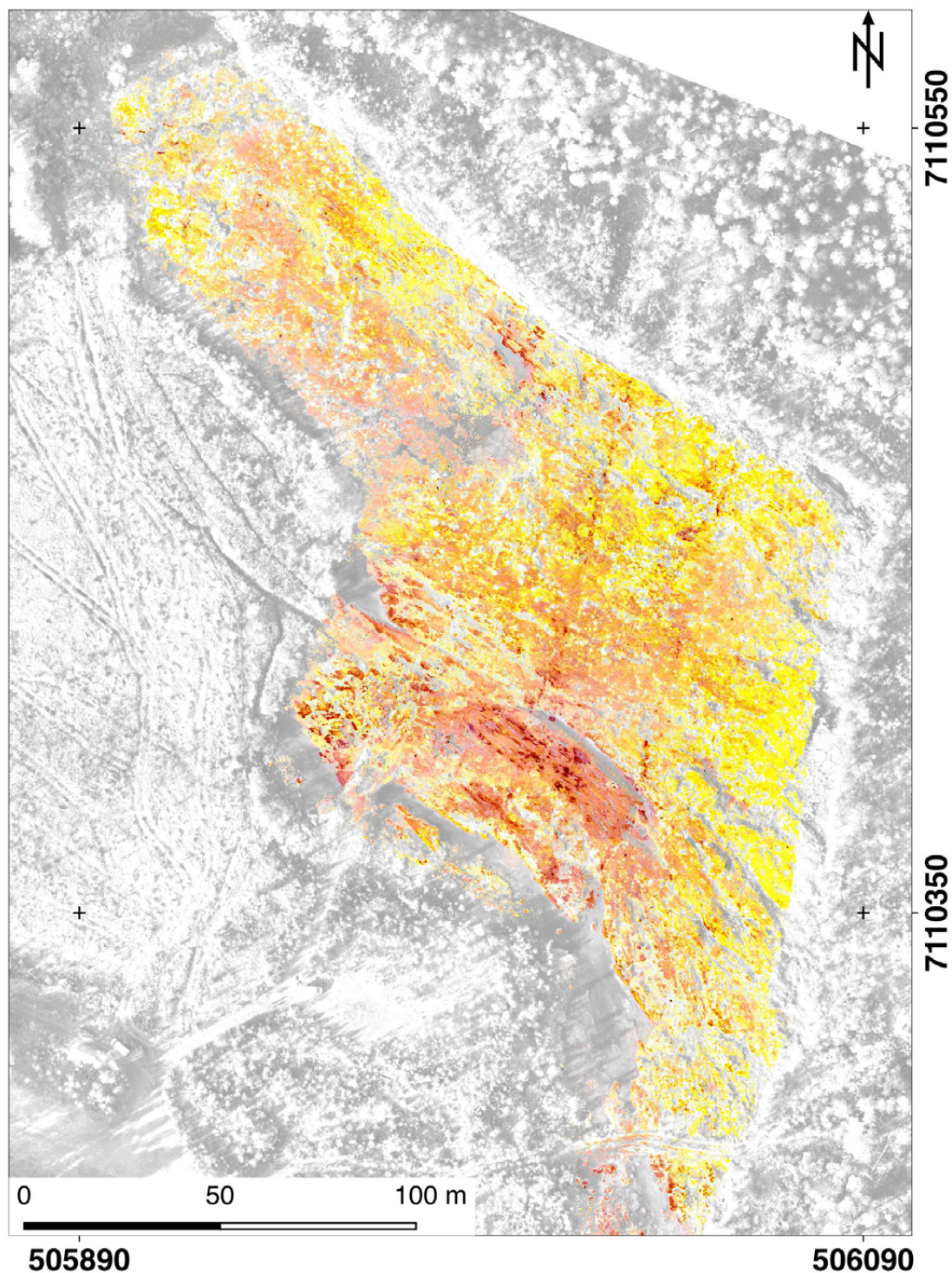


Fig. 55. MNF components (bands 4,3,1) presented as an RGB false colour from the multispectral mosaic across the Metsämalmi outcrop.

The ratio (Fig. 56) of band 3 (735 nm) divided by band 4 (790 nm) was calculated from the Sequoia dataset. This ratio indicates iron-related absorption, as it maps the left shoulder of the Fe<sup>2+</sup>/Fe<sup>3+</sup> charge transfer absorption (Hunt 1977) around 850 nm. However, the band ratio should be interpreted carefully. The FWHM of the 735 nm band is 10 nm, while the 790 nm band has a FWHM of 40 nm, and thus covers several iron mineral reflectance peaks

(e.g. from hematite, goethite, jarosite, schwertmannite). This means that fine spectral features are mixed together or left out in only two bands. Therefore, it does not provide a detailed result compared to the Rikola HSI band ratios, and specific minerals cannot be determined here. Nonetheless, multispectral classification demonstrates that it is generally able to indicate areas abundant in iron-bearing mineral occurrences from

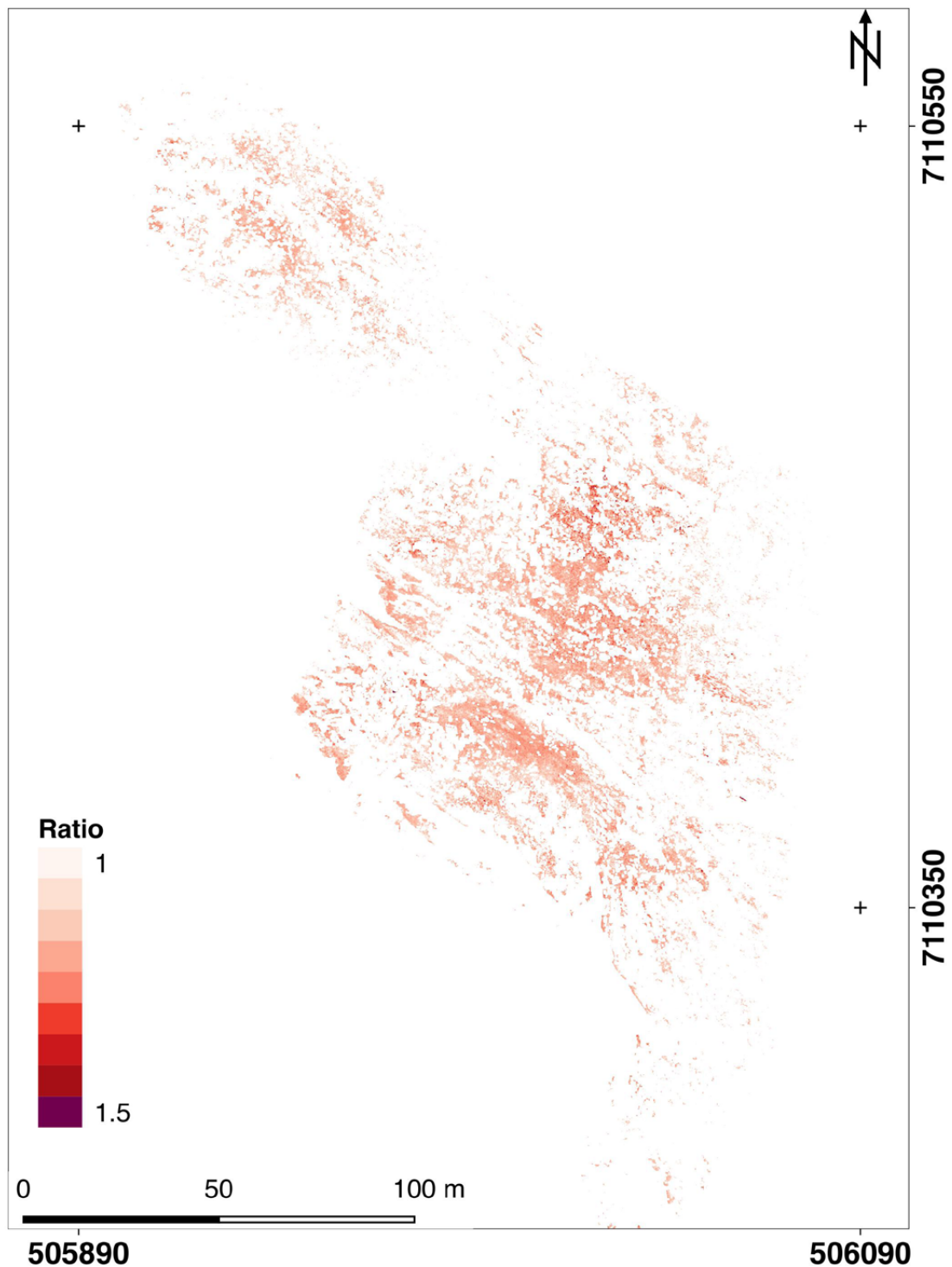


Fig. 56. Band ratio of Sequoia bands (band 3 / band 4) as an indicator of surficial iron alteration.

alteration and weathering processes, with the advantage of covering broad areas, where the use of a multi-copter remains unfeasible.

#### 3.2.2.4 Rikola HSI copter-borne results

Figure 57 shows the different HSI scenes as a true-colour RGB mosaic (nand positions at 650 nm,

550 nm, 504 nm) across the Metsämalmi outcrop (total area of scenes: 17,180 m<sup>2</sup>). Ground reconnaissance performed in the area prior to the survey suggested that the eastern outcrop area (Fig. 58) is the most promising location for remote sensing studies, because it is relatively free of lichen coverage and vegetation. This eastern area was captured by

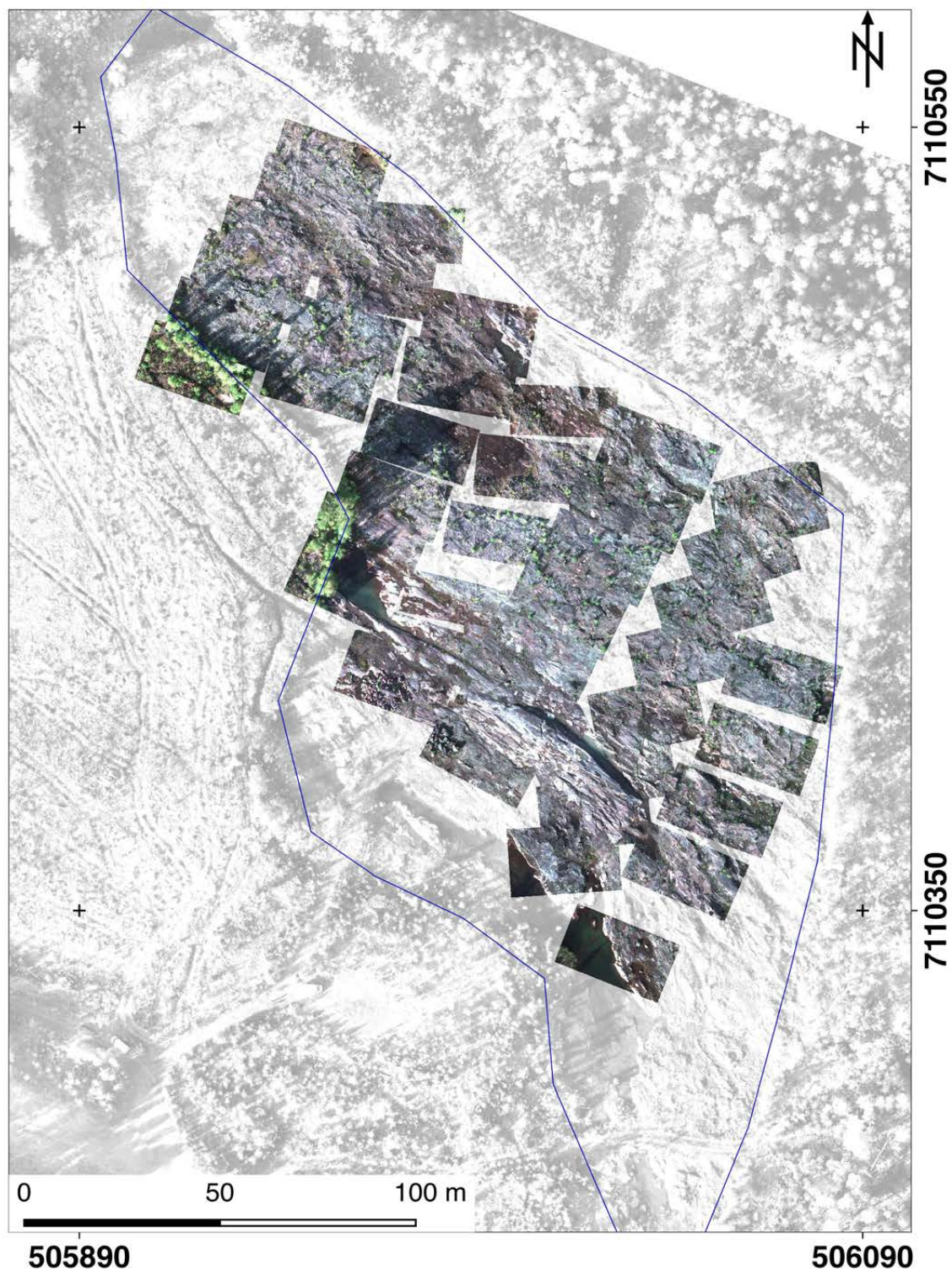


Fig. 57. HSI overlay on a greyscale orthophoto in the Metsämalmi outcrop. The three vertical rows of HS images form the eastern part of the mosaic, which was investigated more detailed.

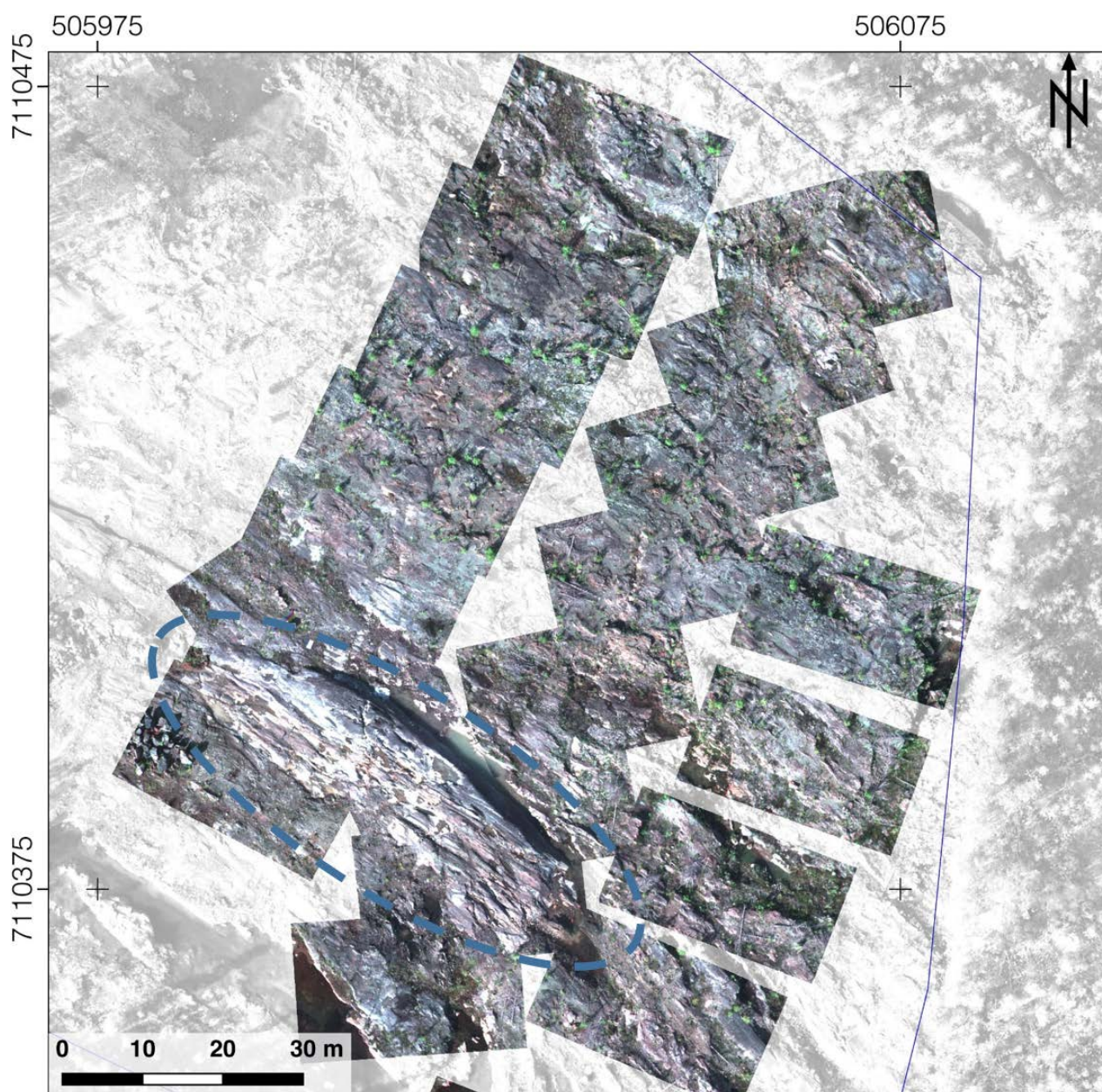


Fig. 58. HSI true colour RGB (bands 650 nm, 550 nm, 504 nm) mosaic of the eastern part of the larger mosaic (20 single image frames). An important feature is the southern ridge, seen as a horizontal-striking white–grey rock formation.

three rows of overlapping HSI scenes (total area of scenes: 8370 m<sup>2</sup>).

The remaining western part was covered by four shorter rows of HSI scenes (total area of scenes: 8810 m<sup>2</sup>), which were dominated by vegetation. This area was discarded from further investigations. A practical advantage of splitting the study area into two sections is also a reduction in the data file size and thus an increase in the processing speed. However, one HSI mosaic still reached a file size of 10 GB. Pixels that were significantly affected by vegetation were identified by NDVI and

afterwards clipped in a similar way as already described for the multi-spectral data in the previous sections.

#### **Results from the eastern area (less vegetation and lichen cover)**

The following discussion and presented maps (Figs. 59–63) only focuses on the eastern area of the Metsämalmi outcrop. About 30% of pixels from the eastern mosaic were associated with vegetation and were removed before image classification. The brighter patches on the southern ridge are

associated with gabbroic rocks surrounding Fe–Ti ore bodies (outlined in Fig. 58), which were identified during the ground-based field survey.

To reduce noise and increase the visible contrast of image properties associated with different geological features, an MNF transform was applied to the hyperspectral mosaic. After manual inspection of 50 HSI input bands from the first principal components analysis, manual reduction to 20 bands was decided by the user. The combination of the first three to five bands usually contains the most significant information. However, from experience with HSI and PCA/MNF imagery, image features

(e.g. geological textures) can even occur in the last bands after sorting them according to noise content in ascending order. Figure 59 presents the main image features in the study area by plotting the first three MNF bands with an RGB colour setting. The differences in the MNF components can be related to the main textural and spectral features in the image mosaic. While blue and violet colours (Fig. 59) highlight outcropping bedrock surfaces, green and yellow colours emphasise the remaining (inactive) vegetation, not removed by the NVDI, and pixels containing soils and debris. As in the multispectral data, a large barren area

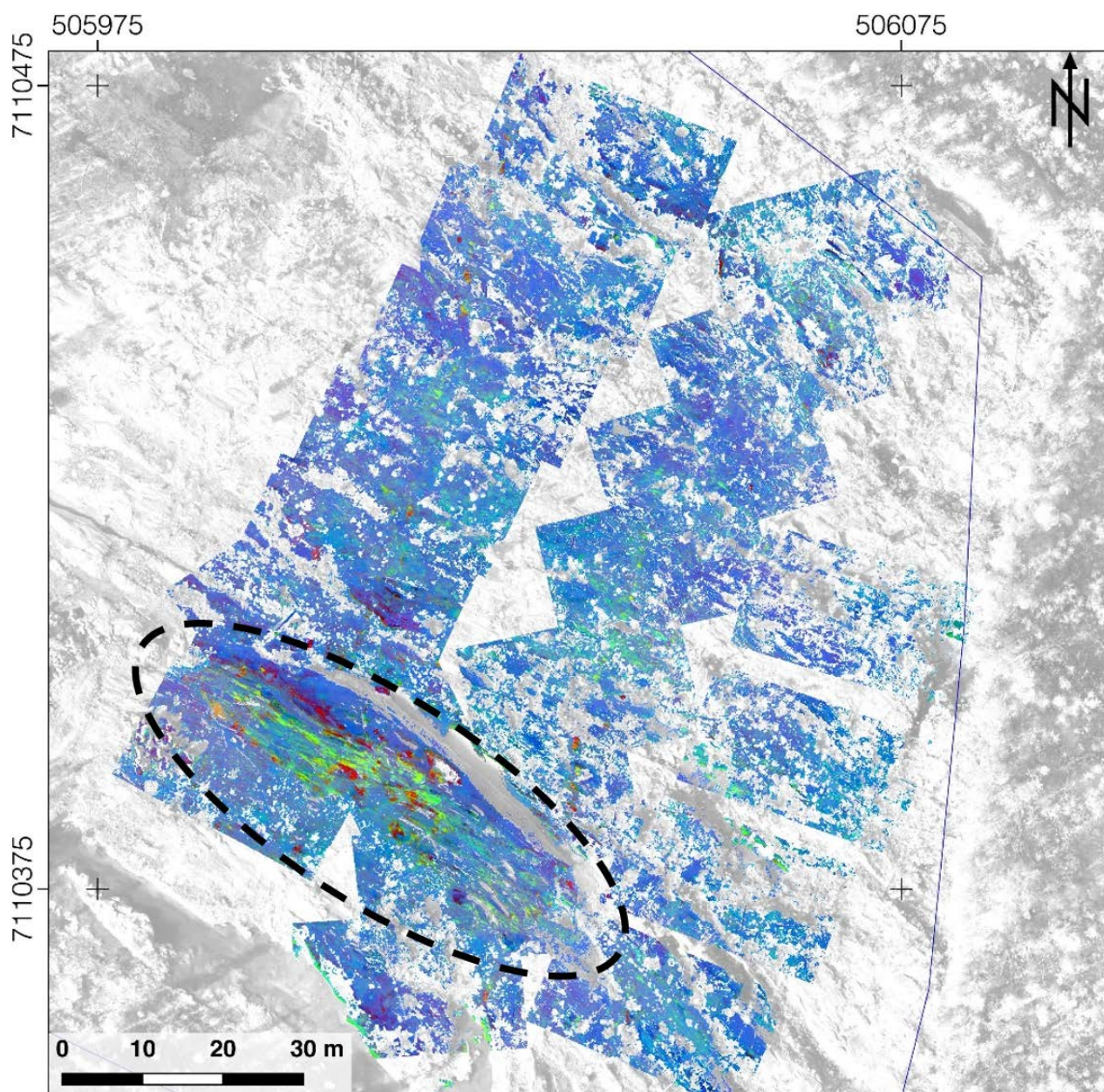


Fig. 59. RGB false colour plot of MNF bands 3, 2, 1 from the hyperspectral images superimposed onto a grey-scaled orthophoto. The RGB colours can be associated with the main surface structures. The black dotted ellipse highlights the southern ridge.

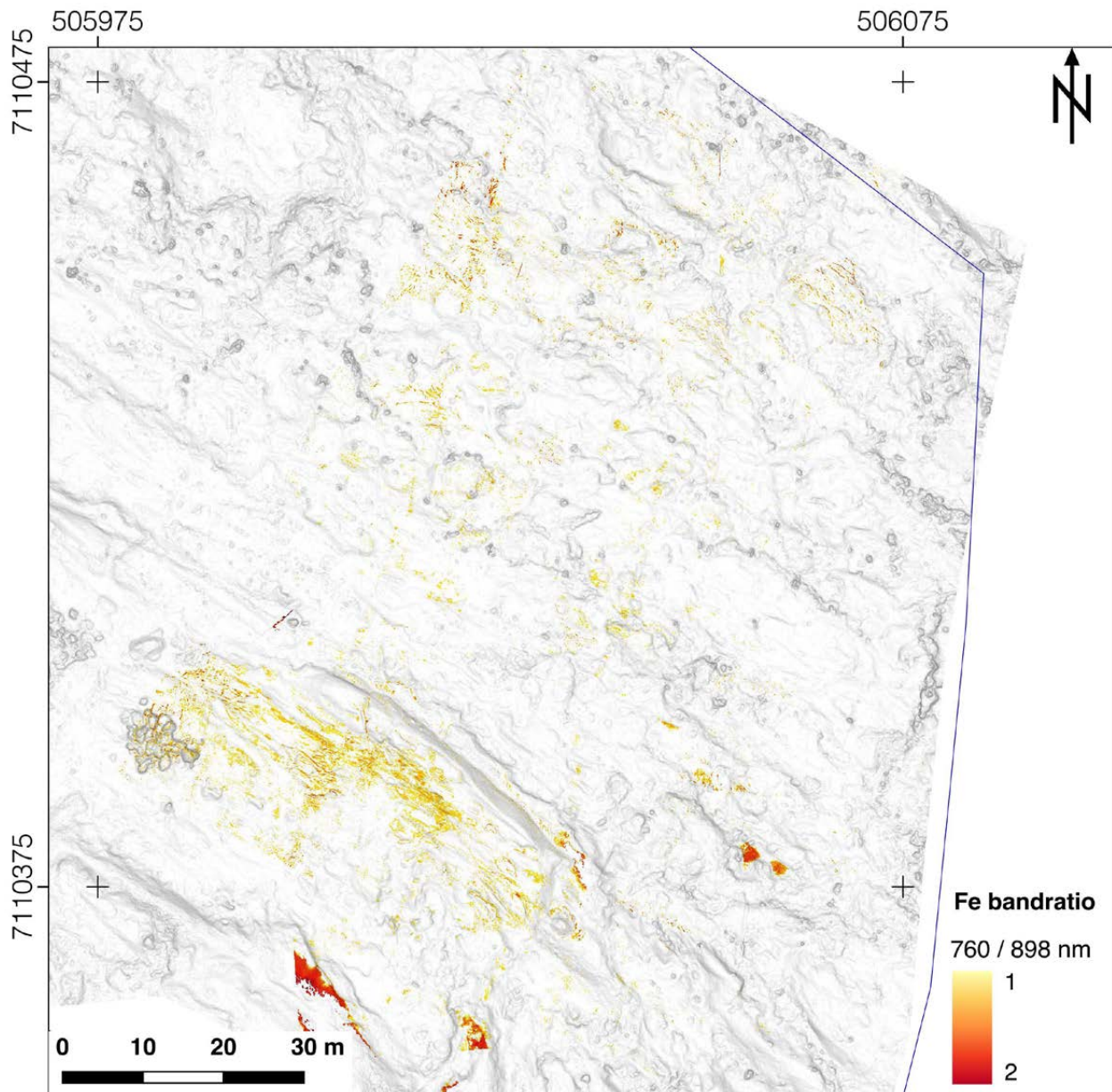


Fig. 60. HSI iron indicative band ratio for 760 nm / 898 nm, where the higher wavelength band contains an Fe absorption. Projected onto DSM for increased contrast.

shows up in the southern central parts, while the northern outcrop areas become increasingly covered with vegetation and soil. In an unsupervised image classification with the k-means method, which is described later, the MNF mosaic is used as input. The advantage of this is a decreased noise fraction of the input data and, hence, highly reduced redundant band information.

The iron band ratio (Fig. 60) calculation is used as a first proxy to identify zones of a specific absorption. The ratio between one diagnostic and one control band is calculated, similarly to the results for multispectral data in Figure 56. A simple ra-

tio may indicate whether an absorption feature is present and is robust for further image operations, e.g. continuum removal. The band at 760 nm (iron indicative of e.g. goethite, a spectral reflectance peak) is divided by the band at 898 nm (iron indicative with a deeper absorption feature) for the Rikola camera. Quotient values of  $>1.0$  indicate iron abundance and pixels with values of  $>2.0$  are grouped together in one colour class for increased visibility in the colour gradient. The large blank areas in the HSI data in Figure 60 are also caused by the vegetation and gaps in data coverage.

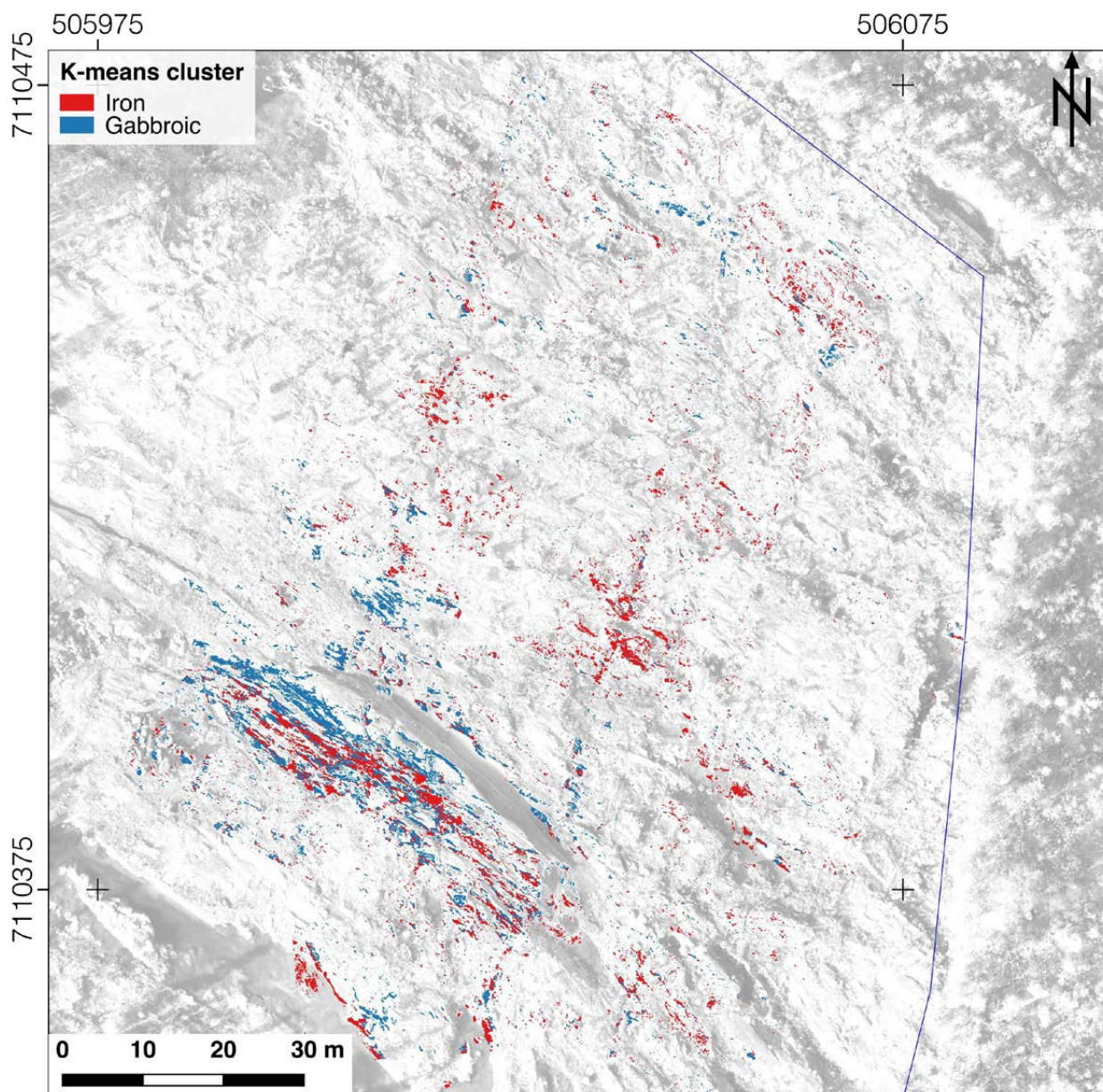


Fig. 61. Unsupervised k-means classification with 9 output classes. Two classes are presented that can be associated with distinct lithology.

K-means (Tou et al. 1974) unsupervised classification was applied to the NDVI-filtered HSI MNF data with the first 20 bands of the MNF as input (see Fig. 61). Nine output classes were set as start parameters. The number of classes was estimated from the expected resulting features (gabbro, iron-bearing minerals, water, remaining vegetation, soil debris, noise) and was based on preliminary experiences with the Rikola data at geologically similar targets, as well as their unsupervised classifications. After running the k-means classification (100 iterations), only two of the classes could be associated with distinct lithologies. The four discarded classes were related to noise, vegetation

pixels that remained after NDVI and potentially redundant features caused by illumination changes. K-means showcases that hyperspectral data, with up to hundreds of bands, is prone to redundancy due to cross-correlated bands, as well as propagation of image noise along the spectral dimension, and it is not necessarily sensitive to small spectral changes. Therefore, the unsupervised separation of classes only splits spectrally similar mineral groups to some degree. In the Metsämalmi case, the class distinction predominantly accounted for iron-rich and iron-poor rock surfaces. Further examination and correlation of classification results with field observations and photography

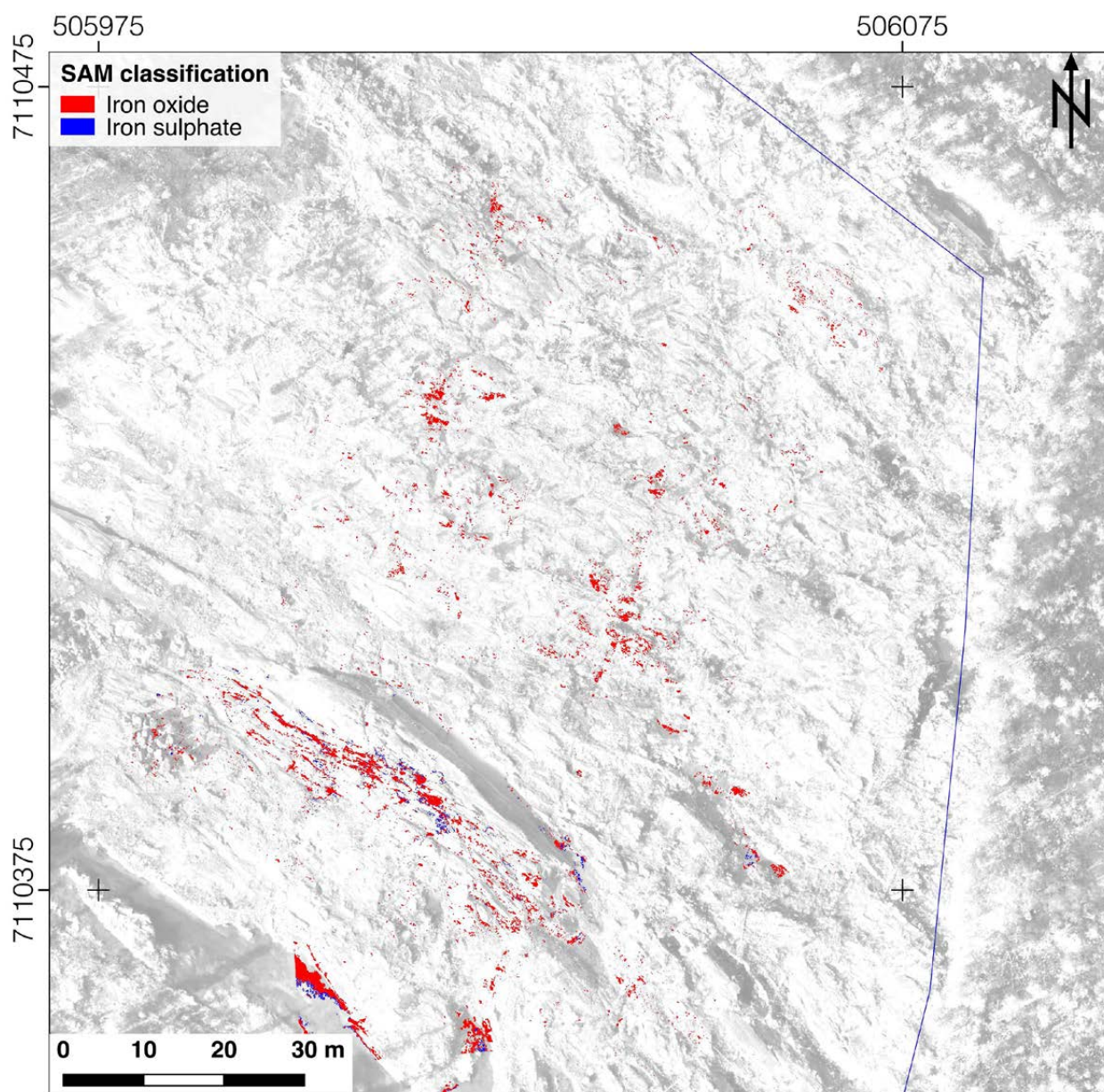


Fig. 62. Supervised classification by applying the spectral angle mapper to the HSI mosaic.

(see Section 3.3.2.5 and Fig. 69 for near-surface geology) implied that the remaining classes were associated with both iron-rich and gabbro-containing areas.

Finally, supervised spectral classification was applied to the processed HSI (see Fig. 62) by using the Spectral Angle Mapper (SAM; Kruse et al. 1993). Previous studies have demonstrated that the SAM technique is well suited to hyperspectral images featuring similar iron-bearing mineralogy to that observed in the target area (Jackisch et al. 2018, Kirsch et al. 2018). While an unsupervised classification, e.g. k-means (see Fig. 61 and discussion above), detects the pixel content using

a random classifier and a pre-defined class separation threshold, SAM directly compares mineral standard mineral spectra from libraries (as ground truth) and data spectra.

Experiences with Fe-related spectra have shown that the application of spectral smoothing to the input HIS with a Savitzky-Golay filter (Savitzky et al. 1964) of second order and a filter width of 3–5 units (depending on the spectral resolution width) increases the quality of SAM classifications by removing image noise to a reasonable degree.

The obtained SAM results for iron minerals were visually comparable to those of the k-means classification but contained significantly fewer pixels.

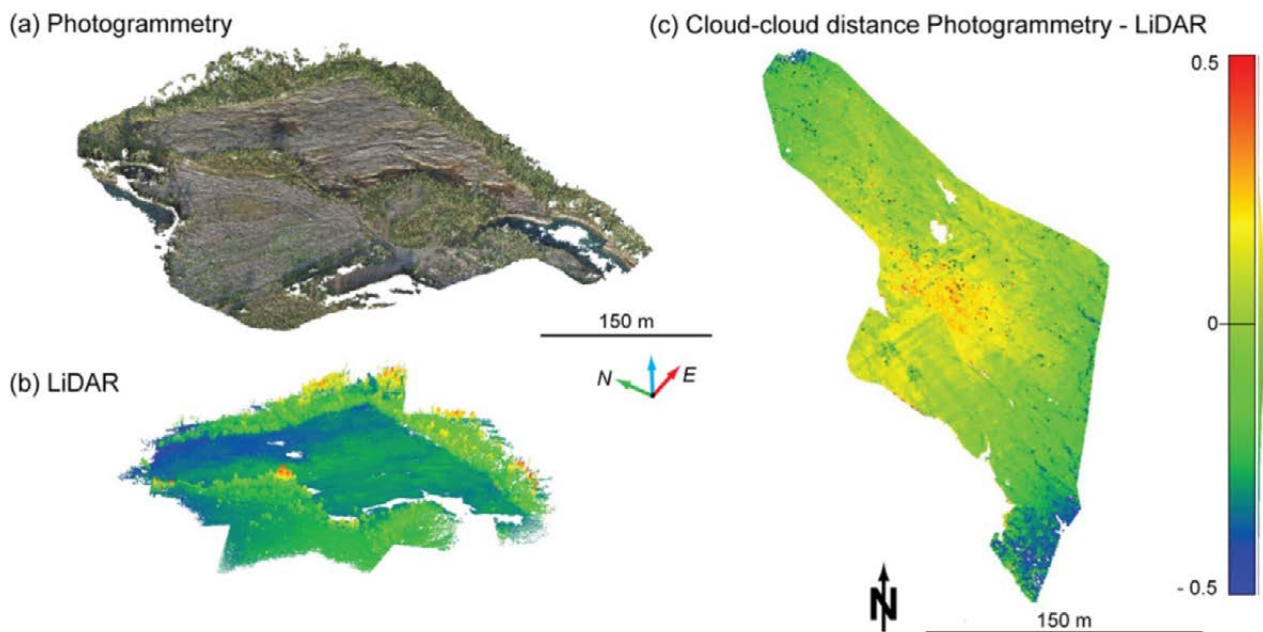


Fig. 63. (a) Point clouds resulting from photogrammetry shown with RGB colours. (b) Elevations from LiDAR measurements (colour scale from blue to red). (c) The computed cloud–cloud distance from photogrammetry and LiDAR data. The colour scale is in m.

Since only the spectral shape is compared in SAM (but not the amplitude level), it is insensitive to reflectance fluctuations caused by illumination changes and mixed surface materials, and the results can therefore be considered as more robust.

### 3.2.3 UAS LiDAR

LiDAR data were collected over the Metsämalmi outcrop by HZDR-HIF on 7 September 2018. A Yellowscan Mapper II UAS LiDAR system was mounted on the Tholog THO-R-PX-8/10 multi-copter to survey the study area. The LiDAR system comprised onboard data storage, an Applanix AP15UAV GNSS INS/IMU system, and an ibeo LUX 2010 LiDAR scanner. The LiDAR can operate at a flight altitude of up to 100 m and produces 3D point cloud data with 4 laser beams at  $\pm 2.5$  cm accuracy over a  $90^\circ$  field of view (Yellowscan 2018). The flight speed was set to 3 m/s with 50% side overlap and 3 tie lines were flown.

During processing of the raw data, the optimized smooth trajectory was calculated using a fusion of GNSS and INS/IMU data. Altitude variation was minimal during the surveying. The resulting heading errors were  $<20^\circ$ , and roll/pitch errors were  $<5^\circ$ . The estimated positional accuracy was  $<10$  cm, which lies inside the accuracy margins given by the manufacturer.

The LiDAR scanner produced 3D point cloud data with an average point density of 40 points/m<sup>2</sup>. To compare the LiDAR and the photogrammetric point cloud, the M3D2 algorithm in CloudCompare software (James et al. 2017a; see Fig. 63) was used. The average cloud–cloud distances were 0.1 m with higher deviations in the central and southeastern part of the study area. The main reason for these deviations was less image overlap along the image corners.

## 3.3 Ground-based measurements

### 3.3.1 Ground magnetic survey

A systematic detailed ground magnetic survey was conducted by GTK in the Metsämalmi exposed area to provide a reference dataset for the UAS-

based surveys. The size of the survey area was 160 x 310 m and it covered the whole outcrop area. Due to the relatively flat terrain and good accessibility, the survey path lines were almost parallel and the only gaps were at positions where it was

physically impossible to bring the magnetometer. The line spacing was 10 metres and the line direction 70 degrees anticlockwise to E. Measurements were carried out during three days, on 28 August and 6–7 September 2018, by research assistant A. Illikainen and geophysicist J-P. Kujasalo. A GEM GSM-19 Overhauser magnetometer from GEM Systems was used in walking mode, which leads after data processing to an average station spacing of 0.5 metres along the lines. Diurnal variation in the magnetic field was removed (= base station

correction) using base station recordings measured outside the anomalous Otanmäki gabbro intrusion.

Because of very high total values and strong gradients in the anomalous magnetic field, there were in some locations great difficulties in obtaining reliable readings, even though the gradient tolerance of the Overhauser magnetometer is documented to be greater than 10 000 nT/m. The calculated International Geomagnetic Reference Field (IGRF), which is considered as the background field in the area, was about 53 000 nT. The largest measured

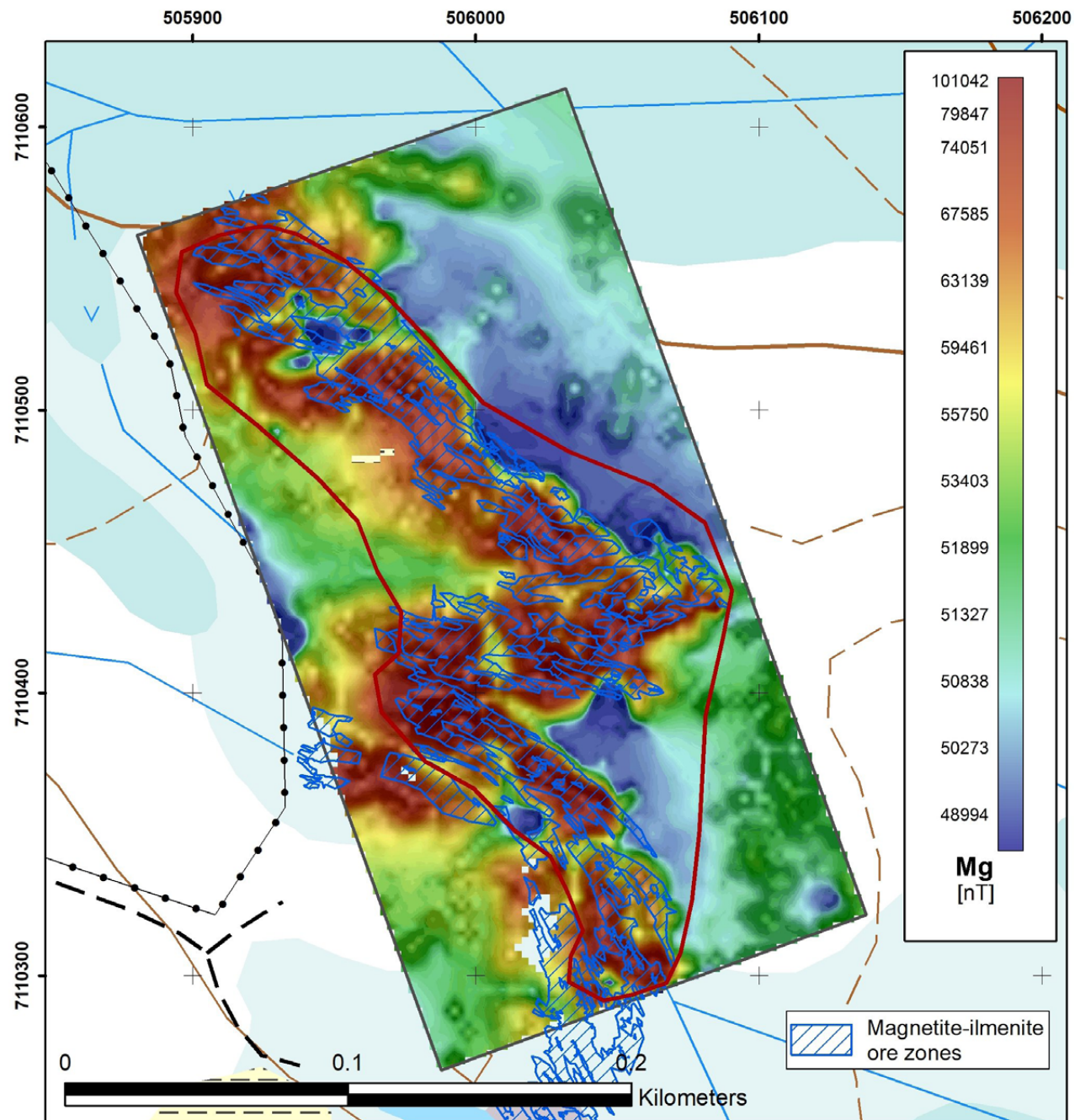


Fig. 64. Magnetic map of ground surveys in Metsämalmi. The magnetic total field is colour coded and the tilt derivative (TDR) is overprinted as a transparent background. The mapped magnetite–ilmenite ores lenses are highlighted by blue colours (Basemaps © National Land Survey of Finland).

field value was 136 662 nT, which even exceeds the upper limit of the specified operating range of 20 000–120 000 nT. However, by performing measurements at a slow walking speed and watching the readings, fairly good results were achieved. Readings over the limit of 120 000 nT were kept in the dataset, although they are probably prone to higher error.

The magnetic intensity of ground measurements is presented in Figure 64. It is observed that the total field anomalies correlate very well with known magnetite–ilmenite ore lenses in Metsämalmi. The total field values measured on the ground over the known ore zone are broadly in the range of 70 000–80 000 nT and anomaly variations are up to 20 000–30 000 nT. The results

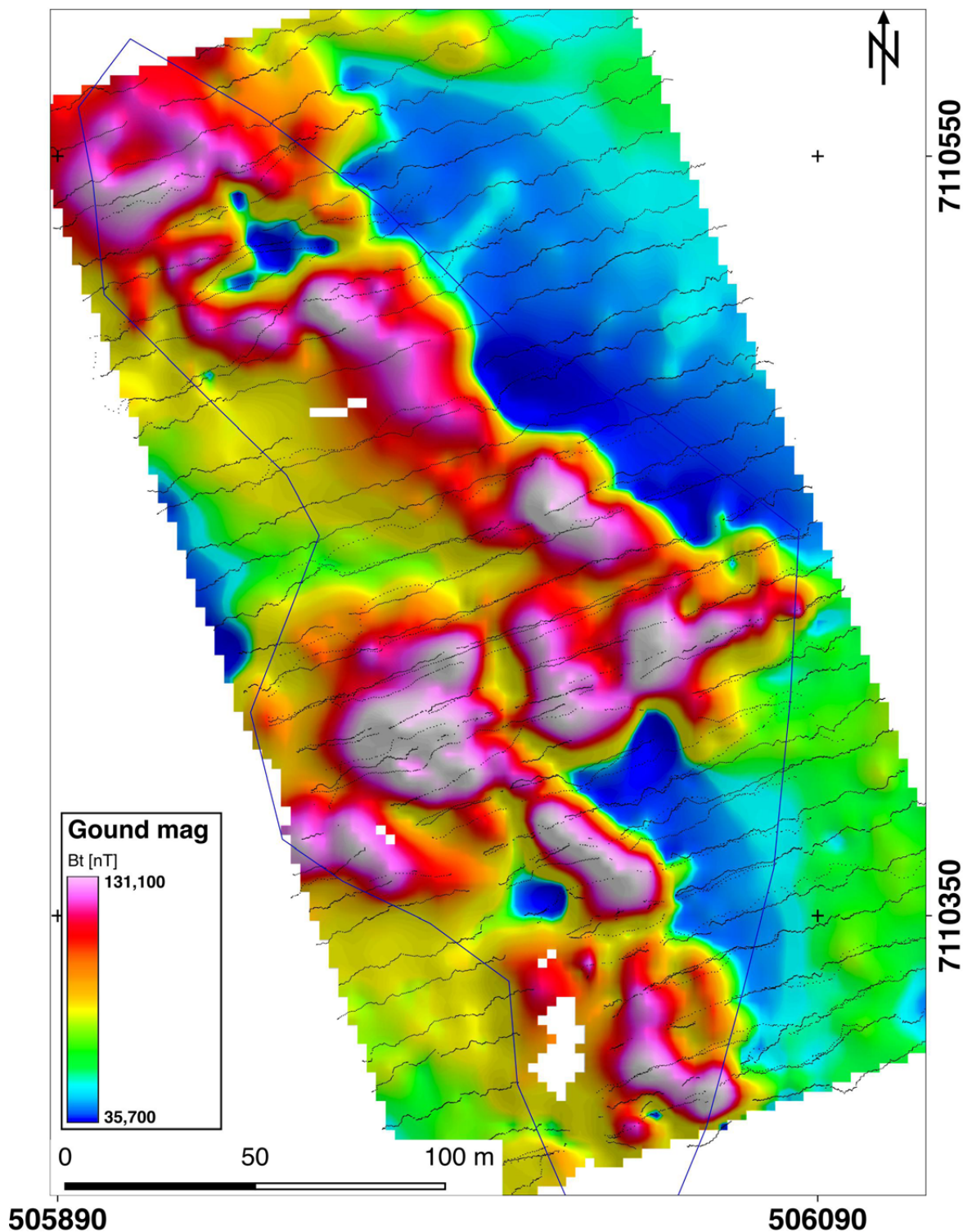


Fig. 65. Ground-based magnetic survey by GTK. Measurement locations are depicted as black points.

indicate a very strong influence of the magnetite, which is expected when one considers that the highest grade ores in Otanmäki contain 35–40% magnetite (Illi et al. 1985).

The survey path lines are presented in Figure 65. Deviations from straight profiles result from obstacles blocking the path for the surveyor.

### 3.3.2 Other ground measurements

In order to validate the drone-borne data, field samples were acquired with a well-adapted and specified set of tools. This ground-truthing procedure is constantly enhanced and improved by HZDR-HIF,

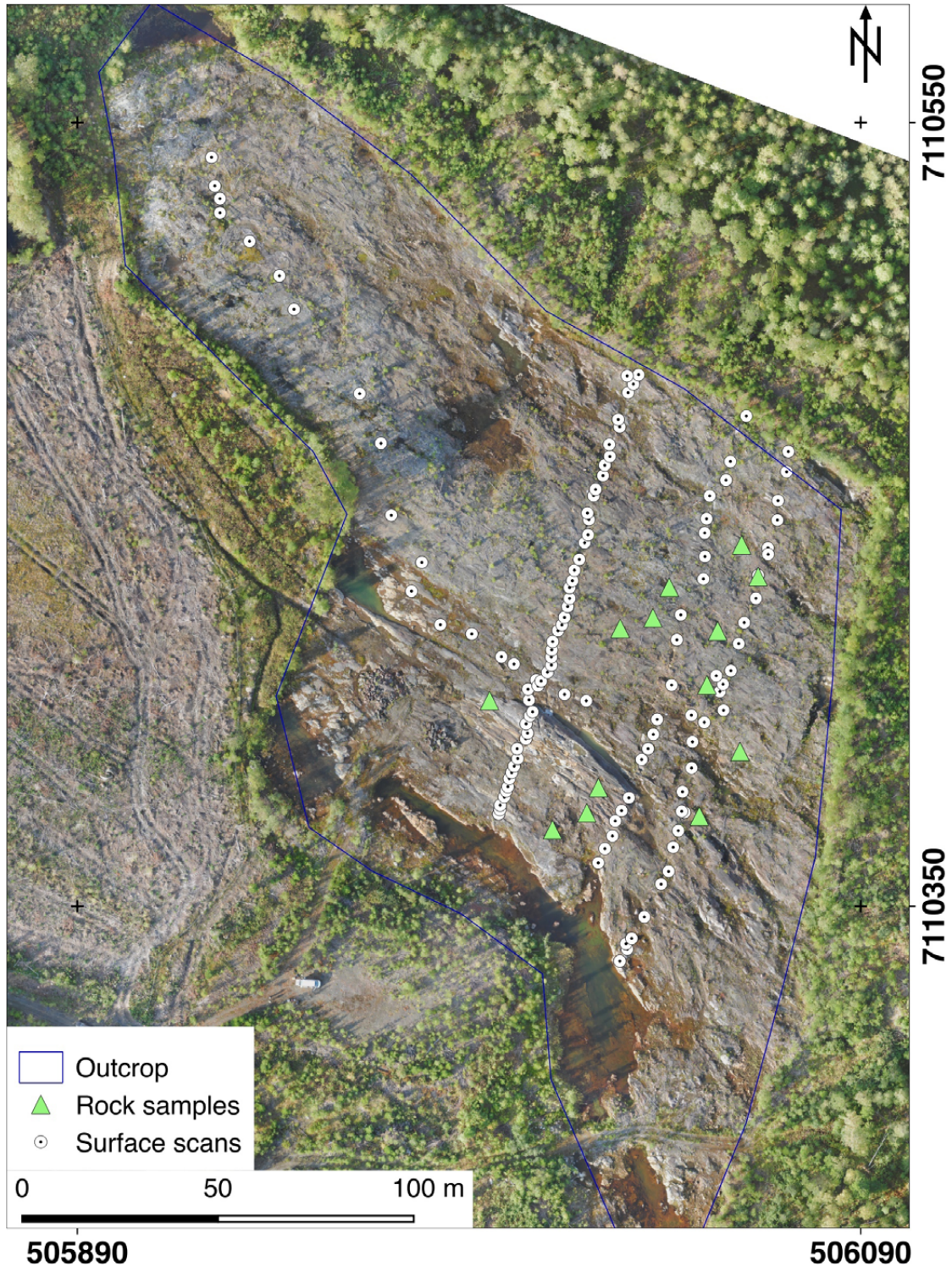


Fig. 66. Rock sample locations and measurement points from different handheld devices (spectroscopy, magnetic susceptibility, XRF, GNSS, n = 123) in the Metsämalmi outcrop area. Selected spectra are presented in Fig. 67.

relying on approved methods to characterize the surface parts that are covered by a UAS survey.

A set of ground spectroradiometer readings ( $n = 51$ ), hhXRF readings ( $n = 48$ ) and local measurements of magnetic susceptibility ( $n = 88$ ) was collected. The number ( $n$ ) of measurements differed between the devices, because the operation of some of the instruments required specialized training (e.g. handling of X-ray devices), the devices differed in their handling or were not available for the whole period of the field campaign. Another reason was the surface conditions in the area, which varied to a great degree such that reasonable measurements were not possible with all the mentioned methods at exactly the same points, for example due to the different sampling contact point sizes of the spectrometer, the hhXRF and the susceptibility meter. The coordinates of validation points ( $n = 123$ ) were determined using a precise differential GNSS system. No additional laboratory hhXRF measurements were performed during this stage of this report.

Additionally, we sampled 13 handheld specimens of different rock types (including ore samples) and vegetation. These samples were stored for later investigation. The sampling locations are marked in Figure 66.

Our sampling was mainly performed along a number of profiles that followed the old scan lines and surface cuttings performed by Otanmäki Mine Oy (see Figs. 6 and 66). These complementary magnetic susceptibility measurements provided by Otanmäki Mine Oy were sampled with spatial intervals down to two centimetres.

#### 3.3.2.1 GNSS Surveying

To determine the precise coordinates for the validation points, a Trimble R5 GNSS receiver with a Zephyr Z-2 antenna was set up as base station and a Trimble R10 was used as a rover. Both systems were operated in post-processing kinematic (PPK) mode and baseline processing was performed using the software Trimble Business Center version 3.40. The base station was set up to operate for more than 4 h in one fixed position, so its location and height could be calculated with sufficient precision. The observation time per measurement on the rover was set to 10 s. In addition, permanent GNSS stations from the EUREF network were incorporated in the baseline processing to improve the precision of the base station. The nearby (<200 km baseline distance) stations of Aankoski (KIV2), Oulu (OUL2)

and Kuhmo (ROM2) were included in the processing.

In total, 12 ground control points were collected from the study area (see Fig. 50(c)) for accurate georeferencing of the optical UAS data. The positions of the black/white coded tarps were also measured with the above-mentioned setup. A list of the GCPs can be found in Appendix 3.

#### 3.3.2.2 VNIR-SWIR spectroscopy

Spectral measurements of rock surfaces were taken using a Spectral Evolution PSR-3500 portable spectroradiometer. Spectra were recorded for the VNIR/SWIR part of the electromagnetic spectrum (400–2500 nm) with a spectral resolution of 3.5 nm (1.5 nm sampling interval) in VNIR and 7 nm (2.5 nm sampling interval) in SWIR using a contact probe (8 mm spot size) with an internal light source. Radiance values were converted to reflectance using a pre-calibrated polytetrafluoroethylene-based (PTFE) panel (Zenith polymer) with >99% reflectance in the VNIR and >95% in the SWIR range. Each spectral record consisted of 10 individual measurements taken consecutively and averaged.

Non-linear relations between spectra and surface compositions are caused by variation in the structural properties of the samples and the physical properties and measuring principal of the spectroradiometer. This is expressed, for example, as baseline drift, random noise and multiple scattering. Noise could further appear as strong absorption peaks, which are not related to real reflectance behaviour (strong spikes). Thus, it is important to employ some spectral pre-processing techniques to reduce these effects. Spectral processing includes hull curve removal (van der Meer 2004) followed by Savitzky-Golay filtering (Savitzky & Golay 1964) using a 3rd or 5th order polynomial function.

Representative handheld spectra obtained in the wavelength ranges of 350 to 2500 nm from the Metsämalmi outcrop are displayed in Figure 67. The main features identified are iron absorption features between 700–950 nm marked in Figure 67a with a blue frame. These photon absorptions are caused by electronic charge transfer processes, where electrons in the lattice change between different valence states of the ion (Clark et al. 1999). These absorption positions are diagnostic for specific minerals such as hematite, goethite and jarosite. Position changes are also caused, for example, by grain size effects of impurities and cation exchange (Clark et al. 1999). The main iron

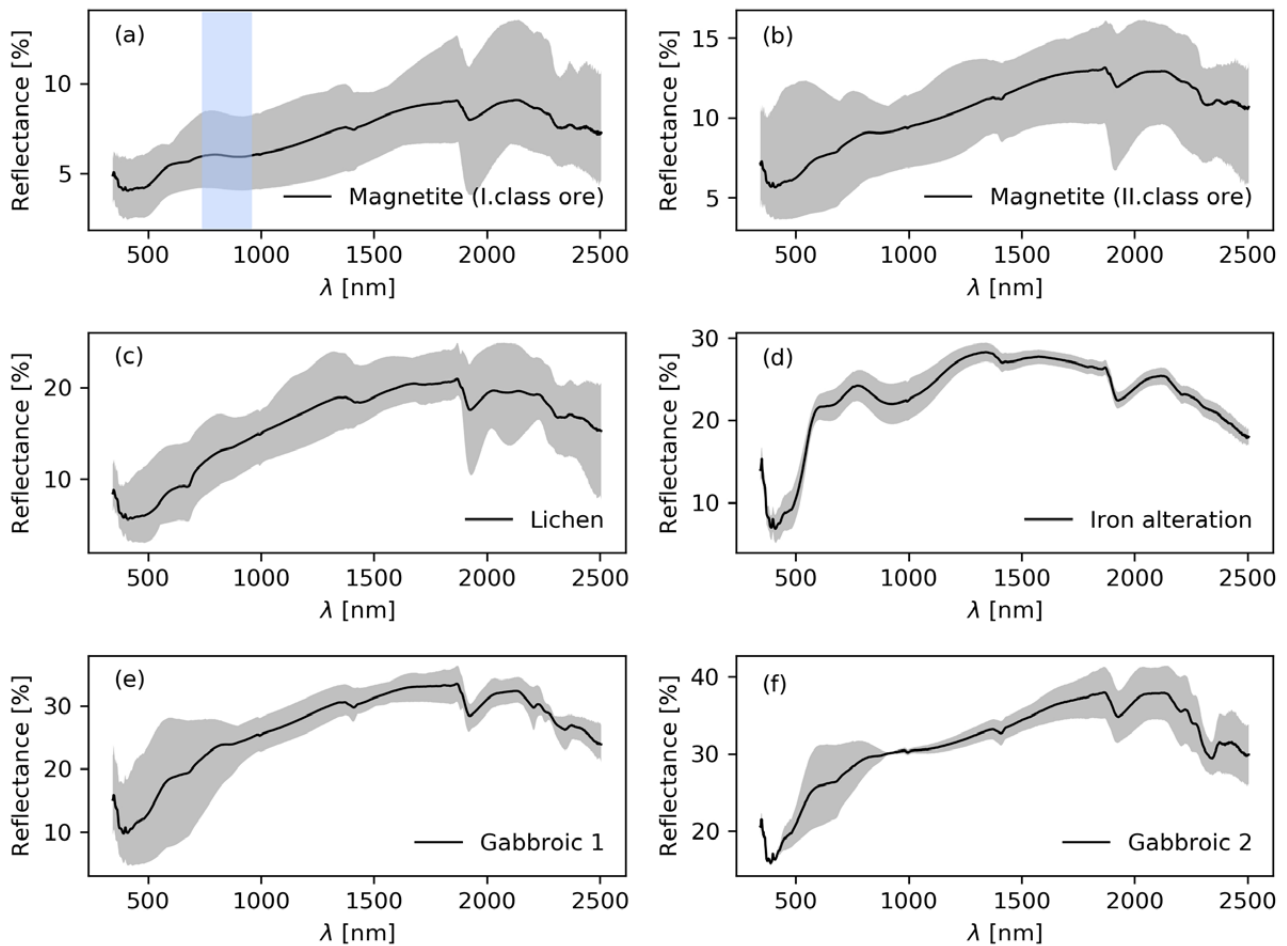


Fig. 67. Spectral plots presenting selected point spectra from the Metsämäalmi outcrop. The legend refers to the sample class. The blue frame marks the position of the occurring iron absorption (Figure modified after Jackisch et al. 2019).

minerals to be identified in this study were hematite ( $\text{Fe}_2\text{O}_3$ ) and goethite ( $\text{FeOOH}$ ). Magnetite ( $\text{Fe}_3\text{O}_4$ ) could be indirectly identified through the aforementioned proxy minerals.

An approach similar to the one from van der Meer (2004) was applied to calculate the minimum wavelength absorption position and absorption depth using the hyperspectral software package Hyppy (Bakker et al. 2014). The resulting absorption depth values were thresholded by a minimum value in order to separate image artefacts from physical spectral absorption. Absorption wavelength positions could then be visualized in scatter plots or used for the statistical determination of surface mineralogical compositions.

The histogram plots (Fig. 68) show the distribution of absorption feature positions for diag-

nostic absorption ranges from all handheld spectra obtained in ground sampling. Further analysis of these feature positions could be used to distinguish, for instance, different kinds of clays or the abundance of iron minerals by combining them with results from, for example, X-ray diffraction measurements.

The cumulative distributions of iron absorption feature positions (Fig. 68(a)) indicate a mixture of goethite and hematite in the handheld spectra, and the increased occurrence of absorption around 940 nm could be an indicator of goethite (Crowley et al. 2003). Magnetite can only be detected indirectly, as it exhibits an overall low reflectance and no iron charge transfer absorption exists due to its spinel structure. The coordinates for spectral readings are included in Appendix 6.

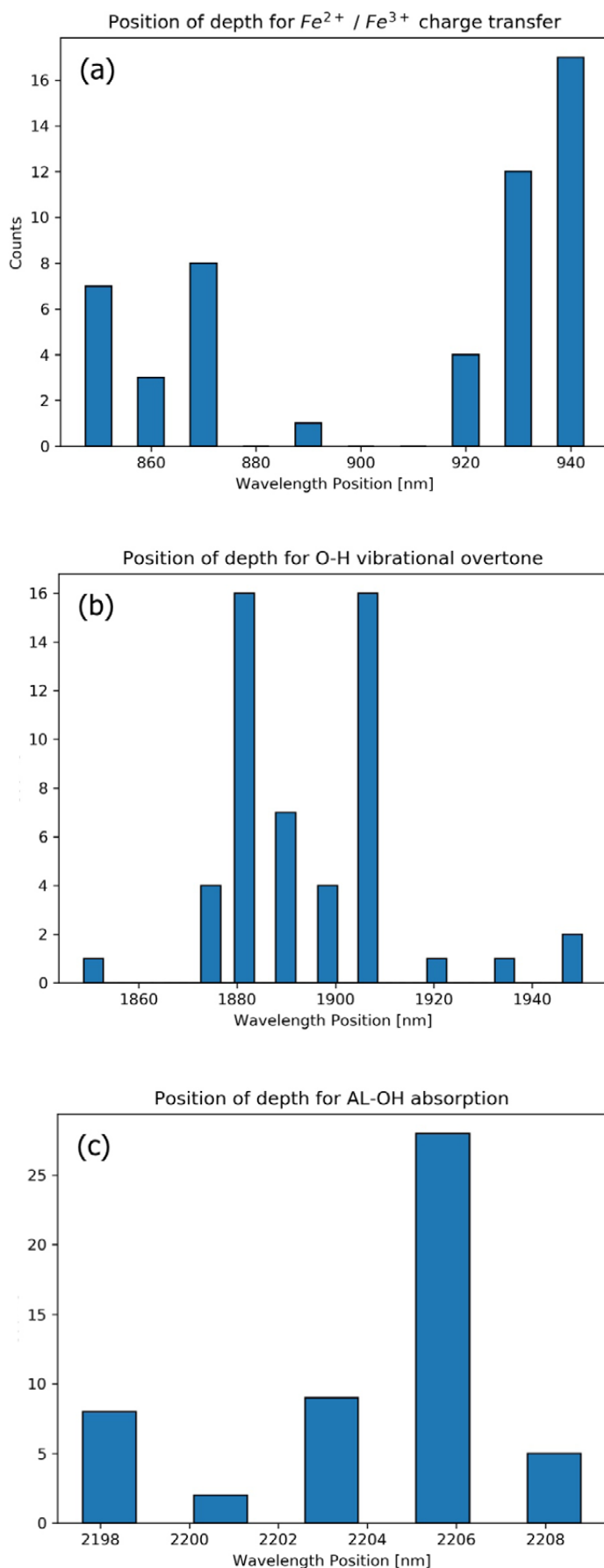


Fig. 68. Cumulative distribution of absorption feature positions for all handheld spectra. (a) Counts for positions of iron absorption. (b) Counts for positions of OH absorption ('water feature'). (c) Counts for positions of Al-OH absorption (referred to as the 'clay feature').

### 3.3.2.3 Magnetic susceptibility

Magnetic susceptibility was measured with a KT-6 Kappameter. A fundamental part of the instrument is an LC oscillator operating at 10 kHz. The primary magnetic field from the oscillating current initiates a secondary magnetic field in nearby material that correlates with its magnetic susceptibility. This secondary magnetic field in turn modifies the resonance frequency of the LC oscillator, and this change in the frequency can be used as a measure of the susceptibility.

The coil is placed in the front of the instrument and magnetic susceptibility is determined in two steps during measurements. (1) The oscillators frequency is measured with the front coil at some distance from the rock (i.e. distant space measurement) and (2) with the front face applied on the rock surface. The assumed susceptibility is calculated from the frequency difference by the aid of the internal CPU and is directly displayed to the user. The sensitivity ranges up to 1 SI unit with a measurement range of  $-999$  to  $9999 \times 10^{-3}$ . The magnetic susceptibility measurement table is shown in Appendix 7.

### 3.3.2.4 Handheld XRF

A Bruker S1 Titan 800 with GeoChem calibration was used for measuring the in situ chemical composition of rock surfaces. The XRF device features a rhodium anode and operates with 50 kV and 9 A. The instrument is pre-calibrated by the manufacturer for geological materials. A check sample (soil standard) is measured on a regular basis to check for instrument drift. For results, see Appendix 8.

### 3.3.2.5 Sampling and geological mapping

Representative samples of the main lithological units were taken for lab-based follow-up analysis and the textural relationships between gabbro, anorthosite and the magnetite–ilmenite ore (referred as Fe–Ti ore in the images) were examined (Fig. 69). Ore, gabbro and anorthosite layers are mostly preserved in their magmatic textural relationship (see Fig. 69c, d, e). In some parts, the succession is folded and sheared (see Fig. 69a, b, f) and the NW part of the outcrop is generally dominated by brittle deformations. The lithologies are generally well distinguishable by visual inspection in parts without lichen coverage.



Fig. 69. Photos from the Metsämalmi test site showing the outcropping surface of the gabbro (host rock) and magnetite–ilmenite layers at Metsämalmi, Otanmäki, Finland. The hammer handles for scale have lengths of about 60 cm (a–e) and 30 cm (f).

## 4 DATA COMPARISON AND INTEGRATION

### 4.1 Relationships between ground-based hhXRF, magnetic susceptibility and spectroscopy data

Surface observations from the different ground-based techniques allow the general characterization of the area. Figure 70a illustrates the four main elemental constituents at the Metsämalmi site that were detected by handheld XRF ( $n = 48$ ). The bulk constituents are silica (21.8% avg.), followed by iron (17.6% avg.), aluminium (6.9% avg.) and titanium (3.1% avg.), all given in the form of oxides and as a weight percentage (wt%). Silica shows the widest spread, while iron had most outliers beyond the upper 75% quantile. The results reflect the local geology and mineralogy (magnetite, ilmenite, anorthosite, gabbro) of the surface mapping results from Otanmäki Mine Oy.

A comparison of handheld susceptibility values and hhXRF iron oxide readings (Fig. 70b) acquired during the campaign revealed a strong correlation after outliers were removed. The outliers resulted from inaccuracies in the measuring locations for the handheld susceptibility data. In order to obtain test samples that could be further evaluated and validated in terms of their physical properties and mineralogy, only points with a precisely measured GNSS location were considered in the regressions. These points were covered by ground measurements using at least one of the following methods: hhXRF, spectroradiometry and susceptibility measurements. We observed baseline errors

of measurements at the same point with a spatially inaccuracy of  $\sim 2$  cm when the device was applied to non-magnetic materials. The measurement points in the field campaign were chosen according to the visual appearance of a significant amount of magnetite. The strong correlation is not surprising, because massive magnetite ore bodies form the highest ore grades and contain the highest iron values, referring to e.g. Hokka and Lepistö (2018). The location with the highest hhXRF iron oxide content (59.4 wt%  $\text{Fe}_2\text{O}_3$ ) measured with the hhXRF was described optically as ‘pure magnetite’ by the chief geologist, Jouko Jylänki from Otanmäki Mine Oy.

Comparison between extracted ground magnetic measurements and iron absorption depths determined from the pixels of the drone-borne HSI dataset demonstrated a positive correlation.

In addition, the HSI band ratio from the UAS measurements (see Fig. 60) was compared with the calculated band ratios of the surface handheld spectra at the validation points. The same spectral band positions were used for the handheld data (760 nm / 898 nm) and regression revealed a positive correlation ( $r = 0.63$ ;  $p < 0.05$ ). See also Chapter 4.8 in Jackisch et al. (2019) for extended statistics.

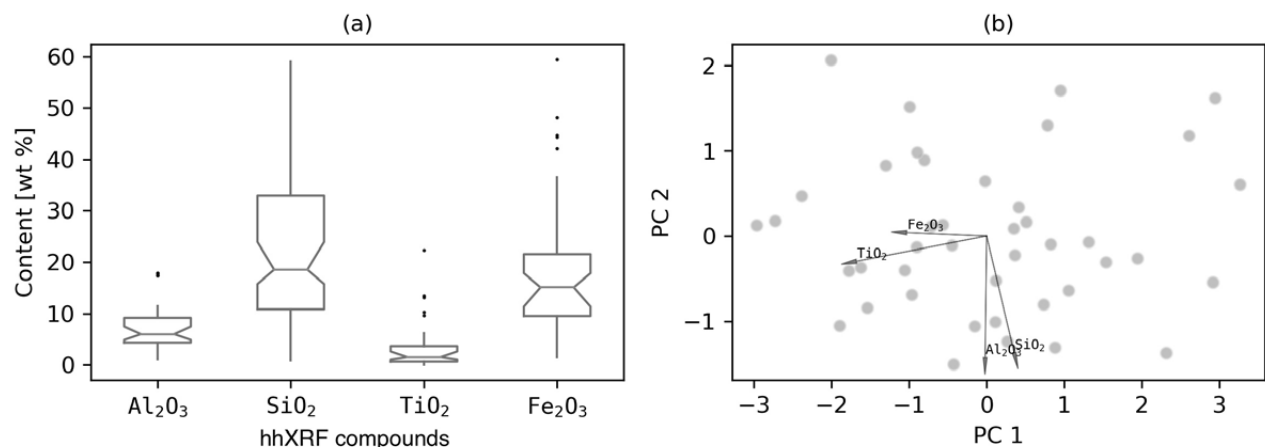


Fig. 70. a) Boxplot diagram showing the four most abundant elements measured with the handheld XRF ( $n = 48$ ); b) Biplot showing the first two principal components (Pawłowsky-Glahn & Buccianti 2011), with the PCA scores plotted as grey dots. After a transformation of four selected compounds (the rays show measured hhXRF compounds), which characterize the major elemental constituents of the outcrop (figure modified after Jackisch et al. 2019).

## 4.2 Data integration

The high resolution of the ground magnetic survey and the low altitude UAS magnetic survey (15 m above ground) allows for a rough comparison between the magnetic susceptibilities, ore zonation and the magnetic responses. Figure 71 displays five

selected surface profiles of susceptibility measurements from Otanmäki Mine Oy ( $n = 4524$ ), whose values range from 0 to 1 SI units. The anomalies in TMI of the ground magnetic, magnetic susceptibility values and the locations of ore zones coincide

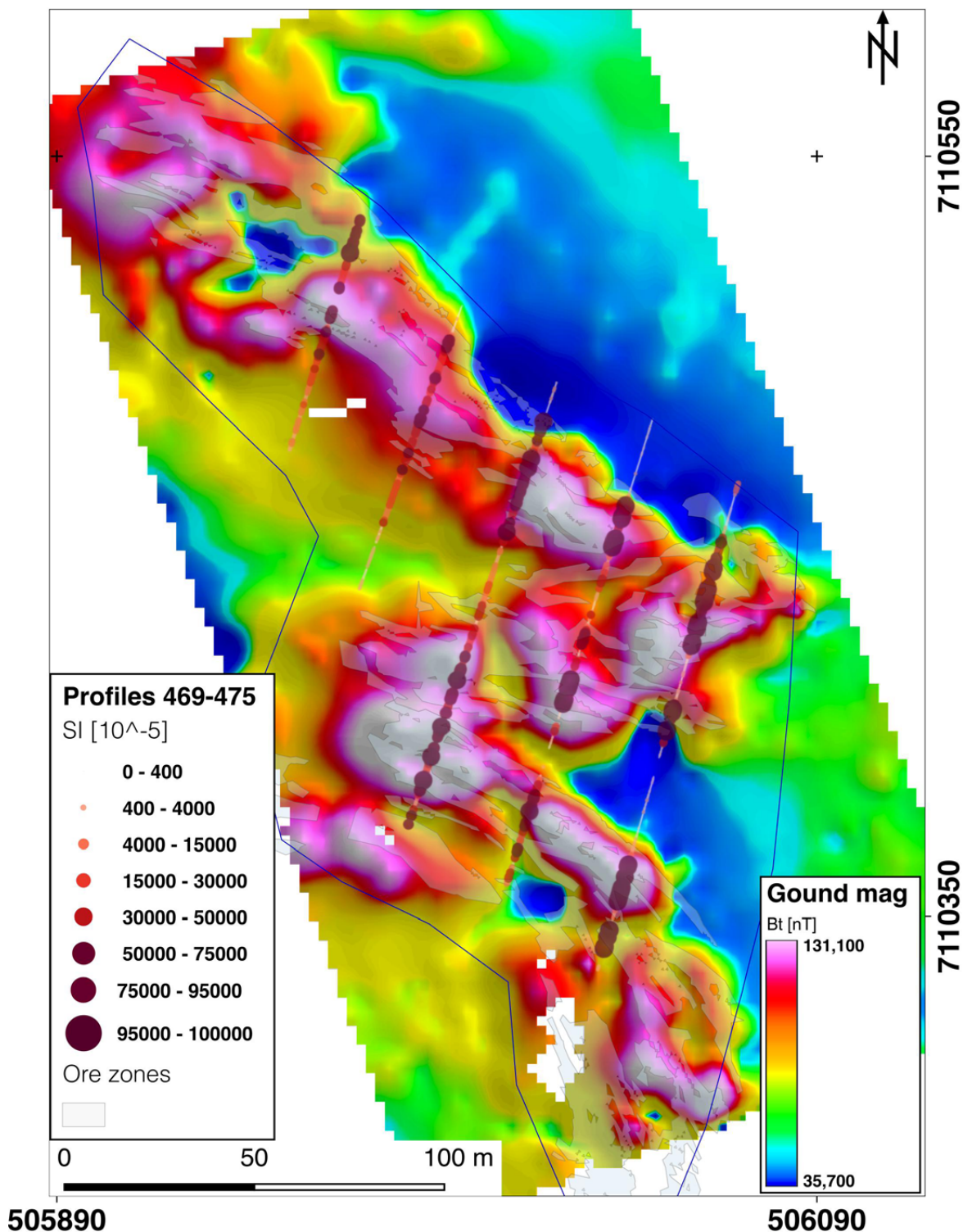


Fig. 71. Magnetic susceptibility measurements from Otanmäki Mine Oy are plotted onto the TMI from the ground magnetic survey.

well. In particular, high total magnetic intensity and susceptibility values are measured inside the high-grade ore zones.

The MagDrone magnetic data for the 15 m altitude flight are plotted in Figure 72 and show similar anomalies to those seen for the ground magnetic in Figure 71. Again, magnetic susceptibility

values from the scan line measurements generally correlated well with the TMI values from the Mag-Drone data.

To investigate how well magnetic and spectral characteristics coincide in detecting iron oxides, susceptibilities from a single susceptibility surface profile (profile 473; see Fig. 6) were compared

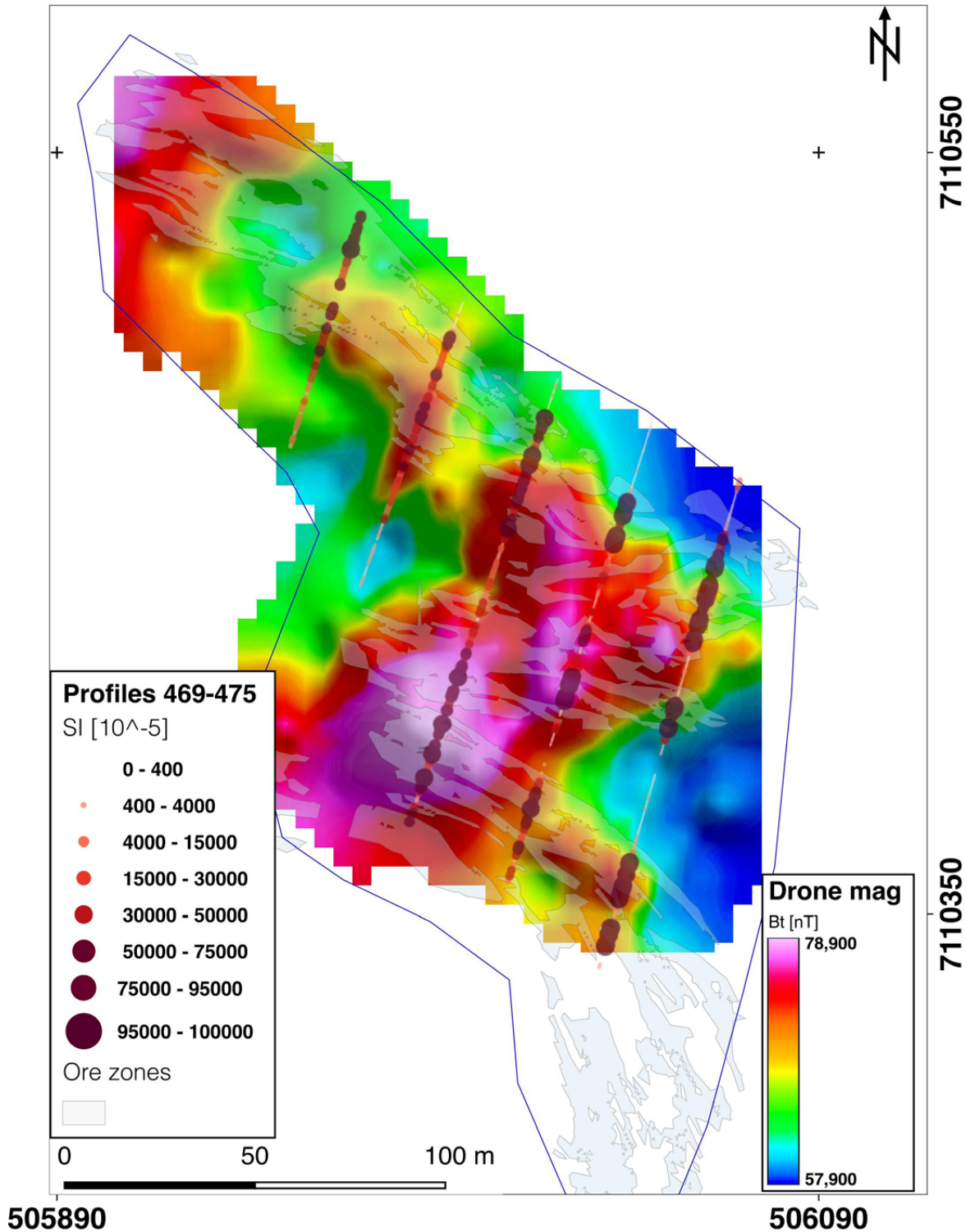


Fig. 72. Magnetic susceptibility measurements from Otanmäki Mine Oy are plotted onto the TMI from the multi-copter survey at a 15 m height. Mapped ore zones are outlined with blue lines.

with the band ratio values from the multispectral Sequoia survey, which indicate iron oxide mineral absorption (band 3/band 4). Figure 73 presents a map in which both the band ratio and the susceptibility measurements are plotted. Vegetation and lichen cover a significant part of the surface,

which impedes the capability to detect minerals on the surface. Therefore, only values with a high band ratio of  $>1.0$  are considered in the correlation of magnetic susceptibility and the band ratio to ensure that the impact of overburden is minor. The correlation is positive ( $r = 0.55$ ,  $p = 0.02$ ), but

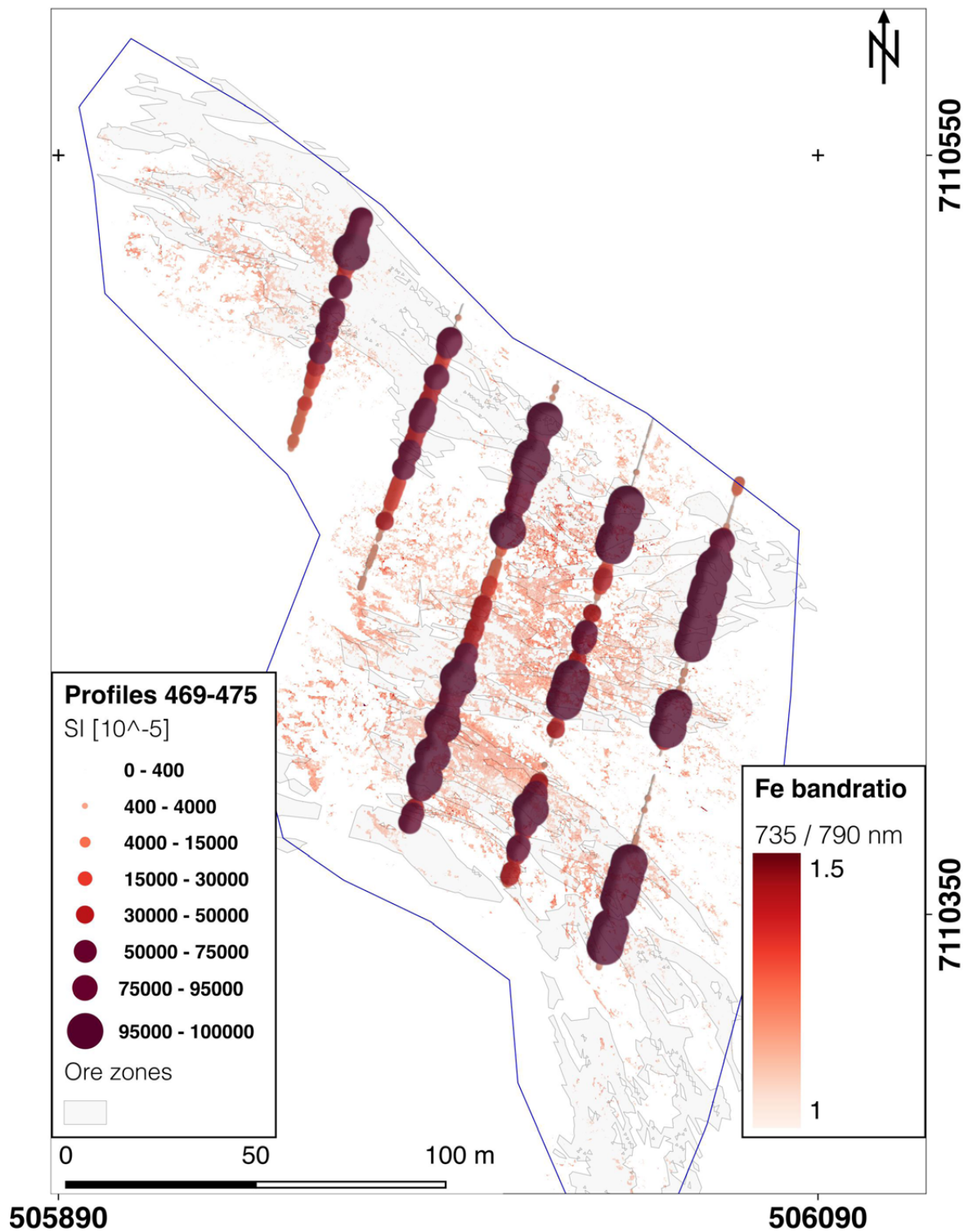


Fig. 73. Sequoia camera band ratio of Band 3 (735 nm) divided by Band 4 (790 nm), which indicates increased absorption from iron minerals. Magnetic susceptibility values of measurements from Otanmäki Mine Oy are plotted on top.

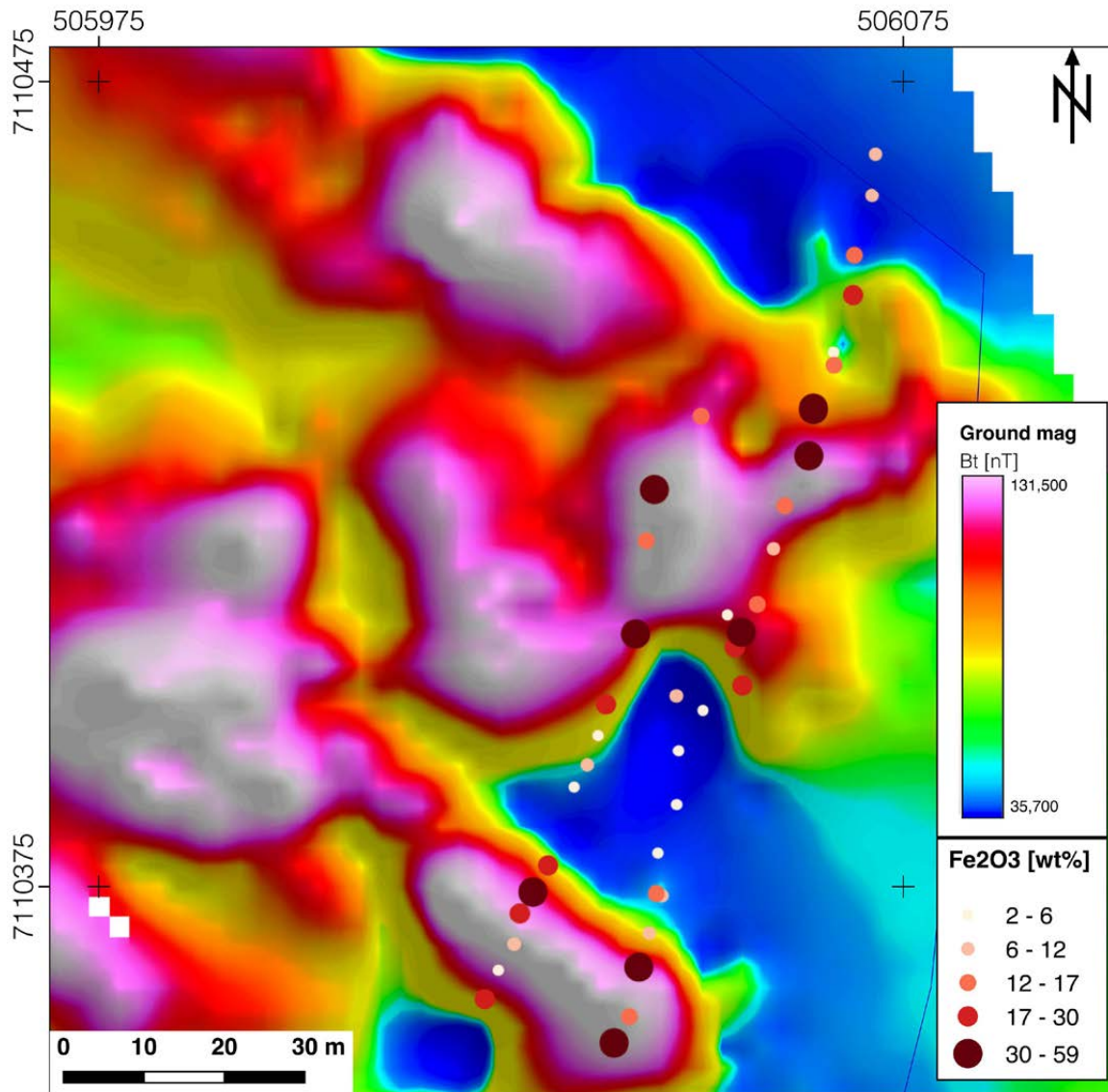


Fig. 74. Handheld XRF iron oxide readings are plotted together with the TMI from the ground magnetic survey from GTK.

not very strong. Reasons could include the different sampling sizes of the two measurements and the limited number of samples, a rather randomly scattered lichen coverage and, as the main factor, the fact that only alteration and weathering products can be spectrally detected, but not the iron ores (e.g. magnetite, ilmenite) themselves.

The iron oxide readings obtained using the handheld XRF are displayed in Figure 74. High handheld XRF values were solely measured in are-

as having a high total magnetic intensity. This indicates the expected strong link between the iron content (high grade ore) along the surface and the magnetic anomalies.

The magnetic susceptibility measurements (Fig. 75) conducted during the MULSEDRO field work were not as dense as those conducted by the mining company. As such, the interpretation of these readings is uncertain and the results are not discussed any further.

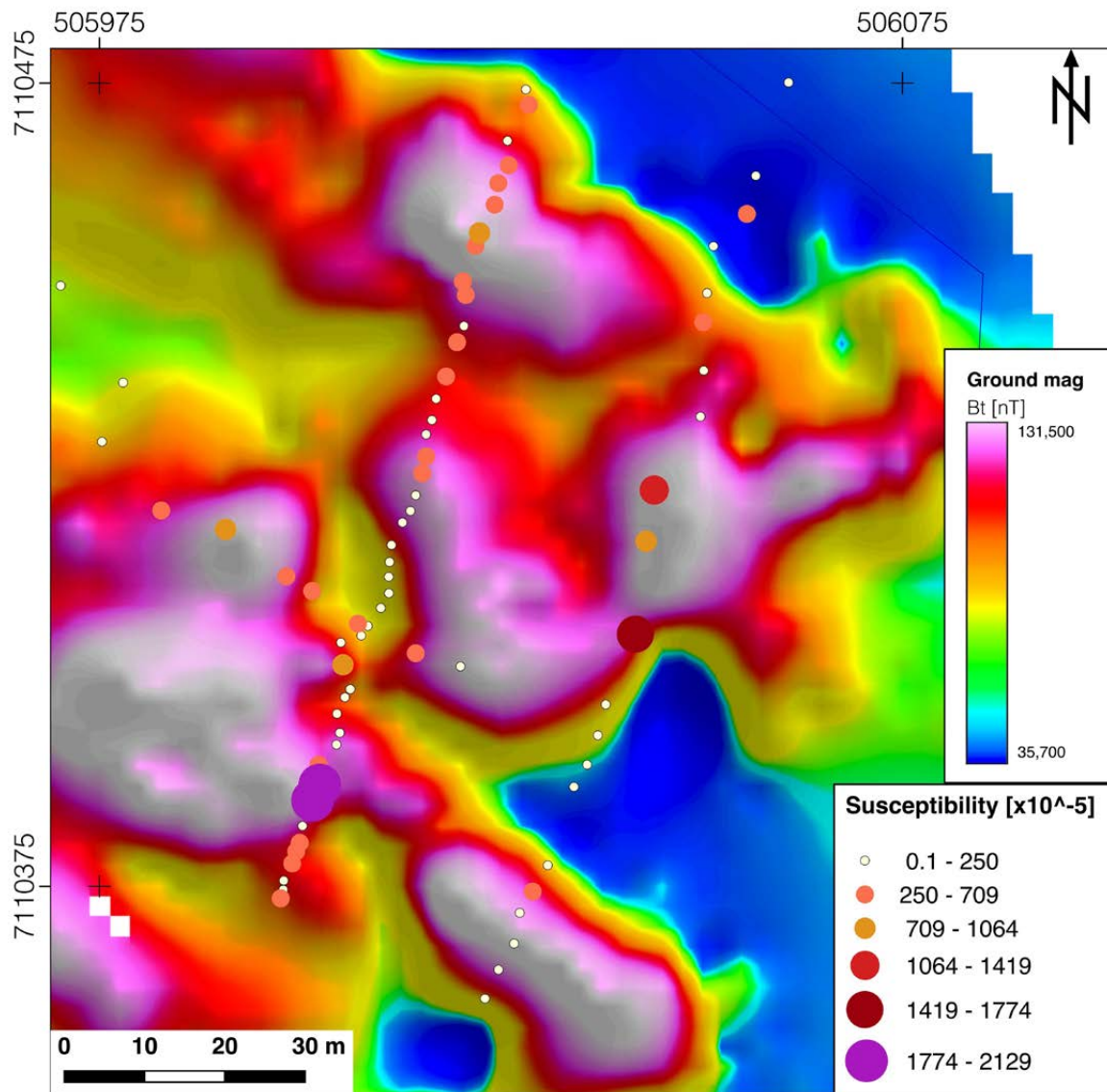


Fig. 75. Handheld susceptibility measurements are plotted together with the TMI from the ground magnetic survey from GTK.

## 5 INTEGRATION OF ALL MAGNETIC DATASETS BY MEANS OF EQUIVALENT LAYER MODELLING

Equivalent layer modelling (ELM) in RadaiPros was used to combine various individual magnetic datasets measured in the Otanmäki survey area and to create one total magnetic intensity map that is consistent with all magnetic data measured across the Metsämalmi outcrop area. This was a particular challenge because the data were gathered from different heights and had very different measuring densities, particularly in terms of line spacing, but also in the inline sampling. We applied here a first test with an advanced approach by combining all the data by means of ELM and calculating the common data response for specific height levels. The data included a) Radai's magnetic UAS survey data (with an RT logger), b) GTK's regional airborne data (measured in 1979), c) GTK's ground magnetic data, d) Helmholtz Institute of Freiberg (HIF) UAS data measured at 15 m above ground level and e) HIF UAS data measured at 40 m above the ground.

The ELM inversion was applied for the whole area of Radai's UAS-based magnetic survey. The results, however, are only presented for the area of the Metsämalmi outcrop, where GTK's ground data were recorded. The 40 x 40 m magnetic susceptibility model obtained from the ELM of Radai's UAS magnetic data was used as a starting point by applying it as a starting model in the inversions presented here. To better model GTK ground magnetic data, the depth to the top of the model was reduced from 5 m to 2 m below the surface and the thickness of the model cells was reduced from 55 m to 40 m. The ELM inversion was then applied such that the model was gradually made denser by increasing the discretization first to cell sizes of 20 x 20 m, then 10 x 10 m, and finally 5 x 5 m. As such, the final model consisted of 272 x 320 = 87 040 elements. The total number of magnetic data points (after data reduction and low-pass filtering) was 20 824. Because neither particularly adapted weighting nor regularization was imposed

on different datasets, the inversion emphasizes the relative importance of ground magnetic data due to its high sensitivity, which limits the approach to fit all datasets equally well. Nonetheless, the inversion provides a convenient means to create a more detailed and consistent view of the magnetic anomaly of the Metsämalmi target area. In the future, we intend to further investigate how to adjust data weighting, regularization and gridding to obtain optimal results that fit all datasets equally.

The fits between different measured and computed datasets are presented in Figures 76–80. GTK's regional airborne data are superimposed on Radai's data in Figure 76. Although the amplitudes of the differences between measured and computed data (Fig. 80) are quite large (several thousands of nanoteslas), the fits are fairly good because the total amplitude of the anomaly is very high (several tens of thousands of nanoteslas).

The magnetic susceptibility model obtained from the combined ELM inversion of the five different datasets was then used to compute the magnetic field and its first vertical derivative on an even grid of 5 m x 5 m at a constant altitude of 5 and 35 meters. The results are displayed in Figures 81–84. Because the focus is on the area where GTK's ground data were measured, the results computed for 5 m altitude depict a very detailed magnetic image of the Metsämalmi target area. Comparison between the results computed at altitudes of 5 m and 35 m reveals an enormous increase in the number of details at the lower altitude. Comparison with the results from Radai's UAS-based magnetic data (Figs. 22 and 24) shows little improvement at the altitude of 35 m, but a considerable increase in detail at the altitude of 5 m. The low measurement height and dense line spacing are the two factors that most affect the resolution of magnetic data.

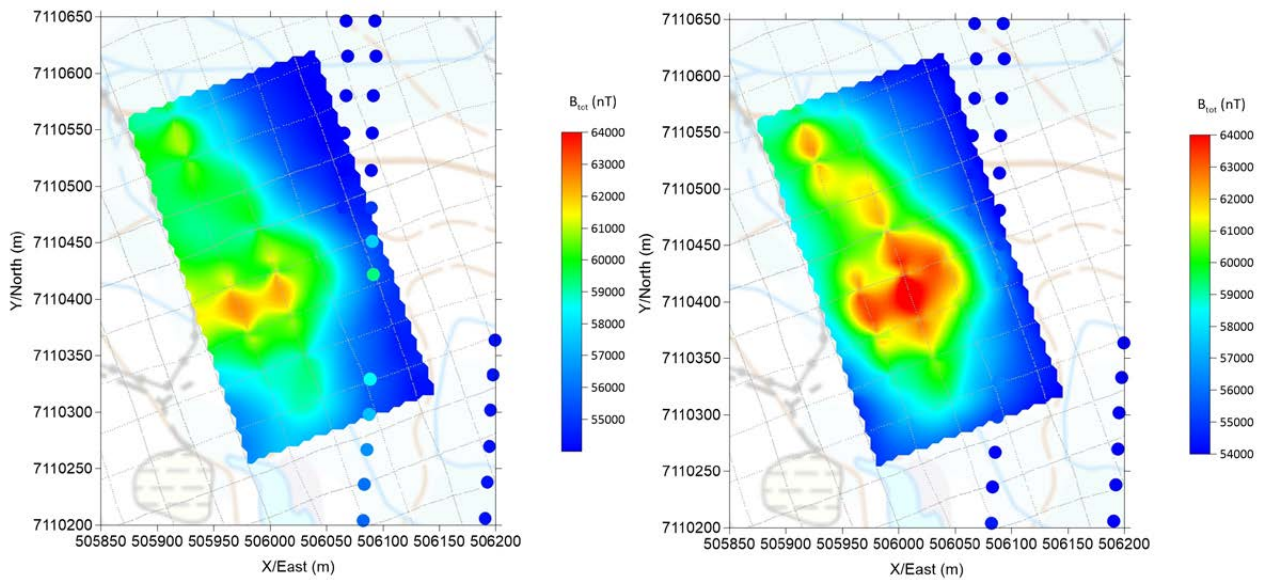


Fig. 76. Total magnetic field measured during Radai's fixed wing survey (left) and computed (right) by ELM. The lines of grey dots depict the location of the data profiles of Radai's survey. The coloured dots represent (measured and computed) GTK's regional airborne data.

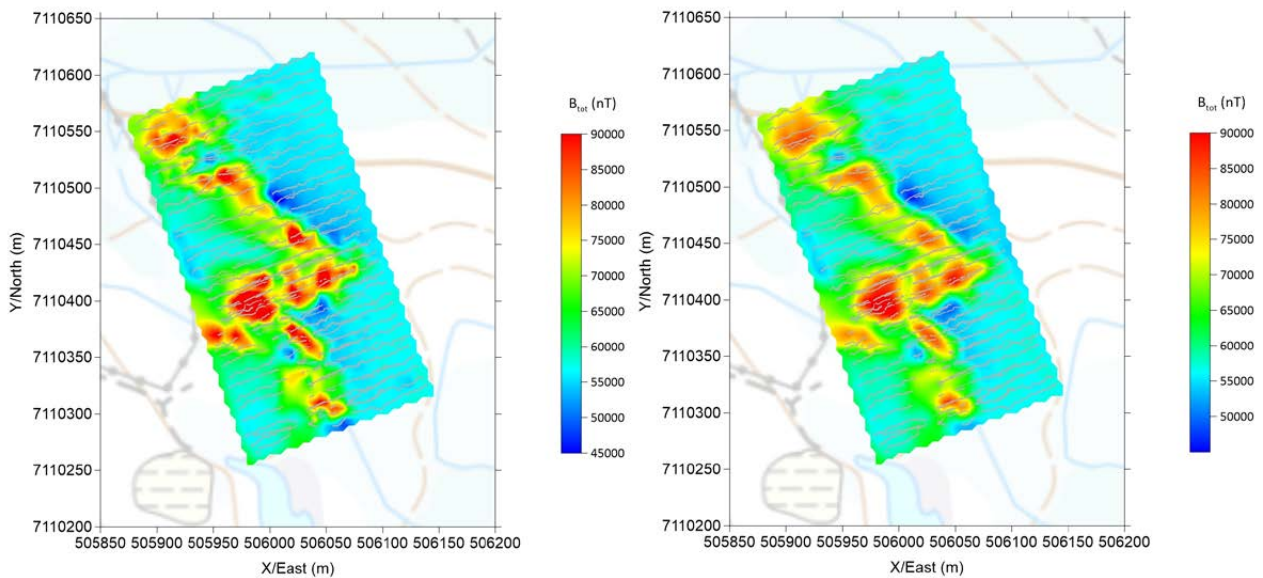


Fig. 77. Total magnetic field measured by GTK at ground level (left) and computed (right) by ELM. The lines of grey dots depict the location of the data profiles of GTK's ground magnetic survey.

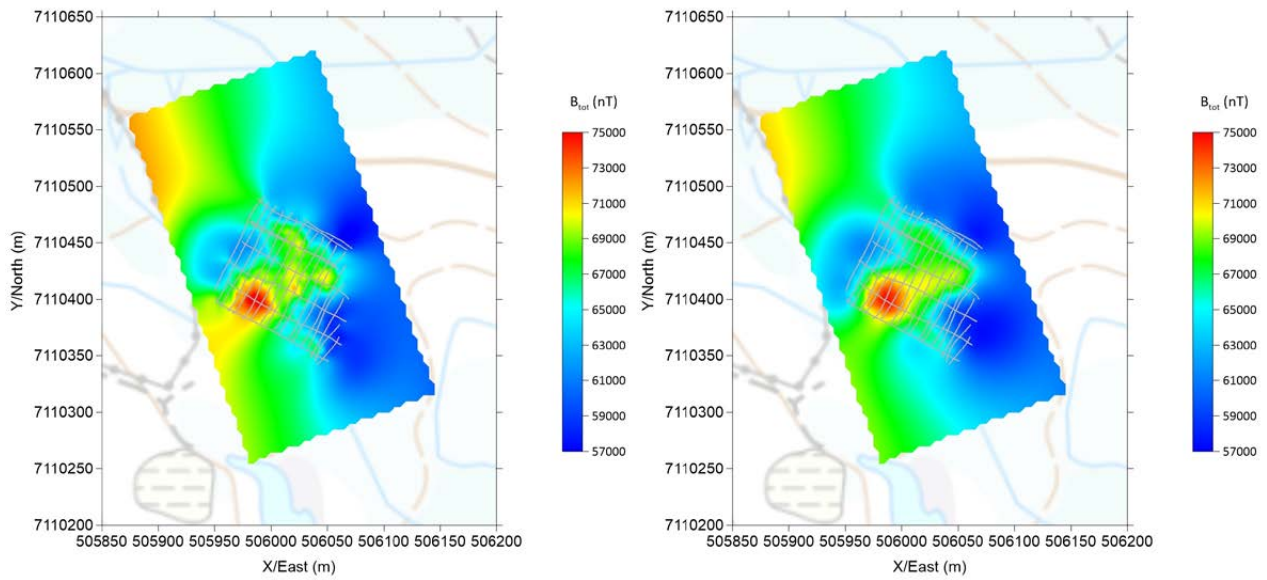


Fig. 78. Total magnetic field measured during HIF's multi-copter survey at 15 m altitude (left) and computed (right) by ELM. The lines of grey dots depict the location of the data of this survey.

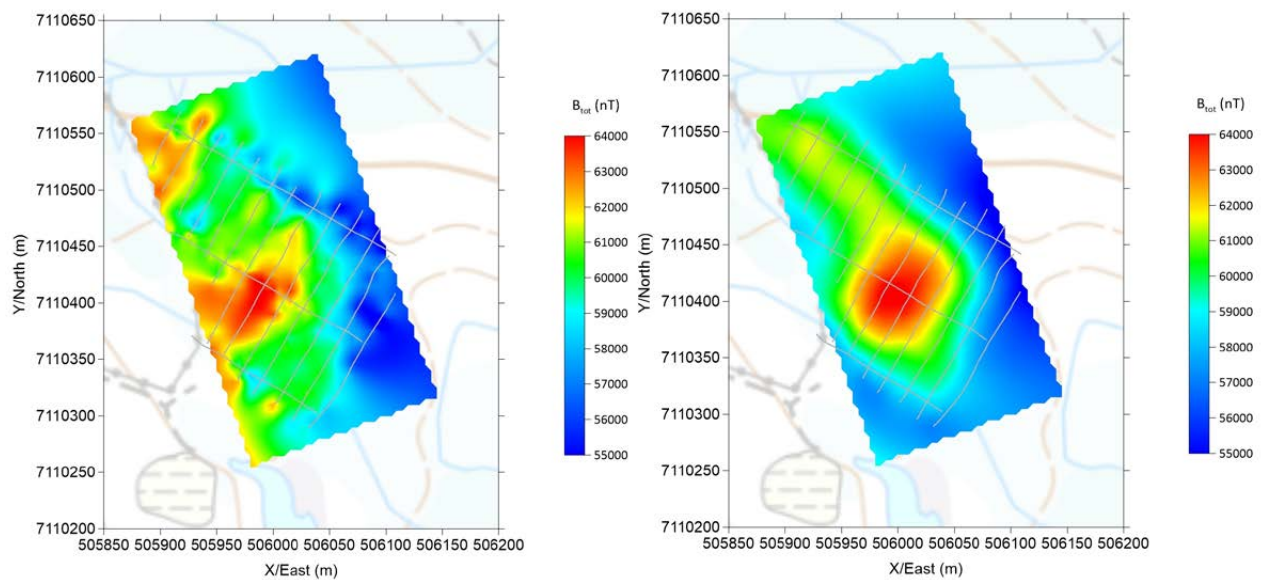


Fig. 79. Total magnetic field measured during HIF's multi-copter survey at 40 m altitude (left) and computed (right) by ELM. The lines of grey dots depict the location of the data of this survey.

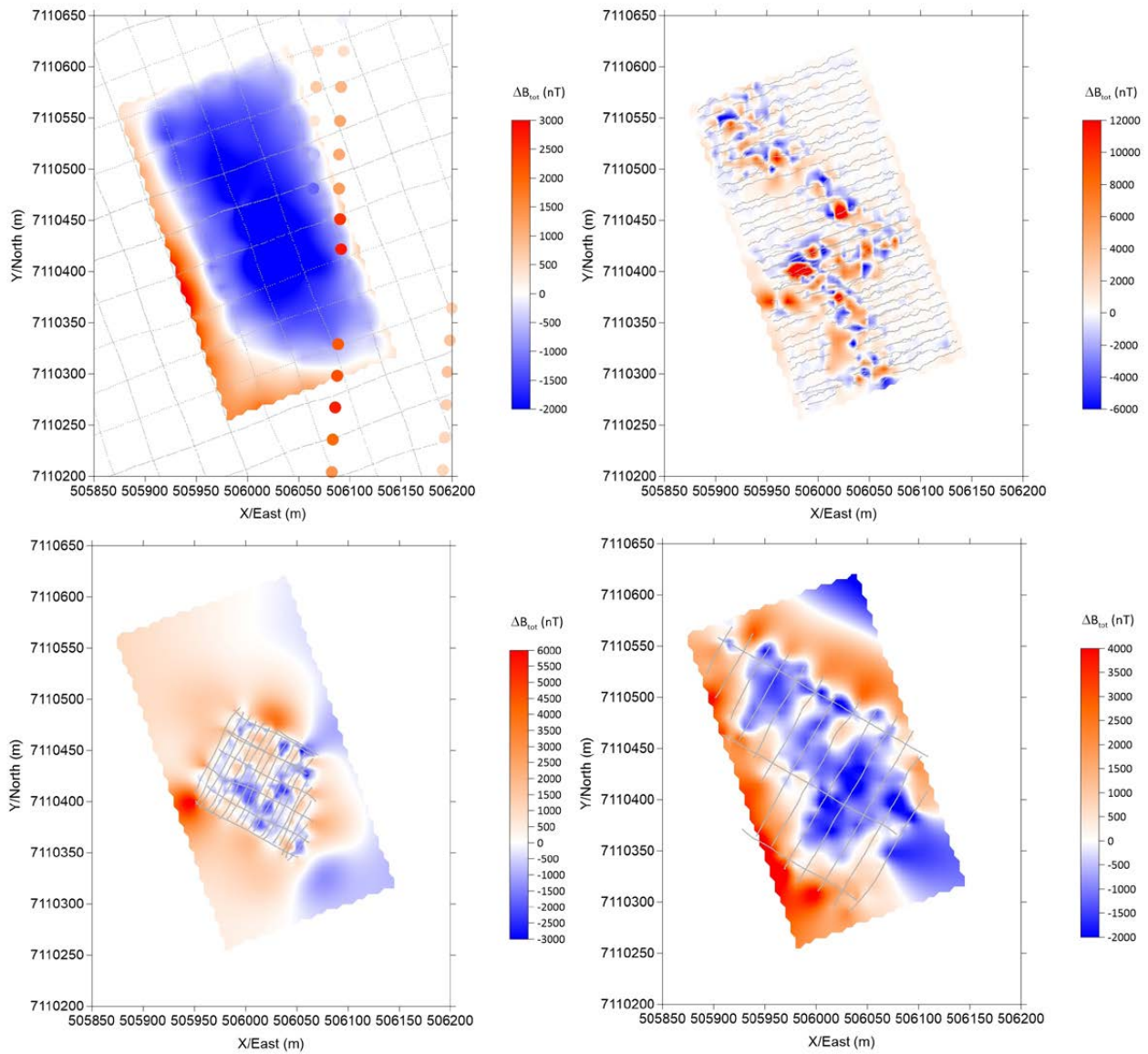


Fig. 80. Difference between measured data and data computed with ELM for Radai's fixed wing and GTK's regional airborne data (top left), for GTK's ground-based data (top right), for HIF's multi-copter data at a 15 m altitude level (bottom left) and for HIF's multi-copter data at a 40 m altitude level (bottom right). The lines of grey dots depict the data location of the corresponding dataset.

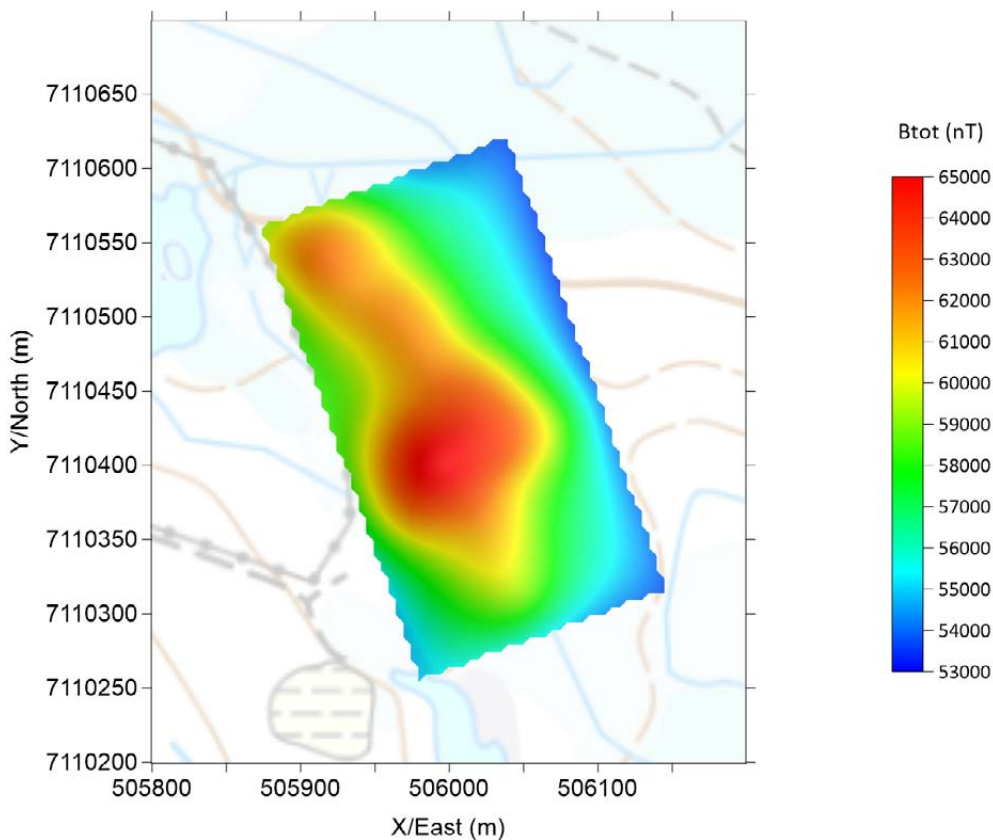


Fig. 81. Magnetic total field (with sun shading) obtained from the combined inversion of Radai's, GTK's and HIF's magnetic data and computed using ELM at the constant height of 35 m on an even grid.

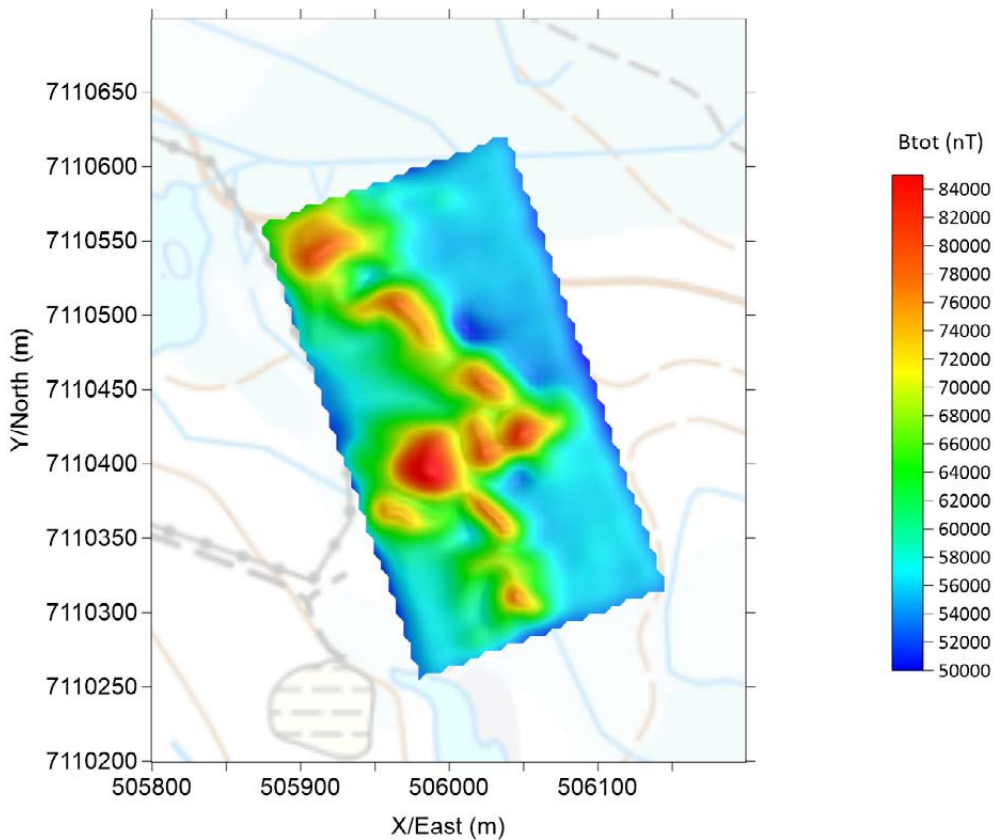


Fig. 82. Magnetic total field (with sun shading) obtained from the combined inversion of Radai's, GTK's and HIF's magnetic data and computed using ELM at the constant height of 5 m on an even grid.

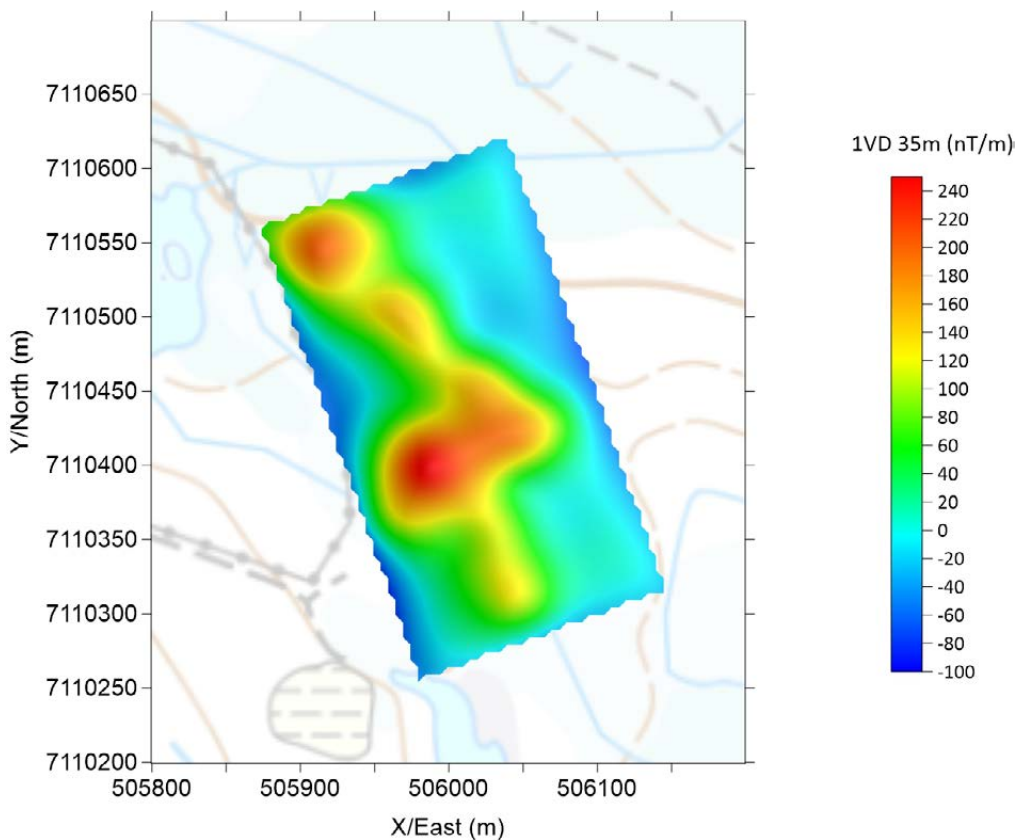


Fig. 83. First vertical derivative of the magnetic total field (with sun shading) computed using ELM on an even grid at the constant height of 35 m.

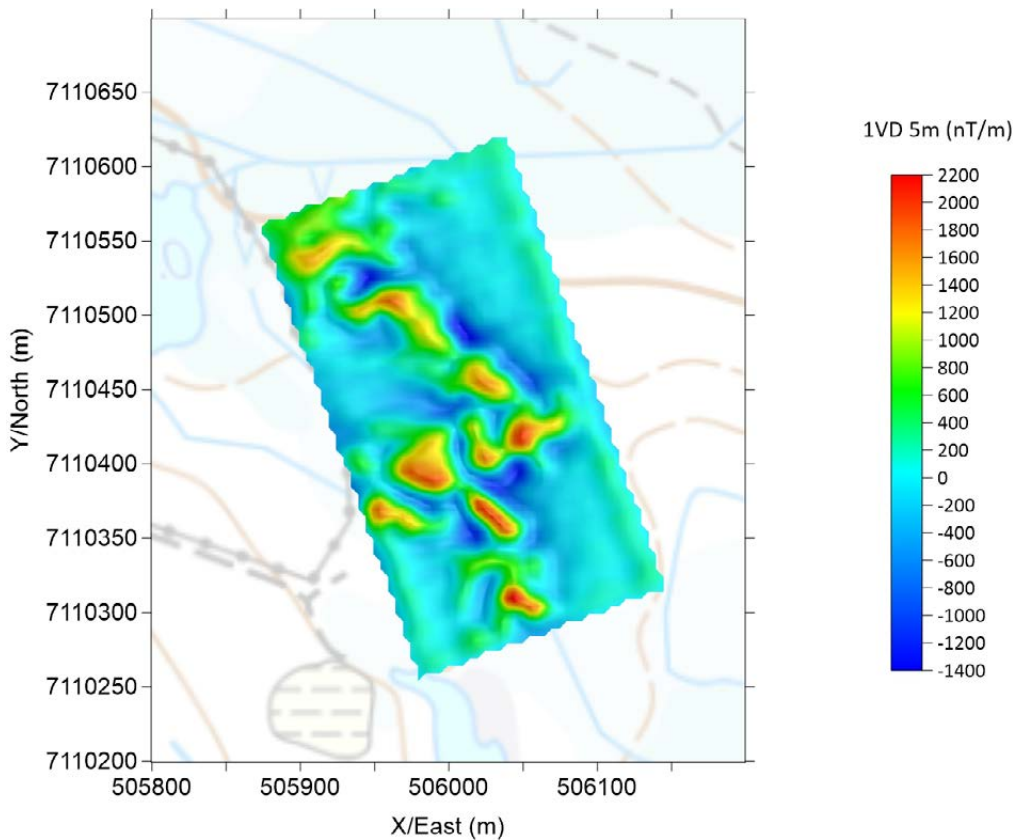


Fig. 84. First vertical derivative of the magnetic total field (with sun shading) computed using ELM on an even grid at the constant height of 5 m.

## 6 CONCLUSION AND OUTLOOK

### 6.1 Closing remarks

In general, the results from the Metsämalmi site are promising and demonstrate that the integrated UAS systems developed within the MULSEDRO project are able to collect data of good quality and relevance to better map the ore zone and evaluate ore grades. The technical readiness level is already high, such that surveys could be performed on a regular basis. The quality of individual datasets is dependent on the adaption of each sensor to its carrier. The experiences of the different partners over the years are important in this respect. For example,

Radai has been able to gather good quality magnetic data for a quite long time, but the results were further improved by increasing the data logger's sampling rate from 10 to 50 Hz and hence more efficiently reducing the noise of their fixed-wing-based magnetic system. Although the HZDR-HIF MagDrone magnetometer system was tested prior to the Otanmäki field test, it had not been tested under survey conditions. Consequently, this survey was of particular importance to evaluate the performance of this newly integrated magnetic UAS setup.

Table 7. Survey area and time duration of magnetic measurements for each of the methods.

Method	Area	Time
Radai Albatros VT3	1 140 000 m <sup>2</sup> (40 m a.g.l.)	1 h
HZDR-HIF MagDrone R1	72 000 m <sup>2</sup> (65 m a.g.l.)	20 min
GTK ground survey	50 000 m <sup>2</sup> (1.7 m a.g.l.)	3 days
Visible outcrop surface	28 000 m <sup>2</sup>	–

A major advantage of UAS mapping compared to ground surveying is a reduction in the time spent on data acquisition (Table 7). The GTK ground survey took three working days in the field to cover an area of ~52 000 m<sup>2</sup>. A similar area was covered using two UAS flights in 45 minutes (which is 20 times faster, excluding data processing times). Moreover, the TMI map resulting from the integrated low-altitude UAS shows almost the same level of detail as that of the ground-based survey. In total, only two to three days of fieldwork were required to achieve complete coverage of the Metsämalmi outcrop with all available sensor types that can currently be mounted on our drones.

#### Magnetic UAS investigations

Because the area was covered with four magnetic UAS surveys at different altitudes (15, 40 and 65 m a.g.l.) and/or line spacings, we obtained magnetic information with very different scales of resolution that allowed us to consider both deeper more regional features and high-resolution near-surface features at the same time. All magnetic data were corrected for diurnal variations by using base station data, while magnetic data from the multi-

copter were, moreover, calibrated for the heading and orientation effects of the UAS. For heading correction, it is important to note that the Metsämalmi outcrop had very high geomagnetic anomalies such that the calibration flights from the MagDrone for the heading corrections were still affected by the anomaly from the ground, although the flight height was rather high. UAS flight regulations in Finland restrict the flying height to an altitude of 150 m, and larger magnetic anomalies are therefore likely to be present in the calibration flight data. In traditional airborne magnetic surveys, greater flight heights and ranges allow for inflight instrument calibration away from the magnetic anomalous areas. An outcome of the MagDrone tests is that it is relevant to further investigate different calibration procedures.

For the fixed-wing surveys, no calibration figures were flown for the heading correction, but all systematic noise and artefacts (including that from the heading direction) were instead reduced by using equivalent layer modelling during processing. Experiences from several field campaigns, including the one from Otanmäki, demonstrate that this

procedure is adequate at least for the fixed-wing plane.

For the multi-copter, the impact of engine noise on the magnetic signal quality was considered as a critical issue (due to the short distances between the engines and the magnetometer). However, it was possible to clearly reduce this noise by using frequency-based filtering during data processing. The engine noise of the Tholog octocopter is assumed to be of high frequency in the range from 0.1–2 kHz, depending on the rotation of the rotors (up to 16 000 rotations per minute). The Mag-Drone data are sampled with 200 Hz, which is still below the engine rotations per minute, and the whole spectral range of the noise frequencies cannot therefore not be covered. Hence, aliasing effects may be created and noise introduced into the measured frequency range during the sampling process. The application of a frequency low-pass filter with a cut-off frequency at 10 Hz to remove high frequencies from the spectrum is conservative enough that it is unlikely that geological information will have been removed from the geomagnetic field data, even for the lowest flight height of 15 m a.g.l. (or even less), due to the moderate flight speed of 5 m/s.

The fixed wing has fewer engines and servos and the magnetometer is located in the tail, rather distanced from all electric components, such that electric noise is a minor problem for this type of drone.

With the fixed wing, the survey area was flown two times, recording the magnetic data one time with the older data logger and the other time with the recently developed new data logger. Because of the higher sampling frequency of 50 Hz with the new data logger (compared to 10 Hz), the possibilities for noise filtering were improved, resulting in a higher signal-to-noise level for the final processed data.

Different processing schemes were applied for the magnetic datasets from the multi-copter and the fixed wing. The main difference is that equivalent layer modelling (ELM) was applied to the fixed-wing dataset for levelling and to remove both stochastic and systematic noise from the data. This procedure results in very good quality images with almost no levelling artefacts, although some high-frequency content related to geological features may be removed by the ELM process. For the multi-copter datasets, a more traditional processing workflow of filtering and tie-line levelling re-

sulted in good quality data. However, the presence of some minor levelling artefacts in the 1<sup>st</sup> derivative suggests that fine-tuning of the scheme is required.

In an experiment, all available magnetic datasets from Metsämalmi (not only from the drones, but also ground-based and regional helicopter-borne data) having very different resolutions (due to different height levels and line spacings) were combined in ELM in order to obtain one consistent total magnetic intensity image. The results demonstrate that ELM has the potential to generate such common images, which are consistent with all considered datasets, but additional work is required to better resolve some of the more specific problems, such as finding a proper weighting between the different datasets during the inversion procedure.

### **Hyper- and multispectral UAS investigations**

Hyperspectral and multispectral data were acquired at a high resolution, processed with an in-house developed toolbox and geolocated with precisely spatially surveyed GCPs. Topographic effects were removed and hyperspectral data were co-aligned with a high-resolution orthomosaic. The lichen and vegetation coverage visible in the surface maps unfortunately reduced the total number of visible bare ground pixels. Roughly 30% of the whole scene of the multispectral data had to be masked due to vegetation. Different band ratios and classification algorithms are used to delineate iron-bearing phases on the surface. Their application to the non-masked areas indicated that iron-bearing alteration minerals such as hematite and goethite could be adequately mapped from the UAS-based data. Supporting ground spectroscopic measurements of rock surfaces validated the UAS-based results. Depending on the depth and location of the Fe<sup>+2</sup>/Fe<sup>+3</sup> charge transfer absorption, the spatial distribution of these iron minerals could be properly mapped along the surface of the Metsämalmi test site.

### **Data integration**

Validation of the UAS results was achieved by applying standard field methods such as geological mapping, ground spectroscopy, hhXRF and susceptibility measurements in the exposed areas and by comparing UAS-based results with ground mapping-based parameters. An important outcome was that significant correlations for iron ore diagnostic

parameters exist between ground-based measurements and the UAS surveys. This applies even for a direct comparison of magnetic and spectral properties. One example is the positive correlation of surficial susceptibility measurements and UAS iron index measurements ( $r = 0.80$ ). This indicates that both spectral characteristics and magnetic properties are rather linearly linked with ore properties and particularly the ore grade in this area. However, for more reliable interpretations, more observations/sampling points are needed. Outliers were observed that could not be fully explained. One obvious explanation for the outliers is the very heterogeneous character of the ore deposit with large changes in the ore grade over short distances in combination with the limited spatial resolution of multi-/hyperspectral data and particularly magnetic data (collected at significant distances from the ground for the UAS surveys). Another reason is that the multi-/hyperspectral sensors used are only sensitive to proxy minerals (alteration minerals), but not directly to the ore-bearing minerals (magnetite and ilmenite) themselves, such that a

clear correlation between the abundances of the two groups would increase the correlation.

In summary, the developed non-invasive mineral exploration approach based on the integration of remote sensing and geophysical techniques was successful for the field campaign at the Metsämalmi test site. It persuasively demonstrated that UAS-borne surveys can complement (or even compete with) ground surveying, while requiring just a relatively small initial investment (to purchase drones and equipment, train pilots and adjust software and hardware to suit UAS applications). The general advantages of a flexible, rapid and easily deployable UAS to provide high-resolution data within a short time could be fully confirmed during this test. Moreover, the combination of lightweight UAS technology with multispectral, hyperspectral, RGB cameras and fluxgate magnetometers provides important complementary geoscience datasets for the selected Fe ore target and, hence, results in an excellent basis for integrated data analysis.

## 6.2 Outlook

The field test demonstrated that a number of adjustments and modifications are required to further improve the quality and reliability of drone-borne magnetic measurements. Particularly relevant for multi-copters is the application of electromagnetic shielding to limit the impact of electromagnetic noise emitted from wires, servos and engines (Windsor et al. 2011) on the magnetic measurements. A possible solution would be to use MU-metal or a Faraday cage construction around the drone's electrical parts. However, this would mean an increase in the payload and therefore a reduced operation time, which could be partly compensated by more efficient battery technology. In addition, the influence of any type of highly magnetic permeable material (MU-metal is usually a copper-nickel-iron alloy) needs to be investigated, as it is a potential new source of induced magnetization that has to be considered in the corrections. Alternatively, the magnetometer could be placed further away from the electromotors by modifying its mounting frame.

There are current activities in the MULSEDRO project to implement a multispectral frame camera with 16 bands in the visible and near-infrared spectra on the fixed-wing from Radai. Integra-

tion of the camera in the fuselage and hardware and software implementations have been finalized and a first test has already been flown (September 2019) across another test site in Finland. The quality of the processed images from this survey appears very promising and we are optimistic that surveys with this camera could be performed soon in a standard procedure. An interesting feature of this new camera is that the frame rate is so high that it allows a high-resolution DEM to be created as a by-product.

The used multi- and hyperspectral systems as well as the fixed-wing magnetic system are already on a high technical readiness level, so surveys could be performed on a regular basis and the results are of good quality. However, further improvement by deploying different lightweight spectral sensors is advised. Unfortunately, there is still a lack of lightweight, cheap and robust hyperspectral sensors on the market that can also measure the short-wave infrared part of the electromagnetic spectrum. Such SWIR hyperspectral cameras and scanners are nowadays already in use from the ground and in airplanes and satellites. However, these instruments types are too heavy, fragile and expensive to attach to small drones. We

will therefore investigate the market for sensor types that have the potential to add SWIR information for such drone surveys in the near future.

An advanced 3D inversion of all magnetic data from the Metsämalmi area could be very interesting for future exploration models, because this would also help to determine the ore distribution with depth. Such an approach could be attractive for Otanmäki, because additional information from drill holes located inside the survey area or laboratory measurements including tri-axial susceptibility determination of the remanent magnetization could be used as constraining information

in an inversion. Accordingly, magnetic inversion results should be well resolved and should yield reliable models due to the large amount of both magnetic data and constraining information.

To generate one common magnetic map from various datasets with very different survey parameters using ELM can be a very interesting approach for many applications (e.g. to build a large-scale magnetic compilation from many individual datasets). Therefore, it makes sense to further develop the ELM technique such that it can be used more flexibly in future.

## ACKNOWLEDGEMENTS

This work was financed by the European Institute of Innovation & Technology's RawMaterials community (EIT RawMaterials) through the Mulsedro project. Authors are grateful to all participants of the Otanmäki field campaign in the autumn of 2018; Ari Saartenoja and Timo Åman from Radai Oy, Sara Salehi from GEUS, Benjamin Melzer from HZDR-HIF and Sönke Rapp from DMT GmbH. Jukka-Pekka Kujasalo and Arto Illikainen from GTK are acknowl-

edged for the ground magnetic measurements made at Metsämalmi area before and during the field campaign.

We would like to thank Päivi Kuikka-Niemi for help in the publication process and Viena Arvola for designing the cover pages of the report. Roy Siddall is acknowledged for careful language checking. The excellent layout of the report was provided by Elvi Turtiainen Oy.

## REFERENCES

- Bakker, W. H., van Ruitenbeek, F. J. A., van der Werff, H. M. A., Zegers, T. E., Oosthoek, J. H. P., Marsh, S. H. & van der Meer, F. D. 2014. Processing OMEGA/Mars Express hyperspectral imagery from radiance-at-sensor to surface reflectance. *Planetary and Space Science* 90, 1–9.
- Carrivick, J. L., Smith, M. W. & Quincey, D. J. 2016. *Structure from Motion in the Geosciences*. Hoboken, NJ, USA: Wiley-Blackwell. 197 p.
- Clark, R. N., Swayze, G. A., Wise, R., Livo, E., Hoefen, T., Kokaly, R. & Sutley, S. J. 2007. *USGS Digital Spectral Library Splib06a*. Reston, VA, USA: U.S. Geological Survey.
- Constable, S. C., Parker, R. L. & Constable, C. G. 1987. Occam's inversion. A practical algorithm for generating smooth models from electromagnetic sounding data. *Geophysics* 52, 289–300.
- Crowley, J. K., Williams, D. E., Hammarstrom, J. M., Piatak, N., Chou, I.-M. & Mars, J. C. 2003. Spectral Reflectance Properties (0.4–2.5 μm) of Secondary Fe-Oxide, Fe-Hydroxide, and Fe-Sulphate-Hydrate Minerals Associated with Sulphide-Bearing Mine Wastes. *Geochem. Explor. Environ. Anal.* 3, 219–228.
- Dering, G. M., Micklethwaite, S., Thiele, S. T., Vollgger, S. A. & Cruden, A. R. 2019. Review of drones, photogrammetry and emerging sensor technology for the study of dykes: Best practises and future potential. *J. Volcanol. Geotherm. Res.* 373, 148–166.
- Grebby, S., Cunningham, D., Tansey, K. & Naden, J. 2014. The impact of vegetation on lithological mapping using airborne multispectral data: a case study for the north Troodos Region, Cyprus. *Remote Sensing*, 6(11), 10860–10887.
- Green, A. A., Berman, M., Switzer, P. & Craig, M. D. 1988. A transformation for ordering multispectral data in terms of image quality with implications for noise removal. *IEEE Transactions on Geoscience and Remote Sensing* 26, 65–74.
- Harris, F. J. 1978. On the use of windows for harmonic analysis with the discrete Fourier transform, in *Proceedings of the IEEE* 66, 1, 51–83.
- Heincke, B., Jackisch, R., Saartenoja, A., Salmirinne, H., Rapp, S., Zimmermann, R., Pirttijärvi, M., Sørensen, E. V., Gloaguen, R., Ek, L., Bergström, J., Karinen, A., Salehi, S., Madriz, Y. & Middleton, M. 2019. Developing multi-sensor drones for geological mapping and mineral exploration: setup and first results from the MULEDRO project. *Geological Survey of Denmark and Greenland Bulletin* 43, e2019430302. Available at: <https://doi.org/10.34194/GEUSB-201943-03-02>
- Hokka, J. & Lepistö, S. 2018. JORC mineral resource estimate for Otanmäki V-Ti-Fe project, Finland. Geological Survey of Finland, archive report. (in preparation)
- Huhma, H., Hanski, E., Kontinen, A., Vuollo, J., Mänttari, I. & Lahaye, Y. 2018. Sm-Nd and U-Pb isotope geochemistry of the Palaeoproterozoic mafic magmatism

- in eastern and northern Finland. Geological Survey of Finland, Bulletin 405. 150 p. Available at: [http://tupa.gtk.fi/julkaisu/bulletin/bt\\_405.pdf](http://tupa.gtk.fi/julkaisu/bulletin/bt_405.pdf)
- Hunt, G. R. & Ashley, R. P. 1979.** Spectra of Altered Rocks in the Visible and near Infrared. *Econ. Geol.* 74, 1613–1629.
- Illi, J., Lindholm, O., Levanto, U.-M., Nikula, J., Pöyliö, E. & Vuoristo, E. 1985.** Otanmäen kaivos. Vuoriteollisuus / Bergshanteringen n:o 2, 98–107. (in Finnish with English summary)
- Jackisch, R., Lorenz, S., Zimmermann, R., Möckel, R. & Gloaguen, R. 2018.** Drone-Borne Hyperspectral Monitoring of Acid Mine Drainage: An Example from the Sokolov Lignite District. *Remote Sens.* 10, p. 385.
- Jackisch, R., Madriz, Y., Zimmermann, R., Pirttijärvi, M., Saartenoja, A., Heincke, B., Salmirinne, H., Kujasalo, J.-P., Andreani, L. & Gloaguen, R. 2019.** Drone-Borne Hyperspectral and Magnetic Data Integration: Otanmäki Fe–Ti–V Deposit in Finland. *Remote Sensing* 11(18), p. 2084. Available at: <https://doi.org/10.3390/rs11182084>
- Jakob, S., Zimmermann, R. & Gloaguen, R. 2017.** The Need for Accurate Geometric and Radiometric Corrections of Drone-Borne Hyperspectral Data for Mineral Exploration: MEPHYSTo–A Toolbox for Pre-Processing Drone-Borne Hyperspectral Data. *Remote Sens.* 9, p. 88.
- James, M. R., Robson, S., d'Oleire-Oltmanns, S. & Niethammer, U. 2017a.** Optimising UAV topographic surveys processed with structure-from-motion: Ground control quality, quantity and bundle adjustment. *Geomorphology* 280, 51–66.
- James, M. R., Robson, S. & Smith, M. W. 2017b.** 3-D uncertainty-based topographic change detection with structure-from-motion photogrammetry: precision maps for ground control and directly georeferenced surveys. *Earth Surface Processes and Landforms*. doi: 10.1002/esp.4125
- Jones, E., Oliphant, T. & Peterson, P. 2014.** SciPy: open source scientific tools for Python.
- Kärenlampi, K., Kontinen, A., Huhma, H. & Hanski, E. 2019.** Geology, geochronology and geochemistry of the 2.05 Ga gneissic A1-type granites and related intermediate rocks in central Finland: implication for the tectonic evolution of the Karelia craton margin. *Geological Society of Finland, Bulletin* 91, 57–95. Available at: <https://doi.org/10.17741/bgsf/91.1.002>
- Kirsch, M., Lorenz, S., Zimmermann, R., Tusa, L., Möckel, R., Hödl, P., Booyesen, R., Khodadadzadeh, M. & Gloaguen, R. 2018.** Integration of Terrestrial and Drone-Borne Hyperspectral and Photogrammetric Sensing Methods for Exploration Mapping and Mining Monitoring. *Remote Sens.* 10, p. 1366.
- Kontinen, A., Huhma, H., Lahaye, Y. & O'Brien, H. 2013.** New U–Pb zircon age, Sm–Nd Isotope and geochemical data on Proterozoic granitic rocks in the area west of the Oulunjärvi Lake, Central. In: Hölttä, P. (ed.) *Current Research: GTK Mineral Potential Workshop*, Kuopio, May 2012. Geological Survey of Finland, Report of Investigation 198, 70–74. Available at: [http://tupa.gtk.fi/julkaisu/tutkimusraportti/tr\\_198\\_pages\\_070\\_074.pdf](http://tupa.gtk.fi/julkaisu/tutkimusraportti/tr_198_pages_070_074.pdf)
- Kruse, F. A., Lefkoff, A. B., Boardman, J. B., Heidebrecht, K. B., Shapiro, A. T., Barloon, P. J. & Goetz, A. F. H. 1993.** The Spectral Image Processing System (SIPS) – Interactive Visualization and Analysis of Imaging spectrometer Data. *Remote Sensing of Environment* 44, 145–163.
- Lahti, I., Salmirinne, H., Kärenlampi, K. & Jylänki, J. 2018.** Geophysical surveys and modelling of Nb–Zr–REE deposits and Fe–Ti–V ore-bearing gabbros in the Otanmäki area, central Finland. Geological Survey of Finland, Open File Work Report. 30 p. Available at: [http://tupa.gtk.fi/raportti/arkisto/75\\_2018.pdf](http://tupa.gtk.fi/raportti/arkisto/75_2018.pdf)
- Lindholm, O. & Anttonen, R. 1980.** Geology of the Otanmäki mine. In: Häkli, T. A. (ed.) *Precambrian ores of Finland*, Proceedings on the 26th international Geological Congress, Guide to Excursions 078 A+C, Part 2 (Finland). Geological Survey of Finland, 25–33. Available at: [http://tupa.gtk.fi/julkaisu/erikoisjulkaisu/ej\\_003\\_pages\\_025\\_033.pdf](http://tupa.gtk.fi/julkaisu/erikoisjulkaisu/ej_003_pages_025_033.pdf)
- Madriz, Y. 2019.** Drone-borne geophysics: Magnetic survey for mineral exploration. Master Thesis, Freiberg, Germany. 75 p.
- Mäkeläinen, A., Saari, H., Hippi, I., Sarkeala, J. & Soukkamaki, J. 2013.** 2D Hyperspectral Frame Imager Camera Data in Photogrammetric Mosaicking. *Int. Arch. Photogramm. Remote Sens. Spat. Inf. Sci.*, XL-1/W2, 263–267.
- Mäkisalo, A. 2019.** Geological characterization of anorthositic rocks in the Otanmäki intrusion, central Finland: constraints on magma evolution and Fe–Ti–V oxide ore genesis. MSc thesis, University of Oulu, Oulu Mining School. 200 p. Available at: <http://jultika.oulu.fi/files/nbnfioulu-201903201346.pdf>
- Oppenheim, A. V., Schaffer, R. W. & Buck, J. R. 1999.** *Discrete-Time Signal Processing*. NJ, USA: Prentice Hall.
- Otanmäki Mine Oy. 2017.** Otanmäki mine brochure. 12 p. Available at: [http://www.otanmaki.fi/Otanmaki\\_Mine\\_brochure\\_2017.pdf](http://www.otanmaki.fi/Otanmaki_Mine_brochure_2017.pdf)
- Pääkkönen, V. 1956.** Otanmäki, the ilmenite–magnetite ore field in Finland. Geological Survey of Finland, Bulletin 171. 71 p. Available at: [http://tupa.gtk.fi/julkaisu/bulletin/bt\\_171.pdf](http://tupa.gtk.fi/julkaisu/bulletin/bt_171.pdf)
- Pirttijärvi, M. 2003.** Numerical modeling and inversion of geophysical electromagnetic measurements using a thin plate model. PhD thesis, University of Oulu. 44 p.
- Reeves, C. 2005.** *Aeromagnetic surveys: principles, practice and interpretation*. Geosoft 155.
- Salehi, S., Rogge, D., Rivard, B., Heincke, B. H. & Fensholt, R. 2017.** Modeling and assessment of wavelength displacements of characteristic absorption features of common rock forming minerals encrusted by lichens. *Remote Sensing of Environment* 199, 78–92.
- Savitzky, A. & Golay, M. J. E. 1964.** Smoothing and Differentiation of Data by Simplified Least Squares Procedures. *Analytical Chemistry* 36 (8), 1627–1639. doi: 10.1021/ac60214a047
- Sensys Technical Datasheet 2018.** SENSYS FGM3D Matrix of Technical Parameters Version 1.03. Bad Saarow, Germany: SENSYS Sensorik & Systemtechnologie GmbH, 1–3.
- Spectralon Technical Datasheet 2016.** Reflectance Materials and Coatings; Technical guide. North Sutton, NH, USA: Labsphere, 1–26.
- Tou, J. T. & Gonzalez, R. C. 1974.** *Pattern Recognition Principles*. Reading, Massachusetts, USA: Addison-Wesley Publishing Company.
- Tucker, C. J. 1979.** Red and Photographic Infrared Linear Combinations for Monitoring Vegetation. *Remote Sens. Environ.* 8, 127–150.
- Van Der Meer, F. 2004.** Analysis of spectral absorption features in hyperspectral imagery. *International journal of applied earth observation and geoinformation* 5(1), 55–68.
- Windsor, G. B., Hudik, F. E. & Natale, J. J. 2011.** Magnetic shielding of servo-motors in magnetic detection systems. US Patent US13, 278, 72910.

## APPENDICES

### Appendix 1. ROLE OF INSTITUTIONS IN THE MULSEDRO PROJECT

Partner	Role in MULSEDRO project
DMT GmbH	<ul style="list-style-type: none"> <li>Development of the integrated positioning system (IPS)</li> </ul>
GEUS	<ul style="list-style-type: none"> <li>Project coordination</li> <li>Field applications</li> </ul>
GTK	<ul style="list-style-type: none"> <li>Field applications (<i>main coordinator for the Otanmäki field campaign</i>)</li> </ul>
HZDR-HIF	<ul style="list-style-type: none"> <li>Development of multi-sensor system on multi-copter</li> <li>Key expertise in hyperspectral investigations</li> <li>PhD project within MULSEDRO</li> </ul>
LTU Business A/S	<ul style="list-style-type: none"> <li>Making business plan for developed products</li> </ul>
Radai Oy	<ul style="list-style-type: none"> <li>Development of multi-sensor system on fixed-wing drone</li> <li>Key expertise in magnetic investigations</li> </ul>

### Appendix 2. PARTICIPANTS IN THE OTANMÄKI FIELD CAMPAIGN

Institution	Persons and their involvement
GEUS	<ul style="list-style-type: none"> <li>Björn Heincke (project coordinator. PhD. geophysicist)</li> <li>Erik Vest Sørensen (stereophotogrammetry. PhD. geologist)</li> <li>Sara Salehi (PhD. remote sensing)</li> </ul>
GTK	<ul style="list-style-type: none"> <li>Heikki Salmirinne (organizer of field campaign. geophysicist)</li> <li>Jukka-Pekka Kujasalo (ground magnetic surveys. data processing. geophysicist)</li> <li>Maarit Middleton (remote sensing. Senior Scientist)</li> </ul>
HZDR-HIF	<ul style="list-style-type: none"> <li>Robert Jackisch (data processing and integration. acquired ground-based reference data. PhD student in project. MSc. Geoecologist)</li> <li>Robert Zimmermann (lead data acquisition by HZDR-HIF. data processing. MSc. Geologist)</li> <li>Benjamin Melzer (performed surveys with <i>HZDR-HIF</i> drones. UAS pilot. Geology Technician)</li> <li>Yuleika Madriz-Diaz (data processing. master student in the project. BSc. Geophysicist)</li> </ul>
Radai Oy	<ul style="list-style-type: none"> <li>Ari Saartenoja (performed surveys with <i>Radai Oy's</i> drone. company owner CEO. mathematician)</li> <li>Markku Pirttijärvi (data processing. Ph.D. geophysicist)</li> <li>Timo Åman (performed surveys with <i>Radai Oy's</i> drone. UAS pilot. engineer)</li> </ul>
Otanmäki Mine Oy	<ul style="list-style-type: none"> <li>Jouko Jylänki (providing the relevant background information and preparing site. work on re-establishing mining activities in Otanmäki. CEO of the Otanmäki Mine Oy)</li> </ul>
Oulu Mining School. University of Oulu	<ul style="list-style-type: none"> <li>Kimmo Kärenlampi (expert for the Otanmäki region. geologist)</li> </ul>
DMT GmbH	<ul style="list-style-type: none"> <li>Sönke Rapp (test measurements with IPS. engineer)</li> </ul>

### Appendix 3. GROUND CONTROL POINTS

Elevation above sea level

H\_Prec = Precision in XY direction

V\_Prec = Precision in Z direction

Point-ID	Easting	Northing	Elevation [m]	H_Prec. [m]	V_Prec. [m]
FI18-RJA-101	506011.32	7110369.48	142.9	0.07	0.08
FI18-RJA-102	506023.04	7110380.22	143.3	0.05	0.07
FI18-RJA-103	506048.82	7110372.94	143.4	0.04	0.07
FI18-RJA-104	506059.19	7110389.44	143.1	0.05	0.08
FI18-RJA-105	506050.76	7110406.44	143.1	0.02	0.05
FI18-RJA-106	506063.82	7110434.08	142.3	0.01	0.01
FI18-RJA-107	506053.49	7110420.22	142.6	0.03	0.06
FI18-RJA-108	506036.97	7110423.54	143.4	0.04	0.05
FI18-RJA-109	506028.60	7110420.87	143.4	0.03	0.06
FI18-RJA-110	506041.14	7110431.36	143.2	0.03	0.06
FI18-RJA-111	506059.61	7110442.19	142.3	0.09	0.06
FI18-RJA-112	506020.09	7110373.78	143.2	0.04	0.06
FI18-RJA-113	505995.25	7110402.44	143.1	0.05	0.07

## Appendix 4.

### PROCESSING REPORT

2018/09/05 ebeePlus/S.O.D.A. at Otanmaeki mine 14 September 2018



## SURVEY DATA

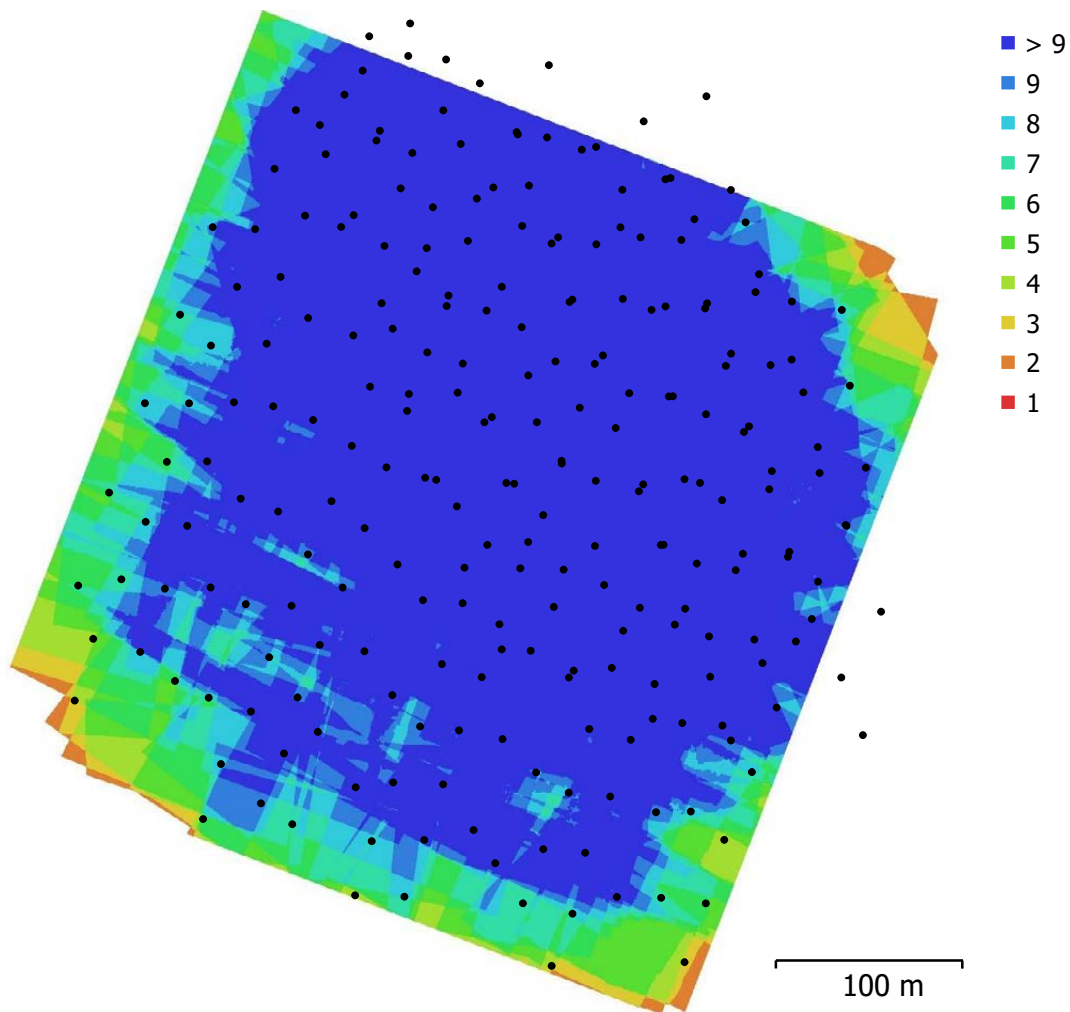


Fig. 1. Camera locations and image overlap.

Number of images:	244	Camera stations:	241
Flying altitude:	103 m	Tie points:	72.854
Ground resolution:	2.19 cm/pix	Projections:	445.027
Coverage area:	0.168 km <sup>2</sup>	Reprojection error:	1.12 pix

Table 1. Cameras.

Camera Model	Resolution	Focal Length	Pixel Size	Precalibrated
S.O.D.A. (10.6mm)	5472 x 3648	10.6 mm	2.4 x 2.4 µm	No

## CAMERA CALIBRATION

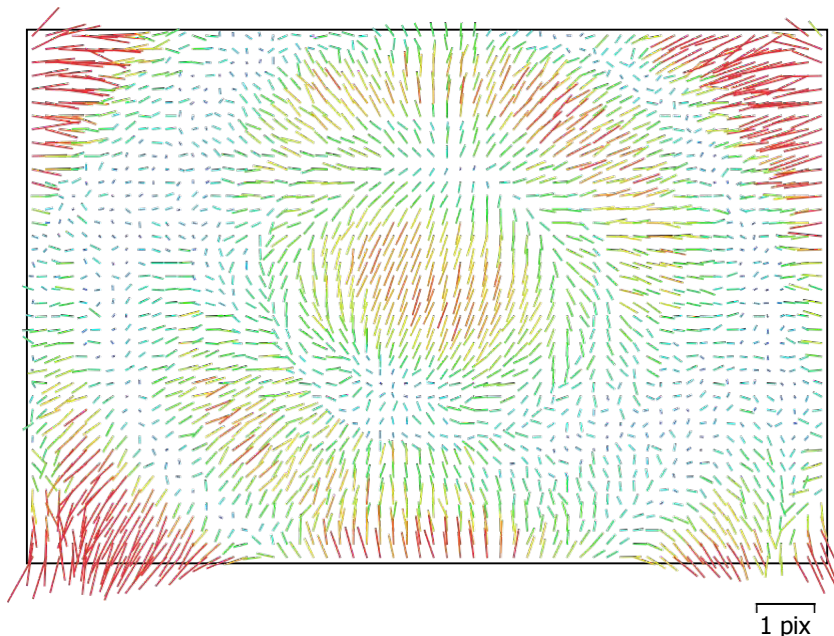


Fig. 2. Image residuals for S.O.D.A. (10.6mm).

### S.O.D.A. (10.6mm)

244 images

Type	Resolution	Focal Length	Pixel Size
<b>Frame</b>	<b>5472 x 3648</b>	<b>10.6 mm</b>	<b>2.4 x 2.4 <math>\mu</math>m</b>

Table 2. Calibration coefficients and correlation matrix.

	Value	Error	F	Cx	Cy	B1	B2	K1	K2	K3	K4	P1	P2
<b>F</b>	<b>4394.93</b>	0.36	1.00	-0.34	-0.87	0.50	-0.36	0.07	-0.10	0.11	-0.09	0.04	-0.18
<b>Cx</b>	<b>25.2057</b>	0.07		1.00	0.33	-0.10	0.62	-0.02	0.03	-0.04	0.03	0.42	0.07
<b>Cy</b>	<b>-42.648</b>	0.14			1.00	-0.65	0.39	-0.13	0.12	-0.14	0.11	0.02	0.33
<b>B1</b>	<b>0.92013</b>	0.016				1.00	-0.24	0.02	-0.09	0.10	-0.08	0.08	0.12
<b>B2</b>	<b>-0.262514</b>	0.014					1.00	-0.01	0.04	-0.05	0.04	-0.05	-0.03
<b>K1</b>	<b>0.0427853</b>	0.0001						1.00	-0.95	0.90	-0.85	-0.04	-0.25
<b>K2</b>	<b>-0.326263</b>	0.00072							1.00	-0.99	0.96	-0.02	0.04
<b>K3</b>	<b>0.668024</b>	0.002								1.00	-0.99	0.03	-0.04
<b>K4</b>	<b>-0.369438</b>	0.002									1.00	-0.03	0.03
<b>P1</b>	<b>0.00169049</b>	2.9e-06										1.00	0.26
<b>P2</b>	<b>-0.00268246</b>	4.4e-06											1.00

### CAMERA LOCATIONS

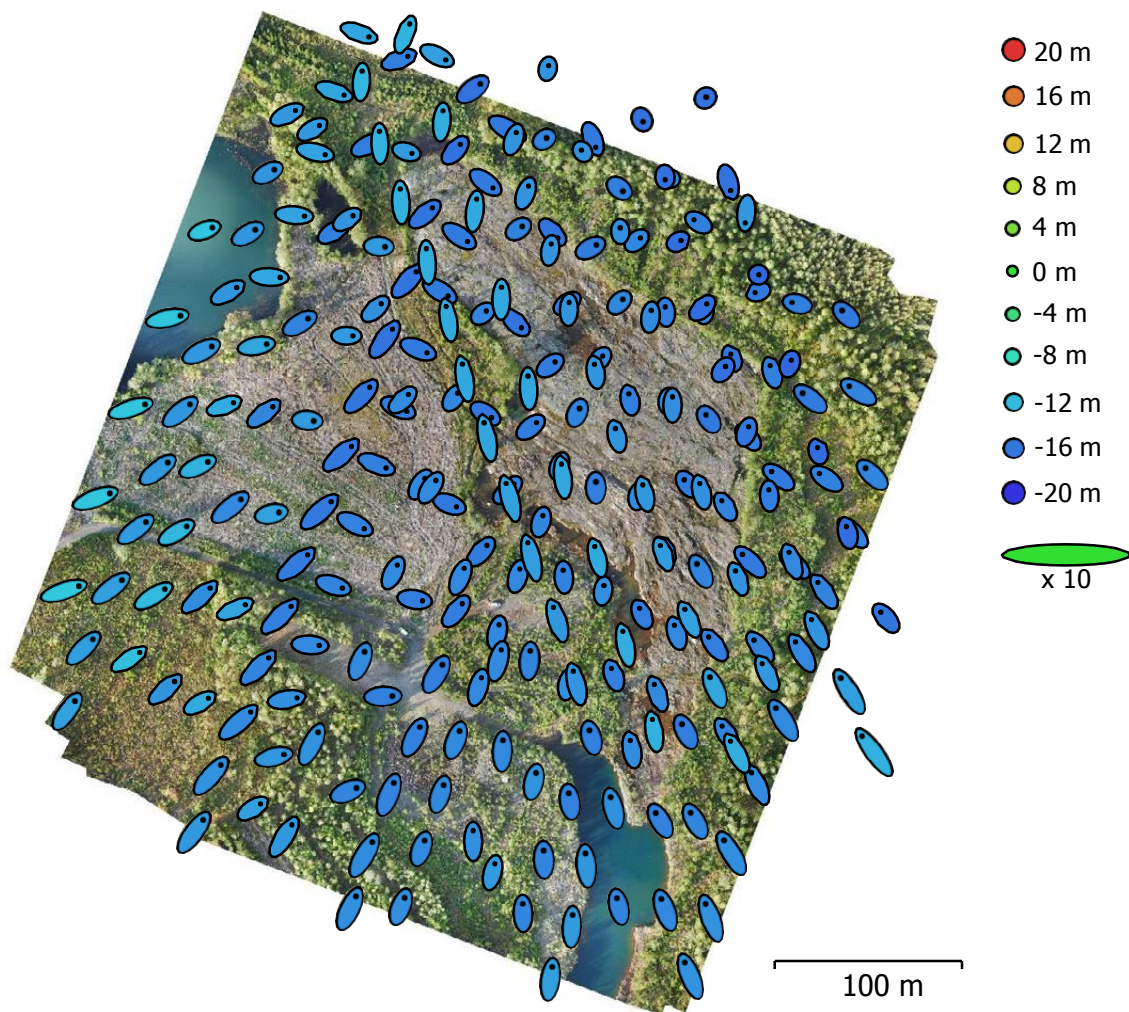


Fig. 3. Camera locations and error estimates.  
 Z error is represented by ellipse color. X,Y errors are represented by ellipse shape.  
 Estimated camera locations are marked with a black dot.

Table 3. Average camera location error. X - Easting. Y - Northing. Z - Altitude.

X error (m)	Y error (m)	Z error (m)	XY error (m)	Total error (m)
0.65179	0.836739	14.7381	1.06064	14.7762

## GROUND CONTROL POINTS

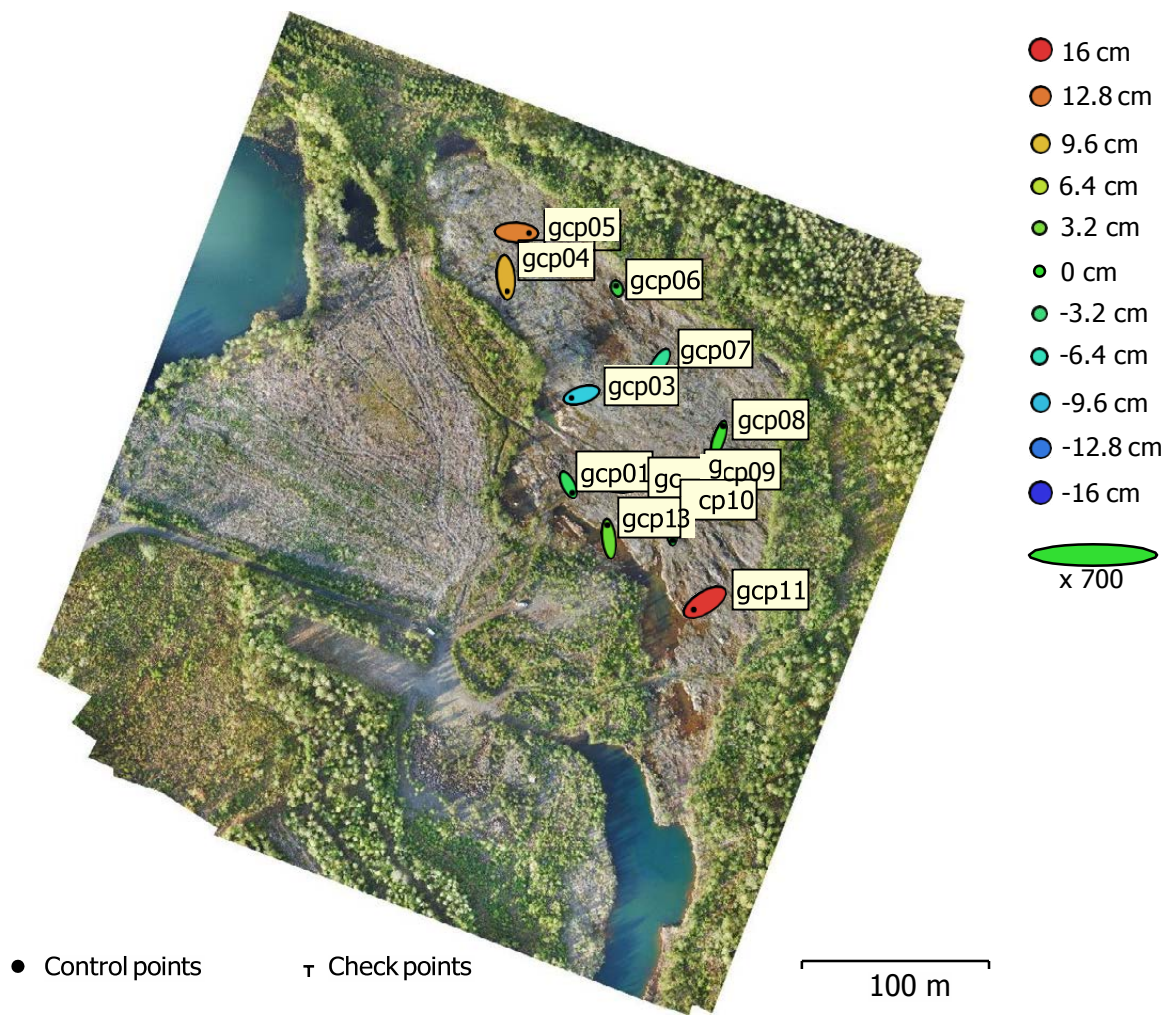


Fig. 4. GCP locations and error estimates.  
 Z error is represented by ellipse color. X,Y errors are represented by ellipse shape.  
 Estimated GCP locations are marked with a dot or crossing.

Table 4. Control points RMSE.

Count	X error (cm)	Y error (cm)	Z error (cm)	XY error (cm)	Total (cm)
12	1.03349	1.35548	7.85844	1.70453	8.04117

X - Easting. Y - Northing. Z - Altitude.

Table 5. Control points.

<b>Label</b>	<b>X error (cm)</b>	<b>Y error (cm)</b>	<b>Z error (cm)</b>	<b>Total (cm)</b>	<b>Image (pix)</b>
gcp01	0.519209	-1.1045	-2.10594	2.43402	0.395 (14)
gcp02	1.72651	0.0574326	-11.0515	11.1857	0.716 (20)
gcp03	-1.47736	-0.432144	-8.74572	8.88014	0.819 (17)
gcp04	0.174911	-2.0614	10.189	10.3969	0.753 (19)
gcp05	1.87829	-0.0843691	12.3786	12.5206	0.600 (16)
gcp06	-0.122748	0.382035	-0.346122	0.529923	0.424 (18)
gcp07	-0.667016	-1.03027	-4.70342	4.86092	0.537 (21)
gcp08	0.554424	1.8788	0.580146	2.043	0.405 (14)
gcp09	0.401621	0.572644	-0.945803	1.17634	0.731 (20)
gcp10	0.155705	-2.47228	-1.77887	3.04972	0.336 (12)
gcp11	-1.68112	-1.00828	15.7342	15.8559	0.404 (15)
gcp13	-0.21594	2.04629	2.59867	3.31467	1.132 (21)
<b>Total</b>	<b>1.03349</b>	<b>1.35548</b>	<b>7.85844</b>	<b>8.04117</b>	<b>0.672</b>

X - Easting, Y - Northing, Z - Altitude.

## DIGITAL ELEVATION MODEL

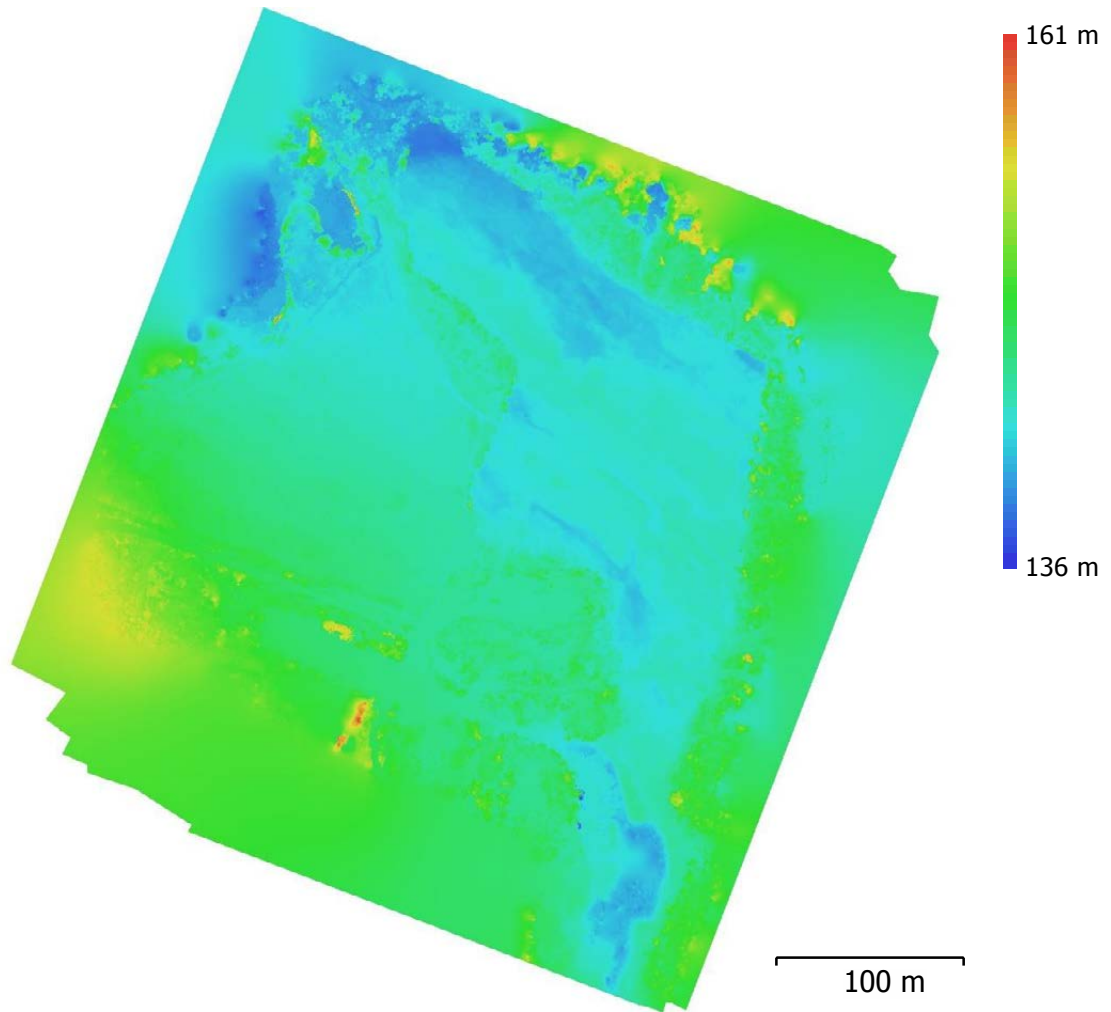


Fig. 5. Reconstructed digital elevation model.

Resolution: 4.37 cm/pix  
Point density: 524 points/m<sup>2</sup>

## PROCESSING PARAMETERS

### General

Cameras	244
Aligned cameras	241
Markers	12
Coordinate system	ETRS89 / UTM zone 35N (EPSG::25835)
Rotation angles	Yaw. Pitch. Roll

### Point Cloud

Points	72.854 of 176.220
RMS reprojection error	0.192178 (1.12365 pix)
Max reprojection error	0.49999 (41.6869 pix)
Mean key point size	5.07434 pix
Point colors	3 bands. uint8
Key points	No
Average tie point multiplicity	4.27585

### Alignment parameters

Accuracy	High
Generic preselection	Yes
Reference preselection	Yes
Key point limit	40.000
Tie point limit	4.000
Adaptive camera model fitting	Yes
Matching time	2 minutes 4 seconds
Alignment time	47 seconds

### Dense Point Cloud

Points	76.167.257
Point colors	3 bands. uint8

### Reconstruction parameters

Quality	High
Depth filtering	Aggressive
Depth maps generation time	14 minutes 42 seconds
Dense cloud generation time	24 minutes 58 seconds

### DEM

Size	12.102 x 12.383
Coordinate system	ETRS89 / UTM zone 35N (EPSG::25835)

### Reconstruction parameters

Source data	Dense cloud
Interpolation	Enabled
Processing time	3 minutes 18 seconds

### Orthomosaic

Size	22.681 x 24.537
Coordinate system	ETRS89 / UTM zone 35N (EPSG::25835)
Colors	3 bands. uint8

### Reconstruction parameters

Blending mode	Mosaic
Surface	DEM
Enable hole filling	Yes
Processing time	13 minutes 2 seconds

### Software

Version	1.4.2 build 6205
Platform	Windows 64

## Appendix 5.

### PROCESSING REPORT

2018/09/05 ebeePlus/Sequoia. at Otanmaeki mine 17 September 2018



## SURVEY DATA

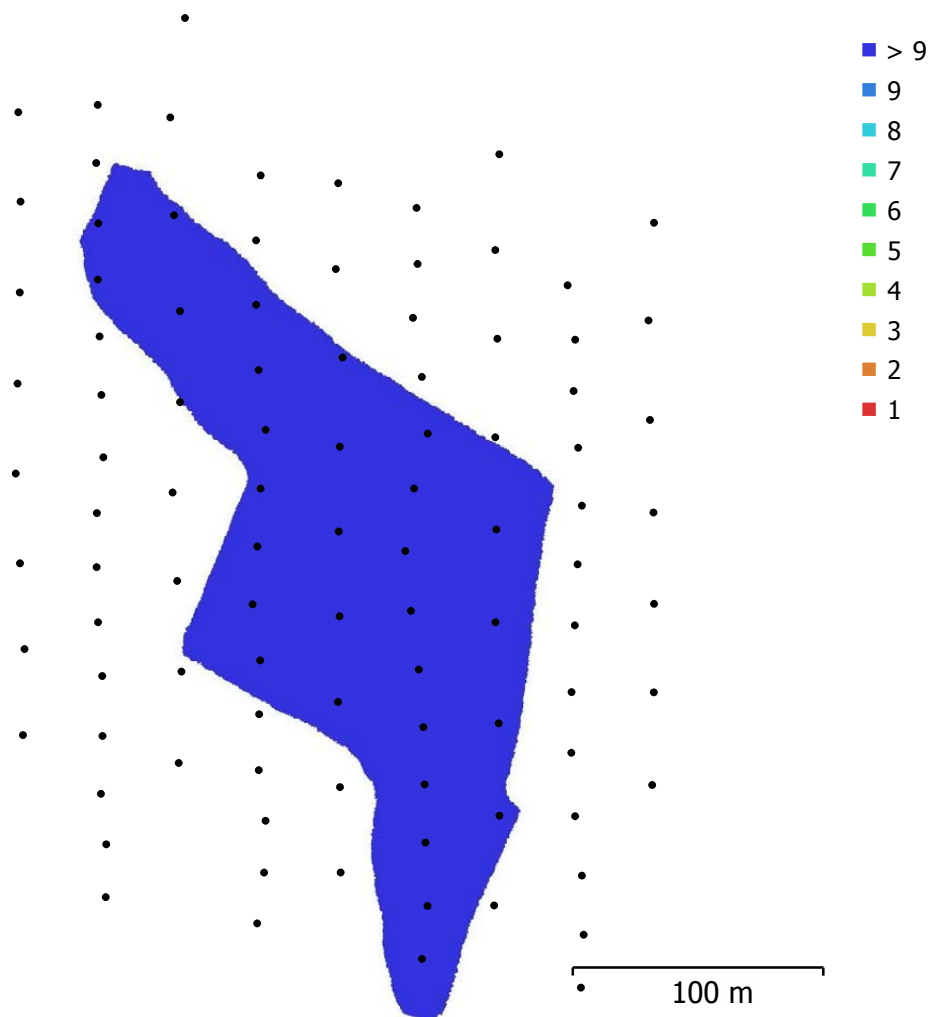


Fig. 1. Camera locations and image overlap.

Number of images:	412	Camera stations:	392
Flying altitude:	83.7 m	Tie points:	98.872
Ground resolution:	7.4 cm/pix	Projections:	372.484
Coverage area:	0.0269 km <sup>2</sup>	Reprojection error:	0.395 pix

Table 1. Cameras.

Camera Model	Resolution	Focal Length	Pixel Size	Precalibrated
Sequoia. Green (3.98mm)	1280 x 960	3.98 mm	3.75 x 3.75 µm	Yes
Sequoia. Red (3.98mm)	1280 x 960	3.98 mm	3.75 x 3.75 µm	Yes
Sequoia. Red edge (3.98mm)	1280 x 960	3.98 mm	3.75 x 3.75 µm	Yes
Sequoia. NIR (3.98mm)	1280 x 960	3.98 mm	3.75 x 3.75 µm	Yes

## CAMERA CALIBRATION

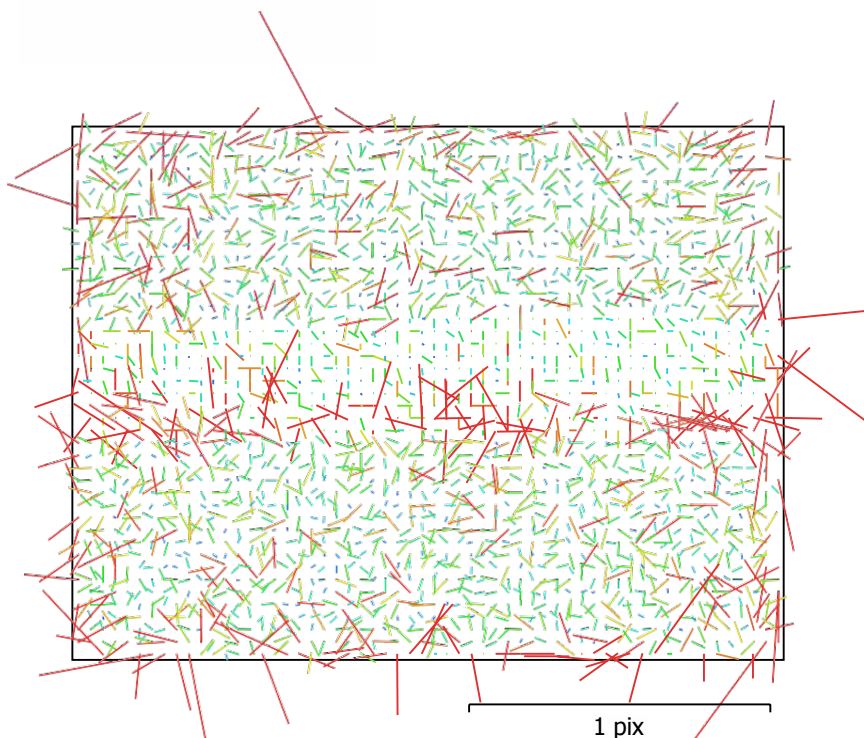


Fig. 2. Image residuals for Sequoia. Green (3.98mm).

### Sequoia. Green (3.98mm)

103 images. precalibrated

Type	Resolution	Focal Length	Pixel Size
<b>Fisheye</b>	<b>1280 x 960</b>	<b>3.98 mm</b>	<b>3.75 x 3.75 <math>\mu</math>m</b>

Table 2. Calibration coefficients and correlation matrix.

	Value	Error	F	Cx	Cy	B1	B2	K1	K2	P1	P2
<b>K3</b>	<b>0.206645</b>										
<b>K4</b>	<b>-0.188559</b>										
<b>F</b>	<b>1061.24</b>	0.23	1.00	-0.21	-0.77	0.17	-0.20	-0.85	0.24	0.24	0.79
<b>Cx</b>	<b>9.98857</b>	0.049		1.00	0.22	-0.08	0.06	0.16	-0.05	-0.80	-0.18
<b>Cy</b>	<b>-4.05969</b>	0.071			1.00	-0.12	0.13	0.57	-0.13	-0.20	-0.87
<b>B1</b>	<b>0.29009</b>	0.022				1.00	-0.07	-0.24	0.06	0.08	0.14
<b>B2</b>	<b>-0.383338</b>	0.021					1.00	0.17	-0.04	0.01	-0.14
<b>K1</b>	<b>-0.0383069</b>	0.00018						1.00	-0.61	-0.23	-0.71
<b>K2</b>	<b>-0.0830429</b>	0.00014							1.00	0.11	0.16
<b>P1</b>	<b>-0.000493117</b>	1.2e-05								1.00	0.22
<b>P2</b>	<b>0.000103777</b>	2.2e-05									1.00

## CAMERA CALIBRATION

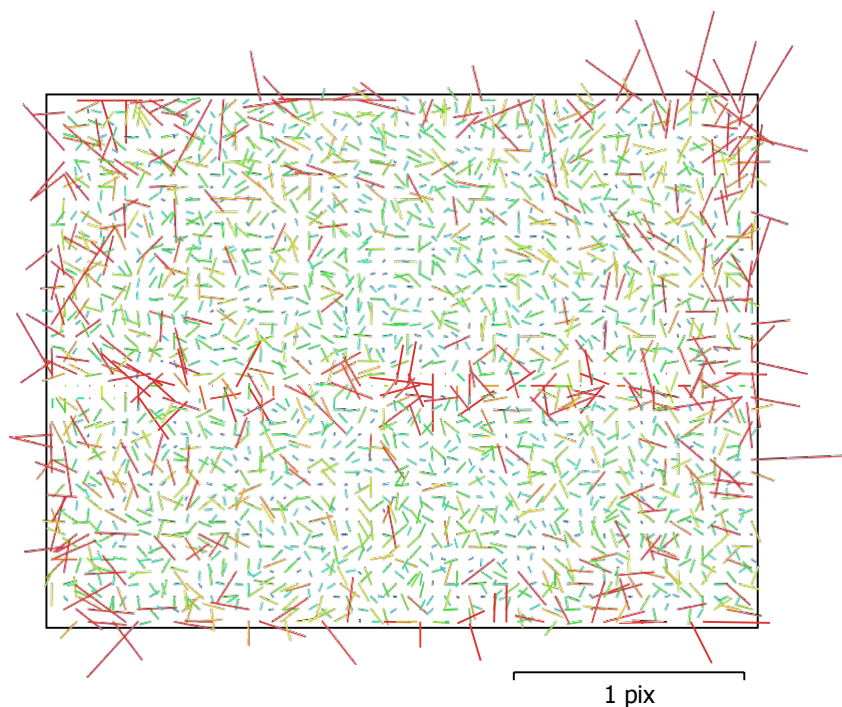


Fig. 3. Image residuals for Sequoia. Red (3.98mm).

### Sequoia. Red (3.98mm)

103 images. precalibrated

Type	Resolution	Focal Length	Pixel Size
<b>Fisheye</b>	<b>1280 x 960</b>	<b>3.98 mm</b>	<b>3.75 x 3.75 <math>\mu</math>m</b>

Table 3. Calibration coefficients and correlation matrix.

	Value	Error	F	Cx	Cy	B1	B2	K1	K2	P1	P2
<b>K3</b>	<b>0.19568</b>										
<b>K4</b>	<b>-0.177694</b>										
<b>F</b>	<b>1057.66</b>	0.23	1.00	-0.22	-0.76	0.16	-0.20	-0.84	0.22	0.25	0.79
<b>Cx</b>	<b>29.2084</b>	0.051		1.00	0.22	-0.07	0.05	0.16	-0.04	-0.77	-0.19
<b>Cy</b>	<b>-21.9984</b>	0.071			1.00	-0.11	0.13	0.55	-0.11	-0.20	-0.86
<b>B1</b>	<b>-0.00947815</b>	0.022				1.00	-0.07	-0.22	0.05	0.08	0.14
<b>B2</b>	<b>-0.0701207</b>	0.021					1.00	0.17	-0.03	0.00	-0.14
<b>K1</b>	<b>-0.0382206</b>	0.00018						1.00	-0.61	-0.25	-0.69
<b>K2</b>	<b>-0.0798041</b>	0.00016							1.00	0.12	0.13
<b>P1</b>	<b>-0.00045448</b>	1.3e-05								1.00	0.23
<b>P2</b>	<b>0.000384668</b>	2.1e-05									1.00

## CAMERA CALIBRATION

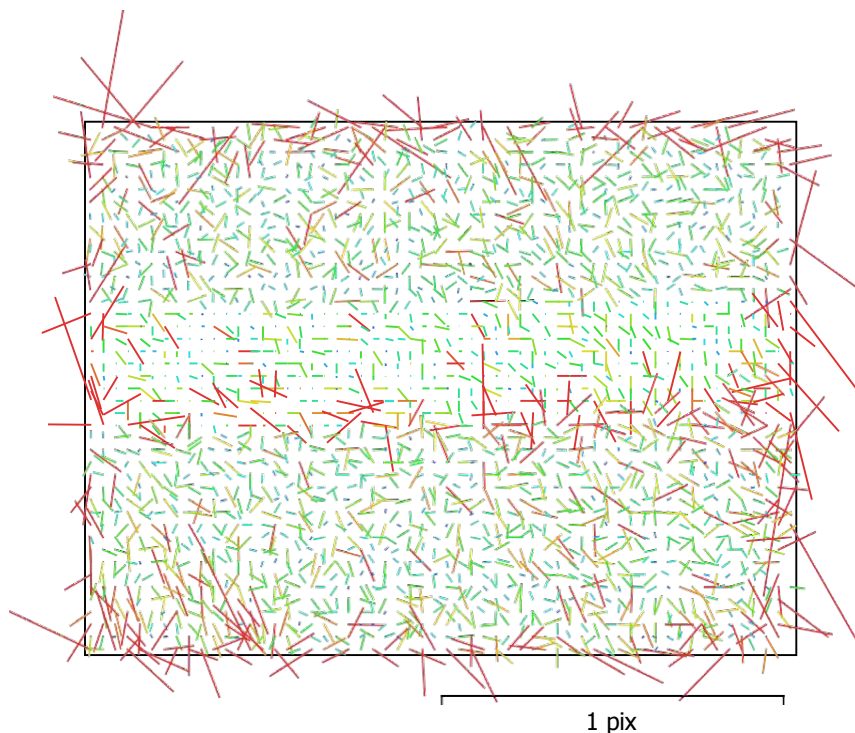


Fig. 4. Image residuals for Sequoia. Red edge (3.98mm).

### Sequoia. Red edge (3.98mm)

103 images. precalibrated

Type	Resolution	Focal Length	Pixel Size
<b>Fisheye</b>	<b>1280 x 960</b>	<b>3.98 mm</b>	<b>3.75 x 3.75 <math>\mu\text{m}</math></b>

Table 4. Calibration coefficients and correlation matrix.

	Value	Error	F	Cx	Cy	B1	B2	K1	K2	P1	P2
<b>K3</b>	<b>0.198665</b>										
<b>K4</b>	<b>-0.180841</b>										
<b>F</b>	<b>1059.1</b>	0.23	1.00	-0.23	-0.77	0.16	-0.21	-0.86	0.27	0.26	0.79
<b>Cx</b>	<b>5.43348</b>	0.049		1.00	0.23	-0.08	0.07	0.18	-0.06	-0.81	-0.20
<b>Cy</b>	<b>13.5543</b>	0.071			1.00	-0.11	0.14	0.58	-0.15	-0.22	-0.87
<b>B1</b>	<b>0.319749</b>	0.022				1.00	-0.07	-0.24	0.07	0.08	0.14
<b>B2</b>	<b>-0.0997751</b>	0.021					1.00	0.18	-0.04	0.00	-0.15
<b>K1</b>	<b>-0.0383773</b>	0.00018						1.00	-0.62	-0.26	-0.72
<b>K2</b>	<b>-0.0795535</b>	0.00014							1.00	0.13	0.19
<b>P1</b>	<b>0.000391478</b>	1.3e-05								1.00	0.25
<b>P2</b>	<b>-0.000219061</b>	2.2e-05									1.00

## CAMERA CALIBRATION

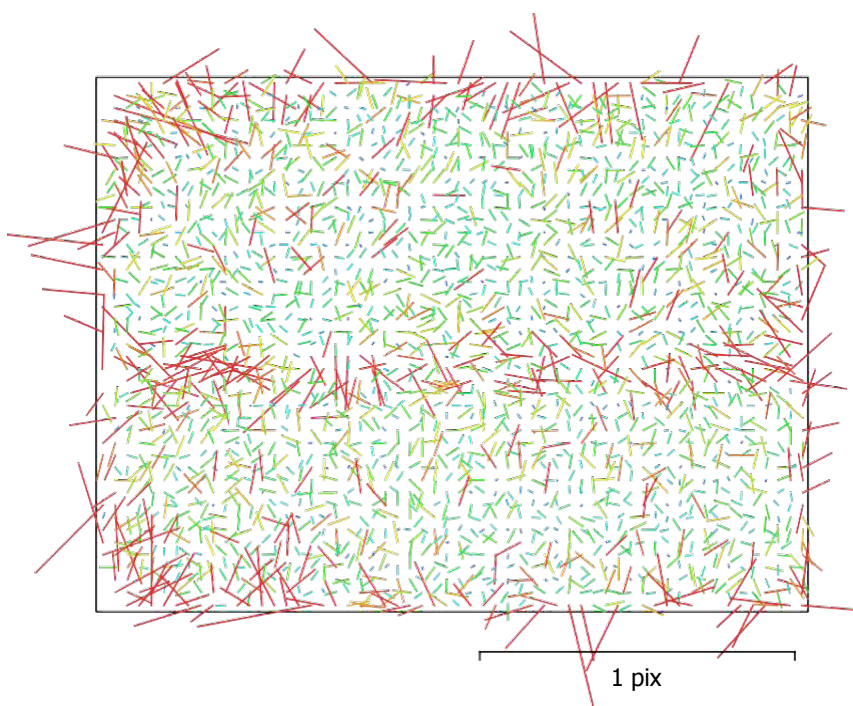


Fig. 5. Image residuals for Sequoia. NIR (3.98mm).

### Sequoia. NIR (3.98mm)

103 images. precalibrated

Type	Resolution	Focal Length	Pixel Size
<b>Fisheye</b>	<b>1280 x 960</b>	<b>3.98 mm</b>	<b>3.75 x 3.75 <math>\mu\text{m}</math></b>

Table 5. Calibration coefficients and correlation matrix.

	Value	Error	F	Cx	Cy	B1	B2	K1	K2	P1	P2
<b>K3</b>	<b>0.300684</b>										
<b>K4</b>	<b>-0.27334</b>										
<b>F</b>	<b>1058.96</b>	0.23	1.00	-0.22	-0.76	0.16	-0.21	-0.85	0.24	0.26	0.79
<b>Cx</b>	<b>36.9937</b>	0.049		1.00	0.22	-0.07	0.06	0.17	-0.05	-0.80	-0.19
<b>Cy</b>	<b>10.8789</b>	0.07			1.00	-0.11	0.14	0.56	-0.12	-0.21	-0.87
<b>B1</b>	<b>0.240218</b>	0.022				1.00	-0.07	-0.23	0.06	0.07	0.13
<b>B2</b>	<b>-0.16146</b>	0.021					1.00	0.18	-0.04	0.01	-0.15
<b>K1</b>	<b>-0.0317433</b>	0.00017						1.00	-0.60	-0.26	-0.71
<b>K2</b>	<b>-0.118054</b>	0.00014							1.00	0.13	0.17
<b>P1</b>	<b>0.000571717</b>	1.3e-05								1.00	0.24
<b>P2</b>	<b>0.000451483</b>	2.1e-05									1.00

### CAMERA LOCATIONS

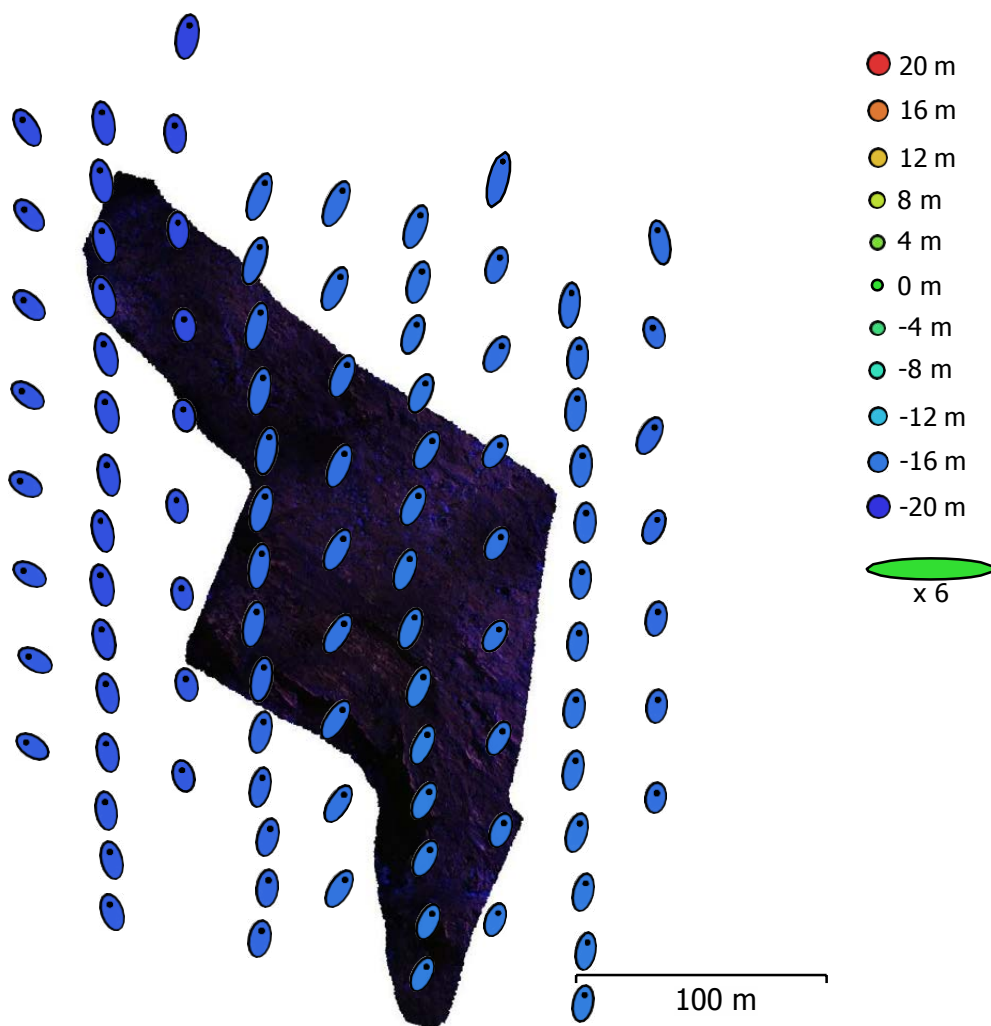


Fig. 6. Camera locations and error estimates.  
 Z error is represented by ellipse color. X,Y errors are represented by ellipse shape.  
 Estimated camera locations are marked with a black dot.

Table 6. Average camera location error.

X error (m)	Y error (m)	Z error (m)	XY error (m)	Total error (m)
0.452791	1.25382	16.9249	1.33308	16.9773

X - Easting. Y - Northing. Z - Altitude.

### GROUND CONTROL POINTS

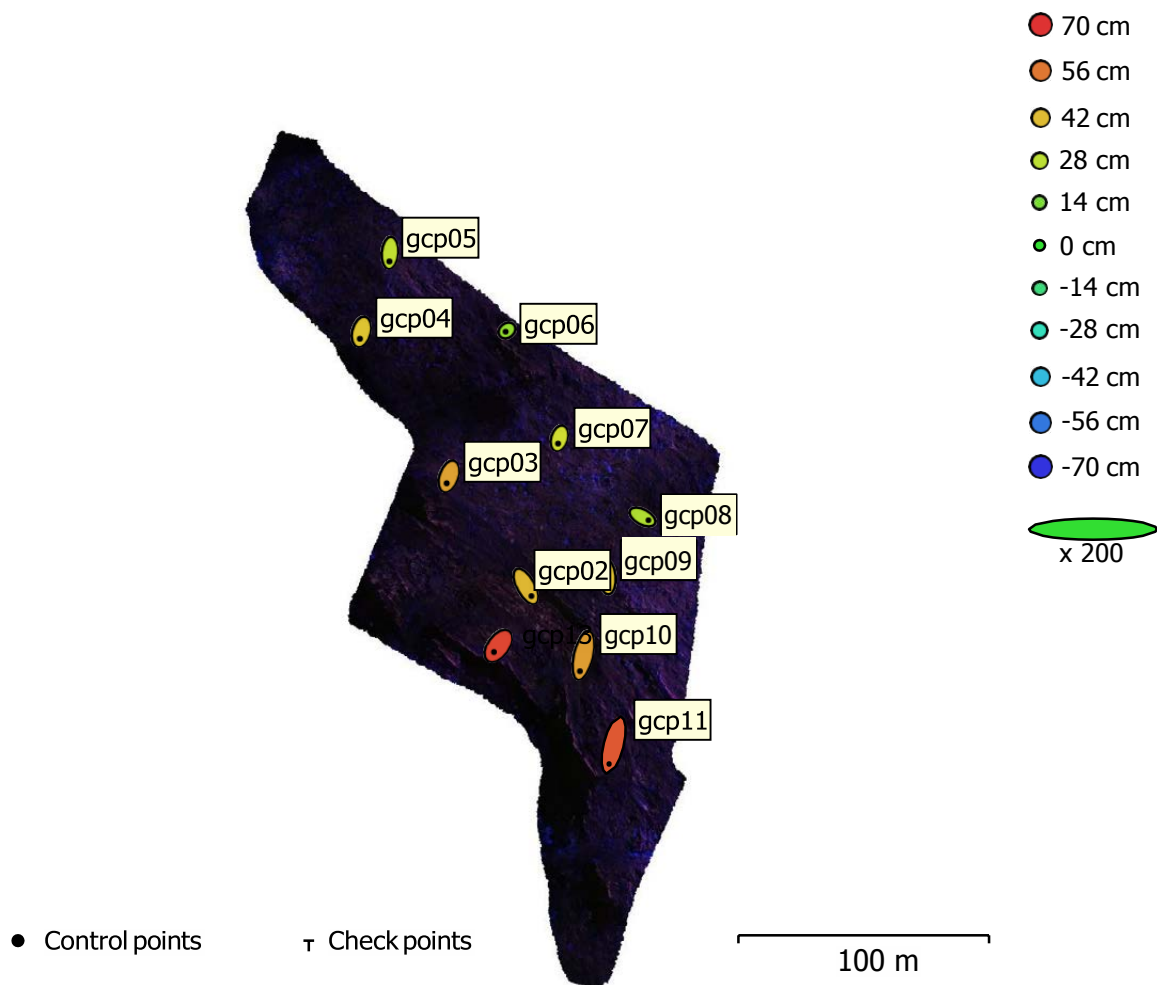


Fig. 7. GCP locations and error estimates.  
 Z error is represented by ellipse color. X.Y errors are represented by ellipse shape.  
 Estimated GCP locations are marked with a dot or crossing.

Table 7. Control points RMSE.

Count	X error (cm)	Y error (cm)	Z error (cm)	XY error (cm)	Total (cm)
11	1.32366	3.80556	43.5435	4.02919	43.7295

Table 8. Control points.

Label	X error (cm)	Y error (cm)	Z error (cm)	Total (cm)	Image (pix)
gcp02	2.01906	-3.69467	42.8288	43.0352	0.226 (10)
gcp03	-0.868311	-2.65974	47.2841	47.3668	0.213 (11)
gcp04	-0.574791	-2.69946	40.2431	40.3376	0.235 (11)
gcp05	-0.226896	-3.28002	28.9557	29.1418	0.333 (14)
gcp06	-0.498631	-0.457345	20.1153	20.1267	0.334 (15)
gcp07	-0.542257	-1.90101	32.4738	32.5339	0.284 (12)
gcp08	2.26268	-1.21474	25.5503	25.6791	0.301 (11)
gcp09	0.368303	-3.74611	40.7789	40.9522	0.336 (14)
gcp10	-1.31735	-6.24638	48.2771	48.6974	0.408 (12)
gcp11	-1.89331	-7.52288	62.2624	62.7438	0.401 (11)
gcp13	-1.71532	-2.36464	65.9257	65.9904	0.286 (14)
<b>Total</b>	<b>1.32366</b>	<b>3.80556</b>	<b>43.5435</b>	<b>43.7295</b>	<b>0.314</b>

X - Easting. Y - Northing. Z - Altitude.

## DIGITAL ELEVATION MODEL

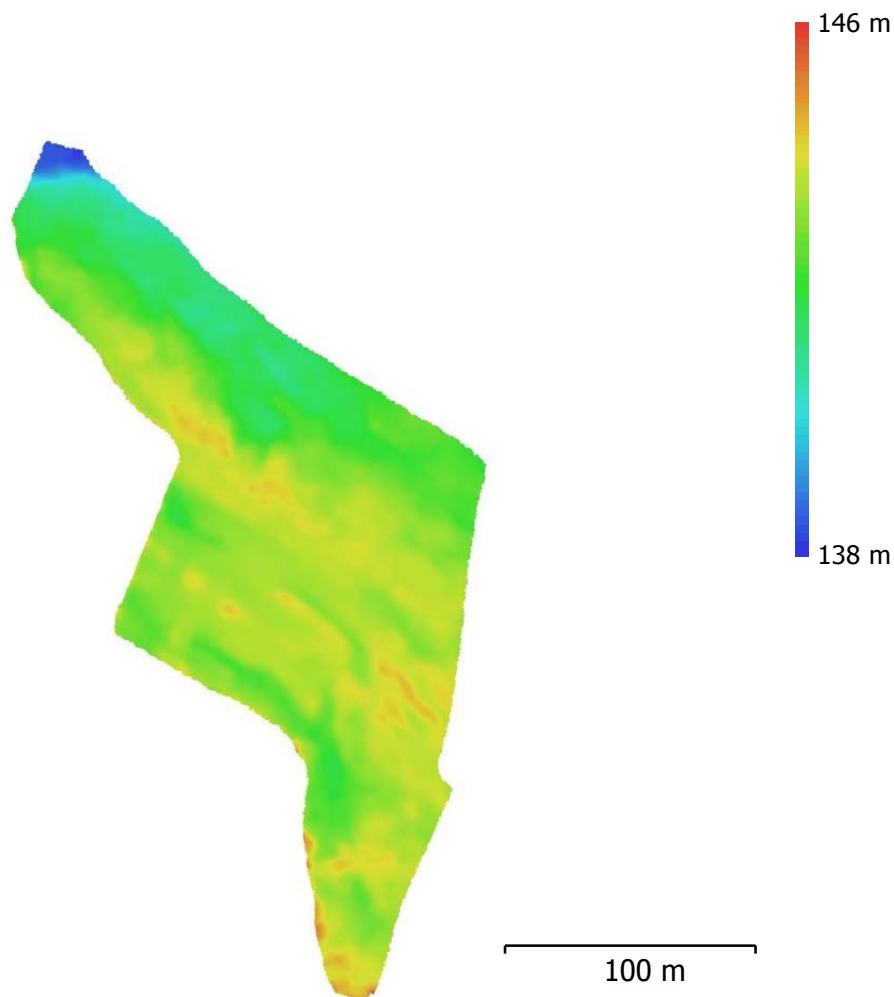


Fig. 8. Reconstructed digital elevation model.

Resolution: 14.8 cm/pix  
 Point density: 45.7 points/m<sup>2</sup>

## PROCESSING PARAMETERS

### General

Cameras	412
Aligned cameras	392
Markers	11
Coordinate system	ETRS89 / UTM zone 35N (EPSG::25835)
Rotation angles	Yaw. Pitch. Roll

### Point Cloud

Points	98.872 of 413.179
RMS reprojection error	0.100547 (0.395166 pix)
Max reprojection error	0.199999 (3.1664 pix)
Mean key point size	3.65487 pix
Point colors	3 bands. uint8
Key points	No
Average tie point multiplicity	3.41863

<b>Alignment parameters</b>	
Accuracy	High
Generic preselection	Yes
Reference preselection	Yes
Key point limit	40.000
Tie point limit	4.000
Adaptive camera model fitting	Yes
Matching time	22 seconds
Alignment time	1 minutes 17 seconds
<b>Dense Point Cloud</b>	
Points	3.863.946
Point colors	4 bands. uint16
<b>Reconstruction parameters</b>	
Quality	High
Depth filtering	Aggressive
Depth maps generation time	15 seconds
Dense cloud generation time	28 seconds
<b>Model</b>	
Faces	79.999
Vertices	41.074
Vertex colors	3 bands. uint8
<b>Reconstruction parameters</b>	
Surface type	Arbitrary
Source data	Dense
Interpolation	Extrapolated
Quality	High
Depth filtering	Aggressive
Face count	772.267
Processing time	1 minutes 33 seconds
<b>DEM</b>	
Size	3.188 x 3.014
Coordinate system	ETRS89 / UTM zone 35N (EPSG::25835)
<b>Reconstruction parameters</b>	
Source data	Mesh
Interpolation	Disabled
Processing time	3 seconds
<b>Orthomosaic</b>	
Size	2.565 x 4.631
Coordinate system	ETRS89 / UTM zone 35N (EPSG::25835)
Colors	4 bands. uint16
<b>Reconstruction parameters</b>	
Blending mode	Mosaic
Surface	DEM
Enable hole filling	Yes
Processing time	37 seconds
<b>Software</b>	
Version	1.4.2 build 6205
Platform	Windows 64

## Appendix 6.

### GROUND TRUTH SAMPLING POINTS (Spectroscopy. hXRF. Susceptibility)

Elevation above sea level. H\_Prec = Precision in XY direction;

V\_Prec = Precision in Z direction

Point-ID	Easting	Northing	Elevation [m]	H_Prec [m]	V_Prec [m]
FI18_met2_10492	506022.999	7110361.028	142.9	0.018	0.066
FI18_met2_10493	506024.6854	7110364.629	143.3	0.019	0.067
FI18_met2_10494	506026.6284	7110367.886	143.3	0.020	0.074
FI18_met2_10495	506027.3359	7110371.705	143.5	0.020	0.065
FI18_met2_10496	506028.9433	7110374.349	143.4	0.021	0.059
FI18_met2_10497	506030.8271	7110377.633	143.3	0.156	0.145
FI18_met2_10498	506034.0782	7110387.391	143.1	0.015	0.024
FI18_met2_10499	506035.7196	7110390.149	143.2	0.015	0.023
FI18_met2_10500	506037.0618	7110393.801	143.0	0.169	0.154
FI18_met2_10501	506038.0451	7110397.632	142.8	0.111	0.092
FI18_met2_10502	506041.7326	7110406.403	143.5	0.091	0.073
FI18_met2_10503	506043.0748	7110417.951	143.3	0.121	0.098
FI18_met2_10504	506044.077	7110424.34	143.3	0.079	0.091
FI18_met2_10505	506049.8443	7110433.477	142.9	0.016	0.017
FI18_met2_10506	506050.2445	7110439.209	142.9	0.080	0.101
FI18_met2_10507	506050.1823	7110445.237	142.4	0.084	0.091
FI18_met2_10508	506050.6653	7110448.851	142.3	0.011	0.014
FI18_met2_10509	506051.4536	7110454.684	141.9	0.103	0.082
FI18_met2_10510	506055.6247	7110458.704	142.3	0.179	0.142
FI18_met2_10511	506056.7384	7110463.454	142.5	0.120	0.112
FI18_met2_10512	506060.8129	7110475.07	142.0	0.099	0.115
FI18_met2_10513	505924.2461	7110541.098	141.6	0.144	0.167
FI18_met2_10514	505925.083	7110533.786	141.6	0.118	0.137
FI18_met2_10515	505926.3959	7110530.553	141.5	0.134	0.156
FI18_met2_10516	505926.4089	7110526.928	142.0	0.109	0.132
FI18_met2_10517	505926.4069	7110526.934	141.9	0.120	0.146
FI18_met2_10518	505933.9457	7110519.668	142.2	0.139	0.188
FI18_met2_10519	505941.583	7110510.858	142.3	0.109	0.133
FI18_met2_10520	505945.3065	7110502.286	143.2	0.059	0.092
FI18_met2_10521	505962.0692	7110480.787	143.4	0.059	0.083
FI18_met2_10522	505967.5125	7110468.127	143.7	0.071	0.104
FI18_met2_10523	505970.1551	7110449.775	143.2	0.052	0.081
FI18_met2_10524	505977.9411	7110437.709	143.4	0.079	0.118
FI18_met2_10525	505975.3015	7110430.356	142.4	0.071	0.097
FI18_met2_10526	505982.6881	7110421.799	142.8	0.090	0.135
FI18_met2_10527	505990.6967	7110419.451	142.8	0.073	0.092
FI18_met2_10528	505998.2781	7110413.605	142.9	0.011	0.015
FI18_met2_10529	506001.4796	7110411.774	143.0	0.081	0.110

Point-ID	Easting	Northing	Elevation [m]	H_Prec [m]	V_Prec [m]
Fl18_met2_10530	506007.1777	7110407.708	143.0	0.086	0.116
Fl18_met2_10531	506014.3839	7110404.017	142.9	0.086	0.122
Fl18_met2_10532	506019.9446	7110402.379	143.0	0.085	0.136
Fl18_met3_0063	506028.5063	7110335.941	142.6	0.121	0.122
Fl18_met3_0064	506030.3857	7110338.974	142.8	0.106	0.117
Fl18_met3_0065	506030.085	7110340.377	142.8	0.108	0.110
Fl18_met3_0066	506031.5309	7110341.731	142.6	0.101	0.100
Fl18_met3_0067	506034.7629	7110347.211	142.9	0.106	0.094
Fl18_met3_0068	506039.0526	7110355.599	143.3	0.068	0.073
Fl18_met3_0070	506040.9705	7110358.862	143.2	0.077	0.077
Fl18_met3_0071	506042.1388	7110365.018	143.3	0.074	0.081
Fl18_met3_0072	506043.4362	7110369.244	144.1	0.100	0.109
Fl18_met3_0073	506045.0449	7110373.911	143.8	0.113	0.116
Fl18_met3_0074	506044.3082	7110374.162	143.6	0.066	0.088
Fl18_met3_0075	506044.5142	7110379.171	143.5	0.046	0.060
Fl18_met3_0076	506046.8258	7110385.21	143.7	0.078	0.086
Fl18_met3_0077	506047.0552	7110391.907	142.7	0.072	0.089
Fl18_met3_0078	506050.0761	7110396.879	143.4	0.043	0.063
Fl18_met3_0079	506046.788	7110398.691	143.4	0.044	0.072
Fl18_met3_0080	506054.9988	7110399.986	143.5	0.042	0.060
Fl18_met3_0081	506054.0567	7110404.742	143.4	0.038	0.061
Fl18_met3_0082	506054.8686	7110406.615	143.4	0.036	0.057
Fl18_met3_0083	506053.1307	7110408.778	143.4	0.035	0.059
Fl18_met3_0084	506056.8596	7110410.081	143.3	0.043	0.062
Fl18_met3_0085	506058.87	7110416.963	142.9	0.039	0.067
Fl18_met3_0086	506060.2696	7110422.328	143.1	0.051	0.076
Fl18_met3_0087	506063.2649	7110428.545	142.8	0.039	0.061
Fl18_met3_0088	506063.8401	7110434.299	142.3	0.059	0.066
Fl18_met3_0089	506063.8422	7110434.417	142.4	0.052	0.069
Fl18_met3_0090	506066.3433	7110441.393	142.3	0.038	0.059
Fl18_met3_0091	506066.3927	7110439.778	142.2	0.068	0.082
Fl18_met3_0092	506068.7451	7110448.5	142.5	0.062	0.078
Fl18_met3_0093	506068.9052	7110453.474	142.4	0.036	0.058
Fl18_met3_0094	506071.1026	7110460.862	142.4	0.040	0.060
Fl18_met3_0095	506071.5343	7110465.99	142.2	0.045	0.068
Fl18_metsa_10441	505997.5663	7110373.506	143.0	0.030	0.043
Fl18_metsa_10442	505997.8815	7110374.584	143.0	0.048	0.059
Fl18_metsa_10443	505997.947	7110375.72	143.0	0.026	0.036
Fl18_metsa_10444	505999.0035	7110377.855	143.0	0.032	0.052
Fl18_metsa_10445	505999.5038	7110379.36	142.9	0.028	0.040
Fl18_metsa_10446	505999.9302	7110380.422	142.9	0.030	0.044
Fl18_metsa_10447	506000.281	7110382.524	143.1	0.029	0.041
Fl18_metsa_10448	506000.8856	7110384.048	143.0	0.030	0.042
Fl18_metsa_10449	506001.5282	7110385.712	143.0	0.028	0.039
Fl18_metsa_10450	506002.4309	7110387.621	142.8	0.029	0.041

<b>Point-ID</b>	<b>Easting</b>	<b>Northing</b>	<b>Elevation [m]</b>	<b>H_Prec [m]</b>	<b>V_Prec [m]</b>
FI18_metsa_10451	506002.2815	7110390.146	142.9	0.030	0.043
FI18_metsa_10452	506004.5046	7110392.649	143.1	0.030	0.043
FI18_metsa_10454	506004.9281	7110394.116	143.1	0.031	0.044
FI18_metsa_10455	506004.5734	7110396.495	143.5	0.030	0.045
FI18_metsa_10456	506005.5674	7110398.542	143.7	0.033	0.048
FI18_metsa_10457	506006.2307	7110399.547	143.7	0.037	0.053
FI18_metsa_10458	506005.3173	7110402.585	142.7	0.040	0.062
FI18_metsa_10459	506005.0601	7110405.352	143.0	0.035	0.056
FI18_metsa_10460	506007.5946	7110406.223	142.8	0.037	0.067
FI18_metsa_10461	506008.4109	7110407.411	143.0	0.035	0.061
FI18_metsa_10462	506010.0316	7110409.651	143.0	0.036	0.061
FI18_metsa_10463	506011.0383	7110411.495	143.1	0.037	0.064
FI18_metsa_10464	506011.0213	7110413.534	143.1	0.039	0.067
FI18_metsa_10465	506011.1227	7110415.379	143.1	0.039	0.068
FI18_metsa_10466	506011.3622	7110417.492	143.1	0.037	0.066
FI18_metsa_10467	506012.7249	7110420.296	143.1	0.039	0.073
FI18_metsa_10468	506013.718	7110421.739	143.2	0.034	0.060
FI18_metsa_10469	506014.3781	7110423.692	143.5	0.032	0.058
FI18_metsa_10470	506015.1834	7110426.419	143.6	0.030	0.053
FI18_metsa_10471	506015.6835	7110428.528	143.6	0.031	0.056
FI18_metsa_10472	506015.6773	7110431.27	143.4	0.034	0.077
FI18_metsa_10473	506016.392	7110433.055	143.1	0.029	0.053
FI18_metsa_10474	506016.9231	7110435.702	143.1	0.033	0.060
FI18_metsa_10475	506018.167	7110438.474	143.0	0.030	0.055
FI18_metsa_10476	506019.5262	7110442.739	143.0	0.031	0.056
FI18_metsa_10477	506020.3869	7110444.758	142.7	0.031	0.067
FI18_metsa_10478	506020.6112	7110448.625	142.7	0.031	0.059
FI18_metsa_10479	506020.2412	7110450.302	142.7	0.030	0.058
FI18_metsa_10480	506021.8107	7110454.72	142.6	0.030	0.057
FI18_metsa_10481	506022.3153	7110456.338	142.7	0.029	0.055
FI18_metsa_10482	506024.2099	7110459.863	141.7	0.028	0.053
FI18_metsa_10483	506024.6585	7110462.535	141.7	0.028	0.054
FI18_metsa_10484	506025.9641	7110464.766	141.6	0.028	0.054
FI18_metsa_10485	506025.8093	7110467.814	141.7	0.031	0.060
FI18_metsa_10486	506028.4645	7110472.29	141.7	0.026	0.052
FI18_metsa_10487	506028.1044	7110474.205	141.5	0.031	0.058
FI18_metsa_10488	506030.6218	7110481.031	141.9	0.030	0.054
FI18_metsa_10489	506031.9669	7110483.22	142.0	0.034	0.060
FI18_metsa_10490	506033.2904	7110485.603	141.9	0.025	0.053
FI18_metsa_10491	506030.376	7110485.337	141.9	0.031	0.057
FI18_metsal_001	505997.564	7110373.535	143.1	0.027	0.037

**Appendix 7.****HANDHELD SUSCEPTIBILITY MEASUREMENTS [10<sup>-3</sup> S.I. units]**

ID values corresponds to last two digits of ID Appendix F

<b>Point-ID</b>	<b>Easting</b>	<b>Northing</b>	<b>Susc. [10<sup>-3</sup>]</b>
Fl18_met2_10492	506022.999	7110361.028	110
Fl18_met2_10493	506024.685	7110364.629	2.2
Fl18_met2_10494	506026.628	7110367.886	6.4
Fl18_met2_10495	506027.336	7110371.705	122
Fl18_met2_10496	506028.943	7110374.349	612
Fl18_met2_10497	506030.827	7110377.633	2.5
Fl18_met2_10498	506034.078	7110387.391	6.6
Fl18_met2_10499	506035.720	7110390.149	0.5
Fl18_met2_10500	506037.062	7110393.801	1.6
Fl18_met2_10501	506038.045	7110397.632	55
Fl18_met2_10502	506041.733	7110406.403	1552
Fl18_met2_10503	506043.075	7110417.951	832
Fl18_met2_10504	506044.077	7110424.340	1330
Fl18_met2_10505	506049.844	7110433.477	3.1
Fl18_met2_10506	506050.245	7110439.209	163
Fl18_met2_10507	506050.182	7110445.237	298
Fl18_met2_10508	506050.665	7110448.851	56
Fl18_met2_10509	506051.454	7110454.684	1.5
Fl18_met2_10510	506055.625	7110458.704	360
Fl18_met2_10511	506056.738	7110463.454	30
Fl18_met2_10512	506060.813	7110475.070	0.1
Fl18_met2_10513	505924.246	7110541.098	679
Fl18_met2_10514	505925.083	7110533.786	470
Fl18_met2_10515	505926.396	7110530.553	369
Fl18_met2_10516	505926.409	7110526.928	567
Fl18_met2_10517	505926.407	7110526.934	680
Fl18_met2_10518	505933.946	7110519.668	0.2
Fl18_met2_10519	505941.583	7110510.858	293
Fl18_met2_10520	505945.306	7110502.286	11.8
Fl18_met2_10521	505962.069	7110480.787	92.5
Fl18_met2_10522	505967.513	7110468.127	33.7
Fl18_met2_10523	505970.155	7110449.775	2.9
Fl18_met2_10524	505977.941	7110437.709	118
Fl18_met2_10525	505975.301	7110430.356	21.3
Fl18_met2_10526	505982.688	7110421.799	291
Fl18_met2_10527	505990.697	7110419.451	1057
Fl18_met2_10528	505998.278	7110413.605	327
Fl18_met2_10529	506001.480	7110411.774	345

Point-ID	Easting	Northing	Suscp. [10 <sup>-3</sup> ]
FI18_met2_10530	506007.178	7110407.708	467
FI18_met2_10531	506014.384	7110404.017	313
FI18_met2_10532	506019.945	7110402.379	76.7
FI18_metsa_10441	505997.566	7110373.506	376
FI18_metsa_10442	505997.882	7110374.584	124
FI18_metsa_10443	505997.947	7110375.720	4.3
FI18_metsa_10444	505999.004	7110377.855	278
FI18_metsa_10445	505999.504	7110379.360	377
FI18_metsa_10446	505999.930	7110380.422	253
FI18_metsa_10447	506000.281	7110382.524	219
FI18_metsa_10448	506000.886	7110384.048	8.3
FI18_metsa_10449	506001.528	7110385.712	2044
FI18_metsa_10450	506002.431	7110387.621	2129
FI18_metsa_10451	506002.282	7110390.146	495
FI18_metsa_10452	506004.505	7110392.649	48.2
FI18_metsa_10454	506004.928	7110394.116	54.8
FI18_metsa_10455	506004.573	7110396.495	1.2
FI18_metsa_10456	506005.567	7110398.542	0.7
FI18_metsa_10457	506006.231	7110399.547	0.6
FI18_metsa_10458	506005.317	7110402.585	755
FI18_metsa_10459	506005.060	7110405.352	3.5
FI18_metsa_10460	506007.595	7110406.223	150
FI18_metsa_10461	506008.411	7110407.411	70.8
FI18_metsa_10462	506010.032	7110409.651	1.8
FI18_metsa_10463	506011.038	7110411.495	5.3
FI18_metsa_10464	506011.021	7110413.534	2
FI18_metsa_10465	506011.123	7110415.379	3
FI18_metsa_10466	506011.362	7110417.492	124
FI18_metsa_10467	506012.725	7110420.296	132
FI18_metsa_10468	506013.718	7110421.739	5.1
FI18_metsa_10469	506014.378	7110423.692	90
FI18_metsa_10470	506015.183	7110426.419	427
FI18_metsa_10471	506015.684	7110428.528	268
FI18_metsa_10472	506015.677	7110431.270	162
FI18_metsa_10473	506016.392	7110433.055	65
FI18_metsa_10474	506016.923	7110435.702	3.6
FI18_metsa_10475	506018.167	7110438.474	360
FI18_metsa_10476	506019.526	7110442.739	383
FI18_metsa_10477	506020.387	7110444.758	52
FI18_metsa_10478	506020.611	7110448.625	315
FI18_metsa_10479	506020.241	7110450.302	598
FI18_metsa_10480	506021.811	7110454.720	479
FI18_metsa_10481	506022.315	7110456.338	713
FI18_metsa_10482	506024.210	7110459.863	349

<b>Point-ID</b>	<b>Easting</b>	<b>Northing</b>	<b>Suscp. [10<sup>-3</sup>]</b>
FI18_metsa_10483	506024.658	7110462.535	436
FI18_metsa_10484	506025.964	7110464.766	510
FI18_metsa_10485	506025.809	7110467.814	200
FI18_metsa_10486	506028.465	7110472.290	401
FI18_metsa_10487	506028.104	7110474.205	5.8
FI18_metsa_10488	506030.622	7110481.031	0.6
FI18_metsa_10489	506031.967	7110483.220	1.1
FI18_metsa_10490	506033.290	7110485.603	0.5
FI18_metsa_10491	506030.376	7110485.337	0.3

## Appendix 8.

### hXRF MEASUREMENTS [wt-%]

ID values corresponds to last two digits of ID Appendix F

ID	MgO	Al2O3	SiO2	S	CaO	TiO2	Fe2O3
47	1.19	2.73	11.38	0.17	2.57	0.12	1.84
48	1.71	2.44	13.15	0.40	3.20	1.12	10.06
50	< LOD	9.92	36.51	0.24	5.87	0.15	2.52
51	< LOD	9.81	23.92	1.25	6.29	0.28	11.34
52	2.32	8.06	28.65	1.12	6.98	4.25	18.62
54	2.04	10.45	29.04	< LOD	5.91	13.42	17.50
55	< LOD	6.12	33.95	0.15	3.32	0.34	4.29
56	2.76	9.35	35.43	0.13	7.59	0.54	11.33
57	1.10	< LOD	0.91	0.18	< LOD	0.04	1.51
58	< LOD	5.98	17.97	0.19	5.13	3.60	18.56
59	5.85	5.55	6.55	0.05	< LOD	10.27	42.11
60	< LOD	4.49	17.33	0.41	2.26	3.13	16.08
61	< LOD	11.37	12.55	5.70	3.04	6.19	36.53
62	5.57	7.56	32.01	< LOD	8.59	9.61	15.71
63	< LOD	10.16	44.21	0.15	4.17	2.23	12.74
64	1.49	2.69	9.71	0.35	4.24	2.90	17.85
65	< LOD	17.44	58.97	0.66	6.81	0.30	3.04
66	< LOD	5.40	26.46	0.72	4.54	0.74	9.78
67	2.48	1.66	6.31	0.08	2.39	3.27	18.39
68	4.91	7.45	18.53	0.13	4.83	5.86	34.24
69	3.60	13.18	34.52	< LOD	4.61	4.91	40.57
70	5.91	17.36	47.17	0.06	7.75	2.63	16.89
71	< LOD	5.30	4.77	4.25	1.18	1.80	35.93
72	1.65	6.75	22.91	0.22	6.82	1.15	11.11
73	1.92	1.94	10.33	0.27	4.73	0.62	10.43
74	7.03	11.44	39.23	0.04	10.00	1.57	12.84
75	1.24	4.57	17.91	0.21	4.73	1.51	4.92
76	< LOD	4.84	17.10	0.19	4.32	0.07	3.41
77	0.98	1.55	10.56	0.03	1.99	0.15	1.61
78	1.10	2.42	12.15	0.14	3.66	0.19	2.19
79	1.17	1.04	10.70	0.19	2.03	0.64	7.30
80	< LOD	7.82	19.86	0.18	4.22	4.01	21.63
81	< LOD	7.38	33.91	0.47	1.06	1.02	24.84
82	< LOD	2.27	1.93	2.93	0.64	4.73	48.09
83	< LOD	6.54	21.68	0.28	5.23	0.56	5.52
84	1.56	3.21	13.34	0.26	5.20	1.46	13.21
85	1.58	4.17	17.41	0.11	5.28	0.96	12.39
86	2.69	5.00	15.74	0.19	5.57	2.63	15.49
87	< LOD	4.20	< LOD	7.13	0.65	1.54	44.69

<b>ID</b>	<b>MgO</b>	<b>Al<sub>2</sub>O<sub>3</sub></b>	<b>SiO<sub>2</sub></b>	<b>S</b>	<b>CaO</b>	<b>TiO<sub>2</sub></b>	<b>Fe<sub>2</sub>O<sub>3</sub></b>
88	4.08	6.48	8.24	< LOD	0.75	13.18	59.41
89	< LOD	4.68	10.95	< LOD	0.41	22.28	44.27
90	1.18	17.85	40.35	0.07	7.93	1.06	5.54
91	< LOD	17.83	36.69	< LOD	18.06	1.19	14.69
92	1.87	2.86	9.51	1.52	4.86	3.85	29.51
93	1.71	4.87	23.31	0.21	4.86	2.48	15.50
94	1.71	5.33	18.85	0.15	4.84	1.09	11.57
95	< LOD	8.99	41.70	0.26	4.71	0.92	9.44



All GTK's publications online at [hakku.gtk.fi](http://hakku.gtk.fi)



Helmholtz-Institut Freiberg für Ressourcentechnologie

